

If you have discovered material in AURA which is unlawful e.g. breaches copyright, (either yours or that of a third party) or any other law, including but not limited to those relating to patent, trademark, confidentiality, data protection, obscenity, defamation, libel, then please read our [Takedown Policy](#) and [contact the service](#) immediately

Discrete Element Modelling of a rotating drum and drum granulation

by

Daksha Bhimji, MSci (Hons)

Department of Civil Engineering and Logistics
Aston University

A thesis submitted to Aston University in fulfilment of the
requirements for admission to the degree of

Doctor of Philosophy

October 2009

This copy of the thesis has been supplied on the condition that anyone who consults it is understood to recognise that its copyright rests with its author and that no quotation from the thesis and no information derived from it may be published without proper acknowledgement.

Declaration

This thesis describes the work carried at Aston University under the supervision of Prof Roger Kettle and Dr Colin Thornton. The work reported in this thesis has been composed by myself and has not, nor any similar dissertation, submitted in any previous application for a degree.

Aston University

Discrete Element Modelling of a Rotating Drum and Drum Granulation

Daksha Bhimji, M.Sci.
Doctor of Philosophy
2009

SUMMARY

This thesis reports the results of DEM (Discrete Element Method) simulations of rotating drums operated in a number of different flow regimes. DEM simulations of drum granulation have also been conducted. The aim was to demonstrate that a realistic simulation is possible, and further understanding of the particle motion and granulation processes in a rotating drum. The simulation model has shown good qualitative and quantitative agreement with other published experimental results.

A two-dimensional bed of 5000 disc particles, with properties similar to glass has been simulated in the rolling mode (Froude number 0.0076) with a fractional drum fill of approximately 30%. Particle velocity fields in the cascading layer, bed cross-section, and at the drum wall have shown good agreement with experimental PEPT data. Particle avalanches in the cascading layer have been shown to be consistent with single layers of particles cascading down the free surface towards the drum wall. Particle slip at the drum wall has been shown to depend on angular position, and ranged from 20% at the toe and shoulder, to less than 1% at the mid-point.

Three-dimensional DEM simulations of a moderately cascading bed of 50,000 spherical elastic particles (Froude number 0.83) with a fractional fill of approximately 30% have also been performed. The drum axis was inclined by 5° to the horizontal with periodic boundaries at the ends of the drum. The mean period of bed circulation was found to be 0.28s. A liquid binder was added to the system using a spray model based on the concept of a 'wet surface energy'. Granule formation and breakage processes have been demonstrated in the system.

KEY WORDS: Discrete Element Method; Rolling; Cascading; Rotary kiln; Granule.

Acknowledgements

I gratefully acknowledge my supervisors Prof Roger Kettle and Dr Colin Thornton for everything they have done for me over the years – from giving me help, advice and support to reading through my thesis and giving me valuable comments.

I would like to extend my gratitude to Dr David Kafui of the Department of Chemical Engineering at Birmingham University, for his time and his help and advice in the use and modification of the original ‘GRANULE’ program described in Chapter 3 and the use of his spray model described in Chapter 6.

I would also like to thank my office colleagues and friends in Lakeside Residence, where I was surrounded by friendly and knowledgeable people who helped me daily, Prabhaker, Hema, Martin, Nupur, Dharmesh, Dheeraj, Bav, Xia and Muriel. My other neighbours, including Michel, Tasos, Mariana, Manos, Gary and Rachel were each a great help in their own way, and thank you all for putting up with me and for your good cooking.

In addition to the people in Aston, I have been lucky enough to have the support of many good friends. I would like to thank my best friend and classmate Clair Atterbury, and also my very good friends Sajid and Mandana, who were always offering me invaluable advice and support while writing.

Financial support from the Engineering and Physical Sciences Research Council and the Unilever group is gratefully acknowledged.

Last but not least I would like to acknowledge my family, and Matthew whose love and support are never taken for granted. Matthew reached hero status in the last three months; he helped me in many ways from proof reading my thesis and giving me valuable feedback to structuring ideas and making me lots of teas and coffees! They gave me great motivation to finally write up, so I dedicate this thesis to them.

Table of contents

Declaration	2
Summary	3
Acknowledgements	4
Table of contents	5
List of figures	9
List of tables	14
1 Introduction	15
1.1 Objectives.....	15
1.2 Thesis outline	16
2 Brief review of rotating drums	19
2.1 Introduction	19
2.2 Rotating drum apparatus	20
2.3 Particle motion in a rotating drum.....	22
2.3.1 Longitudinal motion.....	22
2.3.2 Transverse motion.....	23
2.3.3 Transverse motion in the rolling mode	25
2.4 Theoretical work and modelling techniques	26
2.4.1 DEM Validation.....	28
2.4.2 Previous DEM results	28
2.5 Experimental techniques	32
2.5.1 Avalanche observations.....	32
2.5.2 PEPT experiments.....	34
2.5.3 X-ray filming	35
2.5.4 Scaling relations.....	35
2.6 Measurable parameters	37
2.6.1 Particle motion parameters.....	37
2.6.2 Bulk bed parameters.....	38
2.6.3 Mixing and Segregation	40
3 Simulation model and preliminary simulations	44
3.1 Discrete Element Method simulation model.....	44
3.2 Modifications to GRANULE	45

3.3	Preliminary 2-D drum simulations	48
3.3.1	Settling particles in a two-dimensional drum	48
3.3.2	Equilibrium balance test	55
3.3.3	Tangential force tests	57
3.3.4	Demonstrations of flow regimes	58
3.4	3-D drum simulations	64
3.4.1	System parameters	64
3.4.2	Drum configuration	66
4	DEM simulations in the rolling regime	71
4.1	Description of rolling drum simulation	72
4.1.1	Projected effect of drum and material parameters	73
4.2	Qualitative observations	77
4.2.1	Particles represented as discs	78
4.2.2	Bed velocity field	79
4.2.3	Bed radial velocity field	85
4.2.4	Bed tangential velocity field	87
4.2.5	Particle connectivity	89
4.3	Contact angle measurements	91
4.3.1	Avalanche measurements	94
4.4	Angle of repose	98
4.5	Determination of steady state dynamics	99
4.6	Particle velocities at the drum wall	101
4.7	Particle spin at the drum wall	106
4.8	Particle velocities in the free surface	108
4.9	Particle velocities in the bed cross-section	117
4.10	Summary	123
5	Granulation	125
5.1	Introduction	125
5.2	Granulation fundamentals	128
5.2.1	Bonding mechanisms within granulates	128
5.2.2	Wet granulation mechanisms	131
5.2.3	Measures of granulation (particle size analysis & granulation efficiency)	139
5.3	Granulation equipment	140
5.4	Important aspects of drum granulation	145

5.4.1	Granulation efficiency.....	146
5.4.2	Importance of correct rolling.....	146
5.4.3	The effect of drum speed on drum granulation.....	147
5.4.4	Spray location in drum granulation.....	147
5.4.5	Moisture content.....	148
5.5	Previous experimental work.....	151
5.6	Previous modelling work.....	154
5.7	Summary.....	158
6	DEM simulations of drum granulation.....	161
6.1	Introduction.....	161
6.2	Spray model.....	162
6.2.1	“Wetting” in the spray zone.....	164
6.2.2	Particle “drying” outside the spray zone.....	165
6.2.3	Bond “drying” outside the spray zone.....	166
6.2.4	Spray set-up in drum.....	167
6.3	3D particle trajectories.....	169
6.3.1	Single tracer particle trajectory.....	170
6.3.2	Bed circulation period.....	173
6.4	Qualitative observations of granulation.....	175
6.4.1	Granule number evolution.....	175
6.4.2	Velocity fields.....	175
6.4.3	Granule transport and breakage.....	179
6.5	Summary.....	182
7	Conclusions.....	185
7.1	Results from 2D rolling bed simulations.....	185
7.2	Results from 3D cascading bed simulations.....	187
7.3	Limitations.....	188
7.4	Recommendations for further work.....	189
	References.....	191
	Appendix A. The Discrete Element Method.....	198
A.1	Newton’s second law of motion.....	198
A.2	Force-displacement laws.....	198
A.3	Motion update.....	202
A.4	Program GRANULE.....	207

A.5	Contact detection	208
A.6	Damping	209
A.7	Numerical stability	210
Appendix B.	Modifications to GRANULE for rotating drum work	212
B.1	Data array modifications	212
B.2	Code additions to GRANULE	212
Appendix C.	Ball-wall contacts only	232
Appendix D.	Circulation period of tracked particles	234

List of figures

Figure 2.1: A typical rotating drum from a laboratory experiment <i>Jaeger (1993)</i>	21
Figure 2.2: The path of a particle in a rotating kiln, from <i>Zablotny (1965)</i>	22
Figure 2.3: The different modes of transverse bed motion	24
Figure 2.4: Regions of motion in the transverse plane.....	25
Figure 2.5: Sketch of the drum and bed surface indicating the bottom contact line, A, and the angular position, θ	32
Figure 2.6: Time recording of the bottom contact line position of the particle bed according to Fauve et al. (1991). Drum length=13cm, particle diameter=0.5-0.63cm, (a) $\omega=0.033$ RPM, (b) $\omega=1.25$ RPM	33
Figure 2.7: The active and passive region in the rolling mode and bed depth, wz	38
Figure 3.1 : Particle-wall interaction with wall modelled as a tangential plane.....	47
Figure 3.2: Initial particle generation, before starting to settle the bed.	50
Figure 3.3: Time evolution of ball-ball contacts.....	52
Figure 3.4: Time evolution of the maximum and average particle velocities	52
Figure 3.5: Time evolution of the centre of mass coordinates as the bed settles.....	52
Figure 3.6: Settled bed at time, $t=0.8$ s, when equilibrium is established.....	53
Figure 3.7: Connection diagram of the settled bed.	53
Figure 3.8: A picture of the velocity field of the settled bed.....	54
Figure 3.9: Settled bed of 22 particles.....	55
Figure 3.10: 'cir' image of the system in the steady state, $\omega = 1$ rad/s.....	59
Figure 3.11: Velocity field of the avalanching bed, $\omega = 1$ rad/s.....	59
Figure 3.12: Connection diagram of the avalanching bed, $\omega = 1$ rad/s.....	60
Figure 3.13: 'cir' image of the bed cataracting, $\omega = 12$ rad/s.....	61
Figure 3.14: Velocity field of the cataracting bed, $\omega = 12$ rad/s	61
Figure 3.15: Connection diagram of the cataracting bed, $\omega = 12$ rad/s	62
Figure 3.16: 'cir' image of the bed centrifuging, $\omega = 20$ rad/s.....	63
Figure 3.17: Velocity field of the centrifuging particulate system, $\omega = 20$ rad/s	63
Figure 3.18: A connection diagram of the centrifuging particles, $\omega = 20$ rad/s	64
Figure 3.19: Position of 3D drum with respect to the axes	67

Figure 3.20: After $\sim \frac{1}{4}$ drum revolution the particles have moved almost like a rigid body	69
Figure 3.21: After $\frac{3}{4}$ drum revolution the fast flowing layer of particle develop at the free surface	70
Figure 4.1: Snapshots of the rolling bed animation, cir_1.avi at different times, t.....	79
Figure 4.2: Snapshots from the speed/velocity animations for the drum.....	81
Figure 4.3: Snapshots taken from the radial speed/velocity animations for the drum.....	86
Figure 4.4: Snapshots taken from the tangential speed animations for the drum.....	88
Figure 4.5: Connection diagram snapshots taken from the end_1.avi animation.....	90
Figure 4.6: Time evolution of the total number of contacts.....	90
Figure 4.7: Time evolution of contact angle for the rolling drum	92
Figure 4.8: Time evolution of contact angle between times 3.36s and 6.49s. The high frequency, small amplitude fluctuations correspond to minor avalanches.....	93
Figure 4.9: Time evolution of contact angle between times 5.0 and 5.2s.....	94
Figure 4.10: Avalanche magnitude histogram.....	95
Figure 4.11: Avalanche interval histogram	96
Figure 4.12: Avalanche magnitude plotted against avalanche interval.....	97
Figure 4.13: Avalanche duration histogram	97
Figure 4.14: Time evolution of the angle of repose for the rolling drum	98
Figure 4.15: Time evolution of the angle of repose between times 3.36s and 6.49s.....	99
Figure 4.16: Translational velocity histogram for the particles within a 5mm thickness from the drum wall at t=4.89s	101
Figure 4.17: Rotational velocity histogram for the particles within a 5mm thickness from the drum wall at t=4.89s	102
Figure 4.18: Translational velocity along the drum wall at t=4.89s.....	104
Figure 4.19: Rotational velocity along the drum wall at t=4.89s	105
Figure 4.20: Rotational velocity along the drum wall close to the 6 o'clock position, at t=4.89s	105
Figure 4.21: Particle spin velocity along the drum wall, at t=4.89s	107
Figure 4.22: Particle spin velocity close to the drum wall at increasing drum radii, at t=4.89s	107
Figure 4.23: Characterisation of position in the free surface	108
Figure 4.24: Cascade Velocity Histogram.....	109
Figure 4.25: Cascade Translational Velocity along the distance d.....	110

Figure 4.26: Cascade Translational Velocity along distance l	111
Figure 4.27: Rotational Velocity in the cascade	112
Figure 4.28: Cascade Parallel Velocity Histogram	113
Figure 4.29: Parallel Velocity in the free surface	113
Figure 4.30: Parallel Velocity in the cascade along distance l	114
Figure 4.31: Cascade Perpendicular Velocity Histogram	114
Figure 4.32: Perpendicular Velocity in the cascade along distance, d	115
Figure 4.33: Perpendicular Velocity in the cascade along distance, l	115
Figure 4.34: Cascade Particle Size Histogram	116
Figure 4.35: Characterisation of position in bed cross-section	117
Figure 4.36: Translational velocity histogram in the bed cross section	118
Figure 4.37: Mean translational velocity along the radius, r	118
Figure 4.38: Mean perpendicular velocity in the bed cross-section along, r	120
Figure 4.39: Histogram of radial velocities in the bed cross-section	120
Figure 4.40: Mean radial velocity in the bed cross-section along, r	121
Figure 4.41: Histogram of the particle rotational velocity in the bed cross-section	121
Figure 4.42: Mean rotational velocity in the bed cross-section along, r	122
Figure 4.43: Mean particle size in the bed cross-section along, r	122
Figure 5.1: Classification of the field of granulation according to <i>Sherrington and Oliver (1981)</i>	127
Figure 5.2: Illustration of solid bridges between two particles in a granule	129
Figure 5.3: States of liquid content in a granule	129
Figure 5.4: Interlocking of two strands of fibres and of two particles	131
Figure 5.5: Schematic of granulation processes according to <i>Iveson et al. (2001)</i> : a) Traditional view (<i>Sastry et al. (1973)</i>), b) Modern approach (<i>Ennis et al. (1997)</i>)	132
Figure 5.6: Particle size distribution curve for simple powders from <i>Snow et al. (1997)</i> ..	140
Figure 5.7: Cumulative distribution curve for simple powders from <i>Snow et al. (1997)</i> ..	140
Figure 5.8: Granulator types from <i>Wildeboer (2002)</i>	141
Figure 5.9: Typical industrial (continuous) drum granulator with liquid sprays above the bed by <i>Sherrington et al. (1981)</i>	143
Figure 5.10: Industrial drum granulator with the spray or sparger inserted in the bed, used for example in the fertiliser industry by <i>Browning (1967)</i>	143
Figure 5.11: See saw motion with mass relatively static from <i>Brook (1957)</i>	148

Figure 5.12: Rolling motion without cascading due to low speed of rotation from <i>Brook (1957)</i>	148
Figure 5.13: Ideal cascading motion resulting from correct speed of rotation, from <i>Brook (1957)</i>	148
Figure 5.14: Average pellet diameter d as a function of granulation time and the three regions of growth (42.5% vol. Moisture), from <i>Kapur et al. (1964)</i>	151
Figure 5.15: Pellet size distribution after various granulation times. (42.5% vol. Moisture) from <i>Kapur et al. (1964)</i>	152
Figure 5.16: Simulation model of Granule formation <i>Kano et al. (2005)</i>	156
Figure 6.1: Notional representation of spray zone as a conical region.....	163
Figure 6.2: Accumulation of surface energy for fixed and moving particles in spray zone for $\gamma_{wmax}=0.5Jm^{-2}$ from <i>Kafui et al. (2008)</i>	165
Figure 6.3: Notional drying of wet surface energy outside spray zone for $\gamma_{wmax} = 0.5Jm^{-2}$ and $t_{dmax} = 10s$ from <i>Kafui et al. (2008)</i>	166
Figure 6.4: Increasing adhesive energy during bond drying for various initial wet surface energies from <i>Kafui et al. (2008)</i>	167
Figure 6.5: 3D cascading bed selected as the approximate steady state ready for spray insertion, $t = 0.40s$	169
Figure 6.6: Transverse trajectories of 22 different particles in the 3D cascading bed. For $t=0.4$ to $0.676s$	169
Figure 6.7: Axial trajectories of 22 different particles in the 3D cascading bed. For $t=0.4$ to $0.676s$	170
Figure 6.8: Trajectory of particle 1 in the 3D cascading bed. For $t=0.4$ to $0.676s$	172
Figure 6.9: Time evolution of x-component of all tracked particles, for $t=0.4 - 0.676s$	173
Figure 6.10: Example Sine fits for particle x-position.	174
Figure 6.11: Bed circulation period for all tracked particles.....	174
Figure 6.12: Particulate bed shortly after spray activation, at $t = 0.412s$	176
Figure 6.13: Particulate bed shows few granules leaving spray zone, at $t = 0.420s$	176
Figure 6.14: Granules are shown without the rest of the particulate bed, at $t = 0.420s$	176
Figure 6.15: The granules are shown in more detail and from different angles, at $t = 0.420s$ (particle in the spray zone are also coloured green).....	177
Figure 6.16: Size distribution of granules at times, (a) $t = 0.412s$, (b) $t = 0.420s$ and (c) $t = 0.643s$	177

Figure 6.17: Translational velocity field of the cascading bed, at $t = 0.420s$	178
Figure 6.18: Tangential velocity field of the cascading bed, at $t = 0.420s$	178
Figure 6.19: Radial velocity field of the cascading bed, at $t = 0.420s$	178
Figure 6.20: Particulate bed shows granules leaving spray zone and progressing down the free surface, at $t = 0.643s$	181
Figure 6.21: Granules are shown without the particulate bed except for wet particles in spray zone (indicated also by green), at $t = 0.643s$	181
Figure 6.22: Connection diagram of cascading bed, at $t = 0.643s$	182

List of tables

Table 2.1: Description of the drums used in Parker's PEPT experiments from <i>Parker et al. (1997)</i>	34
Table 3.1: The Gaussian size distribution is used for the particles in the simulation.....	49
Table 3.2: Summary of the mechanical properties for particles and wall.....	49
Table 3.3: Summary of the summed force components acting on the wall and the expected weight of the bed for a system of 22 particles	56
Table 3.4: Summary of the summed force components acting on the wall and the expected weight of the bed for a system of 5000 particles	56
Table 3.5: List of the tangential force components for all ball-wall contacts.....	57
Table 3.6: The Gaussian size distribution used for the particles in the 3d-simulation	65
Table 3.7: Summary of the mechanical properties for particles and wall.....	65
Table 3.8: Summary of system variables for the 3D simulation	67
Table 4.1: Summary of the drum and particle bed parameters.....	72
Table 4.2: Summary of the drum and particle bed parameters.....	72
Table 5.1: Growth regimes according to Stokes number.	136
Table 5.2: Characteristic of typical drum granulators. 1,2 according to <i>Snow et al. (1997)</i> , 3 according to <i>Browning (1967)</i>	144
Table 5.3: Summary of operational characteristics of different types of granulators from <i>Ennis, B.J. et al. (1997)</i>	145
Table 5.4: Moisture content used by various experimentalists in their batch laboratory balling drums.....	150
Table 6.1: Summary of system variables for the 3D simulation	161
Table 6.2: Summary of the spray parameters used in the drum granulator.....	168

1 Introduction

Granulation is an important size enlargement process in the chemical and metallurgical industries. In very general terms, granulation is the formation of larger entities from smaller constituents. One of the most commonly used granulation apparatuses is the drum granulator, due to its ease of operation and simplicity. Raw powdered material is fed into the granulator and a liquid binder is sprayed onto the material whilst the drum rotates. Composite particles, known as granules, are formed due to the presence of the liquid binder.

The transformation from powder to granule is not a simple one. There is a vast literature describing the theories that have been put forward to explain the mechanisms empirically, but very little is known about the micro-mechanics of the process. A better understanding of the granulation process is therefore very likely to improve the granulated product quality, and can give more efficient granulation.

A recent approach, which is complementary to empirical experimentation, is the use of computer modelling of particle motion and granulation. Only recently has it been possible to apply detailed computer modelling to the problem of granulation, because the systems to be simulated are very large, and therefore very computationally expensive. The Discrete Element Method for solving the differential equations of particle motion in a many-body system has been developed over the last 30 years, and is starting to find many new applications with the recent advances in computer power.

1.1 Objectives

This project has been supported by the EPSRC and the Unilever group for the study of granulation in a rotating drum. The project is concerned with the development of a tool that has the potential to realistically simulate granulation in a rotating drum.

An accurate description of the particle dynamics in the drum is the key to the determination of various important parameters of the drum granulator. To simulate the motion of particles in the drum, a general purpose DEM code, GRANULE, was modified to model particle

motion in a rotating drum. A key objective was to show that with these modifications, the tool could be applied to rotating drums to produce realistic particle motion, validated by experimental data.

In addition to generating realistic particle motion, the aim was to show that with the introduction of a liquid binder, the processes of granulation could also be modelled.

1.2 Thesis outline

This thesis presents two distinct analyses: the first is a 2D study concerned purely with transverse particle motion in the rotating drum. The second study is a fully 3D simulation of particle dynamics in a granulating system. Accordingly, the thesis is organized with two main analysis chapters: chapter 4 deals with the 2D simulations, and chapter 6 deals with the 3D simulations. There are two corresponding literature reviews: chapter 2 addresses the published work on particle motion in rotating drums, and chapter 5 reviews the field of granulation. Chapter 3 discusses the common simulation model and details the parameters used for all these studies. Chapter 7 concludes with a summary of the results and recommendations for future work. The following is a brief synopsis of chapters 2-6:

Chapter 2 gives a literature review on rotating drum work. Applications and use of the drum are given. Types of particle motion in the drum are described, focusing on the motion in the rolling drum. Various modelling techniques and results are presented. Finally, chapter 2 lists the relevant parameters to be measured and compared to those measured by other workers.

Chapter 3 introduces the simulation model and code modifications, and further details are given in an appendix. The preparation procedure for the 2D and 3D drum systems is presented. Some simple model validation checks are also given.

Chapter 4 presents simulation results for the 2D rolling drum already described in chapter 3. Particle motion in the rolling regime is qualitatively compared with other published results.

Chapter 5 gives a general literature review of the field of granulation, focussing on drum granulation toward the end of this chapter. The theoretical models for granulation processes are described, and the industrial equipment is reviewed.

Chapter 6 describes a 3D drum granulation simulation. Particle trajectories are analysed in three dimensions, and compared to a simple model of axial transport. The evolution of the granule population is examined.

2 Brief review of rotating drums

2.1 Introduction

Rotating drums are used in a wide variety of industrial applications, including granulation which is discussed in detail later in this thesis. Some key industrial applications of rotating drums are in:

- Mining
- Metallurgy
- Chemical industry
- Agriculture and food handling
- Building materials
- Pharmaceutical industry

An industrial rotating drum can serve several possible purposes:

- Kiln
- Mixing
- Drying
- Chemical reactor
- Granulation
- Coating
- Milling

A comprehensive understanding of the particle motion in a drum under varied conditions and drum dynamics is essential in order to optimise these processes. As a result there has been much research into the flow of material in the drum over the last 10 years; some of this will be described later in this chapter.

2.2 Rotating drum apparatus

Industrial applications of rotating drums often involve processes that require long residence times, and are controlled by heat addition and the exchange of gaseous reagents and products from within the solid phase. Calcination and sintering processes are examples of processes that use heat addition and exchange of gaseous reagents in industrial rotary drums or kilns. For such processes the drum is lined with steel, or refractory brick, which is heat resistant.

Rotating drums are often used as vessels for chemical reactions, because this allows mixing of large volumes of reactants. Gaseous reagents are passed over the material bed, mass transfer occurs through the surface of the bed. Heat transfer occurs through radiation and convection through the bed surface, and also by conduction between the drum wall and the material in contact with it. If mixing of the material bed with a gaseous reagent is required, then lifter bars can be fitted to the inner wall of the drum. The lifter bars raise the material out of the bed and drop it into the gas stream.

In milling, the drum (mill) may contain steel balls or rods (or flint or porcelain.. etc) in addition to the mill material to cause breakage and size reduction within the material. The mill is operated at a rotational speed to give flow patterns in the material that give high collision rates (i.e. for cascading and cataracting motion, see section 2.3.2).

There is a lot of literature and research that uses a small laboratory drum to investigate the behaviour of the material inside rotating drums. Therefore we shall give a brief description of a typical laboratory drum: the drum rests on rollers to allow free rotation. Bracket rims to fix the drum position are mounted on the outside of the drum. A gear wheel attached to the outside of the drum is driven through a system of gears by an electric motor to rotate the drum. A typical laboratory drum is shown in Figure 2.1. In the figure the drum is made of perspex however industrial drums are usually made of steel. The drum is partly filled with granular material and is rotated about its axis at a constant angular velocity. Its axis of rotation is commonly inclined, to assist material transport through the drum.

A drum granulator is basically a rotating drum that is fitted with a binder device such as a spray or sparger to deliver binder to the material inside it. Drum granulation is one of the most commonly used granulation processes for its simplicity and ease of operation. A more detailed description of a rotating drum and drum granulators can be found in section 5.3 in drum granulator equipment.

Mixing is very important in many industrial applications ranging from the blending of powders for pharmaceuticals to mixing the ingredients to making cement or glass. There are many types of drum mixers, such as pug mills, paddle mills, low-speed mixers. These devices have horizontal troughs in the drum that rotate central shafts with attached mixing blades or bar, rod, paddle etc. Some mixers such as low shear mixers are finding increasing use in granulation, here a spray is inserted in the mixer to cause particles to bind within the material. One advantage of mixers is they are less sensitive to operating conditions when compared to the simple rotating drum.

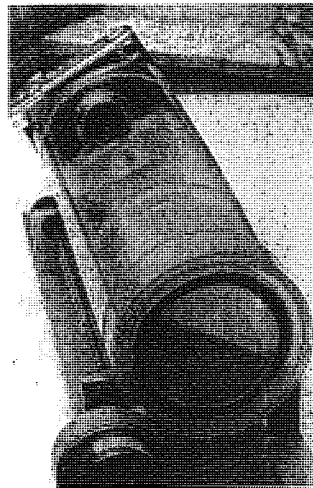


Figure 2.1: A typical rotating drum from a laboratory experiment *Jaeger (1993)*

Even with the development of newer equipment such as high shear mixers, or fluidised beds, rotating drums continue to have applications today because they can handle different materials with varying properties and wide size distributions.

2.3 Particle motion in a rotating drum

There are two types of particle motion in a rotating drum: transverse (rotation) and longitudinal (the flow through the drum).

2.3.1 Longitudinal motion

Longitudinal motion of the charge in a rolling mode is due to the inclination of the drum. However, the inclination of industrial drums is usually smaller than the angle of slide of the charge material. This means that if the drum were stationary, there would be no longitudinal motion of the charge through the drum.

The bulk of material in a rolling bed has no relative motion with respect to the drum. So if a single particle is traced in the drum it will describe a circular path at a distance r from the drum axis, in the transverse plane of the drum. The angular velocity on this arc is equal to the angular velocity on the drum wall. When the particle reaches the surface of the material it cascades downwards on the surface, along a straight line, progresses a short distance axially through the drum, it comes to rest at some lower point, the cycle is then repeated (Saeman (1951), Kramers et al. (1952)).

Figure 2.2, shows a similar diagram to that used by Zablony (1965) to describe the motion in a rolling drum. In the figure, longitudinal motion occurs for a particle tracer between points 1' and 2, but not between points 1 and 1'.

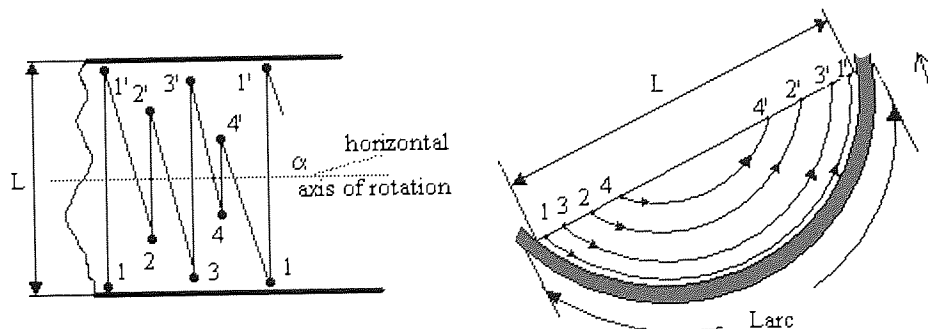


Figure 2.2: The path of a particle in a rotating kiln, from Zablony (1965).

In the rolling drum, a charge particle travels longitudinally along the drum axis whilst in the free flowing surface. Particles lower down the bed, close to the drum wall, say at point 1, do not travel longitudinally, but instead move together with material along the arc between 1 and 1'. They then fall under the influence of gravity along the free surface from 1' to 2 and once again move with the material along the arc 2 and 2', etc. *Zablotny (1965)*.

2.3.2 Transverse motion

The transverse charge motion in the drum can be classed into six categories as described by *Rutgers (1965)* and *Henein et al. (1983)*. These are as follows, in order of increasing drum speed:

1. Slipping.

At very low speed the material in the drum, or charge material slips and therefore remains at rest. This is well understood to give poor mixing of the drum material, but the conditions giving rise to bed slippage are only partially understood

2. Slumping.

If the drum speed is slightly increased, but low such that the effect of centripetal acceleration can be neglected, then the displacement of the centre of gravity of the charge will increase until the tangential force at the drum wall is equal to the frictional force. In this case the whole charge slips back, the material is continuously lifted by the drum wall, and periodically falls down the surface in discrete avalanches. This is known as *slumping*.

3. Rolling.

The period of time between slumps decreases as the rotational speed increases until eventually avalanches are no longer detectable and a continuously surface flow is observed, the charge motion exhibits rolling motion. In this motion the charge will travel along circular arcs concentric with the drum perimeter until

the point of instability is reached, after which they roll down the surface in a series of parallel layers, a thin layer of these continuously falling particles make a plane free surface. At low speeds the rolling bed takes up a flat planar surface and the inclination of this surface is constant. The falling layer is found to make up between 8 to 45% of the bed depth. Radial mixing of the bed is poor in the slipping mode so the drum is normally operated in the slumping or rolling mode to give good mixing. In industry rotating drums are usually operated in the slumping or rolling mode.

4. Cascading.

Increasing the speed further leads to cascading, characterised by a curved free surface as material is carried higher up the drum wall before detaching and mixing into the sliding layer, see Figure 2.3(d).

5. Cataracting.

At higher speeds the charge carried up the wall is projected into free space, the charge is said to cataract, Figure 2.3(e).

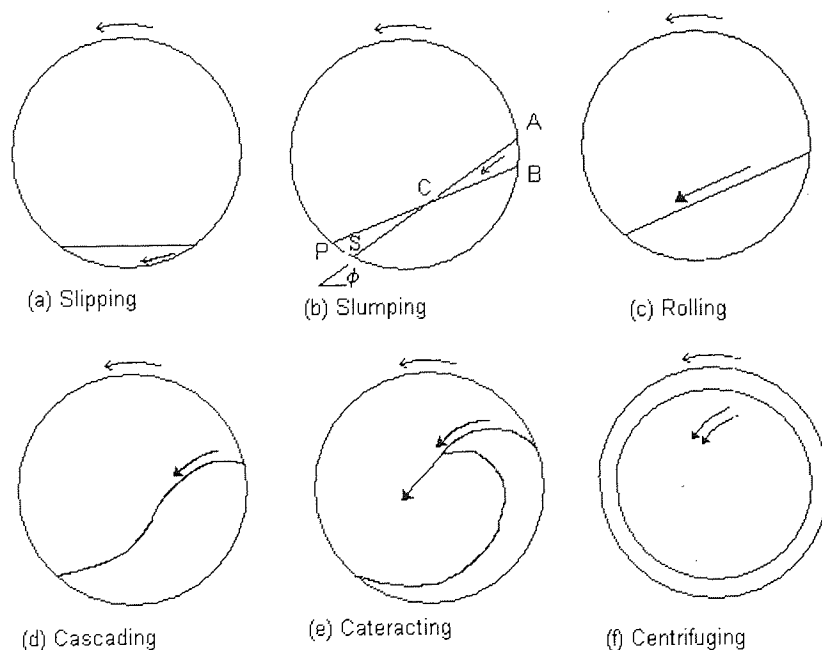


Figure 2.3: The different modes of transverse bed motion

6. Centrifuging.

At very high drum speeds, the charge no longer is projected but lies against the drum wall and is carried around continuously with the drum wall. This type of motion is classed as centrifuging. Centrifuging of the outermost layer of particles occurs when the drum is operated at the critical speed. (Refer to end of section 2.5.4 and Equation 2.1 which describes the drum critical speed)

The speed ranges over which these regimes occur are not well defined and are a function of the drum wall and material properties.

2.3.3 Transverse motion in the rolling mode

In the rolling mode the material can be divided into the active region where material flows down (cascades down) the sloping upper bed surface, and the passive region. The two regions are shown in Figure 2.4. In the passive region or the underlying bed region, the particles are carried by the drum wall, and the material moves as a rigid solid body and particle mixing is negligible in this region. Mixing mainly occurs in the active region and so solid motion in this region is important and so is the exchange of particles between these two regions. Many workers have investigated the rolling regime by separately considering the material in these two regions. *Ding et al. (2001)* propose a solid exchange coefficient to describe the exchange of particles between the two regions and give a theoretical expression of it in terms of drum operating parameters i.e. drum speed and fill, and bed rheological properties.

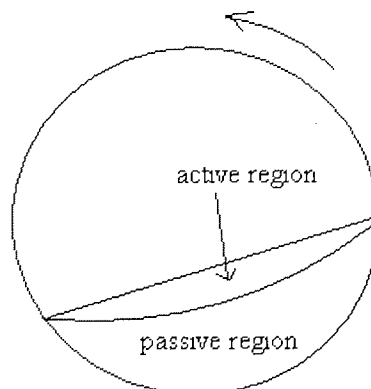


Figure 2.4: Regions of motion in the transverse plane

2.4 Theoretical work and modelling techniques

Theoretical work on particle motion in a rotating drum has focussed mainly on the rolling regime, since this is most relevant for industrial granulation. The theoretical work to date falls into 4 main categories:

1. Simple modelling based on geometrical and stochastic analysis. These models start from experimental work, which suggests the type of motion in a rolling drum is like that depicted in Figure 2.2. It is then assumed that cascading material in the active region follows a straight path, which is determined by resolving gravity in the plane of the free surface. From geometrical arguments, the longitudinal transport per cascade is derived. Assuming the cascade time to be negligible compared to the time in the passive bulk region, the rate of cascades can be found from further geometrical arguments *Saeman (1951)*. Given the cascade rate and distance travelled per cascade, the time of passage, average volumetric flow rate, and hold up *Kramers et al. (1952)* can all be calculated.
2. Eulerian methods treat the material as a continuum and the material flow properties such as velocity are continuous functions of position. *Ding et al. (2001a)* used a continuum model in many of their investigations. They used the differential equations of continuity (mass conservation) and momentum, and a differential energy equation, based on dense-gas kinetic theory to characterize possible scaling relationships for rotating drums. They used a thin active layer approximation to describe granular motion in the active layer of a rotating drum in the rolling mode. *Ding et al. (2001a)* characterises velocity in the active layer as a function of α and β . They defines α as the depth from the bed surface where granular motion has zero velocity in the direction of the free surface (the "zero x-wise velocity line"). He defines β as the interface boundary between the active layer and the passive layer. At depth β from the free surface, the component of velocity in the x direction (parallel to the free surface) is $\omega\beta$, i.e. the motion is equivalent to solid body rotation with the drum.
3. Lagrangian mechanics has been shown to give good predictions for fluid-like flow of granular materials. However extending the approach to complex flows

such as that in the rotating drum is difficult. It has been shown that decomposing the granular flow in a rotating drum in distinct regions of uniform simple flow can give agreement with experiment. *McCarthy et al. (2000)* define 2 different regions in the rotating drum, the active region and the underlying bed. Motion in the underlying bed is assumed to be solid body rotation with the drum. Simple equations of motion for particles in the active region are set up. Although they demonstrate convincing segregation and mixing in a drum using Lagrangian Simulation (LS) methods, a key limitation is that distinct regions of simple flow must be assumed in the system. Additionally Lagrangian equations have terms that are dependant on experimental data to be fitted.

4. Particle Dynamics (PD) or the Discrete Element Modelling (DEM) of granular flows involves following the trajectories, spins and orientations of all the particles and predicting their interactions with other particles and with their environment. A key difference between PD and LS is that the PD simulation considers interactions at the particle level, whereas LS methods use generalized equations of motion, which may not be based on the physics of the system. The term discrete element method is a family of numerical methods for computing the motion of a large number of particles like molecules or grains of sand. Cundall originally applied the method in 1971, analysing the behaviour of soil using two-dimensional disc assemblies, *Cundall (1971)*. Discrete element methods are processor intensive, which limits either the number of particles or the length of a simulation. Consequently, many early DEM simulations were only two-dimensional; only the last few years have seen DEM work in three-dimensions.

Experimentally it is difficult to measure the bulk properties of material such as porosity, stress, and strain. Even though there are many non-invasive experimental techniques such as nuclear Magnetic Resonance Imaging (MRI) and Positron Emission Particle Tracking (PEPT), computer simulation of granular flow has been widely accepted as a practical alternative and complement to such experiments.

2.4.1 DEM Validation

Several different techniques have been used to validate DEM simulation results with real experimental data. *Yang et al. (2003)* validated DEM results by comparing both the dynamic angle of repose and the spatial velocity fields with the experimental PEPT data of *Parker et al. (1997)*. The dependence of the dynamic angle of repose on the drum rotation speed showed good qualitative agreement with the PEPT data.

McBride et al. (2004) gives a detailed consideration of DEM validation and proposes two kinds of metric for transverse flow which avoid subjective interpretation:

1. Coordinates of the centre-of-circulation (CoC). The CoC point is the position in the bed around which bed “circulates”. This can be defined by the intersection of mass flux equilibrium surfaces in the horizontal, vertical and radial directions.
2. Binned probability and absolute velocity errors. These are produced by dividing the transverse cross-section of the drum into square bins. For each bin, the normalised probability (particle density) and absolute velocity is computed, for both the DEM simulation and experimental data. The discrepancy at each bin position $(v_{\text{DEM}} - v_{\text{meas}}) / v_{\text{meas}}$ can then be plotted to visualise the agreement.

Pandey et al. (2006) validated DEM simulation results with video imaging of a comparable physical system, using two metrics: dynamic angle of repose and mean cascade velocity in the free surface. They claim that the steady state has been reached in the simulation when the dynamic angle of repose stabilizes, which is after approximately 3/4 of a drum revolution in the rolling mode.

2.4.2 Previous DEM results

Yang et al. (2003) studied particle flow in a similar horizontal rotating drum to that of *Parker et al. (1997)*. The results were generated by DEM for a drum of diameter 100mm and thickness 16mm. Periodic boundary conditions were applied along the axial direction to avoid end effects, and allowed realistic dynamics to be simulated with a small number of particles. The drum was filled approximately to 35% by spheres of diameter 3mm, and the particles and the drum wall were assumed to be of the same

material. A total of 2000 particles were used. The drum rotational speed was varied from 10 to 65rpm.

Yang showed that the dynamic angle of repose increased linearly with the speed of rotation over the Froude number range 0.022 to 0.236 (see section 2.5.4 for a definition of Froude number). In a later paper, *Yang et al. (2008)*, it is shown that for higher drum speeds, the relationship is no longer linear, and the angle of repose increases *faster* at higher speeds.

Yang compares spatial velocity fields with PEPT data by plotting the angular velocity of particles along a radius perpendicular to the free surface for several drum rotation speeds. The numerical agreement with the PEPT data is excellent for those particles in the solid bed, but deviates from the PEPT data for those particles in the free surface. Yang suggested that this deviation may be due to the DEM simulation treating the particles and the drum wall to be of the same material.

Yang analyzed the DEM data for the following variables which cannot easily be measured with PEPT: (1) Flow structure variables: bed porosity (e) and coordination number (C_N), and (2) agglomeration variables: relative collision velocities and collision frequency.

Yang computed porosity and coordination number as local means. He found that at a Froude number of 0.099, the porosity of the rolling bed was highest in the free surface (including the toe and shoulder regions). The lowest porosity was observed in the solid bed. He noted that the porosity does not appear to be directly related to the particle velocity, since a high porosity is also observed at the top of the bed where particle velocity is not particularly high. Yang concluded that high rotational drum speeds give higher mean bed porosity. By plotting the probability density of local mean porosity, Yang shows that the peak of the distribution is around $e=0.4$, which corresponds to random loose packing. He concludes that the majority of the bed is in that state. The probability density of local mean coordination number was shown to have two peaks: one peak at $C_N=1$ (in the free surface), and one peak at $C_N=7$ in the solid bed.

By computing relative collision velocities as local means, Yang showed that at a Froude number of 0.099 the most vigorous particle-particle collisions occur in the toe region of the bed. Changing the drum rotation speed does not affect this result. He also showed that the probability density for local mean collision velocity is bi-modal: at low drum speeds, a lower collision velocity dominated, whilst at higher drum speeds, a higher collision velocity dominated.

Yang showed that the local mean collision frequency follows a similar spatial distribution to the collision velocity: he finds that the highest collision frequency is in the toe region. He finds that both the mean collision frequency and the mean collision velocity increase roughly according to $O^{0.5}$, where O is the drum speed.

The study is extended in *Yang et al. (2008)* where simulation conditions were similar to those used in the previous study. The particle flow went through different flow regimes as the drum was rotated at different speeds. Steady state flow was obtained for slumping, rolling, cascading, cataracting and centrifuging regimes for Froude numbers 4.9×10^{-5} , 8.7×10^{-2} , 1.2, 2.2 and 3.2 respectively. Note that the transition from cataracting to centrifuging does not have to correspond to a Froude number of 1, as is discussed by *Mellmann (2001)*.

Yang considered the effect of an axial periodic boundary condition by comparing with simulations of drums with fixed lengths of L , $2L$, $4L$ and $16L$ with fixed endcaps. He showed that the periodic boundary simulation has a free surface profile similar to the longer drums ($4L$, $16L$): in these cases the surface is quite flat in the cascading regime, with no noticeable 'S' shape curve. In shorter drums with endcaps, the surface has a more pronounced 'S' shape in the cascading regime. Yang therefore attributes the S shape curve of the surface to endcap effect. He also finds that compared with shorter endcap drums, the rolling regime commences at a higher drum speed for longer drums and drums with periodic boundaries.

Pandey et al. (2006) performed 3D DEM simulations without periodic boundaries: "real" end walls were used in order to study their effect. However, to keep the simulation time under control, they choose an axial drum length of only 10 particle diameters.

Yang showed that for rolling, cascading and cataracting regimes, the probability distributions for particle velocity normalised to the drum speed and collision energy normalised to the mean collision energy can each be described by a single curve. Therefore he suggests that the particle velocity profile for these regimes may be described by a simple scaling law.

Finnie et al. (2005) also compare 2D DEM simulations with 3D DEM simulations by qualitatively comparing the flow regimes for different drum speeds. Qualitatively, they showed that identical flow regimes are produced by both 2D and 3D simulation, but they find that centrifuging starts at a lower drum speed in their 2D simulations compared to 3D. They also find that the speed of transverse mixing is higher in 2D simulations than in 3D at equivalent drum speeds. This is attributed to the 2D particles having fewer nearest neighbours and therefore being less constrained than in 3D.

Comparisons of 2D simulations of circular particles with 3D simulation of spherical particles have also been performed by *Cleary et al. (2003)*. They perform a full 3D simulation of a drum of finite length with endcaps, and also a 3D slice simulation with periodic boundaries which neglects end-wall effects. They find that all three models give qualitatively similar charge dynamics. The mill in Cleary's model is rather short: 200mm (approximately 20 particle diameters), and the periodic slice used in his 3D simulations is 100mm (approximately 10 particle diameters). They find that the charge in full 3D simulation exhibits a pronounced "S" shape, and this is absent in both their 2D and periodic boundary 3D simulations. This is in agreement with *Yang (2003)* since the end-wall effects on the charge dynamics would be significant for such a short drum. Cleary et al. find that, compared to experimental data, the 2D simulation predicts a lower toe and shoulder position by up to 10° (i.e. the charge is more slumped, and doesn't ride as far up the drum wall). This is because the 2D packing of the circular particles is less constrained than the 3D packing of spherical particles, and therefore the microstructure of the charge is weaker in 2D and tends to collapse more easily.

McBride et al. (2004) consider the qualitative differences between 2D and 3D DEM simulation of the same drum system in a cascading mode, and compare to experimental data. In agreement with *Cleary et al. (2003)*, they find that the simulations give very

similar qualitative bulk behaviour, but their 2D simulation exhibited an enhancement in the toe region (i.e. a slumping of the charge) which was not evident in experimental validation data.

2.5 Experimental techniques

2.5.1 Avalanche observations

Fauve et al. (1991) studied avalanches in a rotating drum with constant angular velocity. He detected avalanches when the slope of the material was increased beyond the “critical angle of repose”. The critical angle of repose is defined to be the maximum static slope of the free surface for which the charge is stationary. His apparatus optically measured the angular position θ , of the “bottom contact line” A, which is the lower-most contact point between the free surface of the material and the cylinder wall (see Figure 2.5). He detected avalanches by plotting the time evolution of θ as the drum was rotated. Figure 2.6(a) is a crude drawing of a typical signal from Fauve’s investigation. At low rotational velocity, Fauve found that θ increased linearly due to the constant rotation rate of the drum. He also observed discontinuous changes in θ which occurred randomly in time. His apparatus was designed to prevent slippage of the charge with respect to the cylinder wall. He therefore attributes the discontinuous jumps in θ to avalanches in the free surface, which decrease the slope of the charge and produce a step change of the bottom contact line.

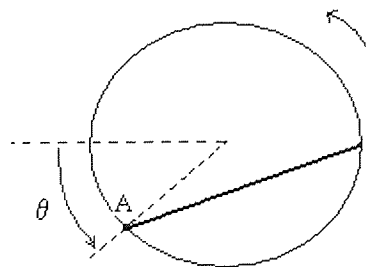


Figure 2.5: Sketch of the drum and bed surface indicating the bottom contact line, A, and the angular position, θ .

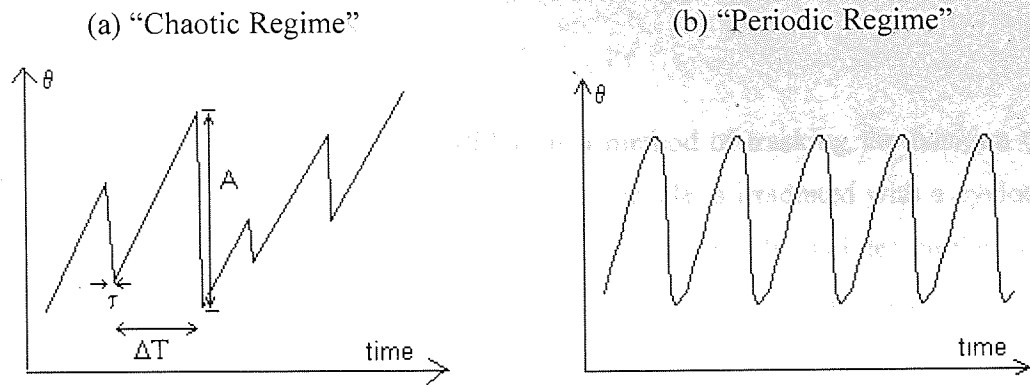


Figure 2.6: Time recording of the bottom contact line position of the particle bed according to Fauve et al. (1991). Drum length=13cm, particle diameter=0.5-0.63cm, (a) $\omega=0.033\text{RPM}$, (b) $\omega=1.25\text{RPM}$

Fauve's apparatus was able to measure several variables depicted in Figure 2.6(a):

- The amplitude of an avalanche, A
- Duration of an avalanche, τ
- Waiting time between avalanches, ΔT

Fauve's experiments were conducted over a range of speeds and he observed some distinct regimes of motion. At low rotational velocity he observes a chaotic regime, where avalanches occur randomly in time and with varying amplitudes. In this mode, the power spectrum of the contact line fluctuations, i.e. a plot of amplitude A against frequency f where $f = 1/\Delta T$, exhibits a broadband distribution. *Fauve et al. (1991)* also observed that this power spectrum has a maximum at the mean avalanche frequency, $1/\overline{\Delta T}$, and that A follows a f^{-2} decay law up to a cut-off frequency of τ . Fauve observed that τ is constant at a given rotational velocity. There is some correlation between A and ΔT , i.e. a longer interval between avalanches is generally followed by a larger avalanche. As the drum rotational speed was increased, Fauve observed a smooth transition into a periodic regime, where the avalanches are nearly time periodic. This regime is depicted in Figure 2.6(b). During the transition $\overline{\Delta T}$ decreases and approaches the avalanche duration τ . In this mode all the avalanches have nearly the same size. Finally Fauve observes a sharp transition from periodic to stationary flow above a critical value of the drum speed, ω . In this regime a constant slope is observed.

2.5.2 PEPT experiments

Positron Emission Particle Tracking (PEPT) is a method of tracking the position of a tracer particle in a particulate system. The tracer particle is irradiated with a cyclotron and reintroduced into the particulate system. The resulting radionuclides on the tracer decay by positron emission and the resulting back-to-back gamma rays can be detected. Given several pairs of back-to-back gamma rays the position of the tracer particle can be reconstructed.

Parker et al. (1997) uses PEPT to study the motion of spherical particles of uniform size in a rotating drum. They used these three different drum sizes and a different particle size for each of these drums as shown in Table 2.1.

Drum diameter (mm)	Drum length (mm)	Particle size (mm)	Fill (%)
136	780	1.5	32
144	650	3	33
100	650	3	36

Table 2.1: Description of the drums used in Parker's PEPT experiments from *Parker et al. (1997)*

The particles used were spherical glass balls and the drum was made of Perspex. There was considerable slip between the drum wall and particles, so they used a thin wire mesh of 1mm squares to line the inside of the drum which reduced much of the slip. Each drum runs at 5 different drum speeds, from 1-7rad/s. At low drum speed the free surface is approximately flat with angle of repose 30° . As the drum speed is increased the profile becomes curved suggesting transition from rolling to cascading motion. The PEPT data yielded spatial velocity fields throughout the entire drum volume. Cross sections through the drum showing the transverse velocities in this plane revealed that the active layer is quite thick and occupies approximately the same region at all speeds. They found the active layer to be approximately $2/3$ as thick as the bed beneath it.

2.5.3 X-ray filming

McBride et al. (2004) presents an experimental particle tracking technique which is comparable to PEPT. The rotating drum is repeatedly digitally photographed using x-rays in two perpendicular planes. Using a frame rate of 50Hz and a shutter speed of 1/3000s, the 3D trajectory of a tracer particle was captured over a period of 67s. The tracer is coated with a thin layer of silver paint which makes it appear darker on the x-ray images. According to *McBride et al. (2004)* this technique can give superior spatial resolution (25x) compared to PEPT, but has a much more limited capture period (67s compared to 1-2 hours for PEPT).

2.5.4 Scaling relations

The scale-up of rotating drums is still largely empirical with no general method established. A number of workers have tried to develop scaling relationships for rotating drums, such as *Ding et al. (2001a)*, to make drum design easier. They derived scaling relationships from the differential equations of continuity (mass conservation) and momentum, and a differential energy equation, based on dense-gas kinetic theory. They also defined many dimensionless quantities in order to characterize possible scaling relations, but the usefulness of these dimensionless quantities for predicting drum motion is not fully established.

In general, reliable scaling predictions are useful, since this allows cheaper laboratory experiments to be scaled up for industrial production with confidence. The scaling of drum speed with respect to drum diameter is reasonably well understood: *Sherrington et al. (1981)* reported work by Oyama who showed that in drums of different diameter D , similar motion of the material can be obtained if the speed is scaled as $D^{-1/2}$.

Work on scaling relations has generally focussed on a specific measurable parameter and considered only small subsets of the full motion spectrum. For example, *Sepulveda et al. (2005)* experimentally determine a scaling relation for the "front length", ϕ_{max} (the transverse angle at the drum centre, described from the lower contact point of granular material at the drum wall, to the upper contact point). From dimensional arguments, the variables in the scaling equation for ϕ_{max} were determined. However the

form of the scaling equation was determined experimentally, and the scaling equation fit was only tested for small drum filling.

The work of *Santomaso et al. (2003)* considers the scaling of ϕ_{max} as well as bed depth L (see Figure 2.7 for a depiction). They capture experimental data for a rotating drum, and examine the dependence of ϕ_{max} and L on the following variables:

- Drum speed
- Drum volumetric fill
- Particle diameter

They capture data over a wide range of drum speeds (from the rolling regime to the cataracting regime), in the hope of determining relationships for ϕ_{max} and L which are quite general. Their approach is to combine dimensionless variables such as (drum diameter / particle diameter) to find an equation which best fits their data. Whilst they succeed in fitting all data to a single set of equations, the result is of course empirical and not derived from the underlying dynamics. Furthermore, all the results are based on a single type of particle (glass beads), and therefore the generality to other types of particle is unknown.

Material motion in drums of various sizes may be compared using the concept of critical speed. The critical speed, ω_c , is the drum speed at which the outermost layer of particles is subjected to a centripetal acceleration equal to the acceleration due to gravity. The critical speed is defined as:

$$\omega_c = \sqrt{\frac{2g}{D-d}} \quad (2.1)$$

where D is the drum diameter, d is the particle diameter and g is the acceleration due to gravity. At this speed the material is just carried completely around the drum by the centripetal force, assuming there is no slip between the particles and the drum wall

The Froude number F, is often used to discuss scaling, and is simply the ratio of the centripetal acceleration of the drum to gravitational acceleration. Therefore, at the critical speed, the Froude number is one.

$$F = \frac{r\omega^2}{g} \quad (2.2)$$

Equation 2.2 gives the definition of Froude number, F , where r is the radius of the drum, g is the acceleration due to gravity, and ω is the rotational velocity of the drum.

2.6 Measurable parameters

Some of relevant characteristic parameters of motion in the drum are list below. The DEM simulation work presented in this thesis makes use of some of these parameters, and attempts to determine some from simulation.

2.6.1 Particle motion parameters

- *Parker et al. (1997)* measured the **tangential velocity** (i.e. velocity parallel to the free surface) in their rolling drum experiments, and inferred bed circulation. Additionally, **angular velocity** distributions showed evidence for solid body rotation in the passive layer, as well as slipping of particles at the drum wall.
- **Velocity profiles in the free surface.** *Ding et al. (2001b)* measured the velocity of particles along the free surface, and found that the cascading particles accelerate from the top of the free surface top to the mid chord and then decelerate between the mid chord and the bottom of the free surface. The velocity profile and therefore the **fraction of time in the free surface** are important parameters, since the majority of axial transport occurs during the cascade. *Pandey et al. (2006)* showed that the mean velocity in the cascade increases linearly with drum speed. They also find that the cascade velocity distribution is approximately Gaussian along the whole length of the free surface, and the maximum cascade velocity is shown to occur approximately halfway down the cascade, in agreement with *Ding et al. (2001b)*. Higher cascade velocities are reported for higher filling fractions.
- **Axial displacement** and **axial segregation** are both of interest in continuously operated drums. *Fauve et al. (1991)* presents experimental evidence for the axial

segregation of particles in a rotating drum, due to different particle sizes. The segregation is not characterised quantitatively however.

2.6.2 Bulk bed parameters

- **Bed depth:** In a rolling drum where the free surface can be approximated to a straight line, the bed depth is the length perpendicular to the free surface, from the midpoint on the free surface to the drum wall. This is indicated by the length wz in Figure 2.7. Some workers refer to **bed dilation**; experiments show that at high rotational velocities, the thickness of the bed *increases*.

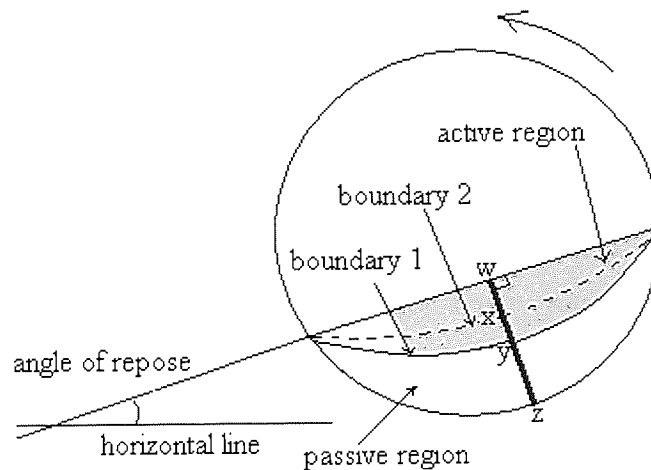


Figure 2.7: The active and passive region in the rolling mode and bed depth, wz

- **Hold-up, X_r ,** in a rotating drum is the fraction of the cross sectional drum area that is occupied by the drum material at a position r_a along the drum axis. The total relative hold-up is the mean value of X_r integrated along the full length of the drum.
- **Active layer thickness:** In the passive region the material moves as a solid body with constant angular velocity and in the active region the material mainly cascades down the sloping upper bed surface. *Ding et al. (2001b)* define the **active-passive boundary** (labelled 1 in Figure 2.7) as follows: below the boundary, linear velocity of the material perpendicular to line wz is equal to the solid body velocity in same direction; above the active-passive boundary, the linear velocity perpendicular to wz is smaller than the solid body velocity in the

same direction. The thickness (w_y) of the active layer is the length measured perpendicular to the free surface, from a midpoint w on the free surface to boundary 1. For a mono-disperse system, *Parker et al. (1997)* reported that the active layer is approximately 40% of the full bed depth. However, *He et al. (2007)* reported that in a binary particle size system the active layer was somewhat thicker: approximately 50% of the full bed depth.

- In practice the angular velocity in the passive region may not be the same as the drum velocity if there is **slippage** between particles and drum wall or between adjacent particles. *Parker et al. (1997)* define slippage as particle velocity near the wall / velocity of the drum wall.
- *Ding et al. (2001b)* show experimentally that material in the active layer is circulating around a point (labelled x in Figure 2.7). At this boundary (boundary 2), the component of particle velocity perpendicular to w_z is zero. *Ding et al.* refer to this boundary as the “**zero x-wise velocity boundary**”.
- **Profile of free surface:** Most researchers work with the assumption that the free surface is a straight line for slowly rotated rolling drums. Usually the profile is described only qualitatively from visual observations.
- **Dynamic angle of repose** is depicted in Figure 2.7: in the steady rolling state, it is the transverse angle of the free surface with respect to the horizontal. *Pandey et al. (2006)* show that dynamic angle of repose increases with drum speed. They also show that dynamic angle of repose increases with increasing filling fraction. For a binary system of two particle sizes, *He et al. (2007)* show that the slope of the free surface increases with a greater number of small particles.
- **Bed turnover time/frequency of circulation:** *Parker et al. (1997)* found experimentally that the time for a tracer particle to cross and re-cross the w_z boundary is independent of radius, except at the very central region around point x . They therefore describe a bed circulation frequency, averaged over all radii, excluding the region around point x . *He et al. (2007)* observed different bed circulation frequencies for small and large particles, and therefore suggested that the difference in circulation frequencies may be a useful measure of macroscopic mixing.
- **Hold-up time:** in continuous drum granulators, this is the mean duration of time that granular material is resident in the granulator. Hold-up time is a function of

the rate of shifting of the charge along the drum. The rate of shifting depends on the angle of inclination of the drum, the diameter, the rotary speed and the flow properties of the charge itself.

2.6.3 Mixing and Segregation

The term “segregation” is used by many workers to describe the separation of an initially homogenous bed into distinct regions, dependent on some particle property. Experimental evidence for segregation due to varying particle density, size and shape has been reported by many workers; see for example *He et al. (2007)*.

By contrast, the term “mixing” is usually applied to systems where no intrinsic segregation is expected (for example, a mono-disperse system). A “mixing” metric for such a system at time t is the degree to which particle positions are randomized, such that the system become more homogenous with respect to an initial heterogeneous state.

There are no commonly accepted methods of measuring mixing or segregation in the drum, but in general most workers have defined a time dependent metric and studied its evolution. The fact that the same metric is not always used makes quantitative comparison of different published result difficult, although some consistent qualitative results can be extracted.

Segregation in the transverse plane was investigated by *McCarthy et al. (2000)*. They used computer simulations and experiments to study mixing in various apparatuses including a rotating drum. They defined the “intensity of segregation”, I_s , for a quantitative comparison of the mixing rates in a system where all particles are labelled as “type 1” or “type 2”.

$$I_s = \left(\frac{\sum_{i=1}^N (\phi_i - \phi_m)^2}{N-1} \right)^{1/2} \quad (2.3)$$

Where ϕ_i is the concentration of one type of particle, sampled at a specific point. A total of N sampling points are uniformly distributed in the system. ϕ_m is the overall concentration averaged over all points. *McCarthy et al. (2000)* start their simulations with a highly segregated configuration of particles, and study the time evolution of I_s . *McCarthy et al.* used the quantitative measurement of segregation to compare computer simulation results to experimental mixing. In a drum mixer they find that segregation due to particle density depends on the duration of the experiment, and also the speed of the drum. Starting from a highly segregated state, they find that for low drum speeds, the intensity of segregation decreases monotonically to an equilibrium value. For high drum speeds, the intensity of segregation decreases to a minimum, after which time the segregation *increases* again until it reaches the same equilibrium value as the slow speed mixing. They observe segregation in the transverse plane after several drum revolutions, and the small, dense particles segregate into the core in this plane.

Axial and radial displacements (dZ , dR) are defined by *Ingram et al. (2005)* to be the change in axial position or radius of the particle during each pass through the active layer. They claim that all the dispersion occurs in the active layer because all the particles in the passive layer are closely packed and have very little relative movement. By using PEPT to capture experimental data, *Ingram et al. (2005)* show that dZ and dR both follow a normal distribution. The variance of dZ they call the "axial dispersion coefficient", D_{axial} (and similarly for D_{radial}). The dependence of D_{axial} on drum size, fill or speed remains unclear. In a particle bed composed of mixed sizes, *Ingram et al. (2005)* find that all particles exhibit similar values for D_{axial} , regardless of size. They conclude however, that the particle size distribution in the bed has a strong effect on D_{axial} : for a bed of essentially monosized particles they find much smaller values of D_{axial} . The radial dispersion coefficient does not exhibit such strong dependence on the width of the particle size distribution and no consistent effect of drum size, fill, or speed was found.

He et al. (2007) addresses macroscopic flow dynamics of a rotating drum in the rolling mode ($F=0.012$) using an Eulerian continuum mathematical model. In particular they investigate particle segregation of a binary mixture of small and large particles. The volume ratio of small to large particles was varied between 1:1 and 1:10 to investigate

the effects on surface profile, tangential and radial velocities, radial particle concentration, and bed circulation frequency. Segregation in the transverse plane is shown to develop quickly: it is apparent after just 1/3 of a drum revolution, and it is claimed to be stable after 2.5 drum revolutions. The smaller particles segregate into the core of the bed, whilst the larger particles segregate outwards towards the drum wall. This is collectively referred to as a "core-shell" structure. The concentration of small particles in the core increases as small particles become more numerous. The mechanism for particle segregation is claimed to be percolation in the cascading layer, where the particle concentration is much lower than in the passive bed.

Finnie et al. (2005) investigated transverse and axial mixing in a horizontal rotating drum using both 2D and 3D DEM simulation. They define local transverse and axial mixing in terms of concentrations of red or black particles. The initial state of the system is configured such that for axial mixing studies, all the particles at one end of the drum are red, and particles at the other end are black. For transverse mixing studies, particles in the left half of the drum cross section are red, and particles in the right half of the drum cross section are black. The system is then evolved using DEM for various filling fractions J and Froude numbers F .

For a horizontal drum, it is expected that mixing in the axial direction will be due to random particle collisions due to the rotation of the drum. *Finnie et al. (2005)* suggest that this can be modelled as a one-dimensional diffusion:

$$\frac{\partial}{\partial t} c(x,t) = \frac{\partial}{\partial x} \left[D \frac{\partial c(x,t)}{\partial x} \right] \quad (2.4)$$

where $c(x,t)$ is the relative concentration at axial position x and time t , and D is the axial diffusion coefficient (units m^2s^{-1}). *Finnie et al. (2005)* proceed by solving the diffusion equation for $c(x,t)$ and then fit the theoretical solution to DEM data with D as a free parameter. They find a good agreement and conclude that the one dimension diffusion correctly describes the DEM data. They also show the D is proportional to the drum speed, and note that D seems to generally increase for bigger filling fraction J .

In general, transverse mixing in a horizontal drum is much more vigorous than axial mixing. *Finnie et al. (2005)* choose to quantify it with an "entropy" metric $S_{i,j}$ given by:

$$S_{i,j} = -kV_{i,j} (p_{i,j} \ln p_{i,j} + q_{i,j} \ln q_{i,j}) \quad (2.5)$$

This is measured for a transverse "cell" (position i,j) with volume $V_{i,j}$ which runs along the full drum length. $p_{i,j}$ is the concentration of red particles in the cell (red particle volume divided by red and black combined particle volume). The concentration of black particles is $q_{i,j} = 1 - p_{i,j}$. From this local entropy, a mixing index for the whole system $M(t)$ is given as:

$$M(t) = \sum_{i,j} \frac{S_{i,j}(t)}{S_{\infty}} \quad (2.6)$$

where $S_{\infty} = -kV(p \ln p + q \ln q)$ where V is the total volume occupied by particles, p is the concentration of red particles in the system and $q = 1 - p$. In the initial state, $M(0) = 0$, and for a perfectly mixed system $M(\infty) = 1$. Finnie et al. find that for their DEM simulations M evolves according to $M(t) = 1 - e^{-rt}$, where r is measure of the speed of transverse mixing. From DEM data they deduce that r is higher for lower filling fractions and higher drum speeds.

Axial mixing for a binary mixture is quantified by *Kwapinska et al. (2006)* using the number of red-black particle contacts. They reason that the more contacts between red and black particles, the better mixed the system, and conduct 2D DEM simulations to compare with experimental data. A "mixing time" metric, t_{mix} is defined to be the time required to achieve perfect mixing: for their DEM simulations, this is assumed to be the point at which the number of red-black contacts starts to randomly fluctuate about a constant value. By varying drum speed, they conclude that t_{mix} decreases with increasing drum speed, and therefore infer faster mixing in agreement with *Finnie et al. (2005)*. In the simulations of *Kwapinska et al. (2006)*, the average error in the 2D simulations versus the experimental data is found to be 12.5% (for the mixing time metric). The authors infer that the t_{mix} scaling depends on the frequency of circulation of the bed, as well as the drum, since that gives a better fit for the data than a scaling on drum speed alone.

3 Simulation model and preliminary simulations

This chapter presents the DEM simulation model, code modifications, and initial validation simulations that were conducted. This thesis presents both 2D and 3D DEM simulations, results from which are reported in chapters 4 and 6. The system configuration and choice of system parameters are described here.

3.1 Discrete Element Method simulation model

The Discrete Element Method (DEM), is a numerical scheme originally developed by *Cundall (1971)* and *Cundall (1974)*, for simulating the behavior of systems of discrete interacting bodies. It is a time dependant technique, which may be used to simulate the progressive movements of discrete particles within a particulate system. DEM has found increasing use over the last two decades in many areas of science as an alternative to the continuum approach for the study of particulate material. Subsequently, *Cundall et al. (1979a)* and *Cundall et al. (1979b)* published details of a computer program 'BALL', for simulation of random assemblies of discs under given boundary conditions in two dimensions. Interactions between contiguous particles in 'BALL' are modeled with linear springs and dashpots. A 3D version called 'TRUBAL' was later developed by Cundall and was first used at Aston University in 1988. Many workers have since modified and enhanced the original code. Global damping terms were incorporate into the equations of motion to dissipate energy and model quasi-static deformation. In the Aston version of the three-dimensional code, algorithms based on theoretical contact mechanics model the interactions between contiguous particles. This later version of the program has been developed to simulate formation and motion of agglomerates (called GRANULE) and is capable of modeling elastic, frictional, adhesive or non-adhesive spherical particles with or without plastic yield at the inter particle contact. For the 2D dynamics study presented in chapter 4, we have used the non-adhesive contact model. The adhesive contact model is used for the granulation simulations reported in chapter 6.

The contact interaction forces in the GRANULE code are modeled according to different theories depending on whether surface adhesion is considered or ignored. In the case of no surface adhesion the theories of Hertz (see *Johnson (1985)* and *Mindlin et al. (1953)*) are used to describe the normal and tangential contact forces. For adhesive particles, the theoretical work of *Johnson et al. (1971)* known as the JKR theory is used to model the normal contact force between the particles, and the *Thornton (1991)* model which combines the work of *Mindlin et al. (1953)* and *Savkoor et al. (1977)* is used to model the tangential force. (The contact force equations with and without adhesion are given in Appendix A.2) The GRANULE code has been used previously for agglomerate impact breakage studies, see for example *Thornton et al. (1996)*, *Kafui et al. (2000)*.

DEM simulation requires the calculation of incremental differences over discrete time intervals, for every particle in the system. Therefore, for every calculation cycle, all the translational and rotational accelerations of the particles are first updated from the resultant forces. Newton's second law of motion is applied to each to determine particle accelerations. Numerical integration of the particle acceleration is then performed over the time interval to give a new velocity and displacement for each particle. Contact forces are updated from the relative displacements between contacting particles. Finally, resolving the contact forces yields the out-of-balance force for each particle. The resultant force will then be used to derive new accelerations at the next iteration of the algorithm. Details of algorithms and equations used in DEM are given in Appendix A.

3.2 Modifications to GRANULE

The work presented in this thesis used the GRANULE program to simulate particles in a two-dimensional rotating drum and a three-dimensional rotating drum of finite length with periodic boundaries and a spray located within it. For this, changes were made to the Aston version of the GRANULE program to enable a two-dimensional rotating drum and a three-dimensional rotating drum wall to be created and interact with particles. Also, a number of graphics subroutines were added to GRANULE in order to render the state of the drum simulation in various ways. A simple spray model was also

incorporated in the GRANULE program. The spray model was originally developed by David Kafui at Aston University for his fluidized bed simulations. Kafui's spray model uses surface energies based on the JKR theory as the binding mechanism. The spray model is described in chapter 6 and in further detail in *Kafui et al. (2008)*. The main code changes implemented into GRANULE are given below. Where applicable, the changes are detailed further in Appendix B.

- A new command was added to GRANULE, called 'CYL' which defines a cylindrical drum wall. The command format is as follows:
CYL (drum radius) (drum length) (displacement from each axis) (drum speed) (material type)
- Data arrays were modified to support cylindrical walls. The wall array in the GRANULE program which stores data for a flat planar wall was modified to contain data for the drum wall such as radius of drum wall, X- and Y- component for the drum centre, drum length, drum speed, X- and Y- coordinate of the drum marker which indicates how far the drum has rotated. Details of the wall array structure can be found in Appendix B.1
- A numerical instability check was added to test for unrealistic particle displacement (and therefore movement) after each discrete time step. See Appendix B.2.1.
- Code was added to model the cylindrical drum geometry. In GRANULE, particle-wall interactions are treated in the same way as for particle-particle interactions except that the plane walls are assumed to be massive and continuous. For a particle-wall interaction, the contact point for the particle and wall is calculated by the intersection of a straight line (line 1 in Figure 3.1) with the drum wall. This straight line is drawn between the centre of the drum and particle coordinates. For particle-wall interactions, the cylindrical drum wall is treated as a tangential plane wall, where the plane (drawn as line 2) intersects the contact point and is perpendicular to line 1. See Appendix B.2.2.

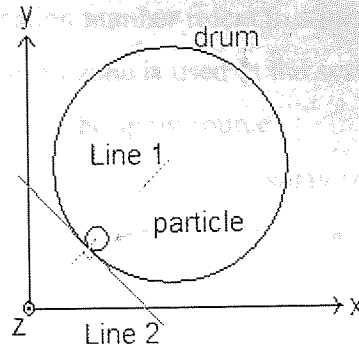


Figure 3.1 : Particle-wall interaction with wall modelled as a tangential plane.

- A new subroutine called **pmill** was written to draw the drum wall. When the program is running, typing 'plot mill' will cause the drum boundary to be drawn. See Appendix B.2.3.
- The following new plotting subroutines were written to plot particle velocities in the system colour coded according to their velocity:
 - **pcolvel** plots colour-coded solid balls
 - **pveloc** plots colour-coded arrows
 - **pradvel** plots the radial velocity component as colour-coded arrows
 - **ptanvel** plots the tangential velocity component as colour-coded arrows
 - **pcradvel** the radial velocity component as colour-coded solid balls
 - **pctanvel** plots the tangential velocity component as colour-coded solid balls

When the program granule is running, typing 'plot (cvel, vel, rvel, tvel, crv, ctv)' will draw the corresponding velocity field. See Appendix B.2.4.

- The code modifications taken from David Kafui's DEM fluidized bed spray granulation program are listed in Appendix B.2.5. These were incorporated into the program to enable the setup of an identical spray model in the drum system. Chapter 6 describes the spray zone and spray model. As a result of these changes a new command was added to GRANULE called 'SPRAY' which defines a spray zone in the system. The command format is as follows:

SPRAY (*sp_id*) (*x_{ss}*, *y_{ss}*, *z_s*) (*θ_c*) (*h_c*) (*d_{fac}*) (*γ_{w max}*) (*t_{dmax}*)

where the parameters in brackets are as given below, and are properly defined in chapter 6:

sp_id : the spray identification number refers to a particular spray zone and is useful if more than one spray zone is used in the system

(x_s, y_s, z_s) : the coordinates of the spray source

θ_c : the conical angle of the spray zone at the spray source

h_c : the height of conical region, measured from spray source to base of cone

$d_{fac} (\geq 1)$: the bond dry out factor, which models an increased energy of the dry bond with respect to initial wet energy before drying

$\gamma_{w\ max}$: the limiting maximum 'wet' surface energy which a particle may take

t_{dmax} : maximum bond dry out period (associated with $\gamma_{w\ max}$)

Also, a new command 'plot spray' was added which draws a conical outline of the spray zone in the system.

- A geometric rotation transform used to incline the spray cone by 50° . See Appendix B.2.6.

3.3 Preliminary 2-D drum simulations

In order to simulate a large system of particles interacting in a rotating drum in two dimensions, a settled bed of particles was first prepared. This settled state was then used as the starting point for a number of different simulations. Particles were confined to the x-y plane of the drum cross-section.

Since the full system simulations required a large amount of CPU time, several preliminary simulations were also performed with smaller systems to validate the code changes and simulation behaviour. These validation system simulations will be discussed in here as well.

3.3.1 Settling particles in a two-dimensional drum

A system of 5000 particles was chosen, comprising of five different sizes in the range of 0.5mm to 1.5mm such to give a Gaussian distribution. Table 3.1 gives the particle size distribution used in the simulation.

Particle diameter [m]	Number of Particles [-]
0.0005	559
0.00075	1182
0.001	1518
0.00125	1182
0.0015	559

Table 3.1: The Gaussian size distribution is used for the particles in the simulation

The next chosen parameter was the size of the drum diameter. A fill of 30% is used commonly in industrial drum granulators and so the same is used in the simulations. From previous two dimensional simulation problems we expect a solid fraction of about 0.82 for a settled bed of particles. These two constraints yield a drum diameter of 0.15m. The material properties assigned to the particles and drum wall are listed in Table 3.2. These properties closely resemble those of glass.

Simulation parameters and material properties	Selected value Particle	Selected value Wall
Young's modulus [GPa]	70	70
Poisson's ratio [-]	0.30	0.30
Friction coefficient between particles, particles and wall	0.35	0.35
Yield stress [Pa]	0.121×10^7	0.121×10^7
Density [kg/m^3]	2.65×10^3	2.65×10^3

Table 3.2: Summary of the mechanical properties for particles and wall

Having selected the material properties for the particles and the wall, the particle size distribution and the drum diameter, these 5000 particles were generated in a random manner over a circular area and within a 15cm diameter drum wall. At this point the particle system has a porosity of 0.4068.

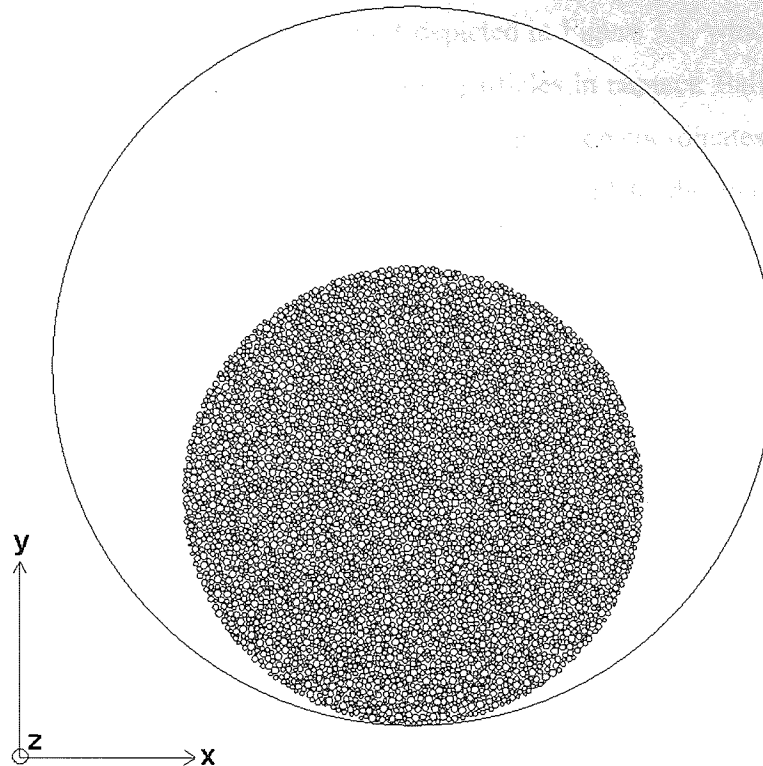


Figure 3.2: Initial particle generation, before starting to settle the bed.

After this state, gravity was switched on in this system and the particles were monitored as they moved under the influence of gravity. Time, $t=0$ at this initial state. At time $t \approx 0.16s$ later, the bulk of the particles had occupied the lower part of the drum. Damping was introduced at this time to dissipate energy in the system and thereby bring the system to a state of near-equilibrium. The global damping was then switched off.

Several quantities were monitored as the bed settled under gravity: the number of ball-ball contacts, average velocity, maximum velocity and the components of the systems centre of mass (see Figures 3.2, 3.3 and 3.4). The figures show that as the deposition evolves, these quantities become constant. After time $t \approx 0.7s$ only very small fluctuations are observed and the system appears to have reached an equilibrium settled state. Figure 3.6 shows the particles and the drum wall at time $t = 0.8s$. The porosity is constant at this time, with a value 0.2259. This settled bed will be the initial state for a number of test drum simulations, these will be discussed at the end of this chapter.

The corresponding connection diagram is depicted in Figure 3.7, which draws a line between the position coordinates of any two particles in contact. Ball-wall contacts are also shown on the plot by a line from the ball position coordinates to the contact point on the wall. The thickness of each line is scaled to the magnitude of the maximum contact force and is proportional to the magnitude of the normal contact force acting between the two particles in contact. The lines are colour coded for connections that correspond to contacts transmitting the less than average force and connections that correspond to contacts transmitting greater than or equal to the average force.

The connection diagram in Figure 3.7 shows well-established connections between the particles in the settled bed. Strong chains of connectivity are observed close to the bottom of the drum wall. The strength of the connection lines appears to decrease as the vertical distance from the bottom of the drum increases. This is expected, as particles close to bottom of the drum have a higher bed weight above it than particles vertically further away from the bottom of the wall.

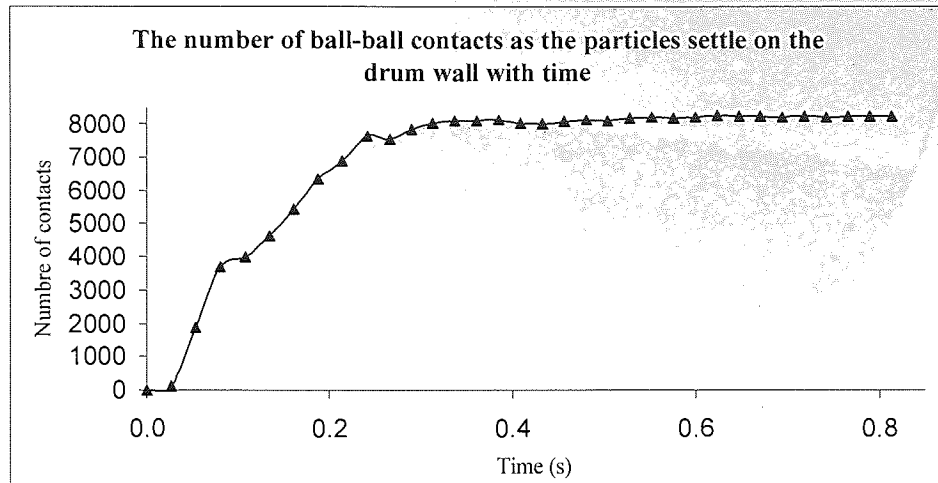


Figure 3.3: Time evolution of ball-ball contacts

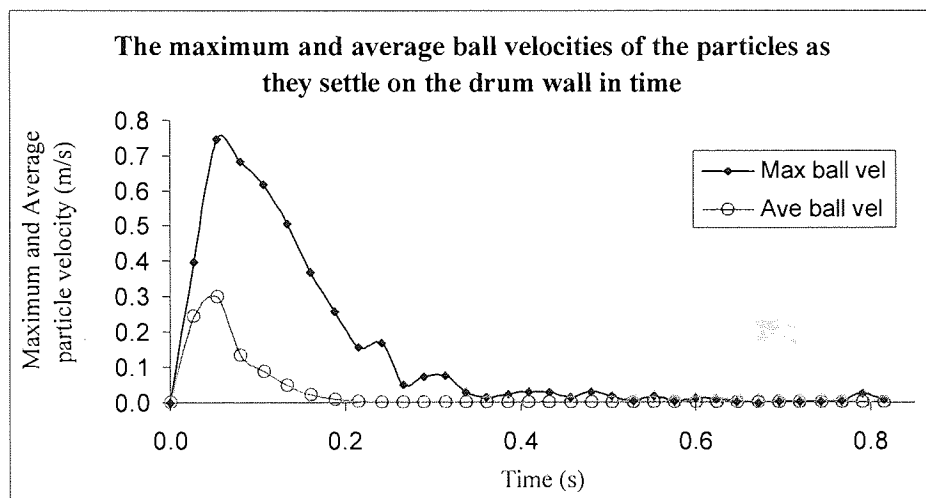


Figure 3.4: Time evolution of the maximum and average particle velocities

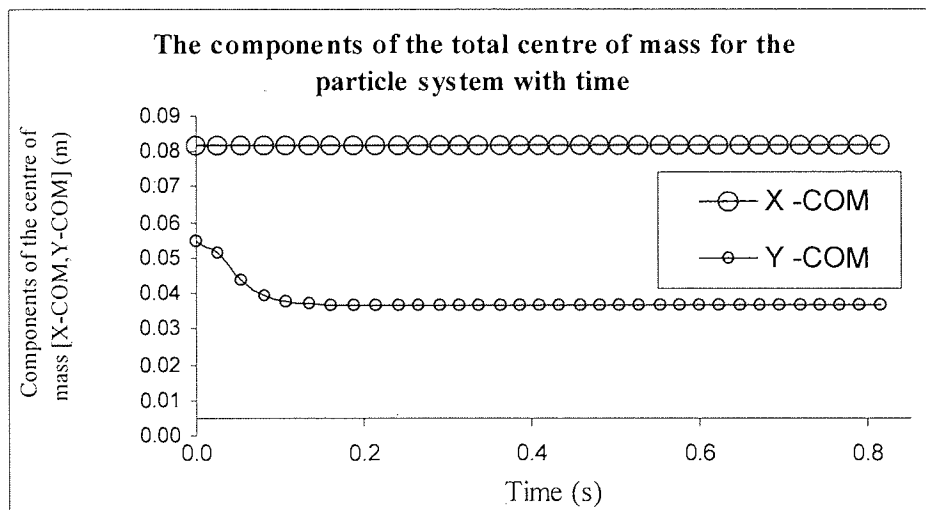


Figure 3.5: Time evolution of the centre of mass coordinates as the bed settles



Figure 3.6: Settled bed at time, $t=0.8s$, when equilibrium is established





Colour scheme:	Ball-ball contact	Wall-ball contact
Less than average force		
Greater than or equal to average force		



Figure 3.7: Connection diagram of the settled bed.
 [Maximum force = 3.93mN, Average force = 0.388mN]

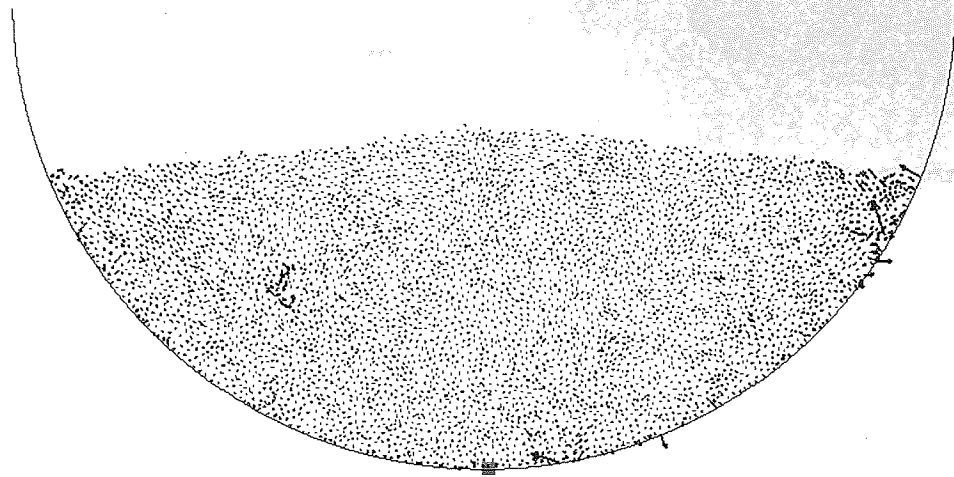


Figure 3.8: A picture of the velocity field of the settled bed.
[Average velocity = 0.023mm/s, Maximum velocity = 1.45mm/s]

The velocity field of the settled bed at time, $t = 0.8\text{s}$ is given in Figure 3.8. The average and maximum particle velocities at this time are 2.29138×10^{-5} and $1.45292 \times 10^{-3}\text{m/s}$ respectively. The figure shows very small changes in position of the particles. On the micro-scale small fluctuations appears in the velocity field, but on the macro-scale the system has reached a near equilibrium state.

3.3.2 Equilibrium balance test

To check the correctness of the model, a simple test case was performed, comparing the results from the simulation with expectations from Newtonian mechanics.

For the settled bed, we expect the sum of the forces exerted by the particles on drum wall to equal the weight of the 5000 particles. The weight force should also be pointing directly downwards, with no horizontal component. Before testing the large 5000-particle system, a smaller and simpler case was first looked at: 22 particles were generated and settled inside the 15cm diameter drum using the method previously described. The forces at the drum wall were checked in the settled state.

For the initial 22-particle check, a particle radius of 0.0095m, and a density of $2.65 \times 10^3 \text{ kg/m}^3$ were chosen. The settled bed is depicted in Figure 3.9. The figure shows the particles superimposed with a simple connection diagram. The sum of all the forces acting on the wall is summarised in Table 3.3 as well as the expected weight of the bed. (A list of all the forces acting on the wall is given in Appendix C.)

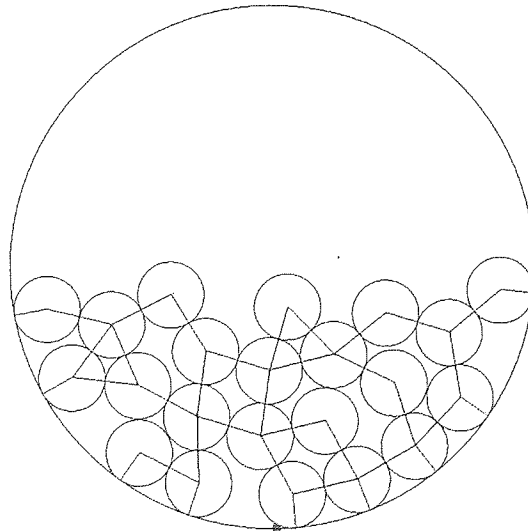


Figure 3.9: Settled bed of 22 particles.

	x-component	y-component
Sum of the forces on the wall	-0.0214872N	- 2.0572918N
Expected weight of the bed	0	- 2.0539837N

Table 3.3: Summary of the summed force components acting on the wall and the expected weight of the bed for a system of 22 particles

The data in Table 3.3 shows the y-component of the summed forces on the wall from the simulation agree within 0.15% of the expected value and the x-component of the summed forces show only a very small non-zero value. The small discrepancies in the results are consistent with the very small fluctuations observed in the settled bed. The small fluctuations in the settled bed suggest that ideal equilibrium is not achieved where the particles are at absolute rest. Similarly results were obtained for the 5000 particle settled bed. These results are depicted in Table 3.4.

	x-component	y-component
Sum of the forces on the wall	+1.39954x10 ⁻³ N	- 0.0751229N
Expected weight of the bed	0	- 0.0855055N

Table 3.4: Summary of the summed force components acting on the wall and the expected weight of the bed for a system of 5000 particles

The data in Table 3.4 shows the y-component of the summed forces on the wall from the simulation agree within 12% of the expected value and the x-component of the summed forces show a very small non-zero value. The increased discrepancy from 0.15% to 12% for the y-component of the summed forces is due to the longer length of time taken to settle a larger system of particles, as a result the 22 particle system appears to be settled closer to ideal equilibrium than the 5000 particle system. The precision agreement with standard Newtonian mechanics in the 22 particles system gives us confidence in the simulation model, but the larger system is concluded to still be in a dynamic state due to the larger discrepancy. Given the constraints on computing resources, it was not feasible to continue to settle the 5000-particle system any further; the given pseudo-settled state is now taken to be the starting point for the rest of the study.

Note that the magnitude of the weight in the 5000-particle system is apparently much smaller than in the 22-particle system, despite roughly similar filling, and the same particle density. This is because the particles are considered 3-dimensional even though the simulation itself is only 2-dimensional. Therefore the 22-particle system, which has much larger particles, has a much larger mass.

3.3.3 Tangential force tests

At any point during the simulation the components of the force sum are saved for every particle and the components of the tangential force and the magnitude of the normal force is stored for every contact in the system in data arrays. In this section the direction of the tangential force will be tested.

For all ball-wall contacts, the direction of the tangential force is expected to be 90° with the line from that contact point to the drum centre, line1. The below table shows the tangential force components, Tx and Ty and ball coordinates, (x,y) for all ball-wall contacts and the computed value the tangential force makes with line1 is given in column Tangle. These results show a good agreement with expected behaviour.

Tx	Ty	Tangle	x	y
0.338E-02	-0.767E-03	0.898E+02	0.703E-01	0.212E-01
-0.372E-01	-0.272E-02	0.901E+02	0.897E-01	0.197E-01
-0.286E-01	-0.109E-01	0.901E+02	0.108E+00	0.238E-01
0.920E-02	-0.633E-02	0.891E+02	0.470E-01	0.316E-01
-0.468E-01	-0.357E-01	0.898E+02	0.125E+00	0.330E-01
0.960E-02	-0.152E-01	0.861E+02	0.274E-01	0.539E-01
0.312E-01	0.432E-01	0.900E+02	0.138E+00	0.466E-01
-0.223E-02	0.239E-01	0.900E+02	0.209E-01	0.718E-01
0.252E-02	0.217E-01	0.900E+02	0.150E+00	0.775E-01

Table 3.5: List of the tangential force components for all ball-wall contacts

3.3.4 Demonstrations of flow regimes

There is no reliable method for determining the expected flow behaviour at a given drum speed, other than to run the experiment. Therefore the 2D settled drum, described in the previous section, was rotated at a variety of speeds in order to investigate the particle flow behaviour.

At a particular point in the simulation, the drum was graphically viewed by rendering the images 'cir', 'vel' and 'cnd'. These images show different information of the drum system as explained in section 4.2. Example animations of the evolving drum system were made from these images at drum speeds 1rad/s and 12rad/s. Refer to the 'Trial simulation' folder on the disk provided with the thesis.

3.3.4.1 Avalanching/Rolling

The animations **cir_1.avi**, **vel_1.avi**, **cnd_1.avi** were produced by rotating the settled bed at 1rad/s. In the animation the settled bed appears to transition to a steady rolling type bed motion. From the **cir_1.avi** animation the drum wall carries the material up and then the material cascades at the free surface. Figure 3.10, Figure 3.11 and Figure 3.12 show snapshots of the **cir_1.avi**, **vel_1.avi** and **cnd_1.avi** animations at a particular time in the steady state.

The velocity field of the system in Figure 3.11, shows rolling motion of material and an avalanching layer at the free surface, indicated by the red band. The bed inclination in Figure 3.10 is 23° to the horizontal and appears to remain steady. The connection diagram in Figure 3.12, draws a line between any two particles in contact. The figure shows stronger and greater connections close to the drum wall and weak particle connectivity in the avalanching layer as expected for freely flowing particles.

Detailed analysis is given for these 2D rolling simulations in chapter 4.



Figure 3.10: 'cir' image of the system in the steady state, $\omega = 1 \text{ rad/s}$

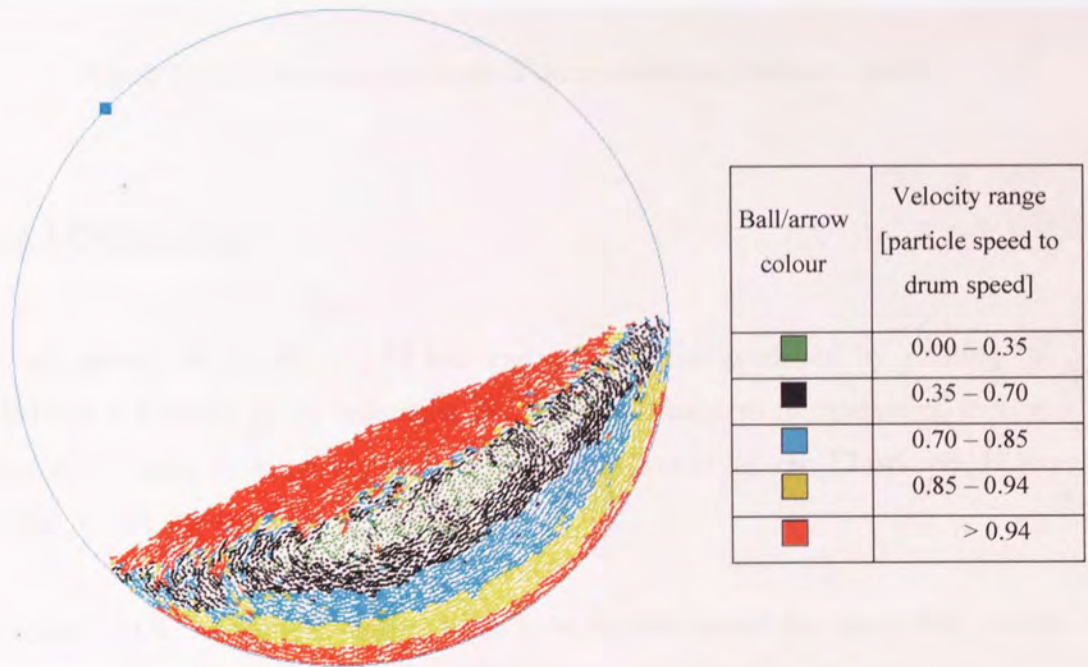


Figure 3.11: Velocity field of the avalanching bed, $\omega = 1 \text{ rad/s}$.
 [Maximum velocity $\approx 250 \text{ mm/s}$, Average velocity $\approx 67 \text{ mm/s}$]



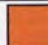
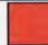
Colour scheme:	Ball-ball / Wall-ball contact
Less than average force	
Greater than or equal to average force	

Figure 3.12: Connection diagram of the avalanching bed, $\omega = 1\text{rad/s}$

3.3.4.2 Cataracting

The animations **cir_12.avi**, **vel_12.avi**, **end_12.avi** were produced by rotating the settled bed at 12rad/s . In the animation the settled bed evolves to cataracting motion. Figure 3.13, Figure 3.14 and Figure 3.15 show snapshots of the **cir_12.avi**, **vel_12.avi** and **end_12.avi** animations at a particular time.

In Figure 3.13 a few particles appear to be carried around the drum wall, which demonstrates centrifuging motion. The critical speed for the drum (see end of section 2.5.4) is 11.5rad/s , so the observation of some centrifuging is expected. The velocity field in Figure 3.14 shows the projected particles from the drum wall, moving faster as they fall freely. The connection diagram in Figure 3.12, draws a line between any two

particles in contact. The figure shows stronger and greater connections close to the drum wall and weak particle connectivity in the avalanching layer as expected for freely flowing particles. The connection diagram in Figure 3.15 shows relatively sparse connectivity in the bed compared to rolling bed at 1rad/s. There are some chains of connection close to the lower part of the drum, between the 4 o'clock and 7 o'clock position, but in general the material is colliding or in free fall, rather than in continuous contact.



Figure 3.13: 'cir' image of the bed cataracting, $\omega = 12\text{rad/s}$

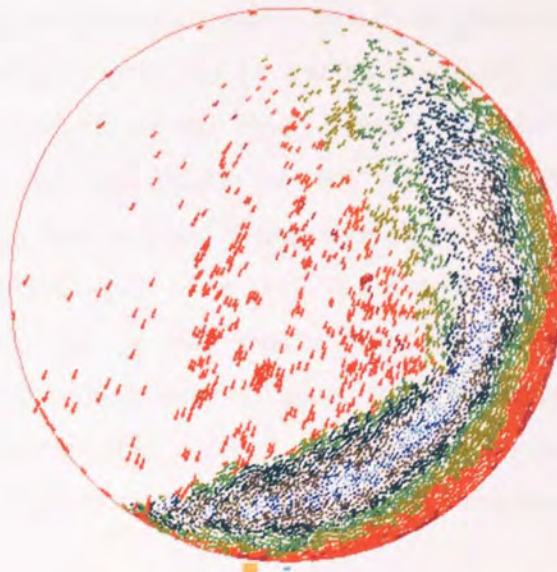


Figure 3.14: Velocity field of the cataracting bed, $\omega = 12\text{rad/s}$
[Maximum velocity = 1.56m/s, Average velocity = 0.53m/s]



Colour scheme:	Contact
Less than average force	■
Greater than or equal to average force	■

Figure 3.15: Connection diagram of the cataracting bed, $\omega = 12\text{rad/s}$
 [Maximum force = 12.5mN, Average force = 0.72mN]

3.3.4.3 Centrifuging

Centrifuging motion was demonstrated at a drum speed of 20rad/s (equivalent to 191 rpm or a tangential velocity of 1.5m/s at the drum wall). A snap shot of the system is shown in Figure 3.16. At this speed virtually the whole bed is centrifuging and forming a ring like layer around the wall, with only a few particles from the inner layer of the ring, detaching and falling freely. In the velocity field plot in Figure 3.17, these few particles appear to be projected away from the drum wall, this suggests cataracting behaviour is also present. As there are several layers of particles centrifuging, the drum is running beyond its critical speed where just one layer of particle(s) centrifuge. The connection diagram in Figure 3.18 shows the stronger particle connections close to the wall and weaker connection further away from it.

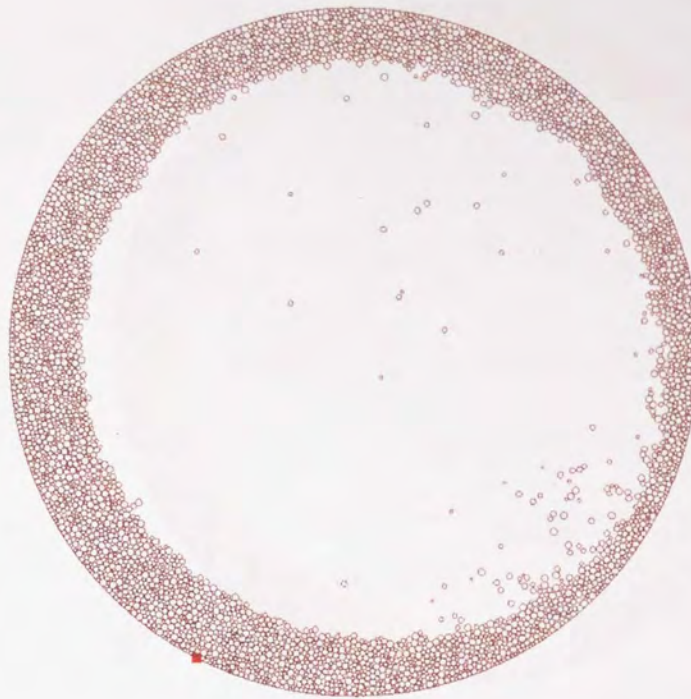


Figure 3.16: 'cir' image of the bed centrifuging, $\omega = 20$ rad/s



Arrow colour	Velocity range [particle speed to drum speed]
Green	0.0 – 0.2
Black	0.2 – 0.4
Light Blue	0.4 – 0.6
Red	0.6 – 0.8
Dark Blue	> 0.8

Figure 3.17: Velocity field of the centrifuging particulate system, $\omega = 20$ rad/s
 [Maximum velocity = 1.51m/s, Average velocity = 1.36m/s]







Colour scheme:	Ball-ball contact	Wall-ball contact
Less than average force		
Greater than or equal to average force		

Figure 3.18: A connection diagram of the centrifuging particles, $\omega = 20\text{rad/s}$
 [Maximum force = 4.03mN, Average force = 0.44mN]

3.4 3-D drum simulations

The above model has been extended to simulate a three-dimensional rotating drum. This will enable drum simulations similar to real experimental or industrial drums where particles are able to move in three-dimensional space, without being restricted in two dimensions as in the previous simulations.

3.4.1 System parameters

For the 3D drum granulation simulation, similar particle parameters were used as by *Goldschmidt (2001)* in his modelling work of fluidised bed spray granulation. Goldschmidt used particles of average diameter $250\mu\text{m}$, deviation in the size distribution of $50\mu\text{m}$ and density 2440kg/m^3 . A system of 50,000 particles was

chosen, comprising of five different sizes in the range of 200 μm to 300 μm such as to give a Gaussian distribution. Table 3.6 gives the particle size distribution used in the 3d-simulation. A drum length, equivalent to an average of 10 particles was selected, 2500 μm .

Particle diameter [μm]	Number of Particles [-]
200	7623
225	11092
250	12570
275	11090
300	7623

Table 3.6: The Gaussian size distribution used for the particles in the 3d-simulation

The next parameter chosen was the size of the drum diameter. From previous three dimensional simulation problems we expect a solid fraction of about 0.62 for a settled bed of particles. A fill of 30% is used commonly in industrial drum granulators so we have used the same. These two constraints yield a drum diameter of 3.4cm. The material properties assigned to the particles and drum wall are listed in Table 3.7.

Simulation parameters and material properties	Selected value Particle	Selected value Wall
Young's modulus [GPa]	3.0	3.0
Poisson's ratio [-]	0.30	0.30
Friction coefficient between particles, particles and wall	0.35	0.75
Yield stress [Pa]	0.03×10^{30}	0.03×10^{30}
Density [kg/m^3]	2.44×10^3	2.44×10^3

Table 3.7: Summary of the mechanical properties for particles and wall

In the table we see a high yield of 0.03×10^{30} Pa is chosen and the Young's modulus as low as 3GPa. This is simply to increase the critical time step, which is described in Appendix A. Increasing the critical time step permits the discrete time step in the

simulation to be increased without incurring numerical instability. The 2D simulations have been found to be very time consuming to produce a single drum revolution. So by increasing the system of particles by 10 times as in the 3D simulation, we expect an even longer time to produce a simulation run to evolve over a similar time frame. As a result of changing the particle and wall properties in this way, the particles have changed from elasto-plastic to elastic particles.

3.4.2 Drum configuration

The 3D drum was simulated by randomly generating the 50,000 particles in a cylindrical region within the 3d-drum of diameter 3.4cm and length 0.25cm. Industrial drums are normally inclined at no more than 10^0 to assist axial transport of the material. We have used an inclination of 5^0 .

The drum length of 0.25cm is clearly very short: approximately 10 particle diameters. Such a short length was chosen to permit a feasible CPU simulation time. With such a short drum length, the transverse dynamics can be heavily affected by the end-wall effects described by *Dury and Ristow (1998)*, *Yang et al. (2003)*. However, granulation processes in the drum are expected to be dominated by traverse mixing (since that is several orders of magnitude larger than the axial mixing), and therefore the traverse dynamics are of primary interest. To avoid excessive end-wall effects due to the very short drum length, periodic boundaries were employed, giving an effectively infinite drum length. A result of this choice is that axial segregation cannot be studied, and the transverse dynamics of the simulation correspond to those in the centre of a long drum, where end-cap effects are negligible according to *Dury and Ristow (1998)*. By using periodic boundaries, it is expected that accurate transverse dynamics can be reproduced, because realistic close packing in 3D is reproduced, even for very thin slices. Other workers (*Yamane et al. (1998)*, *Yang et al. (2003)*, *Yang et al. (2008)*, *Cleary and Sawley (2002)*, *Morrison and Cleary (2004)*) have reported that good agreement with experiment is achieved with periodic axial slices of 10 particles or less, and so we expect a 10 particle slice to be adequate for our purposes.

Figure 3.19 shows the position of the drum with respect to the axes in the simulation.

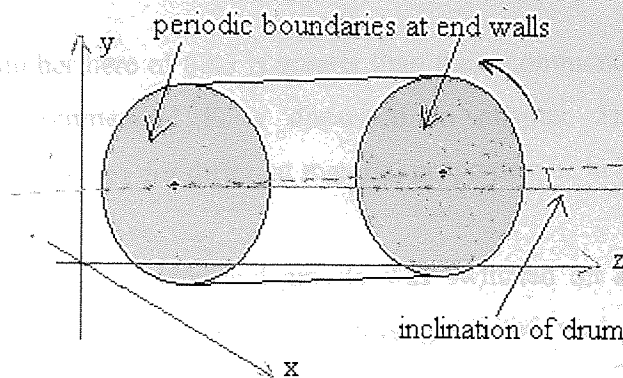


Figure 3.19: Position of 3D drum with respect to the axes

Drum granulators are commonly run with cascading material so we have selected the drum speed to attain similar motion. In the 2D drum simulations, we found cascading motion in the 15cm drum at 10rad/s. By using simple scaling where the Froude number is kept constant, approximately similar cascading motion can be obtained in a 3.4cm drum at 15rad/s.

A 2D drum was created identical to the 3.4cm 3D drum, purely to check that the material cascades as required at 15rad/s. However, at 15rad/s the material motion showed very light cascading. When the drum speed was increased to 20rad/s moderate cascading was observed, and this speed was used for our 3D simulation. The system parameters used for setting the 3D drum are summarised in Table 3.8.

Total number of particles [-]	50,000
Drum Diameter [m]	0.034
Drum Length [m]	0.0025
Drum loading/fill [%]	30
Drum Rotational speed [rad/s]	20.0
Froude Number [-]	0.83
Coordinates of drum centre [m]	(0.0171, 0.071)
(Gap between x-axis/y-axis and drum [m])	0.0001
Time step [s]	1.97×10^{-7}
Gravity [m/s^2]	(0, -9.81Cos5, 9.81Sin5)

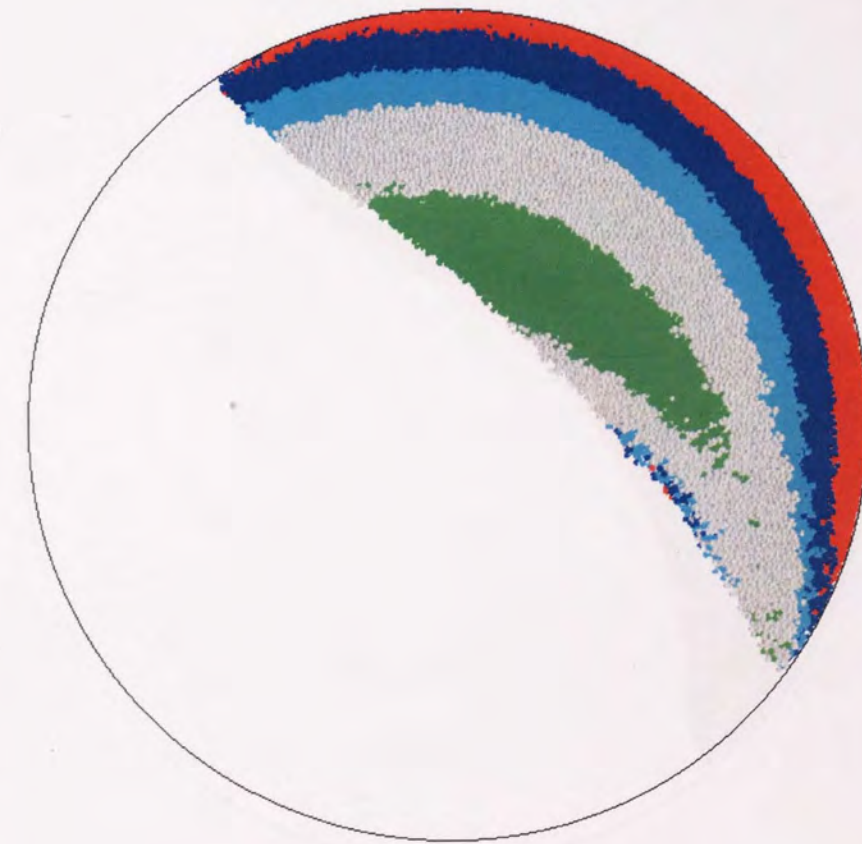
Table 3.8: Summary of system variables for the 3D simulation

Note the Froude number here of 0.83 is greater than the recommended $F \sim 0.3$ to 0.5 for granulation (recommended F is discussed in chapter 5). However, this recommended range can vary for different material properties, as in our system.

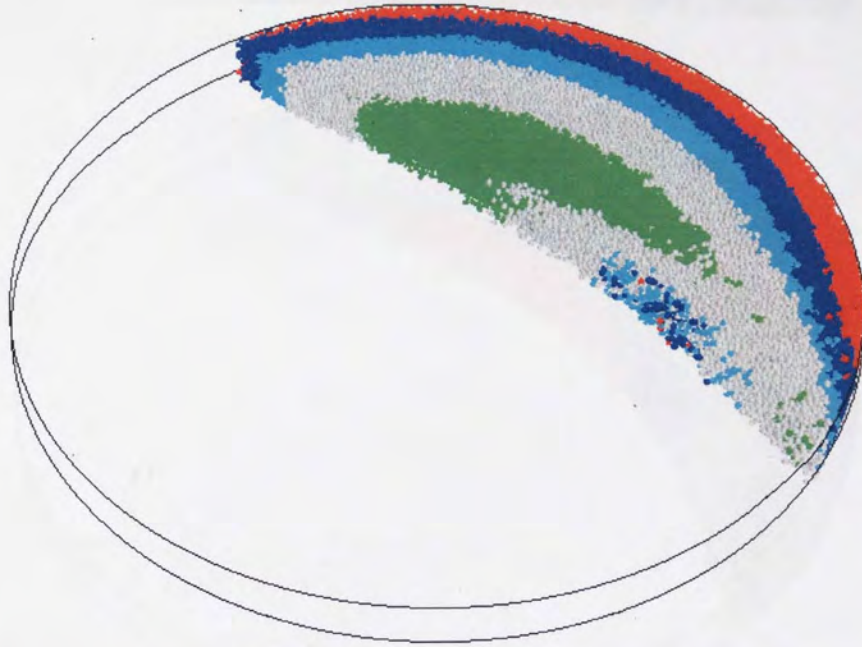
The drum was rotated at 20rad/s, and gravity was switched on at the same time. Consequently, the particles that were randomly generated were not settled in a stationary drum as was done in the 2D simulations.

Figure 3.20 shows the system after approximately a quarter revolution of the drum. The bulk of the material appears to move as a solid body with the drum, and particles are beginning to cascade from the lower part of the free surface.

Figure 3.21 shows the system after approximately three-quarters of a drum revolution. In the figure, the material exhibits a curved free surface and the overall shape looks similar to the kidney shape usually associated with high-speed rolling drums or light/moderately cascading material. This steady cascading drum is used to simulate and study granulation and will be further discussed in chapter 6.



(a) Front view (xy-plane)



(b) 45° rotation through vertical axis



(c) axial view (yz-plane)

Colour scheme:	Ratio of Rotational velocity of particle to that of drum
	< 0.40
	0.40 to 0.70
	0.70 to 0.80
	0.80 to 0.90
	> 0.90

Figure 3.20: After $\sim 1/4$ drum revolution the particles have moved almost like a rigid body

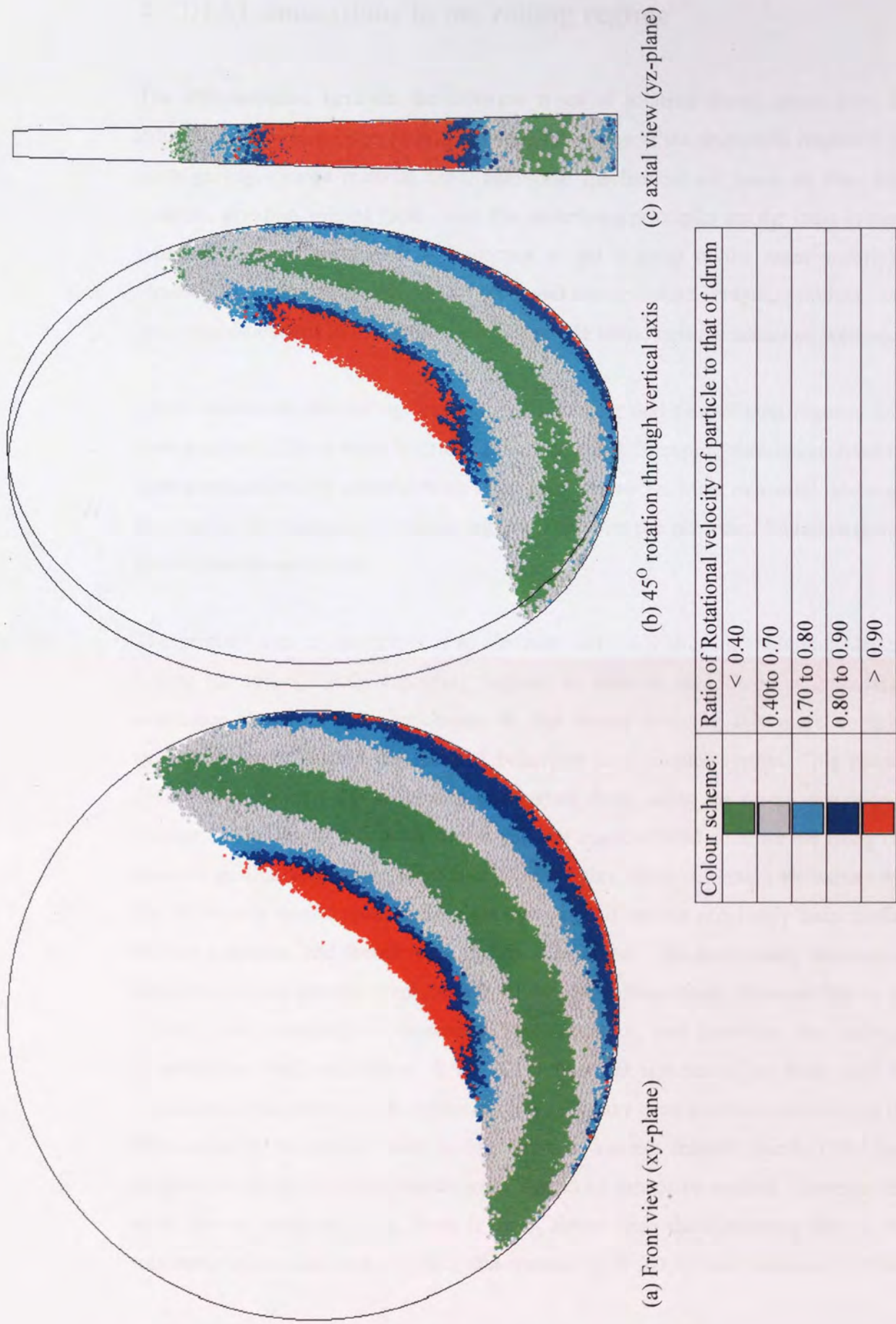


Figure 3.21: After $\frac{3}{4}$ drum revolution the fast flowing layer of particle develop at the free surface

4 DEM simulations in the rolling regime

The differentiation between the different types of rotating drums arises from the different length to diameter ratios involved, inclination of the drum with respect to the earth gravity, charge material used, additional mechanical aid (such as lifter bars, scrapers, grinding, mixing tools ...etc) The underlying principles are the same in many types of drums. Therefore it is important to get a grasp of the main underlying mechanical motion of the cylindrical drum and charge before studying problems with more sophistications in that there are new variable introduced i.e. adhesion, wetting.

DEM simulations for rolling, cascading, cataracting and centrifuging regimes have been produced. These were described in section 3.3.4. Slumping simulations have not been produced due to constraints on computing resources. Most industrial drums are operated in the slumping or rolling regime. Therefore the published literature mainly investigates these regimes.

The primary aim of this thesis is to simulate and study drum granulation, hence a rolling (or rolling/lightly cascading regime) is used in the 3D drum granulation simulation described later in chapter 6. But before studying this more complex system, we have studied the material behaviour in a simpler system. This chapter describes preliminary 2D simulation of a rolling drum, using the set-up described in chapter 3. The aim of this work was to validate that the DEM code we are using can produce qualitatively correct dynamics for a rotating drum. Although we expect that the DEM code should produce the right dynamics, it has not previously been applied to such a system, and therefore validation is required. The preliminary simulations described in this chapter were conducted for the rolling mode, because that is the regime most commonly addressed by the literature, and therefore the expected dynamics are well understood. A 2D rather than 3D simulation has been used for validation of the rolling mode dynamics. It would have been preferable to validate the DEM code in the rolling mode in 3D, but this was not feasible due to CPU time constraints. Because of this choice, axial dynamics cannot be studied. However, the axial flow of particles in the drum is much slower than the circulating flow in the transverse plane, and this suggests that modelling in 2D is still meaningful. Other

workers have compared 2D and 3D DEM simulations and report that qualitatively similar transverse dynamics can be produced by 2D drum simulation, *Finnie et al. (2005), Cleary et al. (2003)*.

4.1 Description of rolling drum simulation

The settled drum bed described in 3.3.1 was used for the rolling drum simulation. The parameters for the drum are summarised in Table 4.1 and Table 4.2. The drum simulation was restarted from the saved state for this settled drum bed and the drum was rotated at a constant angular velocity of 1rad/s. The drum simulation was run for 7.6s real time, which is approximately 1.2 revolutions (the corresponding computational time required was approximately 17 months on an SGI Workstation).

Particle diameters and distribution			Material properties for particle and wall	
Diameter (m)	Weight (%)	Number	Young's modulus [GPa]	70
0.0005	11.2	559	Poisson's ratio [-]	0.30
0.00075	23.6	1182	Coefficient of friction [-]	0.35
0.001	30.4	1518	Yield stress [Pa]	0.12077×10^7
0.00125	23.6	1182	Density [kg/m ³]	2.65×10^3
0.0015	11.2	559	Surface energy [J/m ²]	0.00

Table 4.1: Summary of the drum and particle bed parameters

Total number of particles [-]	5000
Drum Diameter [m]	0.15
Drum loading/fill [%]	30
Drum Rotational speed [rad/s]	1.0
Froude Number [-]	0.0076
Coordinates of drum centre [m]	(0.077, 0.077)
(Gap between x-axis/y-axis and drum [m]	0.002
Time step [s]	5.32×10^{-8}
Total simulation time (rolling drum) [s]	7.61
Total number of drum revolutions [-]	~1.2

Table 4.2: Summary of the drum and particle bed parameters

The simulation state was initially saved to disk every 0.00266s. Due to storage space limitations, the interval between saved states was increased for some fraction of the total simulation time (between real time 1.139s and real time 3.035s). The interval used in this region was a factor of 10 longer (i.e. the simulation state was saved every 0.02662s). This permits us to study the initial transition from static bed to rolling bed with high-resolution time data, whilst also ensuring that at least 1 full revolution of the drum was observed without exhausting the storage space. After a real time of 3.035s, the simulation state was once again saved every 0.00266s, which also allows the steady state motion to be studied with high-resolution time data. To summarize, the simulation state was saved less frequently between real time 1.139s and 3.035s, so the data plots that are presented later in this chapter have a reduced time resolution in this interval.

Due to relocation and reinstallation of the workstation on two separate occasions, there are some saved states from the rolling drum simulation that are missing or lost. No data was available for the following four real time intervals: (i) 0.0266 to 0.269, (ii) 3.857 to 4.358, (iii) 6.491 to 6.541 (vi) 6.597 to 7.020. The loss of these small time intervals has not affected the analysis presented in this chapter.

4.1.1 Projected effect of drum and material parameters

The 2D DEM simulation described in this chapter consumed 17 months of CPU time. Such a long run was necessary to establish dynamic equilibrium and permit validation of the transverse dynamics of the charge. Unfortunately, the long CPU time precluded any investigation of the effects of drum and particle parameters, since those experiments would have required many more simulations of comparable runtime. The key parameters we expect to influence the dynamics of the simulation are:

Drum parameters:

- Drum speed
- Drum diameter
- Drum wall material (affecting particle-wall friction)
- Drum filling fraction

Charge parameters:

- Particle size and shape
- Particle material

Other workers have attempted to qualify the effect of these parameters on various aspects of the charge dynamics. The variation of dynamic angle of repose with drum speed has been investigated experimentally by *Parker et al. (1997)*, and with DEM by *Yang et al. (2003)*. Both concluded that for low drum speeds the dynamic angle of repose increases linearly with drum speed. This metric is useful because it can be unambiguously compared across many different experiments.

The coefficient of friction for particle-wall interactions is another important variable which affects the dynamics. *Mellmann (2001)* has shown by moment analysis that the coefficient of friction is required to be greater than a critical value in order to achieve slumping, rolling, or higher regimes. If the coefficient of friction is below the critical value, slipping will occur and no interesting dynamics can be generated. *Mellmann (2001)* gives the critical coefficient of wall friction, μ_{wc} , as:

$$\mu_{wc} = \frac{2 \sin^3 \epsilon \sin \Theta}{3\pi f(1 + Fr)} \quad (4.1)$$

where ϵ is the filling angle corresponding to the half bed angle of the circular segment occupied with solids (approximately 71° for this simulation), T is the dynamic angle of repose (approximately 23° for this simulation), f is the fractional fill (30% for this simulation), and Fr is the Froude number (0.0076). For our rolling drum we compute the critical coefficient of friction to be approximately 0.23, and we have fixed the particle and wall coefficients of friction to be 0.35. Therefore we expect that slumping, rolling, and higher regimes should be produced with increasing Froude number, and no significant sliding should occur at the wall. In general, as the fractional fill increases, the motion of the charge will transition from slipping to slumping or rolling. This is because the normal force at the wall is larger and therefore the friction force at the wall overcomes the tendency for the charge to slide back down. For this simulation, given the wall coefficient of friction of 0.35, equation 4.1 can be used to calculate a “critical fill” below which we expect the

motion to transition to slipping rather than slumping or rolling. Using the geometrical relationship from *Mellmann (2001)*:

$$f = \frac{1}{\pi} (\varepsilon - \sin \varepsilon \cos \varepsilon) \quad (4.2)$$

we find the critical fill to be approximately 3%, so clearly only very low drum fill would be expected to slip given the other operating parameters we have chosen.

Material effects on the dynamics have been investigated by *Henein et al. (1983)*. From experiments with particles of different sizes and shapes, they conclude that materials with smaller static angles of repose tend to transition from slumping to rolling at lower speeds. *Henein et al. (1983)* state that static angle of repose incorporates the effect of particle shape and size and provides a reliable guide to the relative position of the slumping-rolling boundaries for different materials. In general spherical particles will flow more easily than irregularly shaped particles, and we expect the rolling transition to occur at lower drum speeds for spherical particles compared to irregularly shaped particles.

Mellmann (2001) analyzes the effect of static angle of repose by deriving an equation of motion for the slumping phase to get the “slump time”, (the duration of a single slump event which reduces the angle of repose of the charge). He suggests that the charge motion transitions from slumping to rolling when the slump time is shorter than the time taken to lift the charge by rotation of the drum. This leads to an expression for the critical Froude number for the slumping-rolling transition, Fr_c

$$Fr_c = \frac{3}{2} \left[\frac{\pi(\Theta_0 - \Theta)}{180} \right]^2 \frac{\sin \Theta - \tan(2\Theta - \Theta_0) \cos \Theta}{\sin \varepsilon} \quad (4.3)$$

where Θ_0 is the static angle of repose. We estimate for our simulation that the static angle of repose is 29° and therefore compute the critical Froude number for the slumping-rolling transition as 0.0019 (corresponding drum speed of 0.50 rad/s). It should be noted that the values we have used for static and dynamic angle of repose are only estimates and this introduces considerable uncertainty in the result for the critical Froude number, but it seems likely that for our chosen Froude number of 0.0076 we are well above the slumping-rolling transition.

A different equation for the slumping-rolling transition is put forward by *Liu et al. (2005)*. They define the transition with the same criteria as *Mellmann (2001)*, but instead of making any simplifying assumptions about the angle of the repose of the bed, they express the transition in terms of two angles: α , the “lower angle of repose of the bed” (immediately after avalanching), and β , the “upper angle of repose” (immediately before avalanching). In terms of these two variables, *Liu et al. (2005)* find the critical Froude number for the slumping-rolling transition to be:

$$Fr_c = 8 \frac{d}{D} \frac{1}{\sin^2 \varepsilon} (\beta - \alpha)^2 \sin \beta \quad (4.4)$$

where ε is the filling angle as before, d is the mean particle diameter, and D is the diameter of the drum. Measurement of the angles α and β has not been performed, but taking the approximation $\alpha = T$, $\beta = T_0$, equation 4.4 predicts a critical Froude number for the slumping-rolling transition of 0.00032, which is significantly lower than the value of 0.0019 computed previously from equation 4.3. The discrepancy may indicate that the simplifying assumptions of *Mellmann (2001)* are invalid, or that our approximation $\alpha = T$, $\beta = T_0$ is invalid. It is plausible that the upper angle β may be close to the static angle of repose, but the approximation $\alpha = T$ may be overestimating α and therefore we may be underestimating Fr_c . Additionally, the critical Froude number for transition is very sensitive to the difference $\beta - \alpha$. The conclusion still holds that for our operating parameters we expect to be well above the slumping-rolling transition.

From equation 4.4 we can also deduce the dependence on particle and drum size. In general, larger diameter drums are expected to transition from slumping to rolling at lower drum speeds, which is consistent with the experimental findings of *Henein et al. (1983)*. Smaller sized particles will also roll more easily at lower drum speeds.

Mellmann (2001) also analyses the transition from the rolling regime to the cataracting regime. He defines a critical Froude number for the transition by requiring that the force normal to the drum wall on a particle at the top of the shoulder should be zero. The critical Froude number for the transition is given as:

$$Fr_c = \sin(\Theta + \varepsilon - 90^\circ) \quad (4.5)$$

and we therefore compute the critical Froude number for the rolling-cataracting transition to be 0.070 (corresponding drum speed of 3.0rad/s). Based on this, we do not expect any cataracting motion for the operating parameters we have chosen, and we are well within the rolling regime. From equation 4.5 we can see that increasing the drum fill (and thus increasing e) will also increase the critical Froude number for the rolling-cataracting transition.

We expect that the above analysis of *Mellmann (2001)* can be applied to our 2D simulation since the dynamic angle of repose and the static angle of repose are found from the simulation itself and therefore account for any intrinsic difference in charge structure in 2D compared to 3D.

4.2 Qualitative observations

OpenGL subroutines were written in order to visualize the simulation. Images were captured using the “xv” application. For each simulation state, the following images were rendered:

- “**cir**”: particle positions are represented with simple circles.
- “**vel**”: particle velocity vectors are rendered with colour-coded arrows.
- “**tvel**”: particle velocities tangential to the drum radii are rendered with colour-coded arrows.
- “**rvel**”: particle velocities parallel to the drum radii are rendered with colour-coded arrows.
- “**cvel**”: particle speeds are rendered with colour-coded discs
- “**ctvel**”: particle speeds tangential to the drum radii are rendered with colour-coded discs
- “**crvel**”: particle speeds parallel to the drum radii are rendered with colour-coded discs
- “**cnd**”: a line is rendered between the centre of any two particles in contact

These images were captured for all of the saved states and videos were made for the whole simulation run. These movies will be described in the next section and the movies can be found on the disk provided with the thesis.

In this section the behaviour of the particulate material in the rolling drum is described in a qualitative manner from observations of the rendered animations.

4.2.1 Particles represented as discs

In the video `cir_1.avi`, circular discs represent particles whose radius is proportional to the particle radius. At the start of the movie we see a settled bed that has a peak midway along the free surface. See Figure 4.1(a). The free surface appears to consist of two approximate straight lines from this peak to the drum wall the slope of which seem similar in magnitude. The form taken by the initial settled bed is due to the method that was employed to generate the initial settled state, as described in the previous chapter.

As the drum starts to rotate the shape of the free surface appears unchanged. The upper angular contact point and lower angular contact point of the material and drum (labelled as C1 and C2 in the Figure 4.1(a)) appear to rotate together at the same rate. The material appears to move as a solid body until $t \approx 0.375\text{s}$ (Figure 4.1(b)), at which time particles on the left side of the free surface start to trickle down the surface. Immediately following this the particles in the central peak region (labelled A) and on the right hand side of the free surface flow down the free surface and the peak disappears from the free surface. The particles first start trickling down the free surface at $t \approx 0.375\text{s}$. At this time, the slope of the lower line (AB) is approximately 29° , and slope of the upper line (AC) is approximately 14° to the horizontal. We conclude that the critical angle for avalanching in the static state (or static angle of repose) is therefore approximately 29° . At $t \approx 0.540\text{s}$, we see that the free surface cascades are no longer confined to only the line AB, and the free surface tends towards a single straight line (Figure 4.1(c)). After this time, the upper and lower contact points do not change significantly for the remainder of the simulation. A

cyclical fluctuation in the angle of the contact points is observed, with a magnitude of a few degrees.

For the particles close to the drum wall, there appears to be very little relative motion between neighbouring particles. It appears that the particles in this region are moving like a solid rigid body. However, relative movement between neighbouring particles is apparent for those particles on, or near to, the free surface. The material exhibits this same flow throughout the remainder of the simulation (Figure 4.1(c),(d),(e),(f)). The material appears to be carried up the drum wall as a solid body, and then cascades down at the free surface. The free surface has a constant slope (the dynamic angle of repose) of approximately 23° to the horizontal (from Figure 4.1(f)).

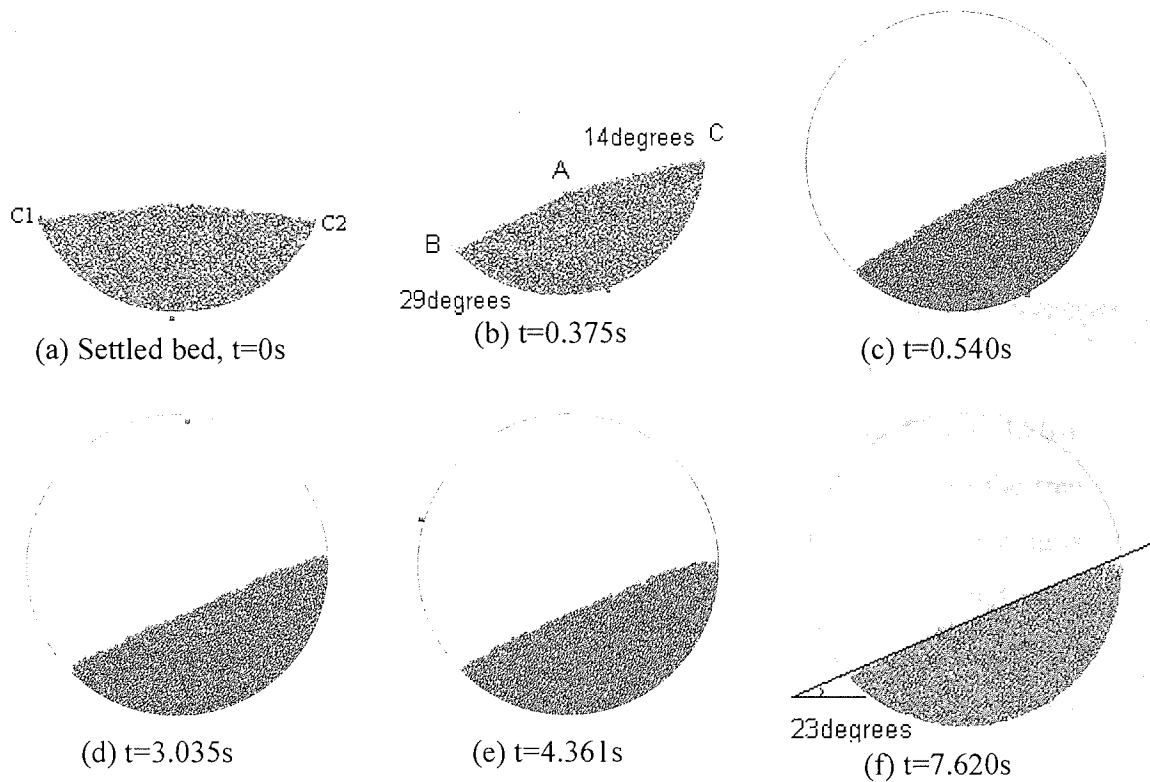


Figure 4.1: Snapshots of the rolling bed animation, *cir_1.avi* at different times, t .

4.2.2 Bed velocity field

The velocity field is represented as colour-coded arrows in the video *vel_1.avi* and colour-coded discs in the video *cvel_1.avi*. In both these videos an arrow (*vel_1.avi*)

or disc (cvel_1.avi) is rendered with the coordinates of the particle centre. The colour of the arrows or discs indicates the linear speed of the particles. The arrows in the cvel_1.avi rendering indicate the direction of movement, and the length of the arrow is proportional to the linear speed. All particle speeds in the plot are scaled to the linear speed of the drum wall. Figure 4.2(b) shows that within 0.002s of the drum rotation, those particles nearest the drum wall have already acquired some velocity. A high velocity region quickly develops close to the drum wall. The particles further away from the drum wall have relatively small speeds initially.

After only 0.024s (Figure 4.2(f)), there is already a clear symmetric velocity gradient along the drum radii. Concentric velocity regions are already well established, despite no apparent movement of the contact points B and C at this time. The highest velocities are observed at the drum wall. The radial velocity gradient continues to develop over time until it is possibly most symmetric at $t \approx 0.272$ s.

Between time $t \approx 0.272$ s and $t \approx 0.428$ s, the region of lowest velocity (initially at the midpoint on the free surface) gradually shifts into the bed. This transition can be clearly seen in Figure 4.2(k,l,m). During this time, the radial velocity gradients become distorted and asymmetric.

The first high velocity avalanching is observed at $t \approx 0.428$ s, in Figure 4.2(o). Initially, high velocity avalanching is only observed on the left hand side of the free surface (line AC). By time $t \approx 0.59$ s, in Figure 4.2(v,w), high velocity avalanching is observed across the whole free surface, not just the left hand side. More and more material close to line AC starts moving down the free surface and then this develops into a thick bow shaped layer of particles flowing at high speed parallel to the free surface. The bow shaped region is already well established by time $t \approx 0.83$ s, depicted in Figure 4.2(x). After this time, there is no apparent change in the velocity field configuration. We can infer that a rolling motion of the bed is established by time $t \approx 0.83$ s.

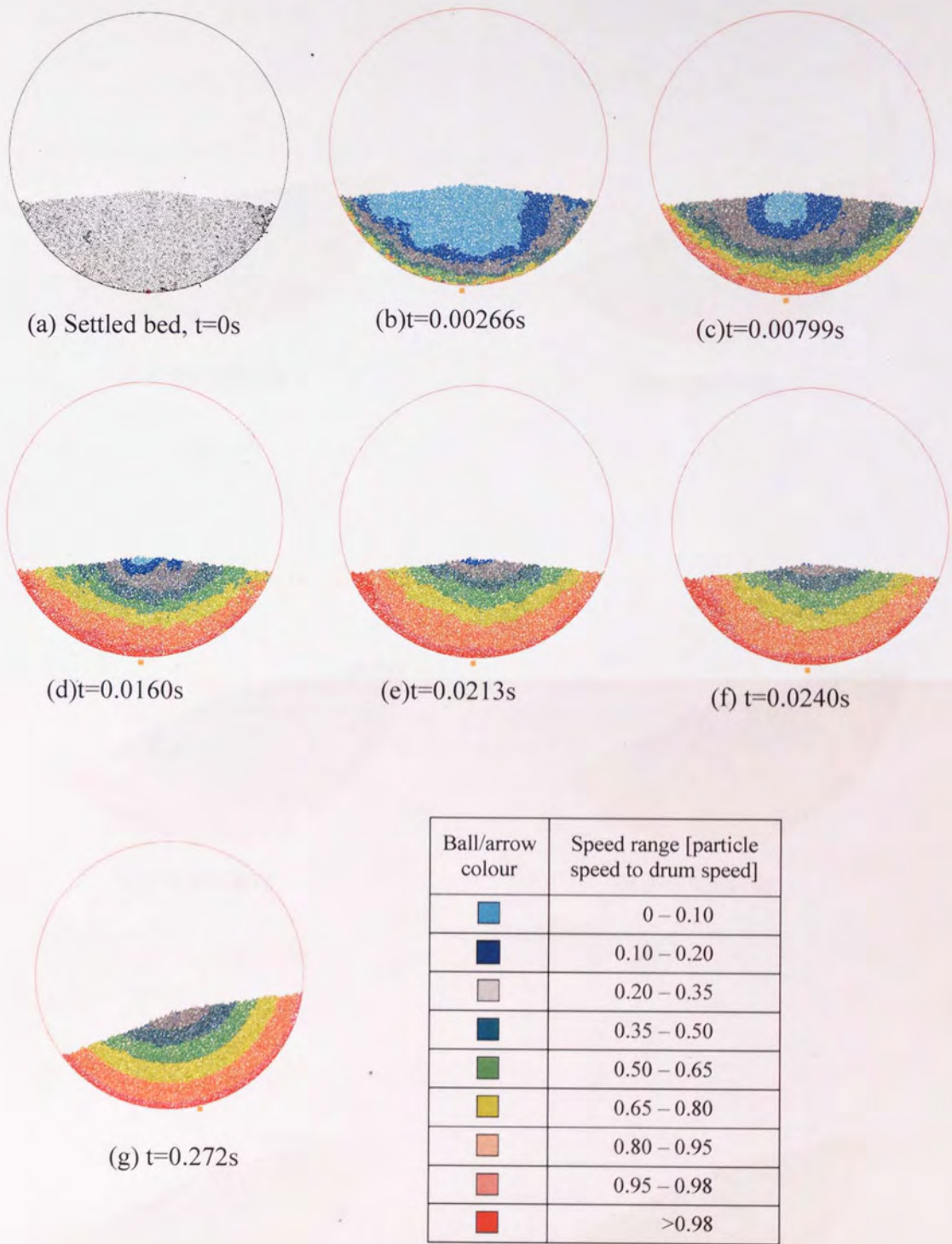


Figure 4.2: Snapshots from the speed/velocity animations for the drum



(h) $t=0.2955153$



(i) $t=0.3221383$



(j) $t=0.3487613$



(k) $t=0.3594105$



(l) $t=0.3753843$



(m) $t=0.3886958$

Figure 4.2 (continued)



(n) $t=0.4046696$



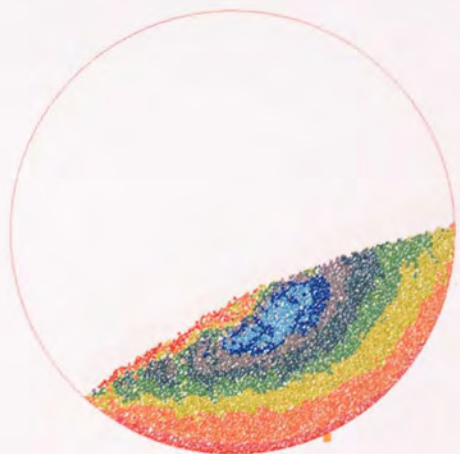
(o) $t=0.4286303$



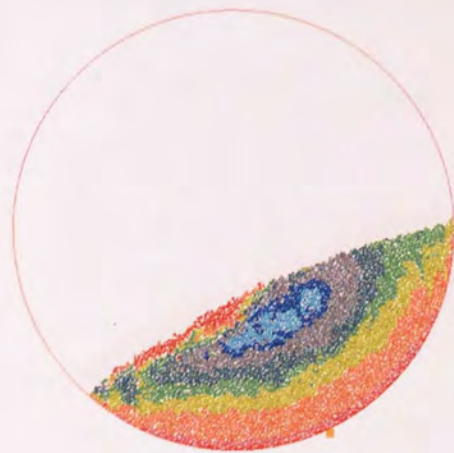
(p) $t=0.4419418$



(q) $t=0.4552533$



(r) $t=0.4685648$



(s) $t=0.4818763$

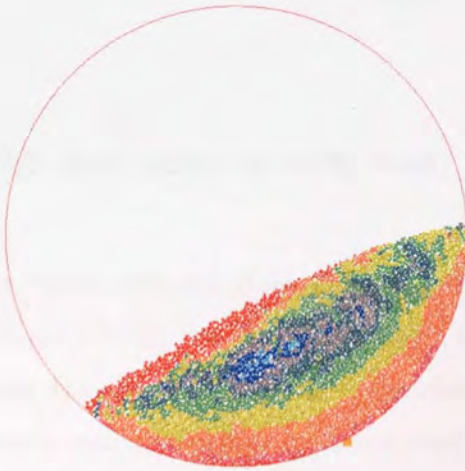
Figure 4.2 (continued)



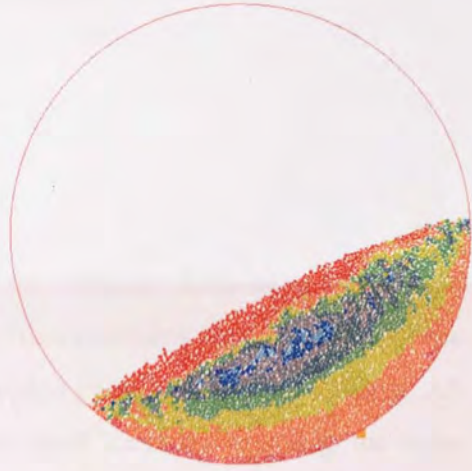
(t) $t=0.4951878$



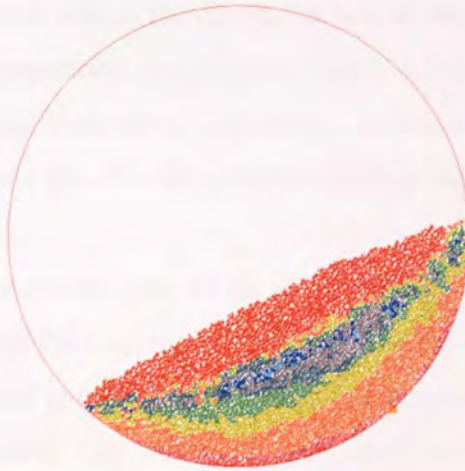
(u) $t=0.5084993$



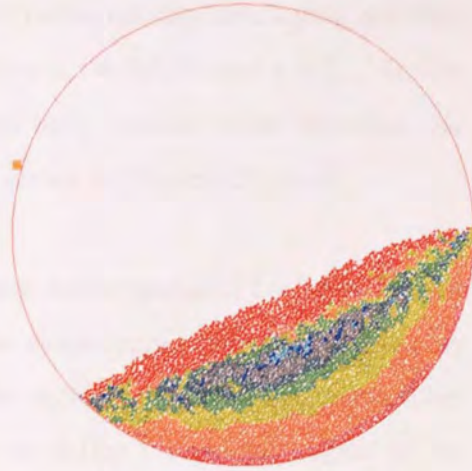
(v) $t=0.5404469$



(w) $t=0.5910306$



(x) $t=0.8306376$



(y) $t=4.3608474$

Figure 4.2 (continued)

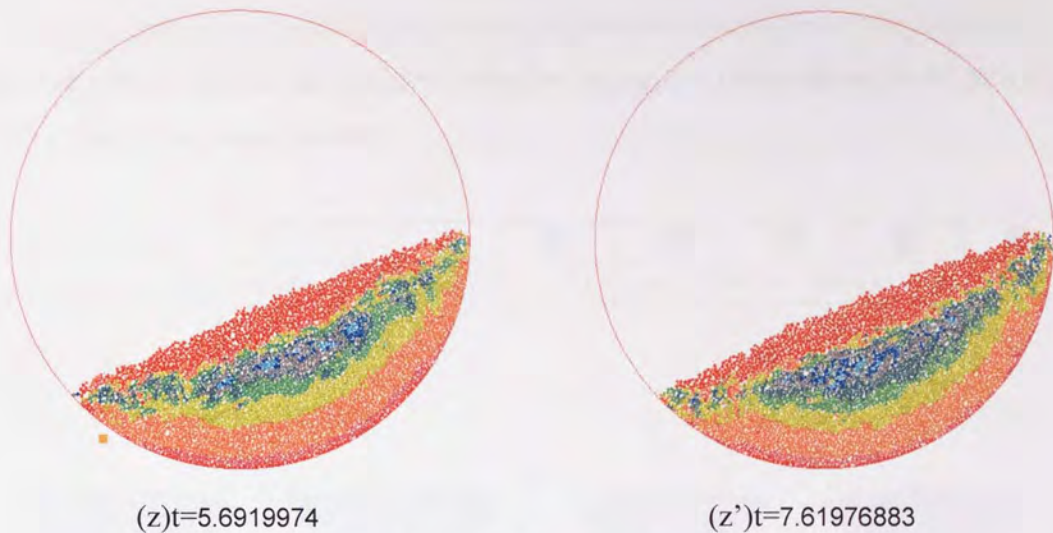


Figure 4.2 (continued)

4.2.3 Bed radial velocity field

The radial velocity field plots are similar to the velocity field plots. The main difference being that the colour-coded arrows or discs represent the component of the linear velocity of the particle in question in a direction parallel to the drum radius. All particle radial velocities in videos **rvel_1.avi** and **crvel_1.avi** are scaled to the drum speed.

At the start of the movie, the bed shows regions of radial velocity developing and then disappearing very briefly, Figure 4.3(a)-(d). Between $t \approx 0.023\text{s}$ and $t \approx 0.338\text{s}$, the radial velocity is very small, consistent with solid body rotation. After this time, the radial speed close to the free surface increases as shown in Figure 4.3(g)-(o).

The general form of the radial velocity field appears unchanged after $t \approx 0.54\text{s}$. By this time, the majority of the bed below the active bow shaped region appears to have only small radial velocity, which is consistent with the solid body inferred in many other studies. This observation suggests another way to define the passive region in the drum bed, by using a radial velocity field plot to identify where the radial velocity is zero or very small.

Figure 4.3 also shows that the radial velocity is zero or close to zero at the midpoint of the free surface. Indeed, all particles in the bed along this radius appear to be moving with a purely tangential velocity.




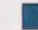

Ball/arrow colour					
Speed range [particle speed to drum speed]	0 – 0.35	0.35 – 0.70	0.70 – 0.85	0.85 – 0.94	> 0.94



Figure 4.3: Snapshots taken from the radial speed/velocity animations for the drum

4.2.4 Bed tangential velocity field



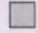

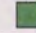
In the tangential velocity plots, the colour-coded arrows or discs represent the component of linear velocity in a direction perpendicular to the drum radii. All particle tangential velocities in videos **tvel_1.avi** and **ctvel_1.avi** are scaled to the drum speed.

The initial development of the tangential velocity field shown in Figure 4.4 appears to be remarkably similar to the development of the speed field shown in Figure 4.2. An initially highly symmetric radial distribution of tangential velocities is observed, with the largest tangential velocities observed at the drum wall.

At $t \approx 0.508\text{s}$, shown in Figure 4.4(n), we start to see significant tangential velocity in the free surface. This is consistent with the postulated high velocity avalanching. Below the bed surface, a band shaped region of low tangential velocity running from toe to shoulder is observed. This feature is not visible in the equivalent images in Figure 4.2, and suggests that another way to characterize the flow of material in the bed is to draw contour lines of uniform tangential velocity. Despite this difference, the velocity field and the tangential velocity field clearly share many similarities, which suggests that the dominant contribution to the total velocity is from the tangential component.

A steady state appears to be established in the tangential velocity field by time $t \approx 1.073\text{s}$, shown in Figure 4.4(o). The determination of steady state dynamics is discussed later in section 4.5.

Figure 4.4: Snapshots taken from the tangential speed animations for the drum

Ball/arrow colour					
Speed range [particle speed to drum speed]	0 – 0.35	0.35 – 0.70	0.70 – 0.85	0.85 – 0.94	> 0.94



(a)t=0.0026623



(b)t=0.0079869



(c)t=0.0106492



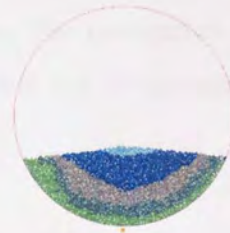
(d)t=0.0133115



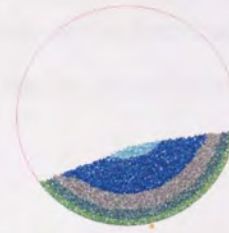
(e)t=0.0159738



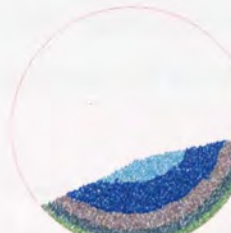
(f)t=0.0186361



(g)t=0.0239607



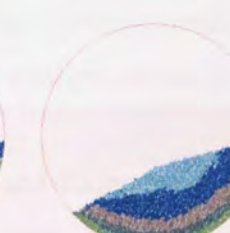
(h)t=0.2715546



(i)t=0.3381121



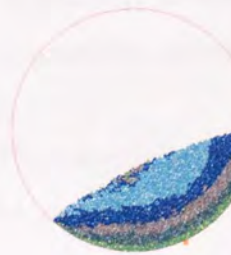
(j)t=0.3753843



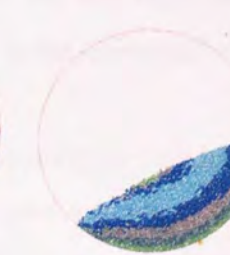
(k)t= 0.3886958



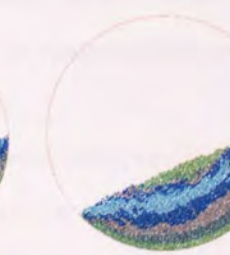
(l)t=0.4046696



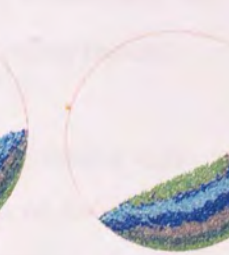
(m)t=0.4818763



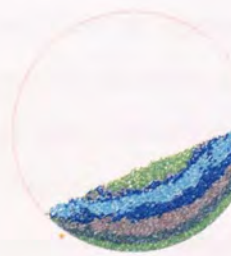
(n)t=0.5084993



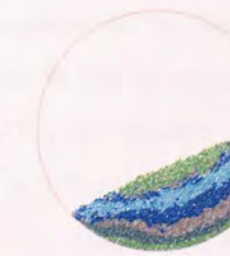
(o)t= 1.0729069



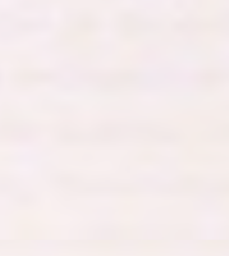
(p)t=4.3608474



(q)t=5.6919974



(r)t=7.61976883



4.2.5 Particle connectivity



In the **cnd_1.avi** video, a connection diagram is used to show any contacts between particles or particle and drum wall. In the diagram, a line is drawn between the centre of any two particles in contact, and for a particle-wall contact a line is drawn from the contact point on the wall to the particle centre for all particle-wall contacts. The thickness of these lines is proportional to the magnitude of the normal contact force acting between the two particles in contact or particle and wall contact and is scaled to the maximum force at that point in time. The connection lines are colour coded as orange for the less than average forces and red for greater than or equal to average forces.

The animation **cnd_1.avi** shows the regions where strongest connectivity is occurring are close to the drum wall. In the animation the connectivity data reveals that there are small regions of strongest connectivity that appear to rotate with the drum wall. It is observed that the strong force chains tend to align on a northeast-southwest diagonal.

At the very beginning of the simulation, and during solid body rotation of the system (i.e. $t < 0.5s$), the connectivity lines are densely packed, with the strongest connectivity at the region close to the drum wall. Near the free surface, the connectivity is weak, but still high density. After $t \approx 0.75s$, a markedly less dense connectivity appears in the upper half of the material (the cascading region).

The decrease in connectivity, which has been observed in the animated data, can also be seen clearly in Figure 4.6, which plots the time evolution of the total number of particle contacts. The plot shows a rapid decrease in the number of contacts, from approximate 8,000 in the initial static state. By time $t \approx 1s$, the number of contacts stabilizes at approximately 6800. Obviously, the exact values for the number of particle contacts shown in the figure are dependent upon the two dimensional nature of the simulation. This is because the number of nearest neighbours for two dimensional packing is lower than for three dimension packing. There is a significant periodic oscillation in the number of contacts. This behaviour has been observed in

many different analyses of the data presented in this chapter. Most of the macroscopic bulk characteristics of the system have this same fluctuating behaviour.

Colour scheme	Contact colour scheme
Less than average force	
Greater than or equal to average force	

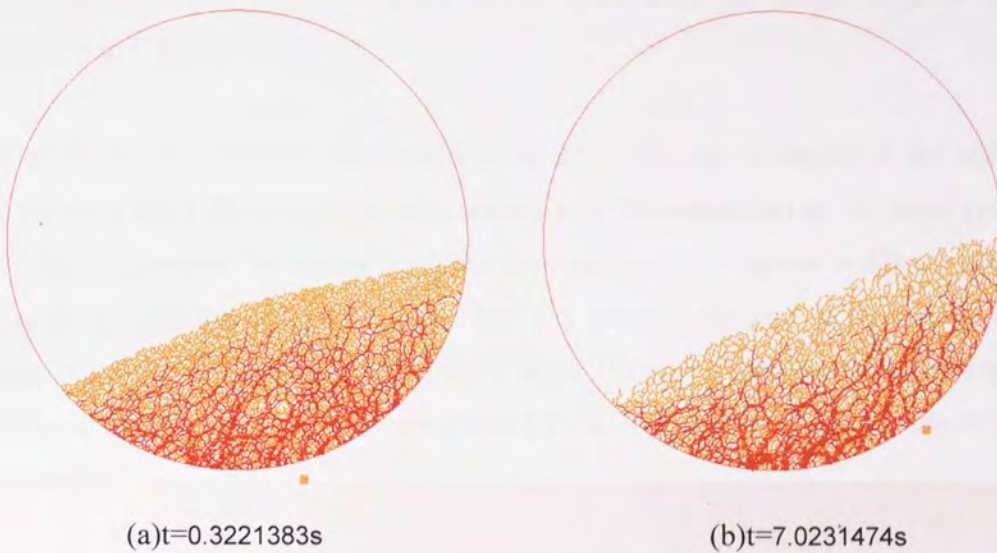


Figure 4.5: Connection diagram snapshots taken from the `end_1.avi` animation

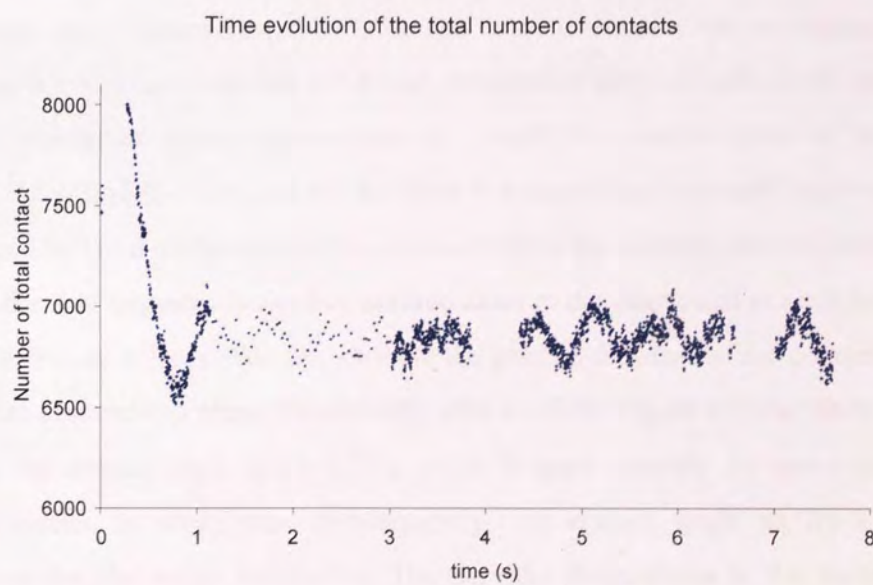


Figure 4.6: Time evolution of the total number of contacts

4.3 Contact angle measurements

Fauve et al. (1991) investigated avalanches by measuring the contact angle in low speed drums; see section 2.5.2 for a brief overview of Fauve's paper. The contact angle in the rolling drum was measured as follows: the particle-wall contact point was obtained for the particle with the lowest x-coordinate in the toe region of the flowing bed. This point is marked as point A in Figure 2.5. The contact angle θ is the angle described by a line from the centre of the drum from the x-axis to point A, as indicated in Figure 2.5.

From *Cleary et al. (2003)*, we expect that the dynamic angle of repose of the bed will be different for a 2D simulation with respect to a 3D simulation of the same system. The bed is expected to assume a higher dynamic angle of repose in 3D simulations because the packing of particles in the bed has greater resistance to shear and is less likely to collapse. Similarly, the contact angle (i.e. the position of the toe region) obtained from our data would be expected to be higher if we had performed a 3D simulation.

The contact angle was measured for all of the saved states for the entire simulation. The results are shown in Figure 4.7. In the figure, the contact angle increases approximately linearly from 22° to 50° at the start of the simulation. The peak value for contact angle occurs around $t \approx 0.5$ s. The linear increase of the contact angle up to this time is consistent with the solid body rotation of the bed. Indeed the gradient of the line before the peak is almost exactly 1 rad/s (the rotation speed of the drum). During the period ($t \approx 0.5$ s to $t \approx 0.8$ s) there is a transition from solid body motion of the settled bed to a continuous rolling motion. From the velocity plots in section 4.2.2 we see the first cascades in the free surface close to the drum wall at $t \approx 0.5$ s (see, for example, Figure 4.2(u)). We can attribute the gradual decrease of the contact angle to the initial avalanching phase immediately after $t = 0.5$ s. Figure 4.7 also shows a sharp drop in the contact angle at $t \approx 0.75$ s, which is approximately the same time that a rolling motion is established. Subsequently, the contact angle shows a periodic behaviour for the entire simulation. The periodic fluctuations in the contact angle appear to have a peak-to-trough magnitude of approximately 5° , centred on a mid-

point value of approximately 45° . The period of the large-scale fluctuations is between 0.5s and 0.7s.

As explained in section 2.5.1, a peak-to-trough transition in the contact angle corresponds to an avalanche. There are three avalanche measurements that can be extracted from the contact angle data (referring to Figure 2.6):

- (i) Avalanche amplitude, A , which is the size of the drop in the contact angle during a peak-to-trough transition.
- (ii) Avalanche duration, τ , which is the time duration from peak to the next trough
- (iii) Interval between avalanches, ΔT , which is the duration from trough to the next peak

Figure 4.8 shows the contact angle data between times 4.36s and 6.49s only. The maximum amplitude of the large-scale fluctuations appears to be approximately $\pm 2^\circ$. Superimposed on the large-scale fluctuation there is a much higher frequency, small amplitude fluctuation in the contact angle. These second-order order fluctuations appear to vary randomly in amplitude.

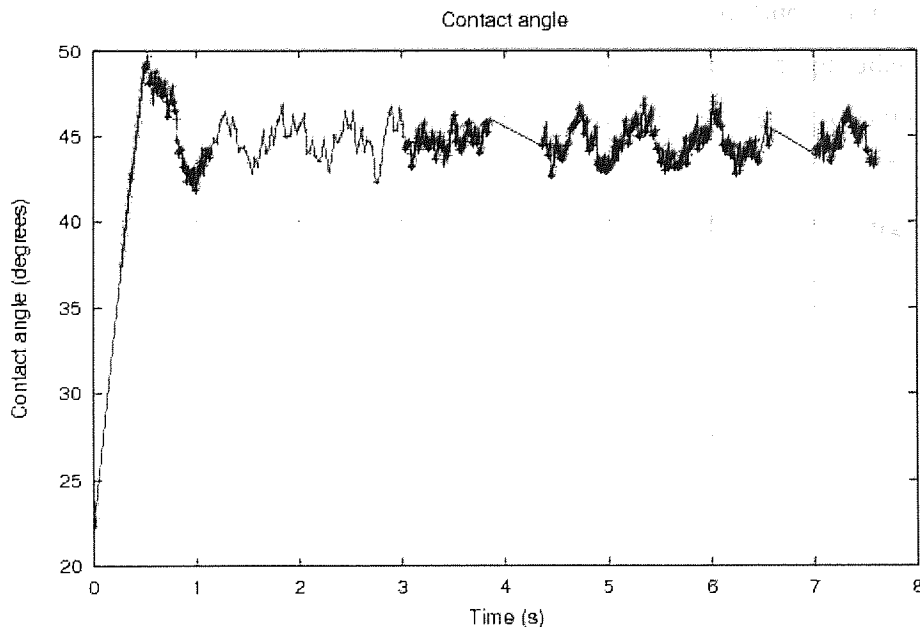


Figure 4.7: Time evolution of contact angle for the rolling drum

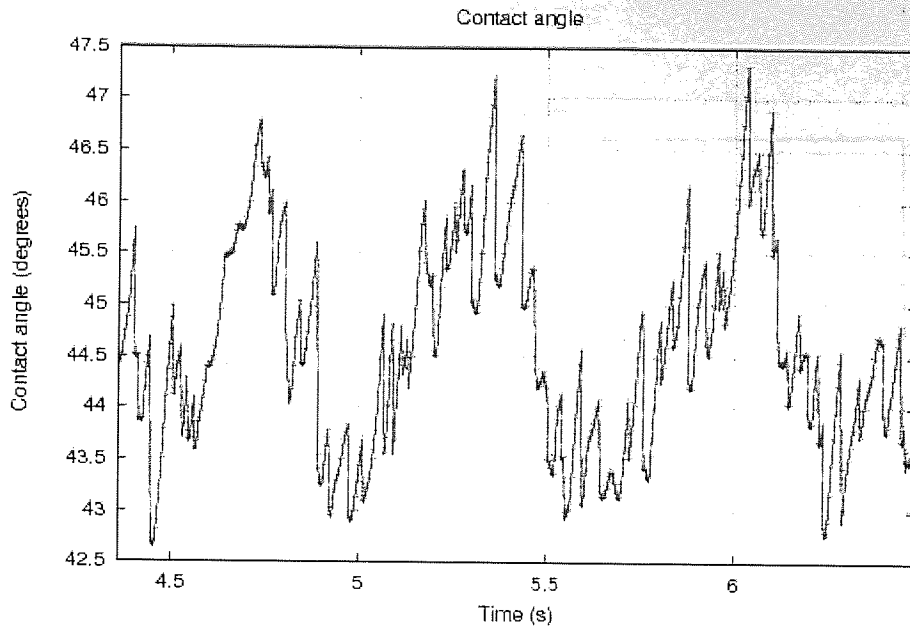


Figure 4.8: Time evolution of contact angle between times 3.36s and 6.49s. The high frequency, small amplitude fluctuations correspond to minor avalanches.

The structure of individual secondary avalanches is shown in Figure 4.9. The plot suggests that, typically, these secondary avalanches result in fluctuations of the contact angle of the order of one degree. These minor avalanche amplitudes are of similar magnitude to the angular sizes of individual particles (the particle sizes, 0.5mm, 0.75mm, 1mm, 1.25mm, and 1.5mm have angular sizes 0.38° , 0.57° , 0.76° , 0.96° , and 1.34° at the drum wall respectively). This suggests that only a single layer of particles has avalanched when the contact angle changes abruptly. On inspection, the intervals between avalanches indicate a continuous increase of the contact angle, at a steady rate. The average gradients from trough-to-peak are roughly the same in all cases, which indicates that particles at point A move with constant angular velocity as soon as they reach the drum wall.

To summarize, the contact angle plots show that as soon as a particle from the free surface hits the drum wall, it acquires a constant angular velocity. It is then carried along the drum wall until another particle(s) avalanches down which causes the contact line to change sharply. Given that particles at point A appear to be acquiring a

constant angular velocity, it is interesting to investigate the angular velocity along the entire arc of the drum wall. The angular velocity distribution at the drum wall will be analysed later in this chapter.

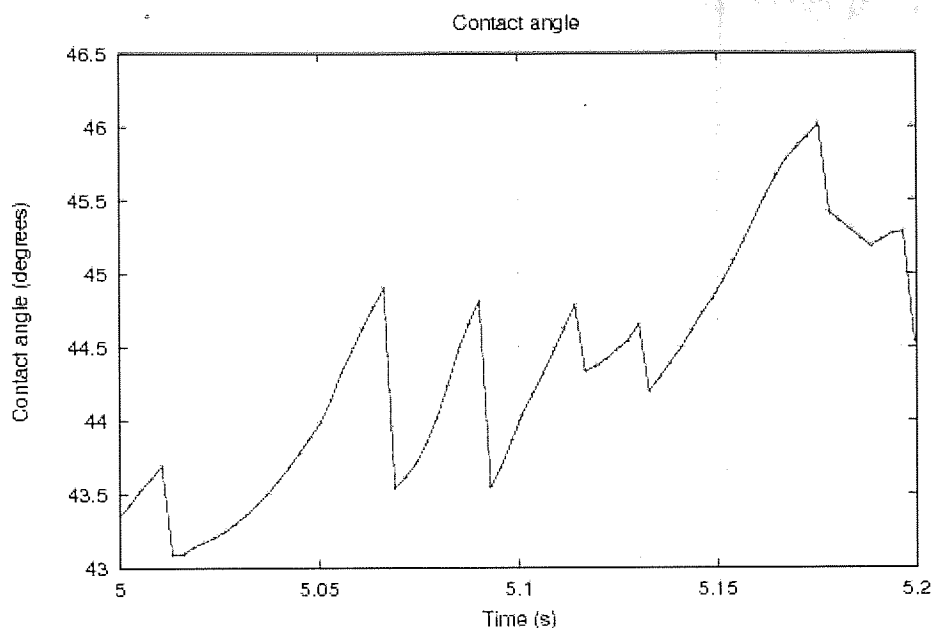


Figure 4.9: Time evolution of contact angle between times 5.0 and 5.2s

4.3.1 Avalanche measurements

The contact angle data was time-ordered, and then analysed to find all local peak and trough positions, in order to measure avalanche characteristics. The magnitude of all avalanches (height from all peaks to the following trough) was measured in our contact angle data for the duration of the drum run. Only the high frequency subset of the simulation data was used. A total of 132 avalanches were recorded, so the statistics are quite small. The results are shown in the histogram in Figure 4.10.

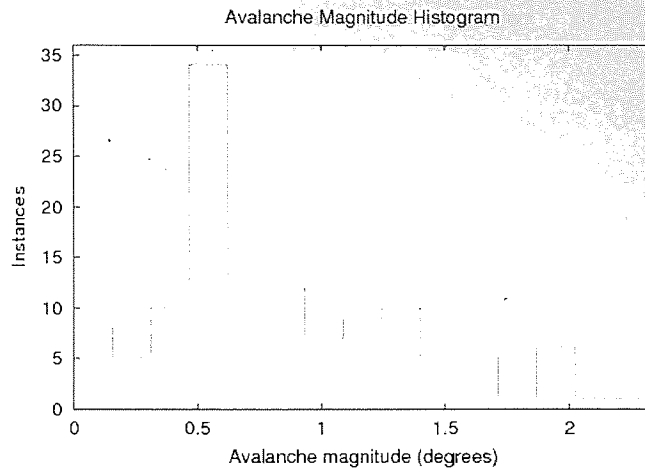


Figure 4.10: Avalanche magnitude histogram

The largest avalanche magnitude in the whole dataset is approximately 2.5 degrees, and the avalanche magnitude histogram has a sharp peak around 0.5 degrees. This is consistent with the hypothesis that the change in contact angle is frequently due to a single particle layer avalanching down the free surface to arrive at the drum wall. Higher time resolution data recordings are required to confirm this. It should be noted that this hypothesis may be contingent on the 2D nature of the simulation. It is known that 3D simulations tend to exhibit higher dynamic angle of repose, and therefore the failure of the structure (and subsequent avalanche) can be expected to occur at higher angles of inclination. In that case, different avalanche dynamics may be generated, possibly with more than a single layer of particles moving down the free surface.

The avalanche intervals or waiting time between avalanches (time periods between all troughs to the following peak) was measured in our contact angle data for the duration of the drum run. Again, only the high frequency time data was used. The results are shown in the histogram in Figure 4.11. For the majority of avalanches the interval is less than 0.04s and decays rapidly as we would expect for a randomly occurring event. The majority of avalanches occur over very short times and fewer at longer times. The longest avalanche interval is about 0.12s. If the data is reanalysed, considering only the data after $t=1s$, the maximum avalanche interval is 0.077s. Therefore, the very long interval event (interval $\approx 0.12s$) occurs at $t < 1s$, when the bed is going through a transition from settled bed to rolling bed.

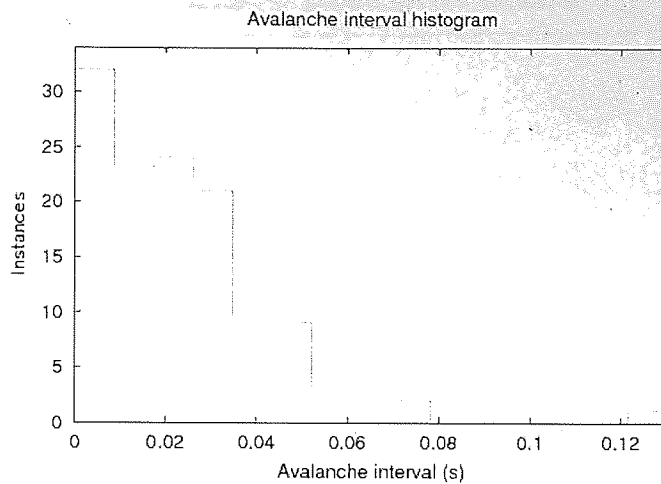


Figure 4.11: Avalanche interval histogram

A correlation between the magnitude and interval of avalanche was investigated, by plotting avalanche amplitude against waiting time. The plot is shown in Figure 4.12; no correlation was found. *Fauve et al. (1991)* observed such a correlation between A and ΔT , (that a longer interval between avalanches is generally followed by a larger avalanche). However, Fauve's observation was made in a chaotic regime, at rotational speeds much slower than the rolling mode (Froude number 0.0003). It does not follow that this should be true for the regime we are investigating (i.e. the rolling mode). Indeed, at Froude number ≈ 0.02 , he no longer detected discrete avalanches of varying sizes, but instead observed a smooth periodic fluctuation in the contact angle. For comparison, the Froude number of the rolling mode simulation presented here is approximately 0.008.

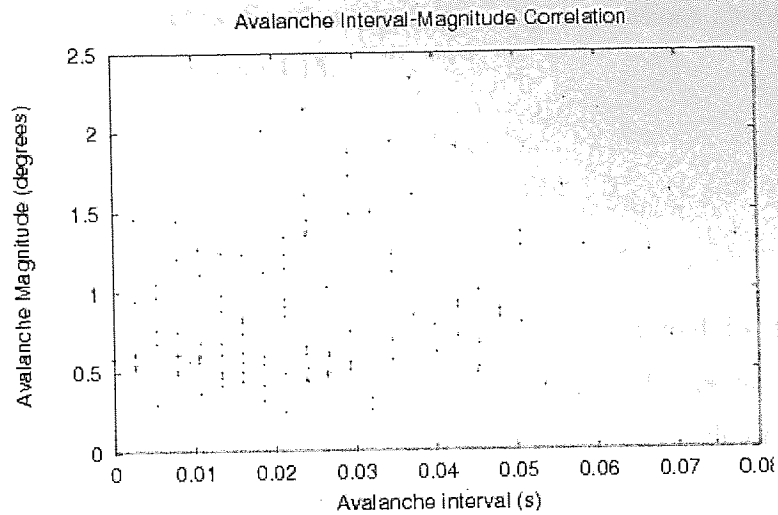


Figure 4.12: Avalanche magnitude plotted against avalanche interval

The avalanche duration (time period between all peak to the following trough) was measured in our contact angle data (after $t=1s$) for the duration of the drum run. The results are shown in the histogram in Figure 4.13.

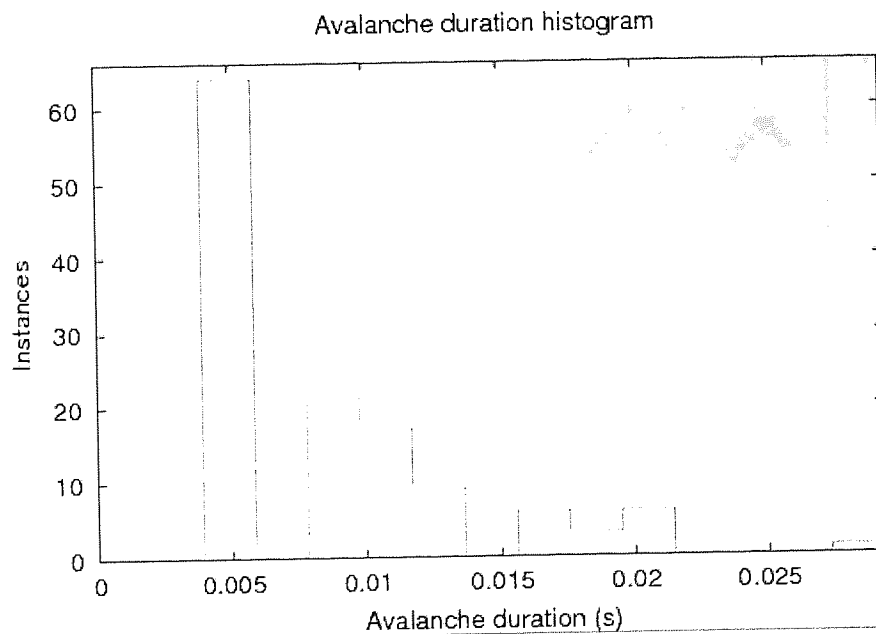


Figure 4.13: Avalanche duration histogram

Recall that the time step for the high-frequency sampling was 0.00266s. The duration of the avalanches is of a comparable time scale, as can be seen from Figure 4.9 and Figure 4.13. As a result the time step for sampling is too large to give good resolution

for the duration of avalanches. So we cannot draw any conclusions about the actual duration of avalanche from Figure 4.13.

4.4 Angle of repose

The angle of repose for the bed material was simply measured by finding the minimum and maximum contact angle. These angles correspond to points B and C in Figure 4.1(b). A line is drawn between these two points and the angle of this line to the horizontal is the angle of repose. The plot shows the initial angle of repose is zero as expected for the settled bed. The dynamic angles of repose varies between 21.5° and 25.8° after $t=1$ s. The mean angle of repose averaged over all data points after $t=1$ s is 23.6° . The changes in the angle of repose plot correlate with contact angle changes in Figure 4.7. On inspection, the high frequency fluctuations in the angle of repose (see Figure 4.15) appear to have similar structure to those of the contact line (see Figure 4.8).

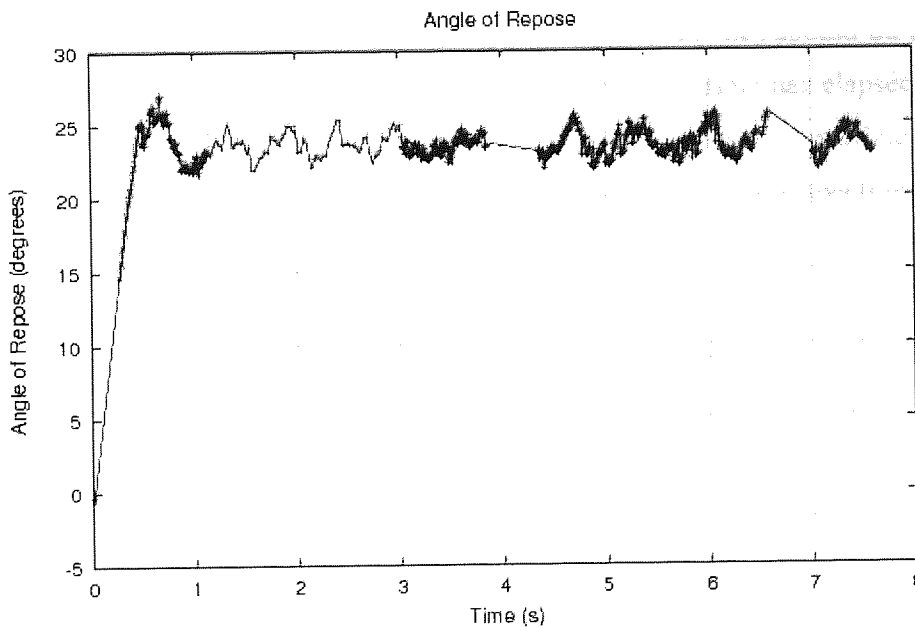


Figure 4.14: Time evolution of the angle of repose for the rolling drum

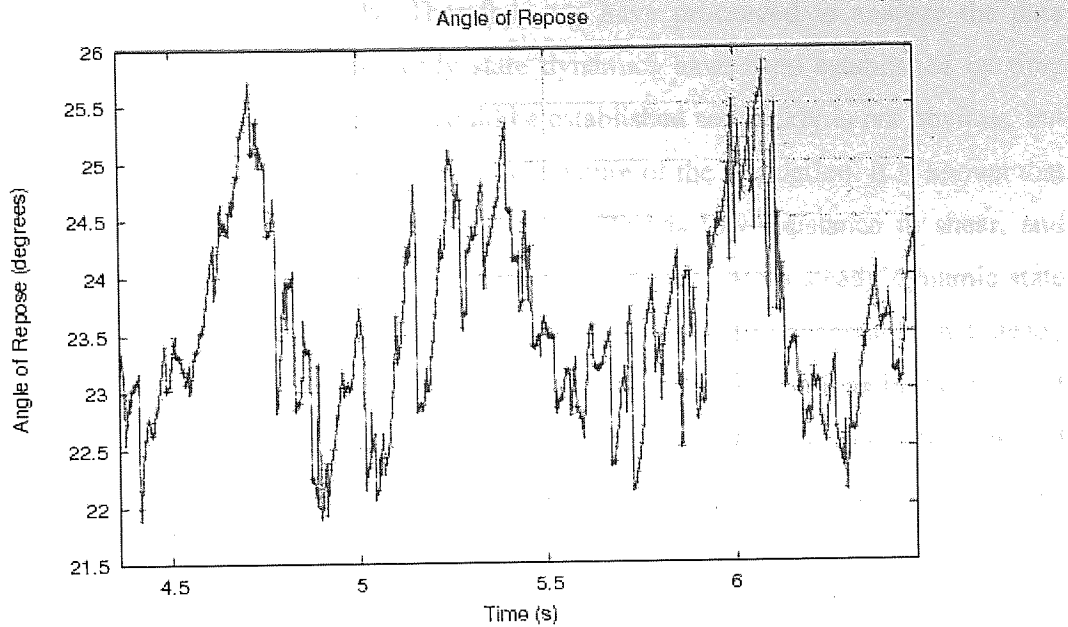


Figure 4.15: Time evolution of the angle of repose between times 3.36s and 6.49s

4.5 Determination of steady state dynamics

It is clear that any meaningful analysis of the bed dynamics should be performed in the steady state; i.e. after a certain period of simulation time has elapsed to allow the bed motion to stabilise. Conclusions should only be drawn for particle motion after that point. Other published DEM work has relied upon visual inspection of the bed to determine the steady state, although this is rather subjective. Some workers, for example *Pandey et al. (2006)*, have suggested that the evolution of the angle of repose may be used to determine a steady state (the angle of repose stabilizes after 0.75 revolutions in their system). Other workers have simulated a fixed number of drum revolutions or monitored other macroscopic variables to infer steady state dynamics. *McBride et al. (2004)* establish steady state by simulating 2 revolutions of the drum whilst monitoring the power draw. They find the power draw stabilizes after approximately 1 drum revolution.

Applying the criterion of *Pandey et al. (2006)* to our simulated angle of repose data leads to a steady state point between $t=1.0s$ and $t=1.5s$. This corresponds to only 0.16 – 0.24 drum revolutions, which is significantly less than the times reported elsewhere, but time $t=1.5s$ is consistent with visual inference of the steady state from the

dynamics discussed previously. Therefore, we have proceeded to analyze the data based on the assumption that steady state dynamics have been established by time $t=1.5s$. How steady state dynamics could be established so quickly is not obvious, but it may be related to the 2D spherical particle nature of the simulation. It is known that the microstructure of close-packed spheres in 2D has low resistance to shear, and therefore our system may possibly collapse more readily into a steady dynamic state upon agitation. This has not been investigated, and it is still conceivable that steady state may not have been reached. The first order periodic fluctuations in the angle of repose are not immediately explainable, and it could be that these fluctuations would gradually decay if many more drum revolutions were simulated. If that were the case, steady state dynamics would only be achieved for $t \gg 7.5s$ (no decay in the first order fluctuations is apparent before this time). On the other hand, it is plausible that the fluctuations are intrinsic to the bed dynamics, and may not decay at all. A hybrid rolling-slumping flow may be present, like that observed by *Cleary (2000)* in simulations of spherical particles in a 2D rotating drum. Cleary suggests that the particle assembly flows partly by avalanching and partly by slumping because the microstructure of circular particles has very weak resistance to shear.

4.6 Particle velocities at the drum wall

The particle translational velocity and rotational velocity about the drum centre was measured for all particles within a 5mm thickness from the drum wall at $t=4.89\text{s}$. The results for the 754 particles that constitute this 5mm thick region are shown in the histograms in Figure 4.16 and Figure 4.17.

In Figure 4.16, the majority of the particles are moving at a translational velocity between 0.06 and 0.075m/s, and in Figure 4.17, the majority of the particles have rotational speed between 0.95 and 1rad/s. The rotational speed of the drum is 1rad/s, so particles close to the wall have a rotational speed within 5% of the drum wall. The data also shows that a small fraction of the particles close to the drum wall have a rotational speed significantly lower than the drum speed. The very small fraction of particles with speeds greater than the drum wall can probably be attributed to avalanching in the free surface.

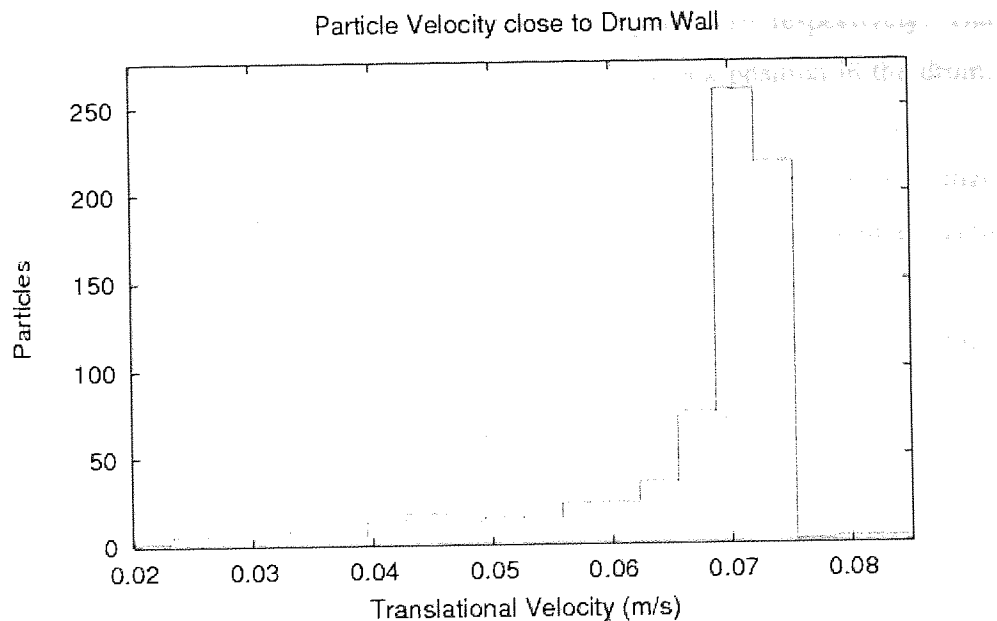


Figure 4.16: Translational velocity histogram for the particles within a 5mm thickness from the drum wall at $t=4.89\text{s}$

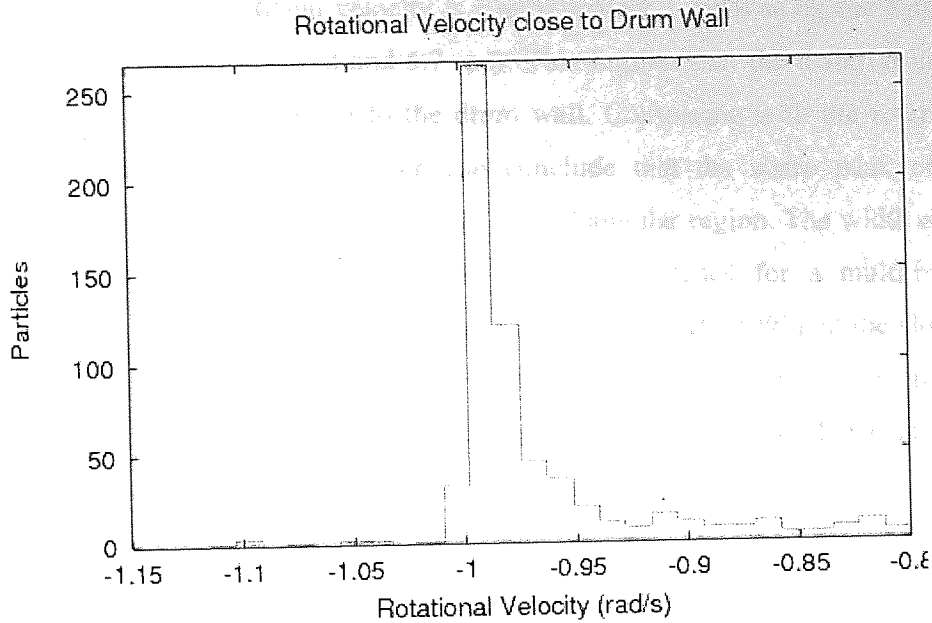


Figure 4.17: Rotational velocity histogram for the particles within a 5mm thickness from the drum wall at $t=4.89s$

The translational velocity and rotational velocity are plotted against the angular position around the drum wall in Figure 4.18 and Figure 4.19 respectively. The angular position is measured anti-clockwise from the 3 o'clock position in the drum. In Figure 4.18, we see that near the 6 o'clock position at the drum wall (between 4.5 rad - 5.7 rad), the translational velocity of the material has a very narrow range (between 0.070 and 0.075m/s). Particles close to the drum wall in this angular region appear to have speeds that are within 7% of the drum wall speed. For particles between angular positions 5.7 to 6.3rad close to the drum wall, the average translational speed decreases as we get closer to the shoulder (near the 3 o'clock position) and a much wider velocity distribution is apparent. In the toe region (between 3.9 rad - 4.5 rad), the variance in particle velocity becomes even greater. We can see that the high-speed tail of Figure 4.16 is indeed due to particles in the toe region (and hence cascades). It is also interesting to see that some particles in the toe region have small velocities (mirroring the behaviour at the shoulder region); this is probably due to the large change of direction at the end of the cascading layer, where particles are presumably moving relatively slowly before they are accelerated with the drum wall.

Figure 4.19 shows the rotational velocity is approximately 1 rad/s along the majority of the drum arc (between 4.5 rad and 5.7 rad). This implies that the material in this region is not slipping with respect to the drum wall. Comparing with the rotational velocity histogram in Figure 4.17, we can conclude that the sharp peak of the histogram comprises all those particles in this central angular region. The width of the histogram peak is only a few percent; there is no evidence for a multi-modal distribution. This is similar to results presented by *Parker et al. (1997)*, at the slowest rotational speeds investigated in that work. Although their results suffer from a substantial uncertainty in the velocity measurement ($\sim 10\%$), they find that at slow speeds, the rotational velocity histogram is indeed a single peak, centred on the drum speed. Additionally, a rotation speed of 1 rad/s in this region, coupled with the measured particle velocity of ~ 0.075 m/s suggests that there can only be a very small radial component of particle velocity at the drum wall in this region. This will be shown explicitly later.

Near the toe and shoulder regions, the mean absolute rotational velocity decreases, in agreement with Figure 4.18. This indicates there is increased slip with respect to the drum wall at the toe and shoulder.

It is worth noting that some simple analyses assume that all particles at the drum wall are moving with the same rotational speed as the drum wall, e.g. *Saeman (1951)*. These results show that even at quite moderate rotational speeds where no slip is occurring in the central region, there can often be substantial slippage at the toe and shoulder. Of the total angular coverage at the drum wall, which is $\sim 140^\circ$ in this simulation, substantial slipped occurs over approximately 60° .

Figure 4.20 shows a subset of the data from Figure 4.19, considering only those angular positions between 4.2 and 6 rad. For reference, the mid-point between the toe and shoulder regions has angular position ≈ 5.1 rad. At this angular position there is an extremely tight velocity distribution across the 5mm radial annulus, so the angular position of minimum slip is almost exactly equidistant between the toe and the shoulder.

In the angular region 4.6 to 4.8 rad (towards the toe region), Figure 4.20 shows some interesting behaviour. There is apparently a region of rotational velocity turbulence, which roughly corresponds to the 6 o'clock position at drum. It is possible that whilst the particles are transitioning from negative y-velocity to positive y-velocity, they may pass through a turbulent region, or perhaps this angular position is somehow strongly affected by avalanching in the toe region. It is also conceivable that in this particular region, there are a large number of particles being forced *out* of the outermost layer, away from the drum wall. This could occur due to a high flux of particles from the high-speed cascading layer "colliding" with the slower moving rotating base layer at the drum wall. If particles were being forced inwards, then the apparent rotational velocity would be decreased.

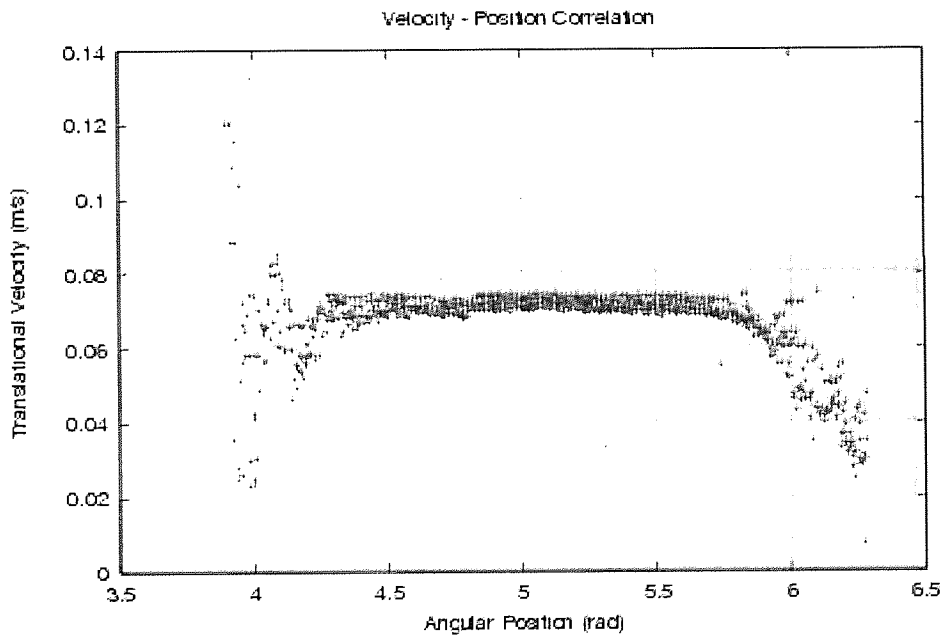


Figure 4.18: Translational velocity along the drum wall at $t=4.89s$

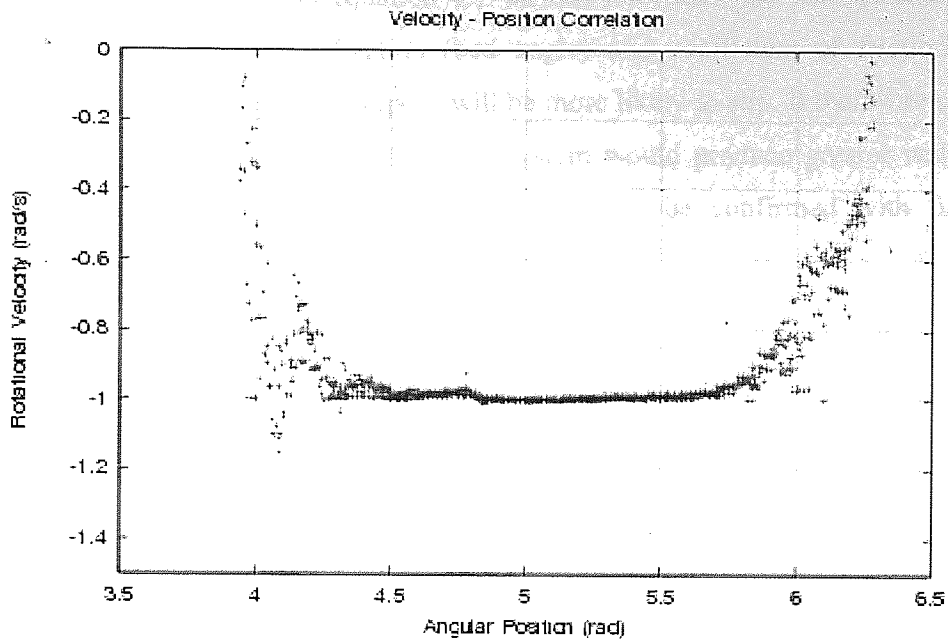


Figure 4.19: Rotational velocity along the drum wall at $t=4.89s$

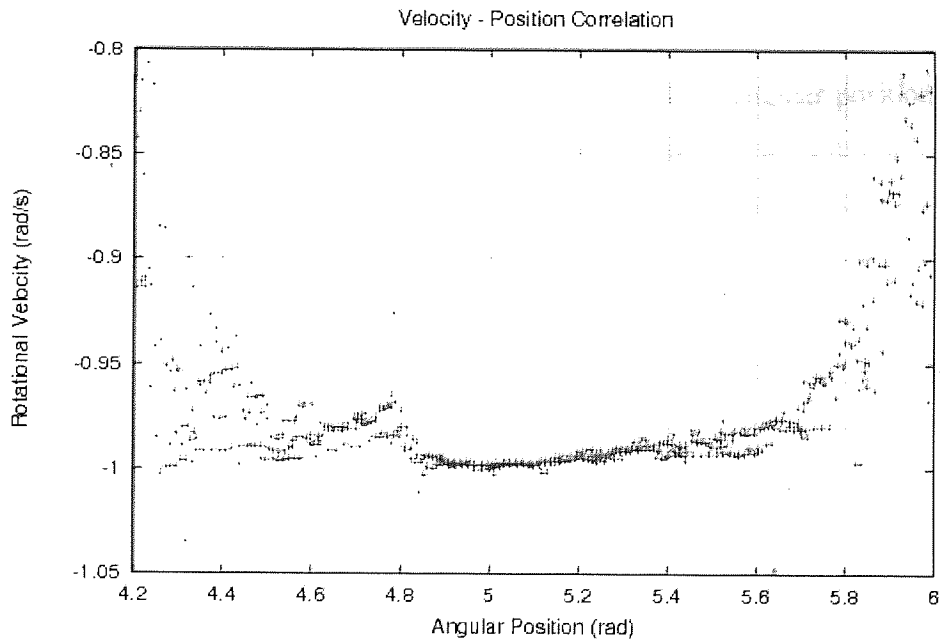


Figure 4.20: Rotational velocity along the drum wall close to the 6 o'clock position, at $t=4.89s$

It is conceivable that the wall-slip behaviour described above is dependent upon the 2D nature of the simulation. It is known that 3D simulations of granular material tend to produce higher dynamic angles of repose due to the greater shear strength of the

granular microstructure. From equation 4.1 we can infer that, for two systems with identical Froude number, fill-fraction (bed angle) and coefficient of friction, the material with the greater angle of repose will be more likely to slip. It therefore seems plausible that a 3D simulation of the same system would produce greater wall-slip than we have observed in 2D. This would need to be confirmed with further simulation experiments.

4.7 Particle spin at the drum wall

One differentiating feature of DEM simulation compared to PEPT experimentation is that many more measurements of particle motion are obtainable. One such example is the particle spin, shown in rad/s in Figure 4.21. The figure shows the spin correlation with angular position at the drum wall. The figure is truncated along the y-axis to depict only those spins in the range -100 to $+100$ rad/s. Although these rotational velocities appear very high, the mean particle diameter is only 1mm, which implies a surface velocity of only 50mm/s. In the full data set there are a few outliers with much higher spin; these are not shown in the plot. There is minimal particle spin in the angular interval 4.5 - 5.6 rad. This interval is centred on the angular position that is midway between the two ends of the free surface (~ 5.1 rad). At the extremities, there is a clear randomisation of the particle spin, which is greatest at the toe or shoulder region.

In Figure 4.22, individual particle spins are plotted for a 5mm thick radial annulus at the drum wall. Particle spins are plotted against the radial distance from the drum centre. No clear correlation is seen with radial position. The maximum radial position observed is ~ 0.0748 m, which is consistent with the smallest particles in the system lying in contact with the drum wall (the smallest particle has a radius of 0.25 mm, so we expect a radial position to the particle centre of $0.075 - 0.00025 = 0.07475$ m).

It should be noted that the magnitude of the spin is expected to be enhanced by the 2D nature of the simulation. We expect that for a 3D simulation, the connectivity will be stronger even in toe and shoulder. Therefore particles would be more constrained, leading to lower particle spin.

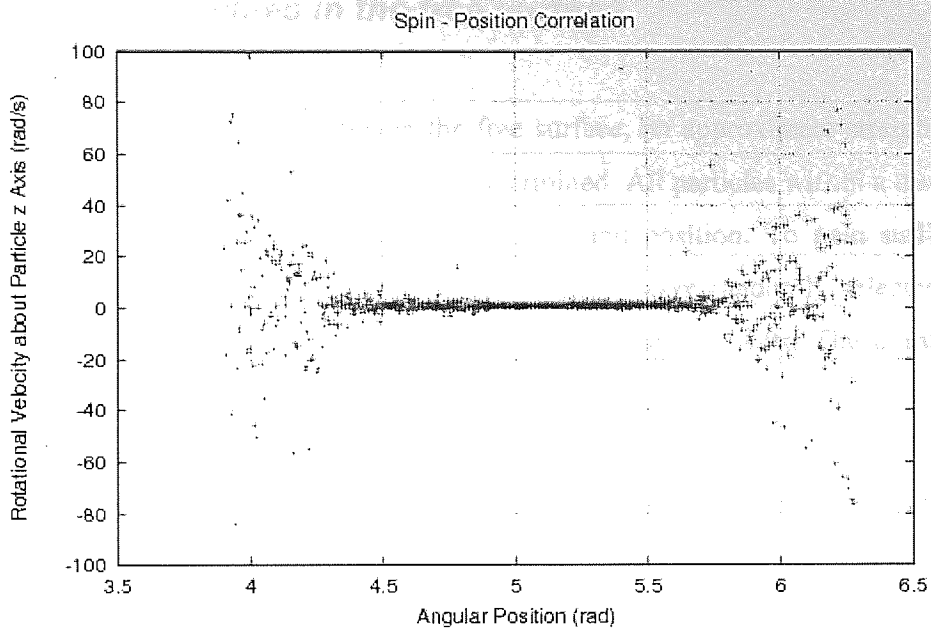


Figure 4.21: Particle spin velocity along the drum wall, at $t=4.89s$

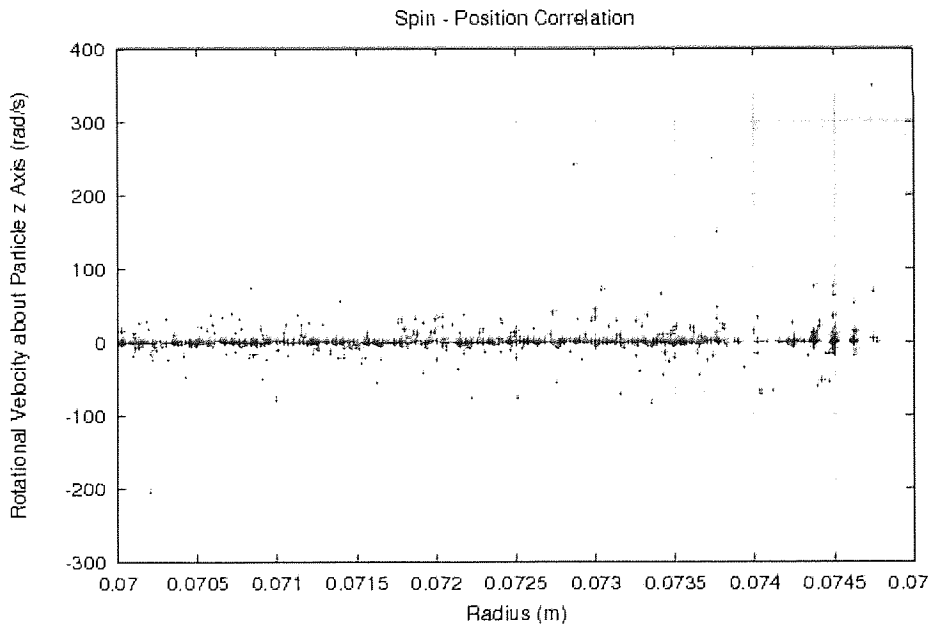


Figure 4.22: Particle spin velocity close to the drum wall at increasing drum radii, at $t=4.89s$

4.8 Particle velocities in the free surface

To investigate the particle velocities in the free surface, an approximate straight line joining the two ends of the free surface was determined. All particles within a distance of 5 mm from the line were queried for velocity and position. To gain sufficient statistics for a meaningful analysis, 6 simulation states were randomly selected and combined into one dataset. All 6 states are for real times $t > 4.9\text{s}$. The combined dataset is 4880 particles within 5mm of the line.

Because the selection line approximates the free surface, the majority of particles selected are below the line. The position of the selected particles was characterized with two variables depicted in Figure 4.23. The distance l is the perpendicular distance of a particle from the line. The distance d characterises the position along the free surface, such that the position $d=0$ is at the very left most toe side. Large positive values for d are at the right most shoulder region. Note that the precise l -coordinate of the free surface is a function of d , because the free surface is not a perfectly straight line.

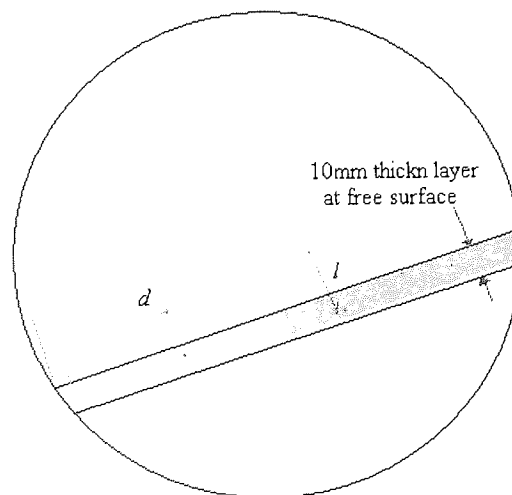


Figure 4.23: Characterisation of position in the free surface

The cascade velocity histogram is shown in Figure 4.24. In the figure, all 4880 particles are histogrammed for their absolute translational velocity. We see a peak in the distribution centred on 0.125m/s, with a much wider distribution (compared to the particle velocities at the drum wall, shown previously in Figure 4.16). The maximum

particle velocity in the cascade is approximately 0.3 m/s (compare to 0.075 m/s at the drum wall).

The absolute translational velocities have been characterised for particle position (d , l). The plots are shown in Figure 4.25 and Figure 4.26 respectively. In both plots, particles velocities have been histogrammed with respect to position. The points plotted are mean values in each histogram bin, and the error bars indicate standard deviations.

The correlation of translational velocity with distance along the free surface is extremely clear in Figure 4.25. The x-range of the plot represents the full length of the free surface. As observed by *Ding et al. (2001b)*, the highest velocity occurs at a position close to the mid-chord in the free surface. Particles in the free surface appear to accelerate as they descend, until they reach the approximate mid-chord of the free surface. They then decelerate as they approach the toe region. There is a good symmetry around the peak, similar to that found by Ding at low rotational drum speeds. The mean velocity at the mid-chord is approximately 0.16 m/s.

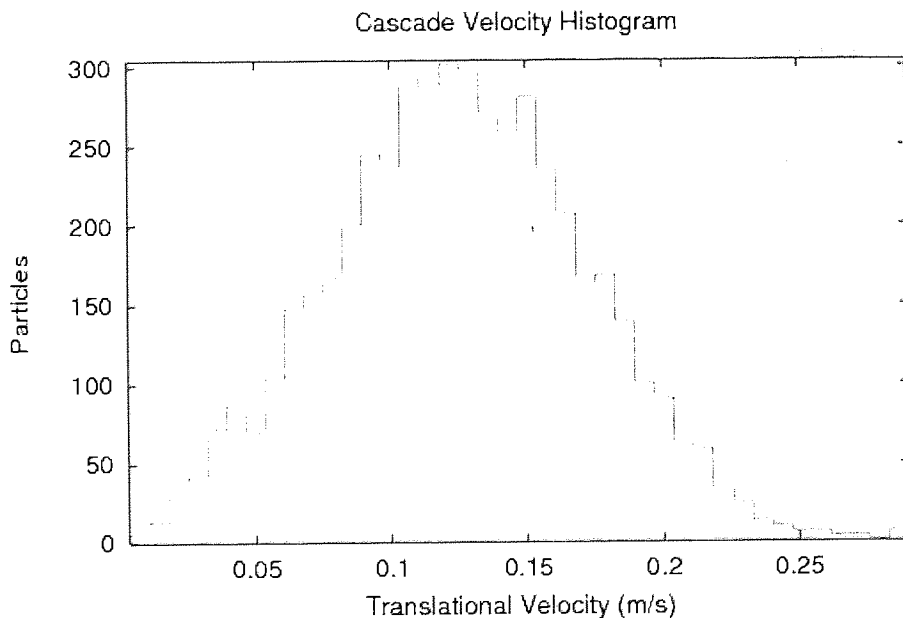


Figure 4.24: Cascade Velocity Histogram

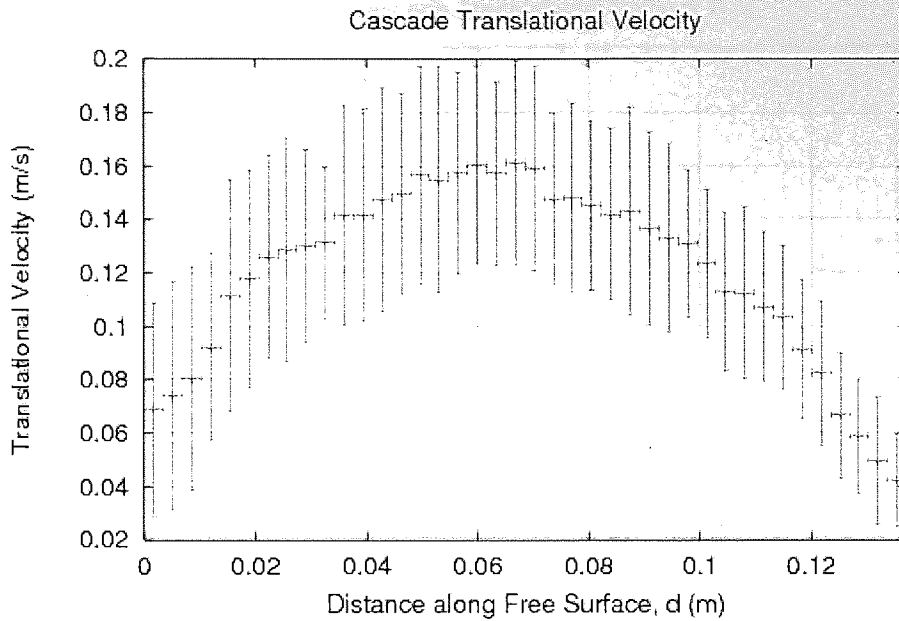


Figure 4.25: Cascade Translational Velocity along the distance d

The correlation of translational velocity with depth l shows that the mean particle velocities are highest at the very top of the free surface (the right-most side of Figure 4.26). There appears to be a roughly linear decrease in the mean particle velocity as we consider particles deeper and deeper into the bed. It should be noted that the mean velocity at each depth l is found by averaging over all particles parallel with the free surface at depth l . Therefore, any curvature of the free surface will mean that certain distances d along the free surface will contribute unevenly to the parallel sample statistics. That is, if the curvature is positive, then small depths l will only sample the very central region of the bed, whereas larger depths l will include more of the toe and shoulder regions as well. This also explains why the maximum mean velocity in Figure 4.25 is only 0.16 m/s, whereas the maximum mean velocity in Figure 4.26 is approximately 0.225 m/s. The latter is sampling only those particles at the very central part of the free surface, and only at the very top layer, whereas the former is sampling a slice through the free surface, which is nearly 1cm thick, and therefore includes many slower particles. Because of this, the maximum mean speed found in Figure 4.26 is a more representative value for the very top layer of the free surface.

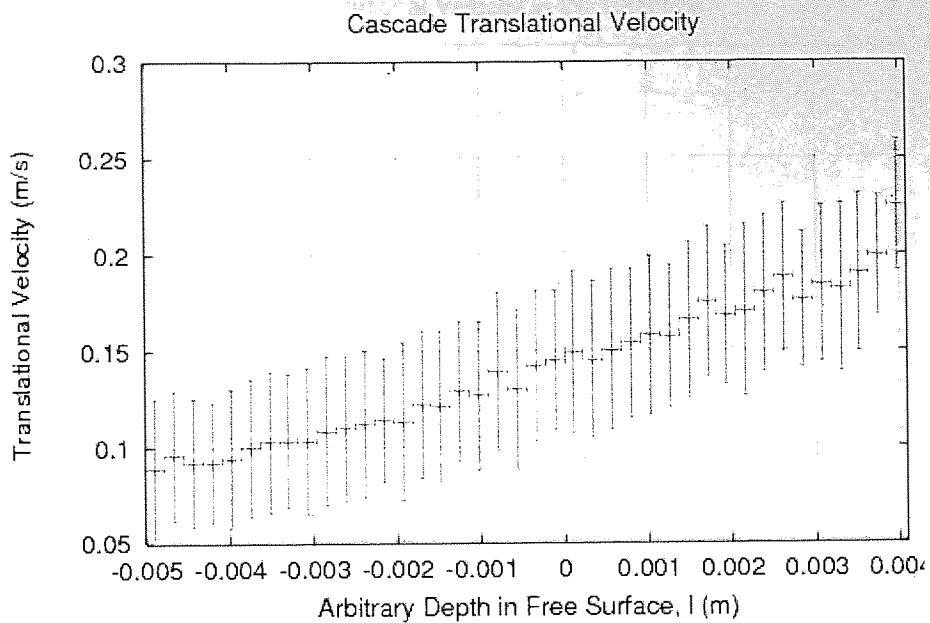


Figure 4.26: Cascade Translational Velocity along distance l

Figure 4.27 shows the average rotational velocity with respect to the drum centre, in the cascade layer for distance, d . In the figure, a rotation rate of -1rad/s corresponds to the drum rotation speed. We see that the majority of particles in the cascade have a positive rotational velocity, i.e. they appear to be rotating in the opposite direction to the drum. As expected the highest apparent rotational velocity occurs at the mid-chord of the free surface and is (a) closest to the centre of the drum and (b) travelling purely tangential to the drum centre.

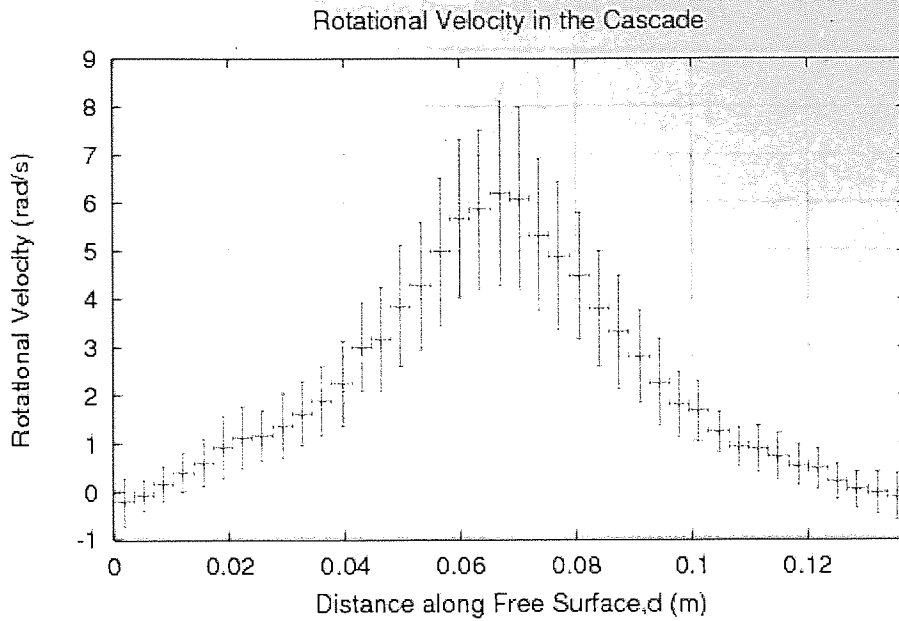


Figure 4.27: Rotational Velocity in the cascade

The translational velocity was decomposed in the d and l directions to give 'parallel' and 'perpendicular' velocities respectively. The histogram of the parallel velocity in the cascade is shown in Figure 4.28. In the figure, the majority of parallel velocities are negative because the direction d was chosen to point up the free surface whereas the bulk of the particles are moving down the free surface. Taking this into account the plot is very similar to the translational velocity histogram in Figure 4.24. We can immediately see that the particles are travelling mostly parallel with the free surface and therefore only have a small perpendicular velocity.

The mean parallel velocity is plotted against d in Figure 4.29, and against l in Figure 4.30. The shape of the curves matches closely with the equivalent translation velocity plots shown previously.

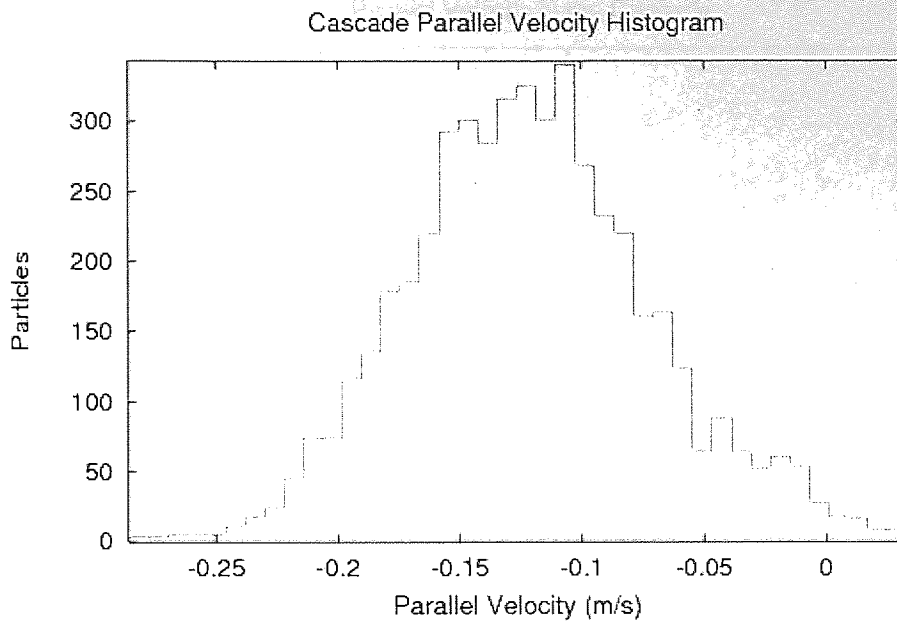


Figure 4.28: Cascade Parallel Velocity Histogram

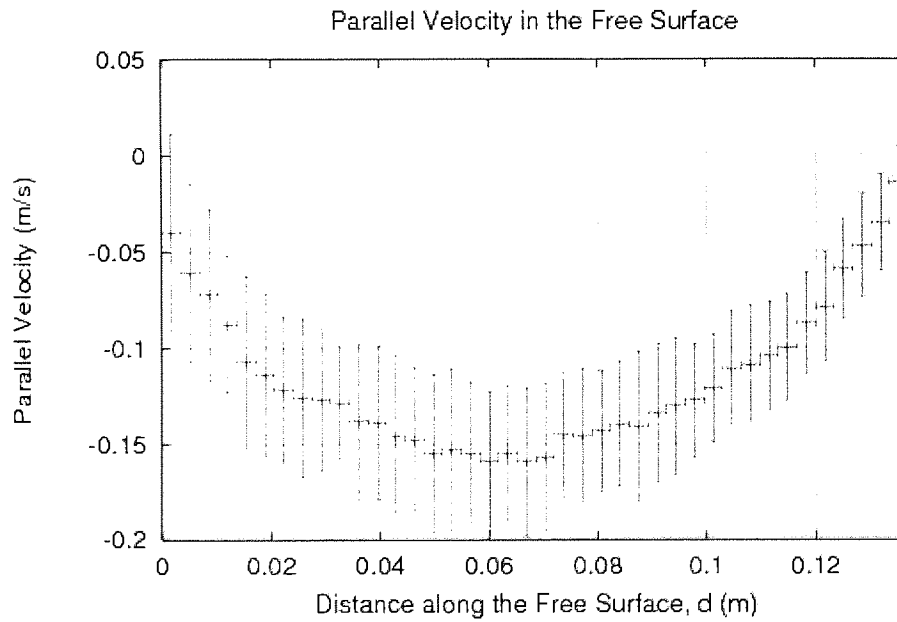


Figure 4.29: Parallel Velocity in the free surface

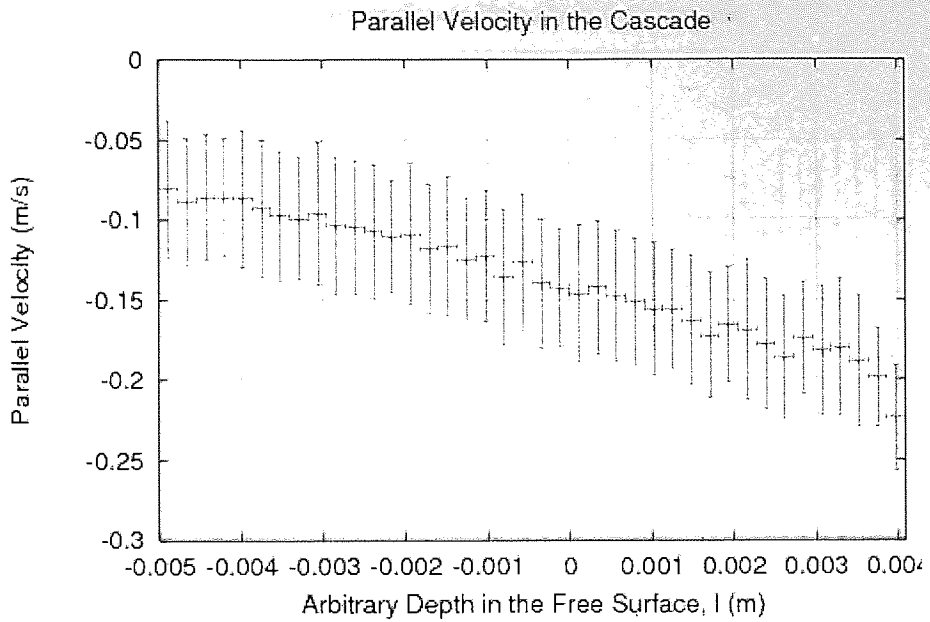


Figure 4.30: Parallel Velocity in the cascade along distance l

Perpendicular velocities in the cascade layer are much smaller than the parallel velocities; see Figure 4.31. The mean perpendicular velocity in the cascade is almost exactly zero.

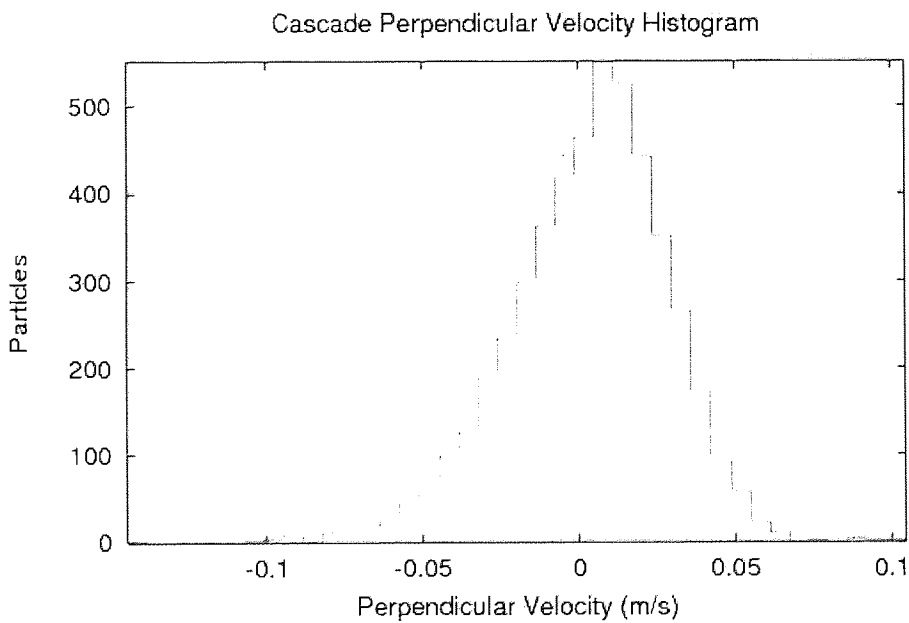


Figure 4.31: Cascade Perpendicular Velocity Histogram

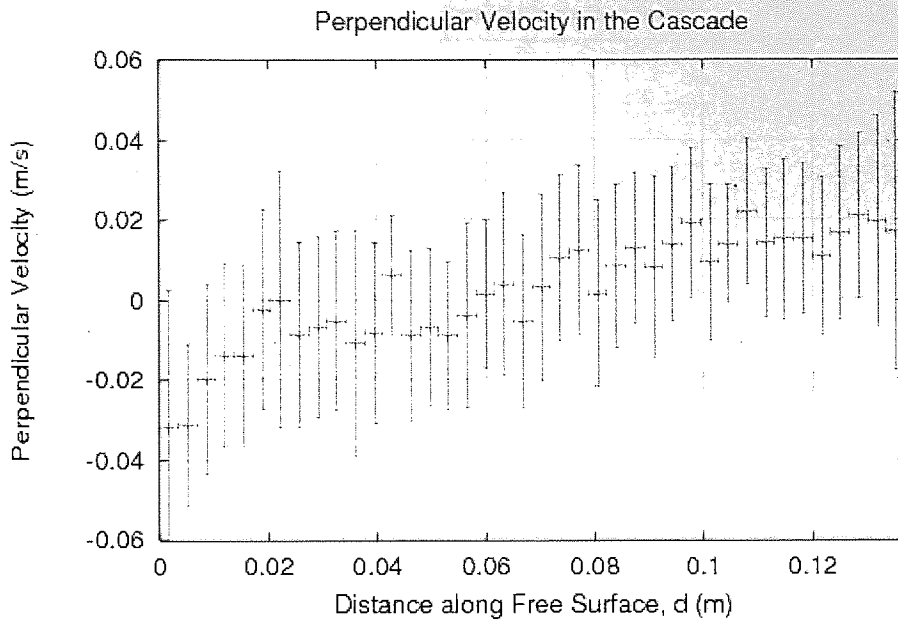


Figure 4.32: Perpendicular Velocity in the cascade along distance, d

From Figure 4.32, we see that there is some perpendicular velocity dependence with d . It appears that particles close to the toe region have mostly negative perpendicular velocities, which means they are moving into the bed in this region. There is no perpendicular velocity correlation with l , see Figure 4.33.

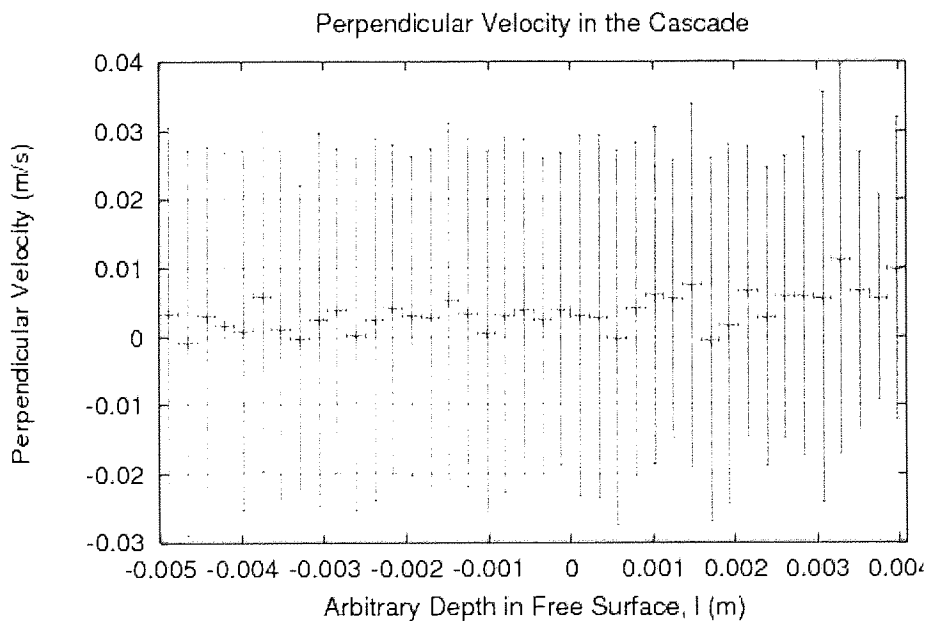


Figure 4.33: Perpendicular Velocity in the cascade along distance, l

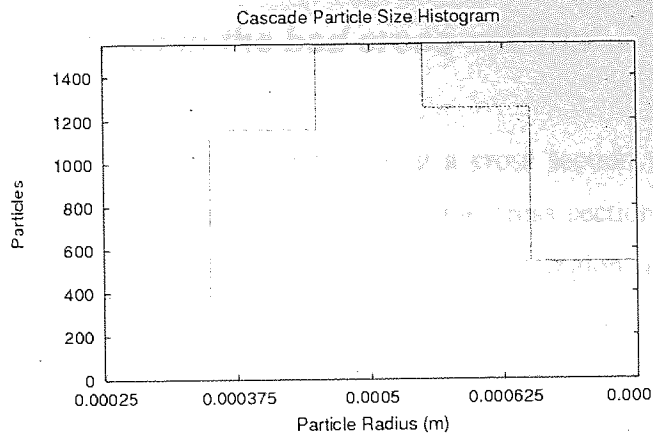


Figure 4.34: Cascade Particle Size Histogram

Figure 4.34 shows that the particle size distribution in the cascade is still quite symmetric, and the relative fractions of particle sizes is still in broad agreement with the initial randomised state.

4.9 Particle velocities in the bed cross-section

It is interesting to study the velocity fields along a cross section through the bed. Some PEPT results for particle velocities through the cross section of a low speed rolling drum have been published in *Parker et al. (1997)*. A region similar to Parker's has been used for particle selection for the cross-section. This region is 1 cm wide; see Figure 4.35. The cross-section is approximately radial with respect to the drum centre, and bisects the free surface at the mid-point. To increase the sample statistics, 6 randomly selected simulation states were combined, to give a total of 2965 particles. All 6 states are for time $t > 4.9$ s. In practice, the cross-section line was defined by drawing a perpendicular bisection of the two contact points in the toe and shoulder regions.

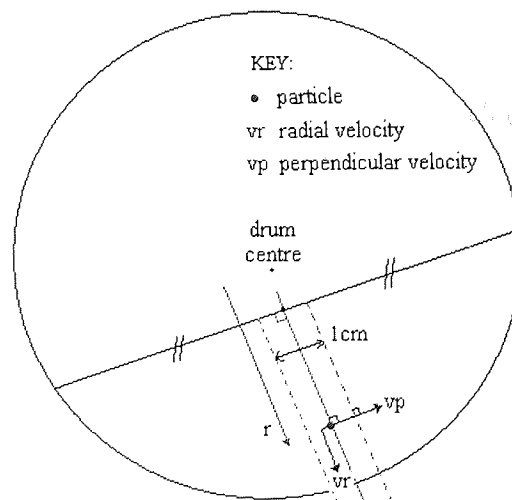


Figure 4.35: Characterisation of position in bed cross-section

The rotational, radial and perpendicular velocities for particles in the cross-section have been characterized in terms of the radius r (the bed surface is at position $r \approx 2$ cm). The histogram of particle translational velocities in the cross-section region is shown in Figure 4.36. From the figure, we see a sharp cut off around 7.5 cm/s, but there is also a long tail with maximum translation velocities > 25 cm/s (which is consistent with the cascade plots shown previously).

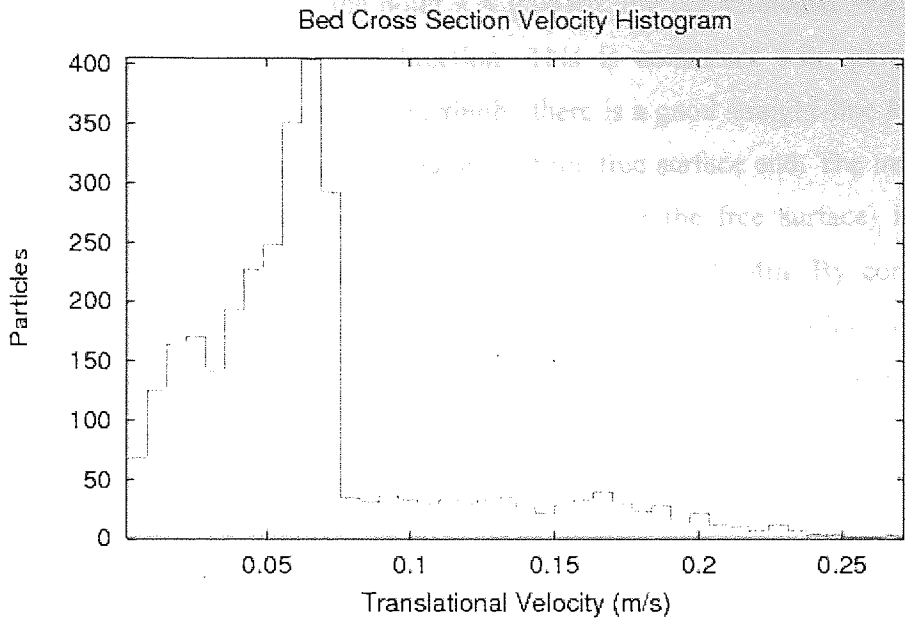


Figure 4.36: Translational velocity histogram in the bed cross section

Figure 4.37 shows the variation of mean translation velocity with particle radius r in the bed cross-section. The y error-bars are standard deviations. The radial position with minimal translational velocity is approximately $r = 0.043$ m. The plot also shows an approximate straight-line behaviour towards the drum wall ($r = 0.075$ m), which is indicative of solid body rotation.

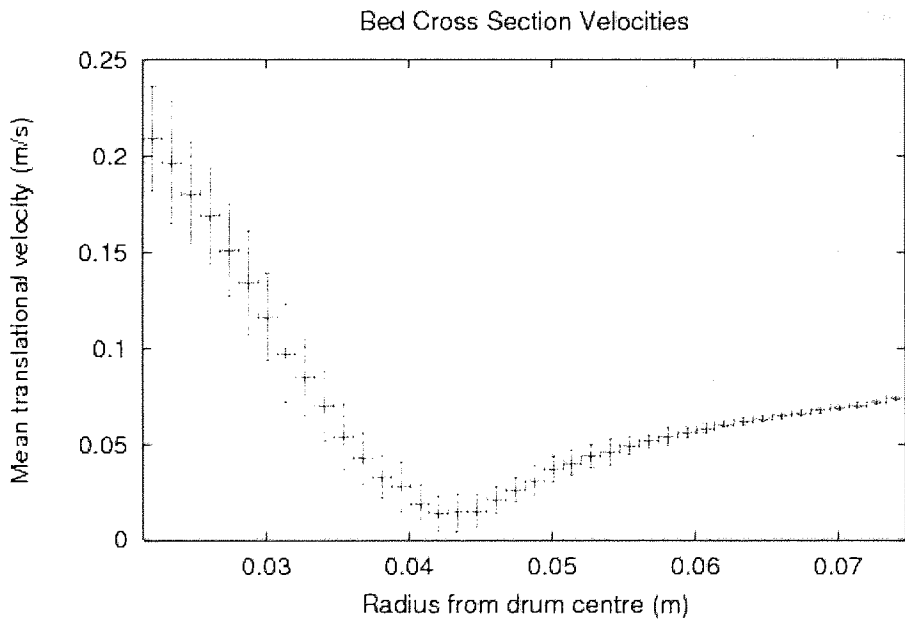


Figure 4.37: Mean translational velocity along the radius, r

Figure 4.38 reveals that at the point $r \approx 0.043\text{m}$, the perpendicular velocities in the bed-cross section change sign/direction. This is consistent with particle rotation around the point $r = 0.043\text{m}$. Interestingly, there is a good straight-line fit not only at the wall end of the cross-section, but also at the free surface end. The material in the cross-section interval $0.02 < r < 0.035\text{m}$ (i.e. near the free surface) is apparently rotating in a solid body fashion, around the point $r \approx 0.04\text{m}$. By considering the gradient of the curve in this region we can derive an effective solid body rotational speed around $r = 0.04\text{m}$ of 11.5 rad/s . From consideration of the gradient of the line in the interval $0.055 < r < 0.075\text{m}$ (i.e. near the drum wall), the material in this region of the cross-section is also rotating as a solid body with angular speed -1 rad/s . The centre of rotation is roughly consistent with the drum centre.

Parker et al. (1997) defines the 'active' region in the cross-section to be all particles above the point of zero perpendicular velocity. Similarly the region below this point is defined to be the 'passive' region. Taking the point $r = 0.043\text{m}$ to be the active-passive interface, the approximate depths of the active and passive regions are 0.023 and 0.032 m respectively. The ratio of active to passive depths is therefore approximately 0.72 . *Parker et al. (1997)* reports an approximate ratio of $2/3$, and shows that the ratio is unchanged at different drum speeds, and even for different drum sizes with equivalent loads. Note that a later paper *Ding et al. (2001b)* redefines the active-passive interface to be the minimum radial position where solid body rotation is evident with respect to the drum wall. We have used the active-passive interface definition from *Parker et al. (1997)*.

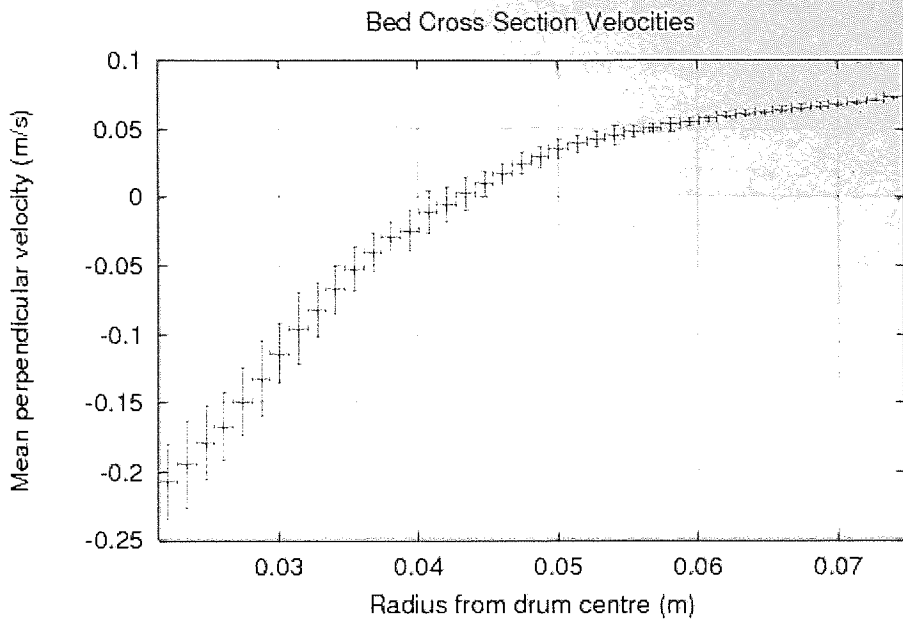


Figure 4.38: Mean perpendicular velocity in the bed cross-section along, r

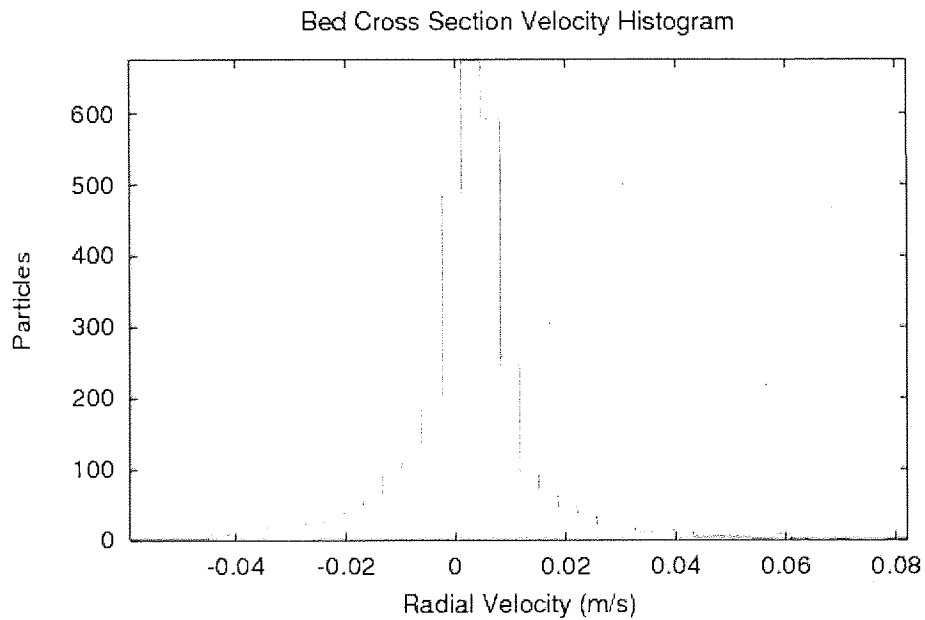


Figure 4.39: Histogram of radial velocities in the bed cross-section

The radial velocities in the cross-section region are histogrammed in Figure 4.39. The distribution is quite symmetric around 0 m/s.

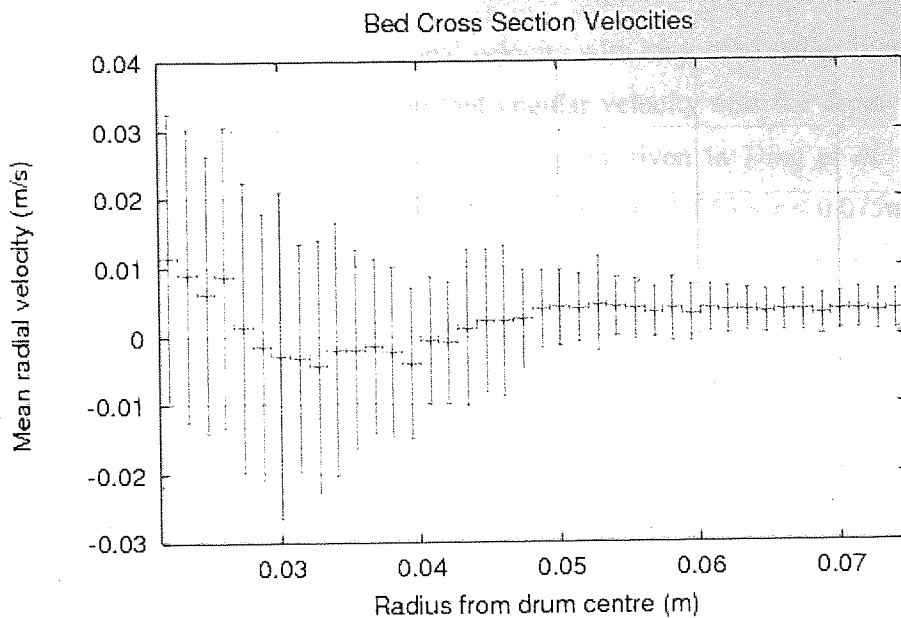


Figure 4.40: Mean radial velocity in the bed cross-section along, r . Plotting radial velocities with respect to radius (Figure 4.40) shows that there is some small positive radial velocity even close to the drum wall. A possible explanation may be that particles are effectively rotating around a point that is not *exactly* at the centre of the drum, but offset slightly (to the left along the x-axis).

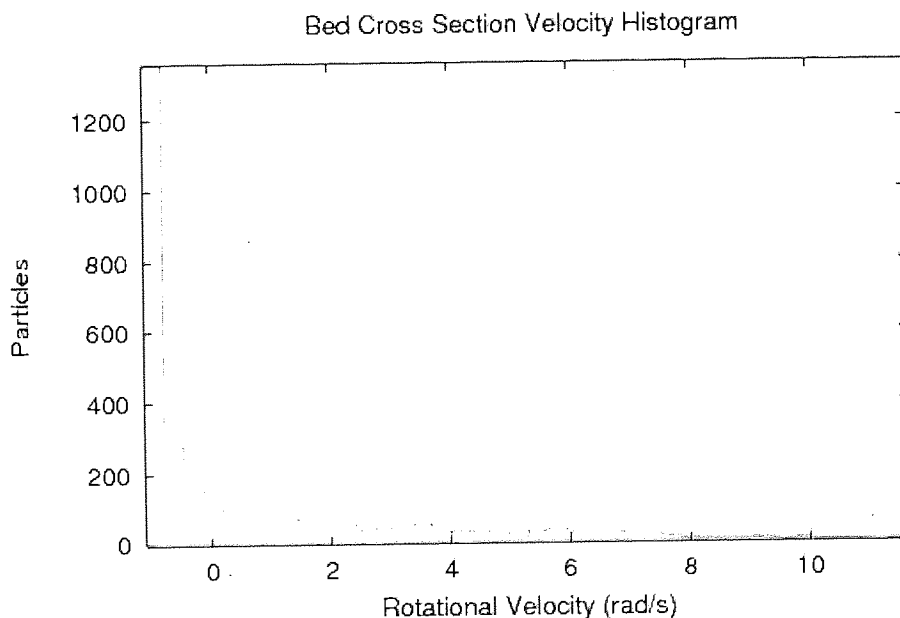


Figure 4.41: Histogram of the particle rotational velocity in the bed cross-section. The rotational velocity histogram in Figure 4.41 shows that an overwhelming majority of the cross-section has a rotation velocity ~ -1 rad/s (which is the drum speed).

Figure 4.42 shows the mean rotational velocity with respect to radius in the bed cross-section. As expected, we see a constant angular velocity near the drum wall. Taking the later definition for the active-passive region given in *Ding et al. (2001b)*, the passive region appears to be approximately defined by $0.055 < r < 0.075\text{m}$.

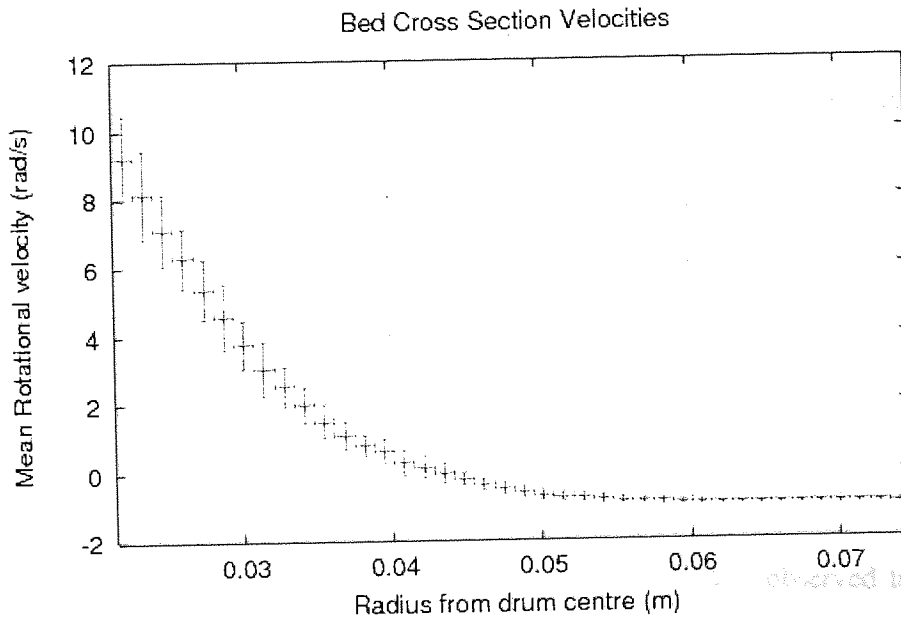


Figure 4.42: Mean rotational velocity in the bed cross-section along, r

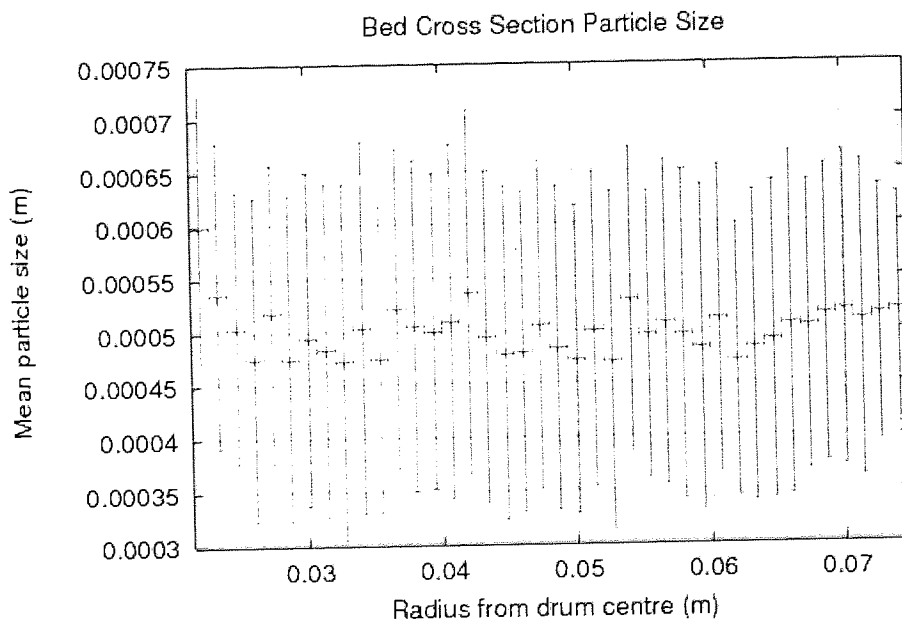


Figure 4.43: Mean particle size in the bed cross-section along, r

Figure 4.43 shows there is no clear radial size segregation in the cross-section at time $t = 4.89\text{s}$. Some published results indicate that we might expect smaller particles to move to the central static region (point of zero tangential velocity), but there is no clear evidence for this over the short time period studied here.

4.10 Summary

Results for a DEM simulation in the rolling regime in a 2-dimensional drum have been presented. A 5000-particle drum system was simulated at a drum speed of 1rad/s . A 30% fill was used, with a drum diameter of 15cm (Froude number is 0.0076 , taking $g = 9.81\text{ms}^{-2}$). A discrete particle size distribution was used; the mean particle diameter was 1mm . The equivalent real-time of the simulation was 7.6s . The particle position, velocity field and connectivity have been characterised qualitatively and show good agreement with PEPT experimental results in the rolling regime.

The DEM simulation was started in a static configuration, which developed into a steady rolling state. During the initial 0.4s the entire bed is observed to rotate as a solid body with the drum. The point at which avalanching first occurs suggest the static angle of repose for the material is approximately 29° . In the dynamic rolling mode, the mean dynamic angle of repose was found to be 23.6° .

After 0.8s of real time, a distinctive bow shaped layer is observed to form at top of the bed, with high velocity avalanching in the top layer, and solid body rotation in the bottom layer closest to the drum wall. This bow shaped region is in good agreement with other published work.

By studying contact angle fluctuations a high frequency component has been shown to be consistent with single layers of particles cascading down the free surface to the drum wall. The form of the contact line evolution is in very good agreement with studies by *Fauve et al. (1991)* at low angular velocities.

Particle velocity fields in the free surface, bed cross-section and at the drum wall have been reported. The slip at the drum wall is shown to be very small ($<1\%$) at the

angular position exactly equidistant between the toe and shoulder. Near the toe and shoulder, much larger slippage is observed, with many particles having 80% or less the rotational speed of the drum. Of the whole angular coverage of the bed (approximately 140°), there is substantial bed slip over approximately 60° .

The maximum velocity in the free surface is found to be approximately 30cm/s (which occurs midway along the free surface). Particles are observed to accelerate down the top half of the free surface, and then decelerate down the lower half towards the toe region. This behaviour is also in good agreement with other PEPT results *Ding et al. (2001b)*.

In the bed cross-section perpendicular to the free surface, the position with minimal translational velocity is found to be at $r = 4.3\text{cm}$. The bed appears to circulate around this point. Taking this point to be on the active-passive interface, we find a ratio of 0.72 for the active to passive bed depths, similar to Parker's result of $2/3$. Solid body rotation near the drum wall is observed over the range $5.5 < r < 7.5\text{ cm}$. No particle size segregation in the bed cross-section has yet been observed at time $t = 7.6\text{s}$.

5 Granulation

This thesis considers the DEM modelling of a drum granulator. Therefore in this chapter a brief overview of granulation is presented, a definition and reasons for granulating are given. In section 5.2, brief overviews are given of some of the important concepts and theories that are fundamental to understanding granulation. Then in section 5.3 four different granulation equipment are discussed and compared, with the drum granulator being the prime focus. Following this, a number of important aspects of the drum granulator are discussed in section 5.4 and 5.5. Further, some selected granulation investigations are mentioned in 5.6. Finally, section 5.7 summarizes the important points that are useful for our drum granulation simulation.

5.1 Introduction

It can be very confusing when there is a range of terminology used to describe this 'granulation' operation in different industries. For example the process of rolling a moistened powder in a rotating drum to produce larger spherical particles may be described in different industries as granulation, balling or pelletization. In the ore industry the term balling is used if it results in an increase in the average particle size. Sintering normally follows balling. If the enlarged particles are to be strengthened by the application of heat in say straight grates, shaft furnaces or rotary kilns the process is called pelletizing. In the cement industry the term nodulizing is used for a similar process, but in other industries this term is used to mean forming larger spherical particles by rolling fine material at a high temperature in a rotary kiln.

The process that is common to all of these industries is the formation of larger entities from smaller constituents. This definition of granulation follows an extensive discussion in *Sherrington et al. (1981)*, where the formation of granules by the comminution of larger bodies is excluded. In the book the authors break down the field of granulation into several categories according to different granulating techniques. These are presented in Figure 5.1 i.e. compaction, extrusion, agglomeration, globulation, nodulization and sintering. The figure shows

agglomeration is when granules are produced by agitated means and generally in the presence of a liquid binder. The focus of this chapter is on agglomeration because this is relevant to what will be discussed in the next chapter i.e. drum granulation. The other granulation processes presented in Figure 5.1 are beyond the scope of the thesis and will not be covered here. Also, the term agglomeration will be used interchangeably for granulation and will mean any process whereby small particles are transformed into larger entities by agitation methods.

Typically materials are granulated to improve one or more of the material properties, as given by *Pietsch (1991)*. Some of these are listed below:

- Improved flow properties
- Improved storage and handling properties
- Improved dosing and metering capabilities
- No segregation of co-agglomerated component
- To densify the material for shipment and storage
- Reduced dustiness; therefore increased safety during handling of, for example, toxic materials, and less material loss
- Improved product appeal due to appearance
- To reduce the tendency of materials, generally hygroscopic, to form lumps or cakes
- To control porosity and surface to volume ratio

These improvements necessitate restrictions on the size distribution and shape of the granulated product. Consequently the use of granulation is extremely widespread in many industries including mineral processing, agricultural products, detergents, pharmaceuticals, foodstuffs and speciality chemicals. It has been estimated that 60% of the products in the chemical industry are produced in granular form and another 20% contain powder ingredients. The annual value of these granular products is estimated at \$1 trillion in the United States alone, *Iveson et al. (2001)*.

It is not surprising that a great deal of research has been prompted by industry in order to better understand and improve the granulation process. There are a very large number of publications dealing with specific aspects of granulation. Much of the work

is empirical in nature, however, and it is difficult to draw generalised conclusions from it, which may be applied to other granulation systems. Indeed there are comparatively few publications that attempt to make generalised conclusions.

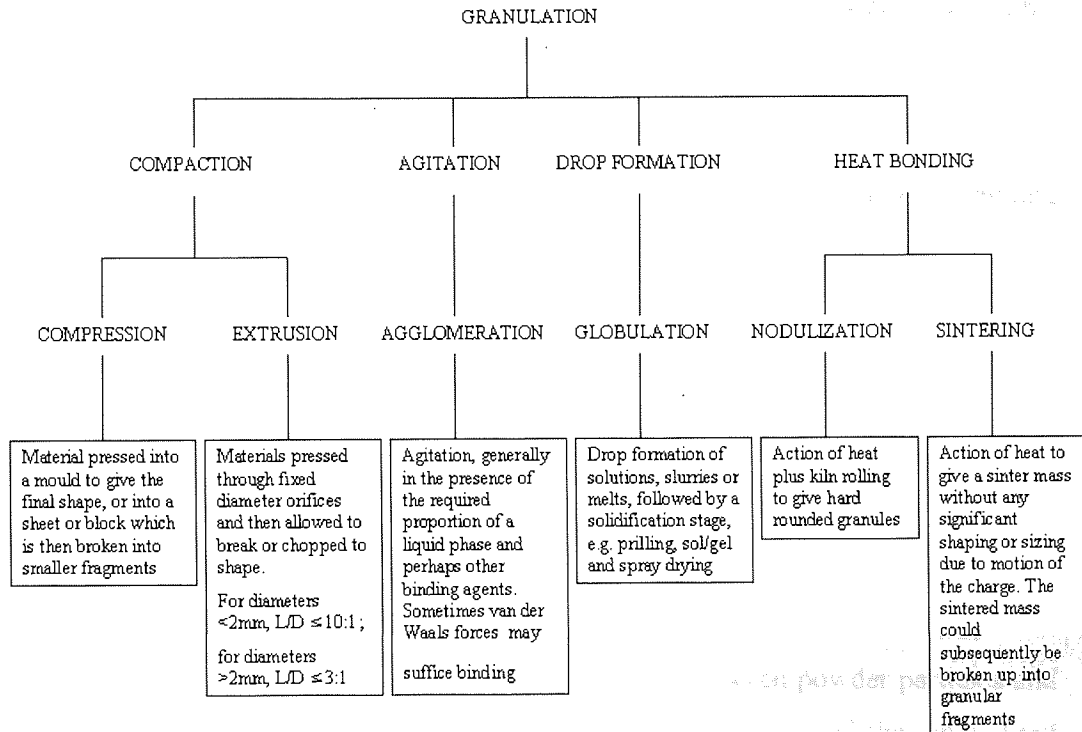


Figure 5.1: Classification of the field of granulation according to *Sherrington and Oliver (1981)*

The remainder of this chapter is organised as follows: in section 5.2, some of the important concepts fundamental to the understanding and study of granulation are covered. The first section here, 5.2.1 highlights the forces between particles on a granular scale. These are broken down into five different groups and a brief mention is given to forces that become significant beyond the particle sizes of granules. In granulation the liquid bridge force is particularly important, so this is covered in a bit more detail, then in section 5.2.2 the granulation rate processes, wetting, growth, consolidation, are discussed as these are also important in the current understanding of mechanisms in granulation. In section 5.3, drum granulation is discussed in more detail since this is the focus of this thesis. Some important factors are discussed here such as spray location and having the correct rolling in the drum. Finally in section

5.3 an overview is given to some of the common granulation equipment, high shear granulators, the disc granulator, fluidised bed and drum granulator, with greater depth given to the latter. The last few sections discuss the past and current work in drum granulation.

5.2 Granulation fundamentals

In wet granulation fine powders can readily be formed into granular masses by mixing with a liquid followed by suitable agitation. A specific type of motion is not required but relative movement of the particles is required in order to achieve a sufficient probability of granulation. In industry many types of equipment exist to provide the relative motion, some of these apparatuses are discussed in section 5.3.

5.2.1 Bonding mechanisms within granulates

For granulation to be successful bonds must be formed between powder particles and these bonds must be sufficiently strong to prevent breakdown of the final dried granules in subsequent handling. Different types of bonds can be formed to bind the powder particles. *Rumpf (1962)* divided granule-bonding mechanisms into five groups as follows:

5.2.1.1 Solid Bridges

Solid bridges, as shown in Figure 5.2, may be formed by the sintering of ores, the curing of flue ash with cement binders, the melting of thermoplastic material under the influence of pressure and friction, the hardening of binders such as resins and the crystallization of dissolved substances such as salt in fertilizers after drying.



Figure 5.2: Illustration of solid bridges between two particles in a granule

5.2.1.2 Interfacial forces and capillary pressure at moveable liquid surfaces

In the presence of a liquid four different types of granules can exist: pendular, funicular, capillary and droplet. These were first described by *Newitt et al. (1958)* and are illustrated by Figure 5.3.

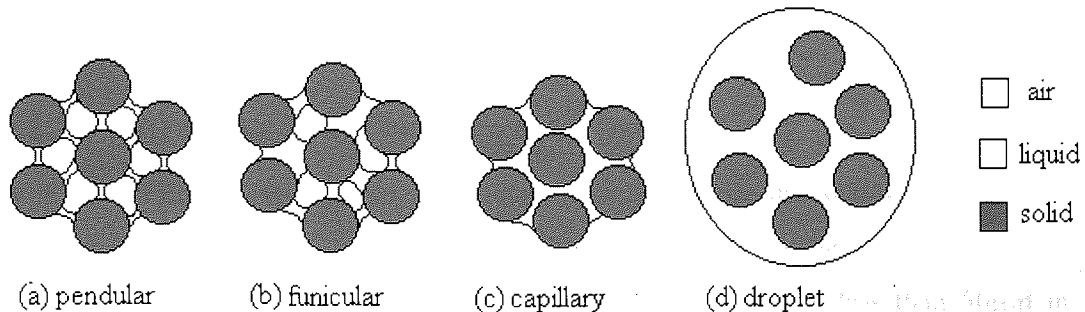


Figure 5.3: States of liquid content in a granule

In the pendular state the liquid bridges are formed between individual particles, here particles are held together by surface tension at the solid-liquid-gas interface and the negative capillary pressure in the liquid bridge. As liquid saturation is increased the pore spaces are completely filled such that concave menisci form at the surface of the granule, this is the capillary state. In the capillary state the contribution of surface tension to the granule strength is negligible and is dominated by the capillary pressure of the liquid. The funicular state is an intermediate state between the pendular and capillary states. Further increase in liquid saturation leads to the droplet state where the particles are completely surrounded by liquid. It should be mentioned that the tensile strength of a granule in the capillary state is far greater than in the pendular state. This is why the moisture in granulating systems is required such to saturate the pore volume of clusters of particles so to strongly bind them in the capillary state to give what is known as nuclei.

5.2.1.3 Adhesion and cohesion forces in bonding bridges which are not freely moveable

In highly viscous materials i.e. materials less liquid like and more solid like such as tar, adhesional forces at the solid-liquid interface and cohesive forces within the binder can be fully used until the weaker one fails.

Absorption layers are immobile although they can touch or penetrate each other. Absorption layers with a thickness of less than 30Å can transmit molecular forces. This force can distort the particles at the contact point and give larger contact areas. When the characteristics of this group are fully exploited the binding forces can be much larger than for mobile liquid binding.

5.2.1.4 Attraction forces between solid particles

With no binding agents agglomeration can occur due to van der Waals' (molecular), electrostatic and magnetic forces, although these are far weaker than those mentioned above these short range forces become significant with particles less than 50µm in size. Thus dry powder systems have a higher probability of forming agglomerates especially if the system is agitated such as to decrease the distance between particles, as in a rotating drum. With large particles the significance of these forces diminishes due to the increased masses and relative particle distances.

5.2.1.5 Interlocking bonds

Fibres or bulky particles can fold across each other resulting in an interlocking type bond. This mechanism requires external forces. Its contribution is generally small in comparison to the other mechanisms. Figure 5.4 depicts interlocking of two strands of fibres.



Figure 5.4: Interlocking of two strands of fibres and of two particles.

5.2.2 Wet granulation mechanisms

This thesis studies wet granulation in a rotating drum and so in this section we will introduce some general concepts that may be applied to any wet granulation process. In wet granulation, particles are bound together by a fluid binder that forms liquid bridges between the particles.

Sastry et al. (1973) proposed five possible mechanisms for growth, being:

(a) *Nucleation*: This is the formation of pellets due to the addition of liquid binder to the agglomerating system. The attractive force due to the negative capillary pressure in the liquid binds the particles to give pellets. The pellets are known as nuclei and they act as seeds for further growth;

(b) *Coalescence*: The production of large-size species by means of clumping two or more colliding granules;

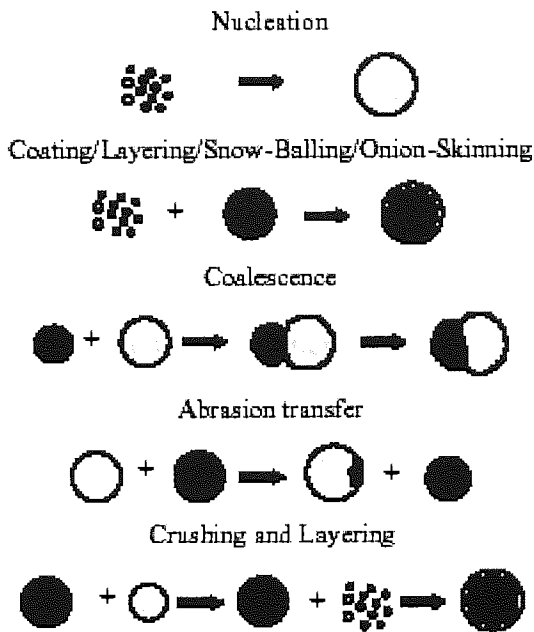
(c) *Breakage*: Breakage of pellets resulting in small fragments of material subsequently can redistribute on to surviving large fragments or pellets. As weaker species are easily broken, breakage results in the formation of stronger pellets;

(d) *Abrasion transfer*: Interaction and abrasion causes a certain mass of material to transfer from one species to another;

(e) *Layering (snowballing)*: In the presence of moist feed and pellets, as in rotary drums in which pellets roll onto fines sprayed with a liquid binder, the pellets collect the moist fines in the form of a layer over the surface.

Most of these are presented in Figure 5.5 (part a). *Iveson et al. (2001)* suggest that it is the cut off size between granular and non-granular material that differentiates between these mechanisms, and they could be considered as cases of coalescence and/or breakage.

(a) Traditional description



(b) Modern Approach

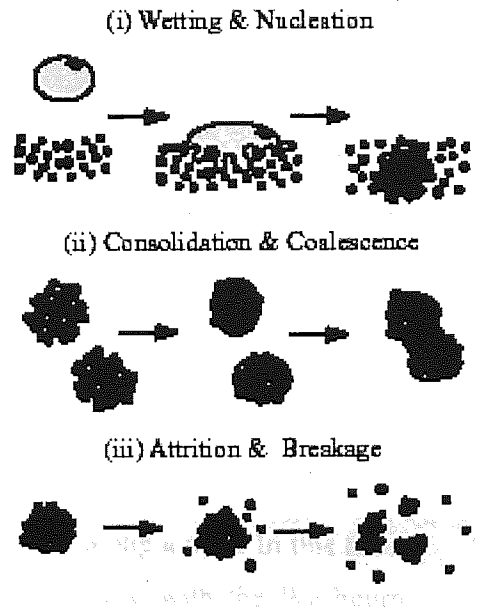


Figure 5.5: Schematic of granulation processes according to *Iveson et al. (2001)*: a) Traditional view (*Sastry et al. (1973)*), b) Modern approach (*Ennis et al. (1997)*)

Further, it is simply the size of the coalescing particles and the availability of surface liquid that varies from case to case. The current approach in the literature distinguishes three sub processes in wet granulation (*Ennis et al. (1997)*), these are a) wetting and nucleation, b) consolidation and coalescence and c) breakage and attrition as shown in Figure 5.5(b).

The wetting and nucleation processes drive the initial formation of granules, and the final size of a granule is governed by the competing mechanisms of growth, breakage and consolidation. These processes are discussed in detail in the following sections.

5.2.2.1 Wetting and Nucleation

Wetting is the processes of saturating voids between particles with liquid by distributing the liquid evenly throughout the powder. The rate of wetting and amount of wetting are very important; too little can result in only a small part of the material granulated. The Washburn equation (Equation 5.1), given below, indicates the rate of capillary take up in a pore, neglecting gravity:

$$\frac{dh}{dt} = \frac{R\gamma \cos\theta}{4\mu h} \quad (5.1)$$

The equation gives the rate of penetration of the liquid dh/dt as a function of R , the pore radius, h , the penetration length of the liquid, θ the dynamic contact angle of the liquid with the powder, and γ the surface tension and μ the viscosity of the liquid. The Washburn equation describes wetting of powder particles by capillary action. In practice, the pores between powder particles are not perfect tubes, and there is a distribution of pore sizes, as well as a variation in diameter along a pore. In this case, liquid penetration into the powder pores can still be described with the Washburn equation, by substituting $R \rightarrow R_{\text{pore}}$, the effective pore radius of the powder *Hapgood (2000)*.

Nucleation is the process of bringing liquid into contact with powder. In wet granulation liquid is distributed in the powder material and nuclei are formed by the initial *coalescence* of primary particles in the immediate vicinity of the drops of liquid. However if primary powder particles are smaller than the liquid drop size then the mechanism of nucleation is by *immersion* of the particles in the liquid drop and not coalescence.

Binder dispersion is an important physical process in the nucleation zone. It describes the degree of mixing of the binder liquid with the powder material. The binder dispersion is highly dependent upon the binder delivery mechanism (spray geometry, spray zone size, etc). Good binder dispersion gives rise to uniform wetting of the powder and controlled nucleation, and this gives a narrow size distribution of

granules. It has been proposed *Iveson et al. (2001)* that a wide size distribution indicates poor binder dispersion.

Powder mixing Efficient powder mixing is important for good binder dispersion. One important aspect of powder mixing is the flux through the spray zone. High powder flux through the spray zone gives more uniform distribution of powder and binder. It is also thought that the mechanical mixing of the powder is also responsible for the attrition and consolidation and coalescence processes, which control granule size. Fluidised bed experiments suggest a fast turbulent flow gives good powder and binder mixing. Additionally the high flux through the spray zone means that the volume of binder available per unit volume of powder is low ("powder dilution"). This gives smaller granules and a narrow size distribution because coalescence does not occur, and the granule size is dictated by nucleation and attrition (mechanical breakage). It is difficult to study powder flux in isolation from other variables because it is related to other mechanical properties of the system which also control granulation e.g. in a drum granulator the drum speed.

5.2.2.2 Growth and Consolidation

The process of growth and consolidation is depicted in Figure 5.5 (ii). Granule growth occurs whenever colliding material in the granular bed sticks together. Consolidation is the process by which a granule becomes denser and, hence, stronger.

5.2.2.2.1 Consolidation

Granule consolidation increases the liquid saturation level of the granule pores, which alters the mechanical properties of the granule. The granule simultaneously becomes stronger, whilst the excess liquid is squeezed to the surface and can help to form bridges with other granules *Capes (1980)*. It is therefore important to consider granule growth and consolidation in conjunction with each other. In fact, the effect of consolidation on granule growth is quite complex. Consolidation increases the strength of the granule, and hence granule deformation on collision with other granules is reduced. This effect actually *reduces* the likelihood of coalescence.

However, consolidation also increases the liquid content at the granule surface, which enhances coalescence

During granulation, granules can move from the liquid saturated state from pendular through to droplet state, see Figure 5.3. This can occur in two ways: (i) addition of liquid binder, or (ii) consolidation which decreases granule porosity, and reduces their size.

5.2.2.2.2 Growth

Granule growth can occur by coalescence or layering. The distinction between these two processes is rather artificial, being based on the cut off size by which granules are distinguished from fines. Granule growth occurs as soon as a binder is added to the agitated powder mass, and can continue even after binder addition has ceased.

The quantity of binder added has a strong bearing on the size of granule produced. If insufficient binder is added, then the granule size is determined by the nucleation conditions, i.e. further growth does not occur.

In a wet granulating system, a collision can result in a pendular bridge holding two granules, or particles within a granule, together. Attractive forces due to pendular bridges are vital for maintaining and stabilizing granule structure. *Ennis et al. (1990)* recognized that during collision (assume low deformability) a static pendular bond would be deformed and become a dynamic pendular bond whose strength will be dominated by the viscosity of the liquid. This is the case in the majority of industrial granulators. It was stated that granules would stick together if the viscous Stokes number of the granules is smaller than a certain critical value, the critical viscous Stokes number. The viscous stokes number, St_v , was defined as the ratio between the relative kinetic energy between colliding particles and the viscous dissipation brought about by the pendular bond. It is given by the following equation,

$$St_v = \frac{8\rho_g \langle r \rangle u_0}{9\mu} \quad (5.1)$$

Here ρ_v is the granule density, $\langle r \rangle$ is average radius of the granules and u_0 the relative collision velocity of the granules. The critical Stokes number, St_v^* , is given by

$$St_v^* = \left(1 + \frac{1}{e}\right) \ln\left(\frac{h}{h_a}\right) \quad (5.2)$$

Here e is the coefficient of restitution of the granules, h the thickness of the binder layer on the surface of the granules and h_a is a measure of the surface roughness of the granule. If the viscous Stokes number is larger than the critical viscous Stokes number, the granules will rebound. Based on this criterion, three growth regimes for granulation were proposed: non-inertial, inertial and coating regimes. These are defined as:

<i>Regime</i>	<i>Criteria</i>	<i>Description</i>
Non-inertial regime	$St < St^*$	All collisions are successful
Inertial regime	$St \approx St^*$	Some collisions are successful
Coating regime	$St > St^*$	No collisions are successful

Table 5.1: Growth regimes according to Stokes number.

In the non-inertial regime the Stokes numbers for the particles and granules are less than the critical value and so all collisions result in coalescence. Here the growth rate is independent of granule kinetic energy, particle size and binder viscosity at steady rate processes. Growth is controlled by the rate of wetting of the liquid. With increase in granule growth comes increase in granule momentum. This give rise to Stokes numbers greater than the critical value. This is the inertial regime where the rate of growth is dependant on liquid viscosity, granule size and granule kinetic energy. Granule growth can be increased by increases in binder viscosity and low levels of agitation.

Ennis estimates u_0 to be $2r\omega$, based on the velocity gradient between layers of tumbling granules, and gives the viscous Stokes number for a drum granulator as,

$$St_v = \frac{16\rho_g \langle r \rangle^2 \omega}{9\mu} \quad (5.3)$$

Adetayo et al. (1993) suggested that a better estimate of u_0 would be the periphery speed of the drum, ωR , as the tumbling speed of a particle is related to the speed of the drum and not the size of the particle. This model yields a modified viscous Stokes number of

$$St_v = \frac{8\rho_g \langle r \rangle^2 \omega R}{9\mu} \quad (5.4)$$

Much work has been done on the granulation mechanisms, which control granule growth. However these theoretical models are difficult to apply industrially (to predict or control granulation processes), because the different mechanical parameters of granules in these models are not well understood (e.g. the yield stress, coefficient of restitution, elastic modulus, etc). Another problem when applying theory to industrial apparatus is that there is no good understanding of frequency and velocity of granule impacts, (velocity is a factor in the viscous Stokes number). DEM simulations have made progress with some of these mechanical parameters, as well as velocity and impact parameters, although much more work is required.

5.2.2.3 Breakage and Attrition

Granule breakage can be divided into two separate phenomena. These are

- Breakage of wet granules: this influences the final granule size distribution; it can help to limit the final maximum granule size or help distribute a viscous binder. Few people have studied granule breakage experimentally, the work that has been done focussed on high intensity mixers such as high shear mixer, and hybrid granulators. Breakage is more likely in these types of devices than drum granulators.

- Attrition or fracture of dried granules: this is usually undesirable as it produces dusty fines

5.2.2.3.1 Breakage

Little quantitative theoretical work has been done to predict the conditions for breakage. *Tardos et al. (1997)* present breakage conditions of wet granules in terms of a new Stokes number, analogous to the viscous Stokes number used to describe granule growth. They express a Stokes deformation number, St_{def} , which is the ratio of granule kinetic energy in collisions to the energy required for deformation. St_{def} is defined as follows:

$$St_{def} = \frac{m_p U_o^2}{2V_p \tau(\dot{\gamma})} \quad (5.6)$$

$m_p = V_p \rho_p$, where ρ_p is the particle density, V_p is the particle (granule) volume, and m_p is the mass of the particle and $\dot{\gamma}$ is the average shear rate in the mixer, U_o is the relative velocity between moving particles and $\tau(\dot{\gamma})$ is some characteristic stress in the granule,

$$\tau(\dot{\gamma}) = \tau_y + k \dot{\gamma}^n \quad (5.7)$$

where τ_y is the yield strength, k is an apparent viscosity and n is the flow index *Tardos et al. (1997)*.

If we neglect the viscosity, then the yield strength is simply

$$\tau_y(\dot{\gamma}) = \tau_y \quad (5.8)$$

Under these conditions, there is a critical value of St_{def} , St_{def}^* , above which granules start to deform and break. The Stokes number increases with increasing size a up to this point. Taking the approximation: $U_o \approx a(\dot{\gamma})$, then the critical point ($St_{def} = St_{def}^*$) defines a limiting granule size to be

$$d_{cr}^{def} = (2\tau_y St_{def}^{\frac{1}{2}} / \rho_p)^{1/2} / \gamma \sim \text{Constant} / \gamma \quad (5.9)$$

5.2.2.3.2 Attrition

Nearly all granulation processes involve drying of granules either during, or directly after granulation. Attrition, or fracture, of the granules during granulation or in later handling is undesirable, so it is important to understand this process and the parameters which affect it *Iveson et al. (2001)*.

Fracture

Little work specific to the fracture of dry granules has been done, but some results can be derived from theory of brittle and semi-brittle materials, e.g. *Iveson et al. (2001)* deals with the cases of semi brittle material failing by crack propagation as well as breakage mechanisms by dry granules.

5.2.3 Measures of granulation (particle size analysis & granulation efficiency)

In granulation the particle-size distribution gives a good description of the powder material. Particle size distributions may be expressed as differential frequency distribution curves or cumulative frequency distribution curves. These are illustrated in Figure 5.6 and Figure 5.7. The two distributions are related, as the cumulative distribution is the integral of the frequency distribution. Some examples are number, surface, mass or volume distributions.

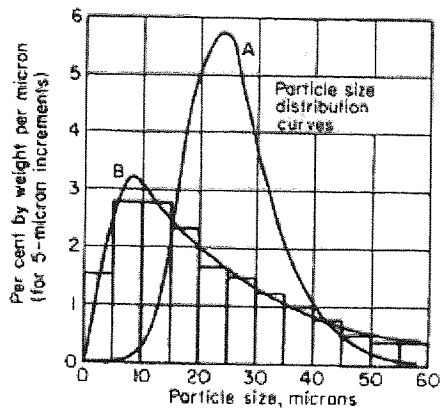


Figure 5.6: Particle size distribution curve for simple powders from *Snow et al. (1997)*

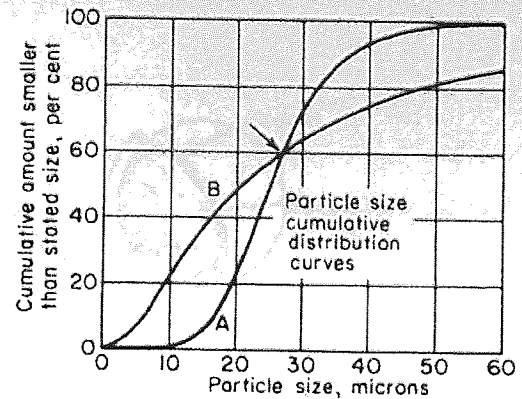


Figure 5.7: Cumulative distribution curve for simple powders from *Snow et al. (1997)*

The shape of the differential frequency distribution from granulation ideally exhibits a single sharp peak. The width of differential frequency distribution indicates the quality of the granulated product. For example, a wide frequency distribution indicates a poor granulated product. Quite often in the initial stage of granulation there can be a bimodal size distribution, so the two different peaks may correspond to the well-developed granules and the powder. This is clearly undesirable for the finished product.

It is often necessary to use a single variable to represent a particle population. This value is usually some kind of mean. Particle frequency distributions may follow a normal distribution, or lognormal distribution, but there is no fundamental reason for this to be true. In addition to the mean size, “top size” is sometimes used to characterize the 100th percentile size, but the 95th or 98th percentile is often used in practice.

5.3 Granulation equipment

There are a limited number of granulator types, of these the most common are: a) high shear granulator, b) rotating pan granulator, c) fluidized bed granulator and d) rotating drum granulator. Figure 5.8 shows a diagram of these granulator types.

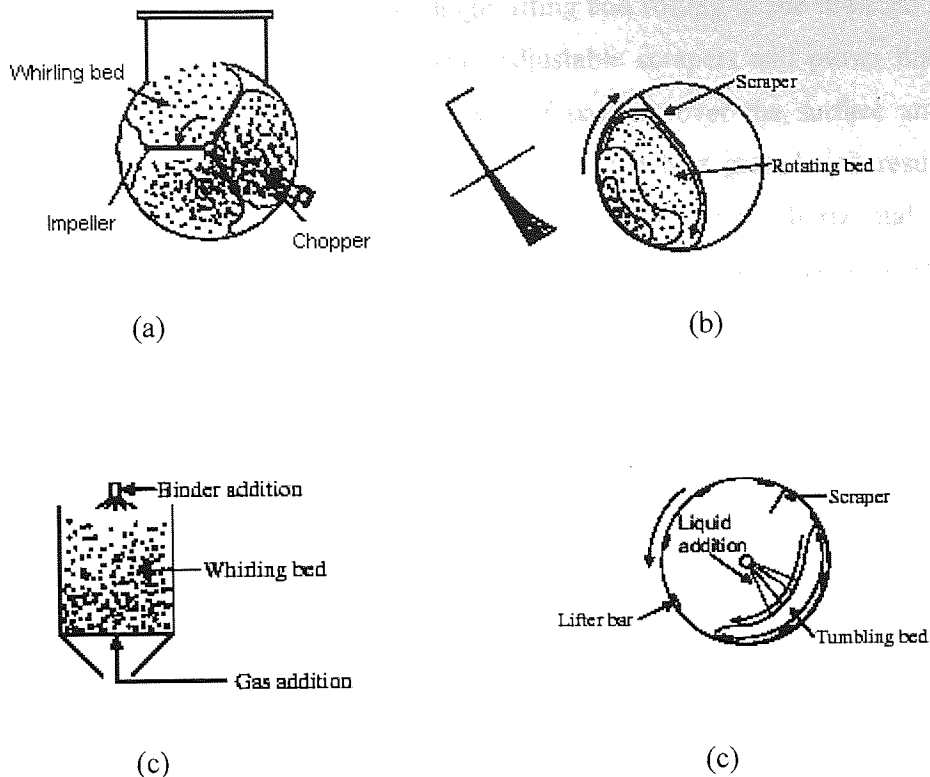


Figure 5.8: Granulator types from *Wildeboer (2002)*

In a high shear granulator *Sherrington et al. (1981)* a series of impellers are mounted along a high-speed shaft rotating in a horizontal or vertical cylinder casing. The impellers push material into the cutting head or chopper and are designed to give close tolerances with the cutter blades and the casing, see Figure 5.8(a). The impellers impart a fluidized type of motion to the general mixer contents. The manufacturer describes the general action as 'whirling'. A liquid binder may be sprayed from the top of the vessel or from a lance for granulation into the centre of action of a cutting head. The cutter serves to break up any large over-wetted granules. These types of granulates are used in the pharmaceutical industry.

There are relatively many types of low shear granulators compared to high shear granulators. The pan, fluidised bed and drum granulators are examples of low shear granulators, these are illustrated in Figure 5.8 (b), (c) and (d).

The pan or inclined disc *Capes (1980)* as it is sometimes referred to, consists basically of a tilted rotating plate equipped with a rim to contain the granulating material. Solids are fed continuously from above onto the central part of the disc and

discharged as granules over the rim. A binder can be added at various locations on the plate surface by using sprays. To encourage lifting and rolling of the material a wall lining of an abrasive coating is provided. Adjustable scrapers and plows that may oscillate mechanically keep a uniform layer of product over the surface and also control the flow pattern of the material. To obtain the best granulation results the angle of the pan is normally kept between 40° and 70° to the horizontal. These granulators are used in many industries including the processing of cement, iron ore and fertilizers.

Fluidized bed granulators are comprised of a vertical cylinder with a distributor plate fitted at the bottom. The distributor plate has small holes through which air is fed during granulation. The upward airflow creates a whirling bed of particles, which are set in motion by the airflow rather than mechanical agitation. The binder liquid is added from the top by a spray nozzle. Particles collide in the granulator and can bind to give granule growth. Granules produced in this granulator are either high porosity granules, this is due to the granulation of powder feed, or high-strength granules layered due to coating of seed particles by liquid feeds. The temperature of the air may be high to enable simultaneously drying of the granules during granulation. Fluidized bed granulators applications include fertilizers, industrial chemicals, agricultural chemicals, pharmaceutical granulation and a range of coating processes.

A drum granulator consists of a rotating cylinder powered by a variable-speed device such as a motor. Industrial drum granulators are typically operated continuously. In a continuous drum granulator, the drum is usually inclined to assist the transport of material from one end to the other (the inclination can be up to 10 degrees from the horizontal and declining towards the discharge end). To avoid material spillage rings are fitted at the discharge and feed ends of the drum. The rings have the effect of increasing the bed depth and the residence time. A detailed diagram of a continuous drum granulator can be found in Figure 5.9 and Figure 5.10. The material in the drum in Figure 5.9 is sprayed from above the bed. This type of drum setup is commonly used for 'instant' agglomerated foods such as milk powder or coffee or for iron ores, limestone and many other mineral materials to mention just a few applications. The drum granulator shown in Figure 5.10 distributes the binder from a sparger that is inserted within the bed volume. This type of drum setup is sometimes used for

fertilizers and is not so commonly used. Drum granulators can also be operated in a batch mode, but this is uncommon for large-scale industrial equipment.

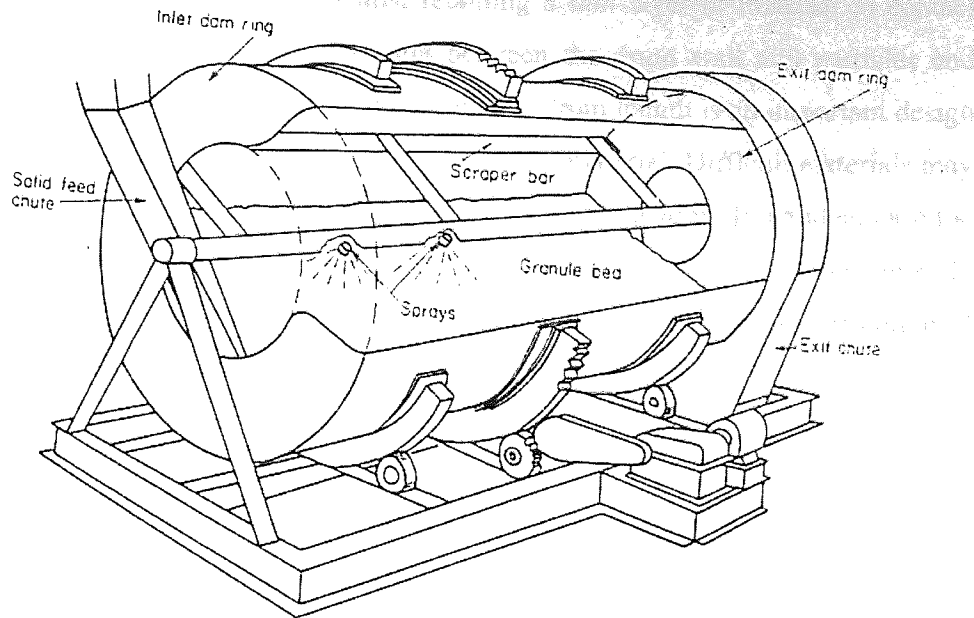


Figure 5.9: Typical industrial (continuous) drum granulator with liquid sprays above the bed by *Sherrington et al. (1981)*.

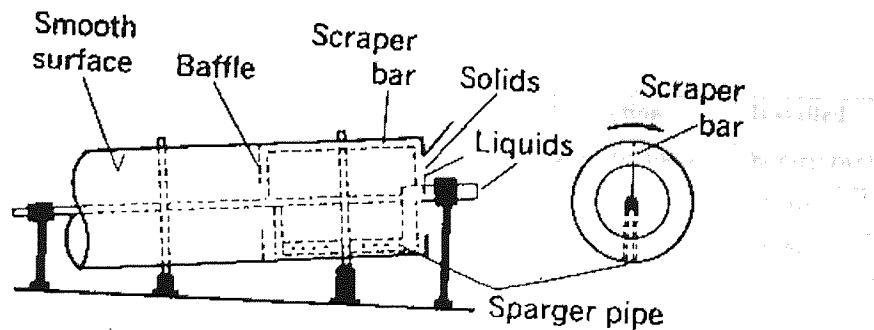


Figure 5.10: Industrial drum granulator with the spray or sparger inserted in the bed, used for example in the fertiliser industry by *Browning (1967)*

In continuous drum granulators, solid feed material and recycled material is fed in at the inlet end of the drum. Granulated material flows out of the drum at the outlet end. The ends of the drum can be fitted with annular rings. At the feed end, a ring prevents material from falling back out of drum. At the outlet end, a ring increases the depth of the bed in the drum and increases residence time of the material in the drum. The solids are wetted near the inlet end by one or more sprays directed on the tumbling bed of solids. To prevent the whole mass from sliding and to promote lifting and cascading of the drum material, industrial drum granulators often have an expanded

metal lining or abrasive coating. In an industrial drum, there is often a scraper bar running longitudinally down the inside of the drum. This restricts the build up of moist material on the drum wall whilst retaining a thin layer of material in contact with the wall. This increases the friction between the drum wall and particles and encourages a better rolling action in the drum. The drum length is an important design consideration as this affects the retention time of the material. Difficult materials may require a longer retention time to achieve the desired granulation. In an ideal case the time for granulate growth for the required size is equal to the residence time. In practice this not achieved, this is mainly because the drum produces a distribution of particle sizes that is rarely a sharp peak distribution.

Typical drum granulators for industrial applications such as in the chemical or metallurgical industries have a length between 2m to 3m, and are normally lined with a steel cylinder, and the ratio of length to diameter is greater than 20. It is partially filled with granular material to give a volumetric hold-up between 10 to 30 percent of the cylinder volume. It is rotated at 1 revolution per 5-10 minutes, *Spurling (2000)*.

Some characteristics of other typical types are granulators are given in Table 5.2.

Application [*]	Diameter, ft	Length, ft	Speed, r.p.m	Production capacity, ton/hr	Installed horsepower
1. Granulation of fertilizers	5-11	7-25	15-9	15-40	25-100
2. Balling of iron ore	9-10	25-30	13-12	30-35	50-60
3. Granulation of fertilizers	8	16	7-9.5	13-20	_____

Table 5.2: Characteristic of typical drum granulators. 1,2 according to *Snow et al. (1997)* , 3 according to *Browning (1967)*

In general, industrial applications involve processes that require long residence times. Brook found that granule growth is complete after 1.5 to 2 minutes residence time for superphosphates in his fertilizer experiments. *Snow et al. (1997)* considers both

* Note: to convert feet to centimeter, multiply by 30.5; to convert tons per hour to megagrams per hour, multiply by 0.907; and to convert horsepower to kilowatts multiply by 0.746

balling of iron ore and fertilizer peletization, and quotes an average retention time of 1 to 2 minutes.

This section has discussed four different granulators. These are summarized in Table 5.3. The table shows that drum and pan granulators can produce a wider size range of granules than the high shear and fluid bed granulator. Drum granulators can be used instead of disc granulators because of the longer retention time for materials difficult to granulate and for their larger capacity.

Method	Product size (mm)	Granule density	Scale of operation	Additional comments	Typical applications
High shear	0.1-2	Low to high	Up to 50 ton/hr	Handles very cohesive material well	Chemicals, detergents, clays, carbon black, pharmaceuticals, ceramics
Drum/pan	0.5-20	Moderate	0.5-800 ton/hr	Very spherical granules	Fertilizers, iron ore, nonferrous ore, agricultural chemicals
Fluid bed	0.1-2	Low (agglomerated)	50 ton/hr	Flexible, relatively easy to scale, difficult for cohesive powders, good for coating applications	Fertilizers, inorganic salts, detergents

Table 5.3: Summary of operational characteristics of different types of granulators from *Ennis, B.J. et al. (1997)*

5.4 Important aspects of drum granulation

Granulation is a complex process and there are a large number of variables that affect granule growth and their properties. System variables and operating variables influence the process of granulation in a drum, such as moisture content, particle size and size distribution of feed material, surface tension of binder liquid and feed rate, drum speed, slope, the position of sprays, the type of sprays, etc. Unfortunately, only a few of these have been subject to systematic investigation. Of these, the most important variables are the moisture content and strength of the granules. Retention

time is also an important variable in the drum granulator. In the normal operating range, an increase in the amount of liquid leads to an approximately exponential increase in granule size. Therefore the process is very sensitive to liquid content. Increased retention times result in larger and denser granulates which have higher wet strength. With proper control of these parameters it is possible (within limits) to influence granulation properties (size and shape, etc).

5.4.1 Granulation efficiency

There is no commonly agreed definition for granulation efficiency. *Brook (1957)* defines granulation efficiency to be the percentage of material within the required size range measured immediately after granulation. Additionally efficient granulation implies good stability and controllability of the process.

Brook suggested that for granulation the optimal rotational speed is half the critical speed, where the critical speed is the speed at which the material in a dry system can be just carried around the drum completely by centrifugal force.

5.4.2 Importance of correct rolling

Optimum granulation is obtained in drum and disk equipment when the correct tumbling, cascading motion occurs in the material. This motion is caused by centrifugal force and is associated to the critical speed* of the granulator. If the granulator is inclined to the horizontal by an angle β , then the formula for critical speed is multiplied by $\sqrt{\sin \beta}$. *Snow et al. (1997)*

Brook (1957), carried out tests at different drum speeds and found it is important to have good rolling of the material in the drum and more importantly a cascading action

* A definition of the critical speed can be found at the end of section 2.5.4

which allows better distribution of water in the material and better mixing of the material, thus preventing material segregation. But the best speed to granulate is influenced by material properties of the granular bed. Too much cascading of the drum material can cause unwanted granule breakage, as for iron ore granulation.

5.4.3 The effect of drum speed on drum granulation

Further, the drum speed expressed as a percentage of critical speed was the best criterion for having similar rolling and cascading material pattern in different size drums. The Froude number, N_{FR} , is commonly used to describe the drum speed, and it is the ratio of drum speed to critical. A Froude number is 1 at the critical drum speed. The drum speed is sensitive to the particle properties and moisture content and it is not clear at which speed range the different regimes occur. In practice, good granulation can be achieved at drum speeds such that the $N_{FR} \sim 30-50\%$. *Sherrington et al. (1981)*

The granule size distribution was measured for a small-scale batch drum granulator at 20% and 50% of the critical speed (Brook, 1957). The size distribution of the drum material for the higher drum speed showed a narrower size distribution and it was centred at a higher granule diameter, this suggests higher drum speeds produce on average larger granules and a smaller granule size distribution. But such generalisations cannot be made base on the size distributions of only two different drum speeds. Further size distribution measurements need to be made at several different drum speeds.

5.4.4 Spray location in drum granulation

Brook experimented with various spray positions of the spray nozzle relative to the bed of rolling and cascading materials, see Figure 5.13. The figure show two different spray positions, (1), and (2). Material granulated with the spray in position 2 gave an immediate reduction in oversize granules and hence an improvement compared to

position 1. The improvement with spray position 2 is due to better penetration and water distribution in the cascading material. When the material is not cascading and just rolls as in Figure 5.12 the spray position did not appear as important.

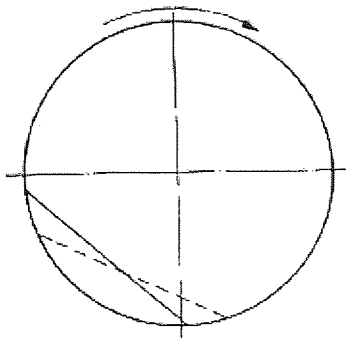


Figure 5.11: See saw motion with mass relatively static from *Brook (1957)*

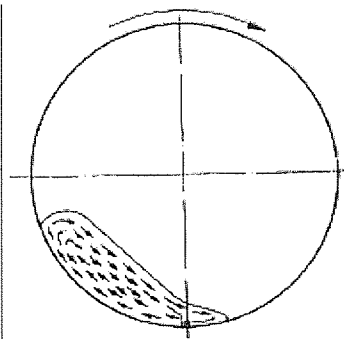


Figure 5.12: Rolling motion without cascading due to low speed of rotation from *Brook (1957)*

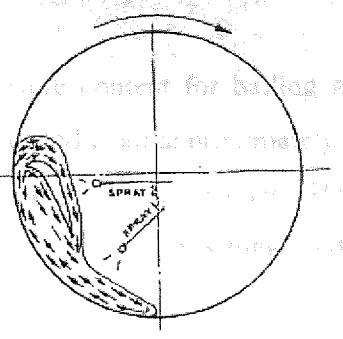


Figure 5.13: Ideal cascading motion resulting from correct speed of rotation, from *Brook (1957)*

5.4.5 Moisture content

The required moisture content in granulating equipment depends upon the particle size distribution and its packing characteristics. The amount and distribution of moisture controls the rate of the different granulation mechanisms, and so moisture plays a significant role in the agglomeration processes. For example, in the inclined dish, the spraying of the binder on the fines and small fragments that are collectively segregated in the dish promotes the growth of new nuclei.

Water is the most commonly used liquid binder in an agitated granulation processes. The amount of water added must be maintained within a narrow range because granule growth is very sensitive to the amount of liquid in the system. Granules formed by wet tumbling are usually considered to be in the capillary state. *Capes (1980)* found the weight fraction of liquid W required for granulation of feed particles with diameter $<30\mu\text{m}$ could be calculated from Equation 5.10. He used a wide variety of material ranging in density from 1000 to 6000kg/m^3 and liquid densities close to 1000kg/m^3 .

$$W = \frac{1}{1 + 1.85(\rho_s / \rho_L)} \quad (5.10)$$

where ρ_s and ρ_L are the densities of solid and liquid, respectively, while with feed particles $>30\mu\text{m}$

$$W = \frac{1}{1 + 2.17(\rho_s / \rho_L)} \quad (5.11)$$

Stanley-Wood (1990) gives numerical values for the moisture content for balling a variety of materials. The moisture content for his material varied from approximately, 7% for lead zinc concentrate to 30% for calcined ammonium metavanadate. He studied the size distribution for a number of powder materials and from this suggested that particles with a narrow size distribution requires a moisture content greater than 60%, for a wide size distribution the moisture content percentage is as low as 40 and 55%.

The amount of water required to produce good granules should be equal to or slightly greater than the critical liquid saturation *Newitt et al. (1958)*, *Kapur (1978)* which is equal to the pore volume of the packed particulate system. In practice, the water content may range from 90-110% of the critical saturation value *Capes et al. (1965)*.

Newitt et al. (1958) measured the moisture content required for granulation of various materials. The porosity was measured when the materials were (a) simply poured in a measuring cylinder, and, (b) vibrated until there was no further reduction in volume and (c) vibrated but with moisture present. The vibration of the bed reduced the porosity of the material by 20%. The moisture required to saturate the bed was determined from the porosity of the wet vibrated material, ϵ_w , as follows:

$$\text{Moisture content} = \frac{\text{Volume of liquid in voids}}{\text{Volume of solid}} = \frac{\epsilon_w}{1 - \epsilon_w} \quad (5.12)$$

The calculated value for the moisture content required to saturate the bed was compared to the critical moisture content for granulation. The computed values were slightly higher than the critical values, but corresponded well. Air in the granules partially explained the discrepancy. The critical moisture content was determined by plotting the rate of growth verses moisture content. An increasing exponential shape

was observed. The critical value for the moisture content was taken at a point below which the rate of growth is considered negligible. The rate of granule growth at particular moisture content was determined by the ratio of the mean granule diameter over granulation time (with a constant drum speed).

The moisture content favourable for granulation is dependent on the width of the particle size distribution. Table 5.4 summaries the moisture content used by three different investigators to granulate powder material in a batch drum. The moisture content is expressed by the volume of liquid in voids to the volume of solid. The table shows a narrow size distribution requires greater percentage moisture content than a wide size distribution.

Drum diameter (m)	Charge description	Moisture content (% Vol)
0.229 ¹	Silica sand with <i>narrow size distribution</i> : (a) 44-53 μ m (b) 124-152 μ m	73.5-90.0 58.7-71.8
0.457 ²	Silica sand with <i>narrow size distribution</i> : (a) 95% of charge is less than 87 μ m 5% of charge is less than 42 μ m (b) 95% of charge is less than 42 μ m 5% of charge is less than 15 μ m Mixed silica sand-silt of <i>wide size distribution</i> : (c) 95% of charge is less than 105 μ m 5% of charge is less than 3 μ m (d) 95% of charge is less than 56 μ m 5% of charge is less than 1.5 μ m	62-72 70 38-48 42-50

Table 5.4: Moisture content used by various experimentalists in their batch laboratory balling drums.

¹ (Newitt and Conway-Jones, 1958)

² (Capes and Danckwerts, 1965)

5.5 Previous experimental work

This section presents some detailed experimental work, which shows the importance of using the correct amount of binder content and demonstrates some drum granulation results.

Experimental evidence suggests binder content is critically important for granulation. It is found that there are critical limits above and below which granulation does not occur. For example *Kapur et al. (1964)* experimented on the green pelletizing of limestone in a small-batch balling drum. They proposed that the granulation of such limestone powder proceeds through three stages of growth, nucleation growth region, transition region and pellet growth region. In the experiments limestone was mixed with water and fed to a drum (12inch diameter, 12inch length) after rubbing through a sieve (of 3.3mm opening) to break up any lumps. The moisture content used was 40.5% of the volume of the limestone, they found it was possible to pelletize the limestone only in the range from 40.5-46.5% vol. moisture. Many investigators have found that there are critical limits above and below which granulation does not occur *Newitt et al. (1958)*, *Rumpf (1962)*, *Kapur et al. (1964)*.

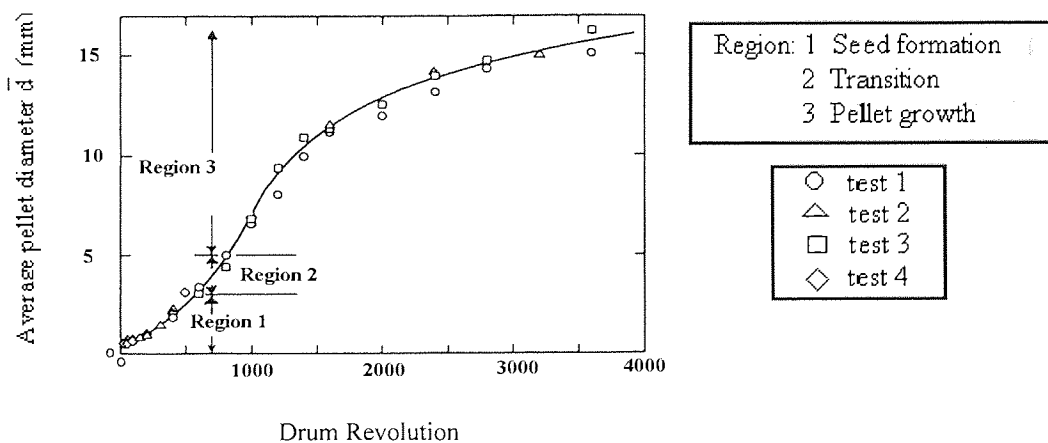


Figure 5.14: Average pellet diameter \bar{d} as a function of granulation time and the three regions of growth (42.5% vol. Moisture), from *Kapur et al. (1964)*.

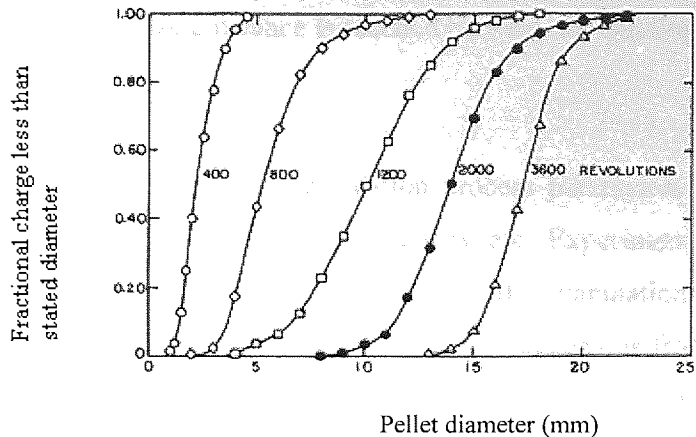


Figure 5.15: Pellet size distribution after various granulation times. (42.5% vol. Moisture) from *Kapur et al. (1964)*

Some results from their experiments are given in Figure 5.14 and Figure 5.15. Figure 5.14 shows that initially nuclei are formed that grow to larger pellets as the drum rotation progresses. In the next figure, the size-distribution moves from a narrow distribution to a broad distribution as the numbers of drum revolutions increases to 2000. With further drum rotation, weakly formed pellets are crushed and the number of agglomerates decreases as is seen at 3600 drum revolutions, see Figure 5.15. Due to mixing of limestone and water loosely held flocs with irregular packing are formed. As the drum rotates, these flocs rapidly rearrange and pack together to give stable nuclei. In the nuclei growth region the size distribution is very narrow as can be seen after 400 revolutions in Figure 5.15. The granules are held together by pendular-funicular type bonds, with densification they grow in size by coalescence with one another. In the transition region, the tumbling of the charge compacts the particles and starts to fill the voidage space with liquid decreasing its volume, eventually to cause the liquid to be squeezed to the surface of the pellet. These granules are soft and held together by surface tension of the enveloping liquid. In the transition region the pellets very easily grow by coalescence, this explains why the size distribution becomes wide at around 1200 drum revolutions. The granule grows by a number of complex mechanisms including coalescence, abrasion, layering and breakage, each contributing in varying degrees. In the final growth region the growth rate of granules is very small because of the low likelihood of coalescence and the other mechanisms of growth are slower. In this region the growth rate increases approximately constantly as with coarse, closely sized material where crushing and layering dominate or decreases as with powders with broad size distribution. When the

granules reach their final size a balance is reached between the binding and disruptive forces.

Many experimenters have examined granulation process parameters such as binder liquid concentration, particle size, mixing intensity etc. Experimental results have been published for a wide range of materials for specific granulation processes with specific parameters. It is difficult to draw generalised conclusions from much of this work. Some recent work characterizes dimensionless relationships between, for example, residence time, and drum dimensions. However, the empirical fits to these relationships were found to depend on the type of materials used, and therefore the predictive capabilities of this analysis are questionable for experimental conditions, which haven't previously been fitted. (*Kramers et al. (1952)*; *Chatterjee et al. (1983)*; *Perron et al. (1990)*).

Although not predictive, particle motion observations have given good insight into the kinetic processes in granulating systems. Particle motion in granulating drums has been studied experimentally in several ways:

- Visual observations. Straightforward visual inspection of granulating drums (using transparent ends of the drum) has given useful insight. *Henein et al. (1983)* found that the active (avalanching) layer is thicker at higher speeds, and thinner at higher hold up (volumetric loading). They reported that 8-35% of the bed thickness is active with volumetric loadings of 6-17%. Other observations with fibre optic probes confirm these trends *Boateng et al. (1997)*.
- Digital imaging/video imaging. These techniques have also been useful to elucidate particle motion in granulating drums. *Khakhar et al. (1997)* measured the angle of repose for various rotation speeds and materials. Coloured tracer particles have also been tracked with video imaging; *Lebas et al. (1995)* found that the fraction of time in the active layer is independent of rotation speed, but sensitive to bed depth.
- Nuclear Magnetic Resonance Imaging (MRI) allows non-invasive measurements of particle motion in granulating systems. It has become

accepted as a velocity measuring technique for fluid flows, and has special advantages in measuring optically opaque flows. No radioactivity is involved and the technique gives concentration, velocity-vector fields, and diffusion coefficients in two and three dimensions. MRI requires that the particles or fluid to be imaged are proton rich. There is often a difficulty in getting NMR signals from solid samples, so a proton rich fluid must be used, and this restriction makes the MRI method not universally applicable to all granular samples. *Yamane et al. (1998)*

- Positron Emission Particle Tracking (PEPT) is a method of tracking the position of a tracer particle in a particulate system. The tracer particle is irradiated with a cyclotron and reintroduced into the particulate system. The resulting radionuclides on the tracer decay by positron emission and the resulting back-to-back gamma rays can be detected. Given several pairs of back-to-back gamma rays the position of the tracer particle can be reconstructed. *Parker et al. (1997)*

5.6 Previous modelling work

Population balance modelling has been very important historically for the modelling of granulation. The population balance method, in general terms, aims to describe the rate of change of $n(v)$, the particle number density for particle size v . The population balance is then a parameterised differential equation, with terms for the different granulation mechanisms i.e. growth, coalescence, breakage. The differential equations are solved with numerical methods to give predictive measurements. The main limitation is that the terms for each process (kernels), are empirically derived, and must be fitted to laboratory data for each system. It is not possible to derive a unified kernel representation using probabilistic methods because the physical processes cannot be generalized to a single curve, or are not well understood. *Wang et al. (2002)*. Kernels that are reliable in one context may give misleading results in another. More general, physically based models are in great demand from the granulation industry, and DEM is one such possible approach.

Although DEM has been used to model granular dynamics for some time, there are very few published results for DEM simulation of granulating systems. An important

detail for DEM modelling of granulation is the representation of the agglomerate. Two approaches are apparent in the literature:

- The “replacement model”: agglomerates are simplified to larger spherical particles, *Goldschmidt et al. (2003)*, *Kano et al. (2005)*, *Link et al. (2007)*. In this approach, the agglomeration of two smaller particles into a larger agglomerate is modelled by *replacing* the original particles with a new particle with a larger diameter according to mass conservation (see Figure 5.16). The advantage of this approach is that it is quite efficient computationally, so relatively large systems can be simulated. The disadvantage is that no information on the morphology of the agglomerate can be obtained. In addition, granule breakage is not “naturally” expressed in the model.
- The “discrete primitive model”: agglomerates are represented as groups of discrete primitive particles, *Kasai et al. (1998)*, *Kafui et al. (2008)*. The computational cost is higher than the former method, but information about granule shape and size can be derived, and granule breakage is implicit in the model.

Goldschmidt et al. (2003) modelled top-spray fluidised bed granulation using DEM and a hydrodynamic model of the fluid phase in two-dimensions. The particle properties were chosen similar to glass, and liquid droplets were modelled as discrete entities in addition to the 50,000 primary spherical particles. In their model, particle-droplet collision can result in coalescence (i.e. wetting of the primary particle). Interactions between particles result in either rebound (governed by hard sphere collision laws) or agglomeration, depending on the fractional liquid coverage of the colliding particles. In the case of agglomeration, a larger sphere replaces the colliding spheres. The model produced reasonable granule size evolution trends and qualitatively illustrates the effect of fluidisation velocity, binder spray rate and spray pattern.

Kano et al. (2005) use the replacement model to examine the effect of drum speed and holdup fraction in the granulation of iron ore. Additionally, the experimenters propose that DEM simulation can be used to extract impact energies and rotational kinetic

energies of the particles, which are both expected to be important for the granulation process of growth and breakage. Although Kano et al. perform experimental observations in addition to their simulation work, they do not attempt to correlate the experimental data with simulation. However, DEM simulation is shown to be useful for studying parameters like the impact energy which is expected to strongly affect agglomerate breakage.

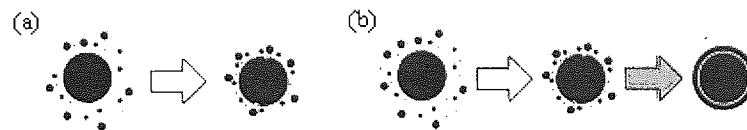


Figure 5.16: Simulation model of Granule formation *Kano et al. (2005)*

Link et al. (2007) use DEM to model granulation in a spout-fluidized bed, using the replacement model. Their aim is to further understanding of the particle size distributions and growth mechanism, which is difficult to investigate experimentally. In their system, the growth mechanism is layering of small liquid droplets onto the surface of spherical particles in the bed. The droplets are injected via a spout at the base of the bed. *Link et al.* assume that no granule growth occurs through agglomeration, i.e. all particle-particle interactions in their simulation are modeled only as normal DEM collisions, and droplet-droplet interactions are neglected. For droplet-particle interactions, the droplet is removed from the system and the radius of the particle is increased. The particle-particle interactions are also assumed to be unaffected by surface wetting. For computational speed, *Link et al. (2007)* model a thin slice of the bed, 6 particles diameters wide with walls on all sides. They identify two separate growth regimes in the bed: “peak growth” when particles are very close to the spout and not obscured by other particles, and “constant growth” which is slower but has a much longer duration. They also find that although the width of the particle size distribution is roughly unchanged by granulation, the growth of individual particles can differ by up to 3 orders of magnitude.

Kasai et al. (1998) model agglomeration of iron ore by sintering using both 2D and 3D DEM simulation, using discrete primitives. Their agglomeration model assumes a liquid coating of all particles (the “melt”) within a “melt zone”. Particles in the melt zone form capillary bonds due to pendular liquid bridges at the surface of the melt.

Kasai et al. (1998) model the capillary bonds with an additional force which is proportional to the surface tension of the liquid. They simulate a relatively small 3D system; they model a cylindrical melting pot 12 particle diameters in diameter, and 12 particle diameters long. The dynamics of the particles in the system are determined by gravity and agglomeration forces only: no mechanical agitation of the system is performed. The agglomeration of particles into clusters is determined from the mean number of particles per cluster. They observe that the mean coordination number of particles in the system increases as agglomeration progresses, and find that the final size and shape of granular clusters is very sensitive to the voidage fraction of the initial system.

Kafui et al. (2008) models fluidized bed spray granulation in three-dimensions using DEM. They implement a “spray-zone” that uses energy of adhesion as the binding mechanism (i.e. pendular liquid bridges are not modeled). Agglomerates are modeled as collections of discrete primitives. Liquid droplets are not modeled: instead simple functional relationships are used to model surface energy pick-up by particles in the spray zone. A simple functional relation is also used to model the drying of interparticle bonds by an increase in energy of adhesion. Surface energy is not “exchanged” upon particle collision, therefore particles are only wetting by entering the spray zone, and not by collision with other wet particles. Qualitatively realistic granule size and mass evolution is demonstrated. The same spray-zone model has been used for the granulation simulation presented in the following chapter and is discussed in detail there.

Although they do not model granulation, *Shi et al. (2008)* give a detailed model for liquid transfer and wet-particle interactions in a rotating drum DEM simulation. They attempt to model the volume of pendular liquid bridges analytically, and from this determine the capillary force between two wet particles. They also model liquid redistribution upon bridge rupture, and therefore their simulation demonstrates wetting of particles by interaction with other, previously wetted particles. Analogous to Kafui’s spray zone, the top layer of the bed acquires maximal moisture content (although unlike Kafui’s model, there is no penetration of the spray zone into the bed). Drying is also not incorporated in the model. Shi et al. find that even after a relatively long time (70s), there are still some dry particles in the interior of the rolling

bed. The evolution of the bed moisture content is analyzed with a "mass coating variability" metric $CV_m = s_m / \mu_m$, where μ_m is the mean mass gain due to wetting/coating, and s_m is the standard deviation. Shi et al. find that CV_m evolves according to $CV_m = 1 / \sqrt{t}$.

5.7 Summary

Over recent years there have been a number of reviews published on the subject of granulation. To mention a few: In *Advances in Chemical engineering* Kapur (1978), a short chapter is provided on balling and granulation, and in the book, *Granulation* Sherrington et al. (1981) a bibliography is provided over a range of industrial practice.

This review chapter has presented a brief overview of granulation, but clearly a complete and full account of all aspects of granulation is beyond the scope of this thesis. An attempt has been made to cover some of the relevant and important aspects of the granulation field for drum granulation. A number of important considerations were identified for the setup of a drum granulator:

The **particle size distribution** gives good description of granulated material. Width of distribution indicates quality of granulated product. A single sharp peak is ideal. In practice the distribution of particle sizes is rarely a sharp peak, and a wide distribution indicates a poorly granulated product.

Large-scale industrial drum granulators are usually operated in continuous mode. The **length** of industrial drums is often large: typical length to diameter ratio is greater than 20 and volumetric hold-up 10-30%. The drum length affects **residence time**. In the ideal case, the time required for granule growth is equal to residence time. Longer retention time leads to denser and larger granule size.

Binder content is important. Some experimental work suggests that there are critical limits above and below which granulation does not occur. Also, granule size increases exponentially with the liquid binder content, so the granulation process is very sensitive to binder content.

Binder dispersion is an important process in the nucleation zone. It is dependent on the delivery mechanism (i.e. spray geometry, penetration depth, binder strength, spray zone size etc). Good dispersion gives uniform wetting of the powder and controlled nucleation and narrow size distribution of granules. Poor binder dispersion gives wide size distributions of granules.

Rolling/Cascading motion: According to Brook, for granulation it's important to have good rolling of material and more importantly a cascading action which allows better distribution of liquid binder in the material and better mixing of material, thus preventing material segregation. Too much cascading of the drum can cause unwanted granule breakage.

According to Sherrington, the **optimal drum speed** for good granulation is such that the Froude number is approximately 30 to 50%. The best speed to granulate is influenced by material properties of the granulator bed. The optimal drum speed is sensitive to particle properties and moisture content. No universal correlation between drum speed and motion regime is described in the literature. However, the ratio drum speed to critical speed is a reasonable criterion for having similar rolling and cascading pattern in different size drums.

Spray position should be over the fast turbulent flow region. High particle flux through the spray zone means that the volume of binder available per unit volume of powder is low, which gives small granules and a narrow size distribution. Because coalescence does not occur, granule size is dictated by nucleation and attrition alone. Brook found that placing a spray above the cascading layer instead of above the rolling surface layer, gave better granulation due to better penetration and binder distribution in the cascading material.

A brief review of DEM granulation studies has been given. There is comparatively little published work in this area, and much of it does not address rotating drum granulation. One study of rotating drum granulation is from *Kano et al. (2005)*, who have analyzed iron ore agglomeration using a simplified replacement model (the newly formed agglomerate is modelled as a single new spherical particle). We expect that a discrete primitive model of granulation should naturally include granule formation, growth, and breakage in a way that the replacement model does not. A

discrete primitive model has therefore been used in the granulation simulation presented in the following chapter.

6 DEM simulations of drum granulation

6.1 Introduction

The 3D drum already described in chapter 3 was used for creating a drum granulator by inserting a spray in the drum. The simulation parameters are summarized in Table 6.1. The details of the spray model are described later in section 6.2. A key feature of the model is that granules are represented by all their constituent particles. The model is therefore capable of simulating the different granulation mechanisms of nucleation, consolidation and growth, and attrition and breakage. Modelling of growth and breakage using discrete particle bonding is of particular interest, since several other DEM granulation studies have modelled this simply by *replacement* of the particle-particle bonded system (the granule) with a single larger particle *Goldschmidt et al. (2003), Kano et al. (2005)*. The latter modelling technique requires fewer discrete particles and hence requires less CPU time. However, the latter technique can be presumed to be less realistic, and in particular it offers no obvious way to simulate granule breakage.

Particle diameters and distribution		Material properties for particle and wall	
Diameter (μm)	Number	Young's modulus [GPa]	3.0
200	7623	Poisson's ratio [-]	0.30
225	11092	Yield stress [Pa]	0.03×10^{30}
250	12570	Density [kg/m^3]	2.65×10^3
275	11090	Coefficient of friction for [-]	0.35, 0.75
300	7623	particle-particle, particle-wall	
Total number of particles [-]		50,000	
Drum Diameter [m]		0.034 (136 particle diameter wide)	
Drum Length [m]		0.0025 (10 particle diameter wide)	
Drum loading/fill [%]		30	
Drum Rotational speed [rad/s]		20.0	
Drum Incline [degrees]		5	
Froude Number [-]		0.83	
Coordinates of drum centre [m]		(0.0171, 0.0171, 0.00135)	
(Gap between x-axis/y-axis and drum [m])		0.0001	
Time step [s]		1.97×10^{-7}	
Gravity [m/s^2]		(0, $-9.81 \cos 5$, $9.81 \sin 5$)	
Total simulation time (cascading drum) [s]		0.676	
Total number of drum revolutions [-]		~2.2	

Table 6.1: Summary of system variables for the 3D simulation

To prevent mass from sliding and promote lifting and cascading of drum material, often a metal lining or abrasive coating is used on the inside of the drum wall. A

Scraper bar is often used to maintain lining of material on the drum wall and increase friction. In our system, the friction for the drum wall is increased to give a similar effect.

6.2 Spray model

The spray zone modeling used here was developed by D. Kafui, for DEM fluidised bed spray granulation studies, *Kafui et al. (2008)*. Rather than model discrete liquid binder droplets, we use a concept of wet surface energy (energy per unit surface area) to model the spray. A liquid drop model for the spray would have been more realistic, but would significantly increase the number of discrete entities in the simulation, and require an unfeasible amount of computational power. This model was not considered.

The wetting mode implied by Kafui's wet surface energy spray model is analogous to "full wetting" of particles, where fine droplets of liquid binder coalesce on a particle to form a uniform film over the particle surface. Such a wetting mode will also occur when there is a very low contact angle between the particulate solid and the liquid binder.

The spray model has the following features:

- The spray zone is completely described by a conical region, with a notional spray source at the apex of the cone.
- Particles inside the spray zone acquire a wet surface energy during "wetting". The increase of the particulate wet surface energy depends on the distance from the spray source and the duration of time in the spray zone.
- Particles that leave the spray zone are notionally "drying", during which time the wet surface energy initially *increases*. The increase is intended to model an increased viscosity in the binder as it dries. During this "active" period, the particle can still bond with other particles. When the active period has expired, the wet surface energy is set to zero, and the "dry" particle can no longer form new bonds.
- When a particle-particle bond forms, the energy or strength of the bond is initially set to the wet surface energy. The energy of the bond increases

asymptotically over time to a final “dried” bond energy. When a bond forms, the spray zone no longer affects it, even if the particles are still in the zone.

The conical spray zone is specified in the simulation with the following parameters (Refer to Figure 6.1):

- (x_s, y_s, z_s) : the coordinates of the spray source
- θ_c : the angle of the conical region
- h_c : the height of the conical region
- $d_{fac} (\geq 1)$: the bond dry out factor, which models an increased energy of the dry bond with respect to initial wet energy before drying
- $\gamma_{w\ max}$: the limiting maximum ‘wet’ surface energy which a particle may take
- $t_{d\ max}$: maximum bond dry out period (associated with $\gamma_{w\ max}$)

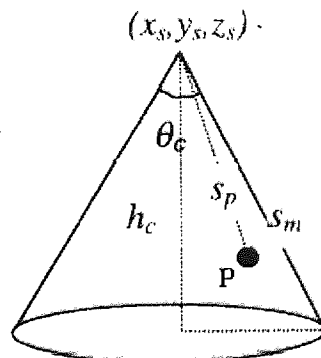


Figure 6.1: Notional representation of spray zone as a conical region

6.2.1 "Wetting" in the spray zone

"Wetting" of particles in the spray zone is modelled by an increase in wet surface energy. The increase in wet surface energy is modelled with simple exponential functions of the particle location and time duration in the spray zone. The principal variables in the wet surface energy spray model are:

- γ_w : the active wet surface energy on a particle (J/m^2)
- $\gamma_{w \max}$: the limiting maximum wet surface energy which a particle may take
- γ_d : the bond energy for a dry or drying bond (J/m^2)
- Γ_d : energy of adhesion per unit area (equivalent to the work done in separating the two adhering surfaces)
- t_b : the age of a drying bond
- t_{db} : maximum bond dry out period

A particle at point P in the spray zone, distance s_p away from the spray source has 'wet' surface energy γ_w as follows:

$$\gamma_w = \gamma_{w \max} e^{-s} (1 - e^{-t_s}), \quad s = s_p/s_m \quad (6.1)$$

$$\Delta\gamma_w = \gamma_{w \max} e^{-s} [(e^{-t_s} - 1)\Delta s + e^{-t_s} \Delta t_s] \quad (6.2)$$

Where the variable s_m is the maximum distance from the spray source within the active spray region. s is the normalized distance of a particle at point P with respect to s_m . Some resulting surface energy time evolution curves are depicted in Figure 6.2. All particles in the spray zone acquire a wet surface energy, which approaches a limiting maximum value over time. The functional form of the equations comes partly from the expectation that particles farthest away from the spray source will acquire less liquid binder, due to closer particles obscuring the spray source, and the inherent decrease in the binder flux per unit area.

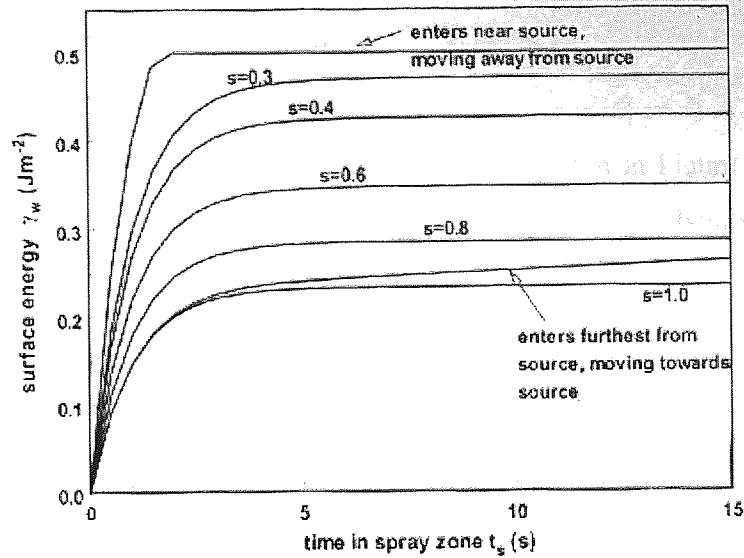


Figure 6.2: Accumulation of surface energy for fixed and moving particles in spray zone for $\gamma_{wmax}=0.5\text{Jm}^{-2}$ from Kafui *et al.* (2008)

6.2.2 Particle “drying” outside the spray zone

For a period of time t_{ds} after a particle has left the spray zone, the particle still has wet surface energy and can still form bonds with other particles. The time limit t_{ds} , depends on γ_{w0} , the initial wet surface energy when the particle left the spray zone.

$$t_{ds} = \frac{\gamma_{w0}}{\gamma_{wmax}} t_{dmax} \quad (6.3)$$

The wet surface energy of the particle after it leaves the spray zone is evolved according to the following equation in t_{so} , the “drying time” since the particle left the spray zone:

$$\gamma_w = \begin{cases} \gamma_{wo} \left(1 + e^{-\left(\frac{t_{so}}{t_{ds}} \right)} \right) & \text{for } t_{so} < t_{ds} \\ 0 & \text{for } t_{so} \geq t_{ds} \end{cases} \quad (6.4)$$

Some resulting evolution curves for drying of γ_w are shown in Figure 6.3. After the drying time t_{so} has exceeded t_{ds} , the particle can no longer form bonds, and the wet surface energy is set to zero.

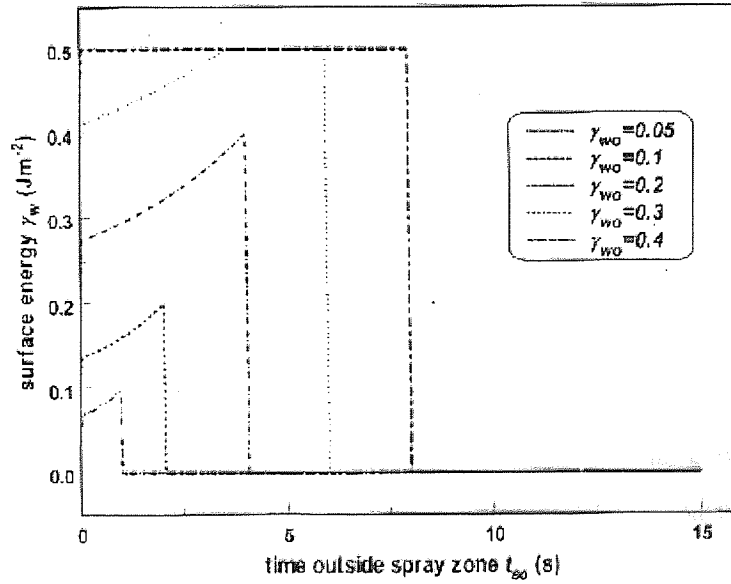


Figure 6.3: Notional drying of wet surface energy outside spray zone for $\gamma_{wmax} = 0.5 \text{ Jm}^{-2}$ and $t_{dmax} = 10 \text{ s}$ from *Kafui et al. (2008)*

6.2.3 Bond “drying” outside the spray zone

The drying of particle-particle bonds in the model is restricted to a time period t_{db} given in the equation below, where $\gamma_{w \text{ pair}}$ is the mean wet surface energy of the two particles which are bonded:

$$t_{db} = \frac{\gamma_{w \text{ pair}}}{\gamma_{w \text{ max}}} t_{d \text{ max}} \quad (6.5)$$

The bond energy, γ_d is evolved over the bond drying time t_b according to:

$$\gamma_d = \begin{cases} \gamma_{w \text{ pair}} \left[1 + (d_{fac} - 1) (1 - e^{-t_b}) \right] & \text{for } t_b < t_{db} \\ \gamma_{w \text{ pair}} d_{fac} & \text{for } t_b \geq t_{db} \end{cases} \quad (6.6)$$

Some examples of the increase in bond energy during drying are shown in Figure 6.4.

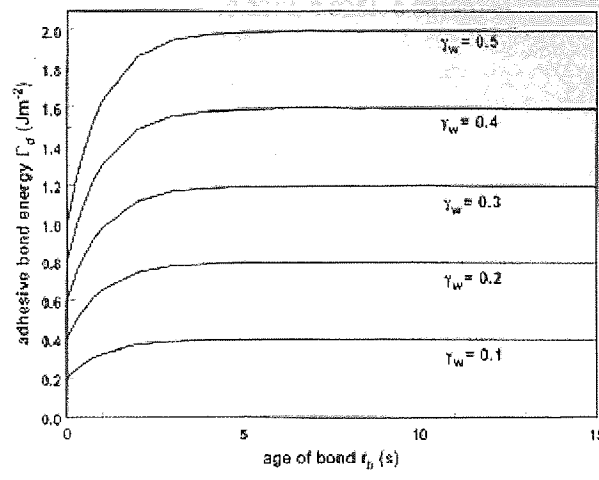


Figure 6.4: Increasing adhesive energy during bond drying for various initial wet surface energies from *Kafui et al. (2008)*

6.2.4 Spray set-up in drum

The spray zone was tilted by angle β , by transforming the coordinate system according to Equation 6.7. This transformation is applied to the particle coordinates and the spray coordinates alike. The transformation is required because the implementation of the spray code expects a vertically aligned spray zone. Therefore all spray zone calculations are performed in this transformed system, and afterwards the inverse transform is applied.

$$\begin{pmatrix} x_B \\ y_B \\ z_B \end{pmatrix} \rightarrow \begin{pmatrix} x_B \cos\beta + y_B \sin\beta \\ -x_B \sin\beta + y_B \cos\beta \\ z_B \end{pmatrix} \quad (6.7)$$

The spray was positioned similar to Brooks investigation; such that material is wetted close the shoulder of the free surface. The source position (x_s, y_s, z_s) , spray coverage angle θ_c , and spray height h_c were chosen to cover a large surface area of the free surface (approximately 1/3 of the total length of the free surface), and give a penetration into the bed of 3-4 particles deep. The spray parameters used are given in Table 6.2.

Spray parameters	
(x_s, y_s, z_s)	(0.0212, 0.0251, 0.00135) m
β	50°
θ_c	80°
h_c	0.00750 m
$\gamma_{w \max}$	1.0 Jm^{-2}
d_{fac}	5.0
$t_{d \max}$	0.157 s

Table 6.2: Summary of the spray parameters used in the drum granulator

The spray is tilted by 50° rotation anti-clockwise about (x_0, y_0, z_0) , with constant z_0 . A spray angle of 80° is used, which is a relatively wide-angle spray in industrial terms. Yule (1998) reports that full cone industrial sprays typically have spray coverage angles no greater than 50° , however we choose a larger value here to increase the surface area coverage and ensure good wetting. The maximum drying time for particles and particle-particle bonds $t_{d \max}$ was chosen to correspond to a $\frac{1}{2}$ drum revolution. The parameters $\gamma_{w \max}$ and d_{fac} were chosen to be similar to those used by Kafui.

The spray model was initially tested by simulating a single particle in the spray zone. The time evolution of γ_w was compared with the expected behaviour over the particle trajectory, and excellent agreement was found. The spray model is then ready to use on the full system.

From visual inspection of the 3D particulate bed, an approximate steady state was identified at time $t = 0.4\text{s}$, where the free surface appears to fluctuate by only a small amount. This state is depicted in Figure 6.5, and corresponds just over to 1.2 revolutions of the drum. At this time the spray was activated.

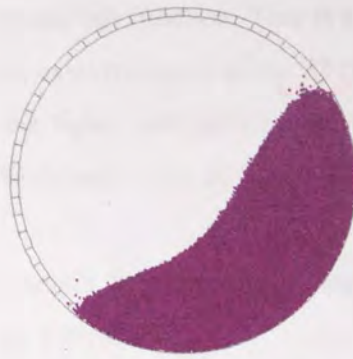


Figure 6.5: 3D cascading bed selected as the approximate steady state ready for spray insertion, $t = 0.40s$.

6.3 3D particle trajectories

The trajectories of 22 particles, labelled 1 to 22, were tracked for the duration of the spray simulation (0.27s, nearly 1 full drum revolution). The trajectories in the x-y plane are shown in Figure 6.6. We can see that frequency of circulation of the bed is higher than that of the drum (since in this time many particles complete more than 1 full orbit, whilst the drum has not *quite* fully rotated).

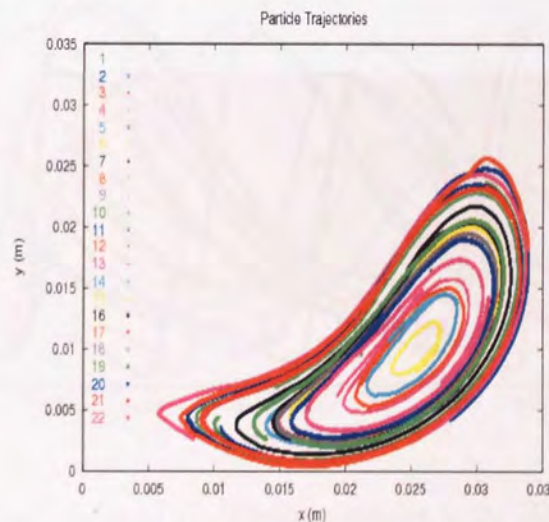


Figure 6.6: Transverse trajectories of 22 different particles in the 3D cascading bed.
For $t=0.4$ to $0.676s$

From Figure 6.6, we can see that all 22-tracer particles are following roughly concentric trajectories, all circulating around a particular point in the bed. The trajectories for each particle were also computed in the axial (z) direction, by “unrolling” the periodic z boundary such that the time evolution of the z coordinate

was made to be a continuous, smooth function. This is analogous to a 3D simulation of an infinitely long drum. The axial transport of the 22 tracer particles is shown in the z-y plane in Figure 6.7. In the figure, all particles travel from the left ($z=0$) to the right. For those trajectories with large radii of circulation, two phases of the motion are apparent:

- (i) Increasing height y in the bed, coupled with only a small axial transit in the z direction.
- (ii) Decreasing height y in the bed, coupled with a large transit in the z direction.

For those trajectories with small radii of circulation, particularly particle 15, there is no distinction between the two regimes, and the z-y trajectory is quite sinusoidal with approximately constant axial velocity.

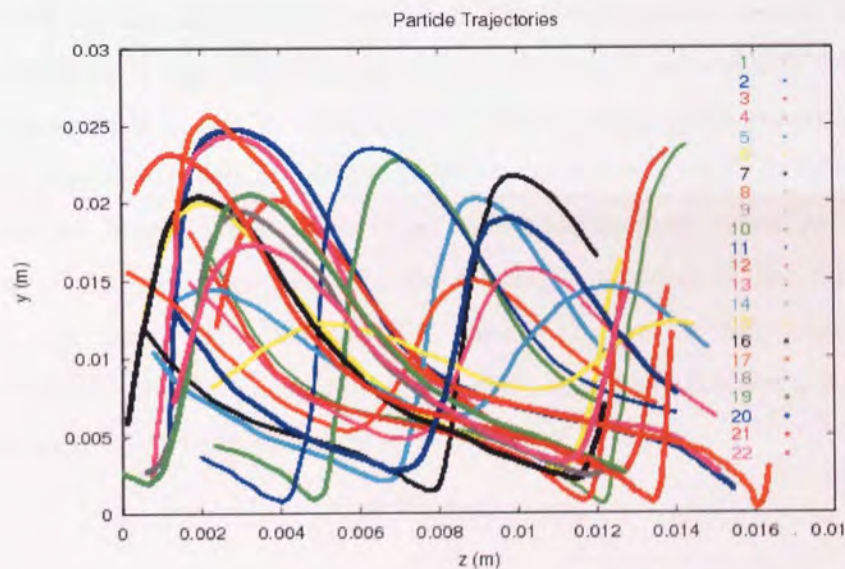


Figure 6.7: Axial trajectories of 22 different particles in the 3D cascading bed. For $t=0.4$ to $0.676s$

6.3.1 Single tracer particle trajectory

The trajectory of the single tracer particle 1 is plotted in the z-y plane in Figure 6.8(a). The particle passes through the periodic boundary at $z = 0.0026$ m and is re-introduced back into the drum at the $z = 0.0001$ m boundary. The corresponding “unrolled” axial position of particle 1 is shown in Figure 6.8(b). [Note: In figures 6.9

the plots do not include for the shift in the x,y,z-coordinates of 0.0001 as mentioned in Table 6.1, as was used in the simulated system.]

From Figure 6.8(e,f,g), we find the particle cascades downwards during the interval $0.4s < t < 0.5s$, and carried up by the drum wall in the interval $0.5s < t < 0.65s$. Note that the simulation does not capture the full cascade of particle 1, so the full cascade duration is slightly longer than 0.1s.

The time evolution of the z-coordinate in Figure 6.8(d) shows an approximately constant axial velocity during the interval $0.4s < t < 0.5s$. In the x-y plane, this constant axial velocity corresponds to the cascade, right up to the toe region at minimum x. In the cascade, the axial velocity of tracer 1 is approximately 8cm/s. After time $t = 0.5s$, the particle passes the toe region and moves into the bed. At this time the axial velocity is substantially reduced. The effective axial velocity whilst the particle circulates in the bed from the toe i) vertically downwards is $\sim 4\text{cm/s}$, ii) vertically upwards is $\sim 1.3\text{cm/s}$. Note that this results contradict the simplistic rolling mode axial transport models of *Saeman (1951)* and *Zablotny (1965)*. In those papers, the assumption is made that there is *no* axial displacement when particles are circulating in the bed. Accounting for the missing component of the full circular trajectory, the mean axial velocity for particle 1 over a full circulation is approximately 4.7 cm/s. For comparison, Saeman's model predicts the axial velocity according to the following equation, from *Perron et al. (1990)*:

$$v_z = \frac{0.955R\omega v}{\sin \phi} \quad (6.8)$$

Where R is the drum radius, ω is the drum speed, v is the drum tilt and ϕ is the dynamic angle of repose. Saeman's model is concerned only with the rolling mode, so we do not expect an exact agreement, but we can derive some upper and lower velocity bounds from the model using the minimum and maximum angles of repose. From Figure 6.5, the angle of repose varies between approximately 20° and 60° along the free surface. These estimates give upper and lower axial velocities of 8.3 cm/s to 3.3 cm/s from Equation 6.8. The DEM simulation result, although in a cascading mode rather than a rolling mode, is precisely between these bounds.

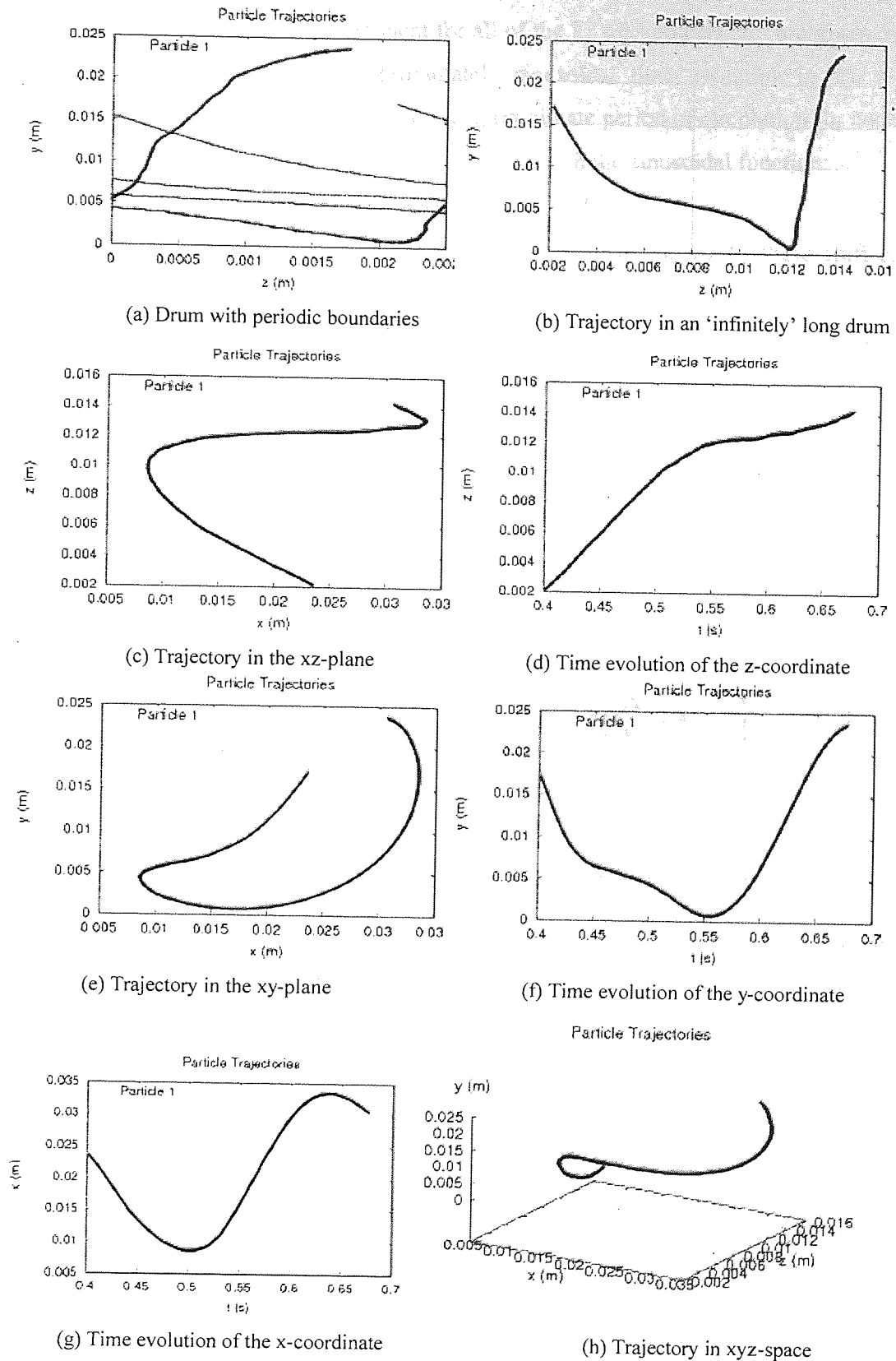


Figure 6.8: Trajectory of particle 1 in the 3D cascading bed. For $t=0.4$ to 0.676 s.

6.3.2 Bed circulation period

The time evolutions of the x-component for all of the 22 tracked particles are given in Figure 6.9. In Figure 6.9, an approximately sinusoidal time evolution in the x-coordinate is evident. This suggests that the approximate period of circulation for each particle can be obtained by fitting the x-t evolution with the sinusoidal function:

$$x(t) = a \sin(bt + c) + d$$

A least squares fit was used to obtain the amplitude a , frequency b , phase shift c , offset (a non-zero centre amplitude) d , for the fitted curve. Some example sinusoidal fits are shown in Figure 6.10 and further details of these fits for all of the tracked particles are given in Appendix D. The period of circulation is then simply $2\pi/b$. The bed circulation period is given in Figure 6.11 for all the 22 tracked particles. The circulation period ranges from 0.19s to 0.38s with an average value of 0.28s.

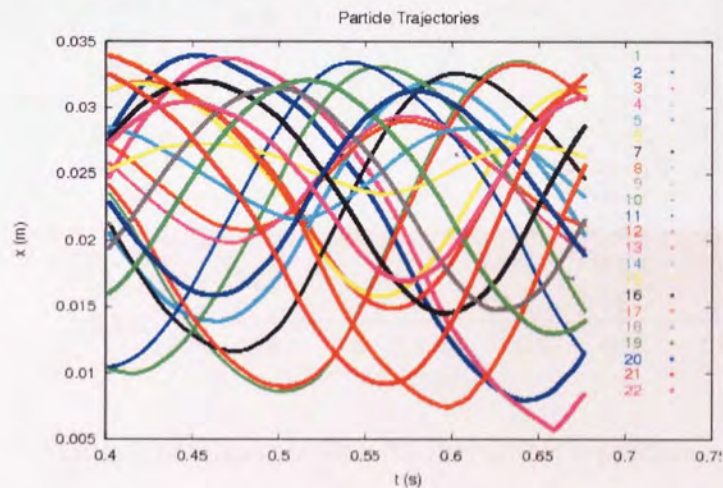
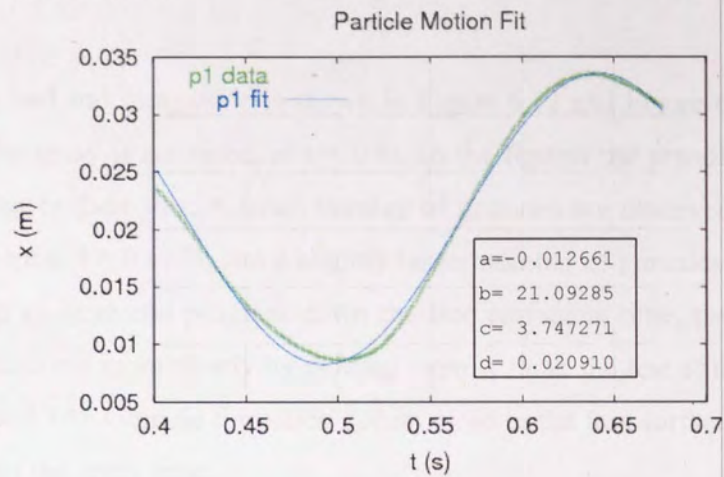


Figure 6.9: Time evolution of x-component of all tracked particles, for $t=0.4 - 0.676s$

(a) Particle 1



(b) Particle 5

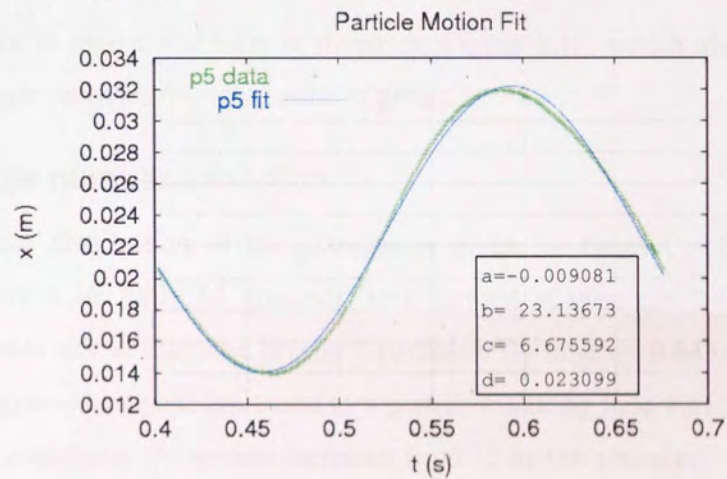


Figure 6.10: Example Sine fits for particle x-position.

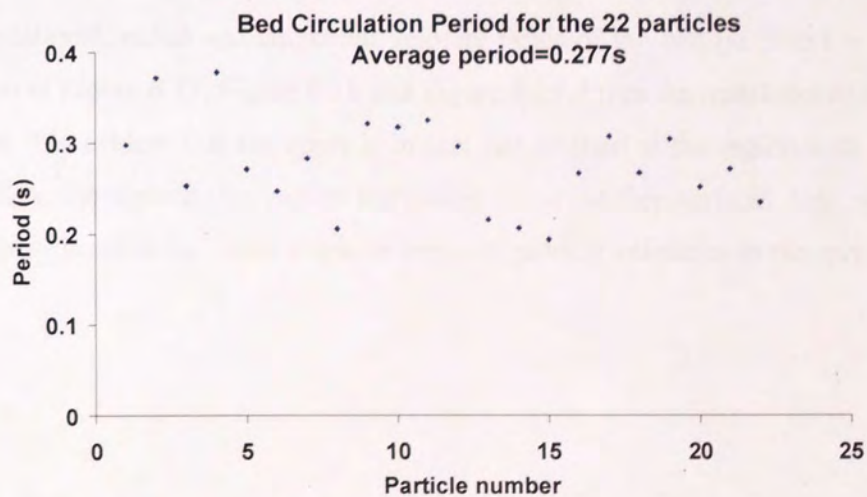


Figure 6.11: Bed circulation period for all tracked particles

6.4 Qualitative observations of granulation

The cascading bed and spray zone is shown in Figure 6.12 and Figure 6.13, depicted shortly after the spray is activated, at $t = 0.4$ s. In the figures the granules are colour coded according to their size. A small number of granules are observed to leave the spray zone by time, $t = 0.412$ s, and a slightly larger number of granules are observed to leave the spray zone and progress down the free surface at time, $t = 0.420$ s. The granules are observed more clearly by plotting them without the rest of the particulate bed (see Figure 6.14). Granule formation occurs close to the free surface and beneath the lower end of the spray zone.

An enlargement at time $t = 0.420$ s is shown in Figure 6.15, which also depicts all those 'wet' single particles the spray zone in green.

6.4.1 Granule number evolution

The number-size distribution of the granules is given for times $t = 0.412$, 0.420 , 0.643 s in Figure 6.16. Only 12 granules have formed at time $t = 0.412$ s, and the maximum granule size at this time is only 5 particles. By time $t = 0.643$ s, we see that the maximum granule size has increased to 9 particles. During time $0.412 < t < 0.643$, the number of granules in the system increases from 12 to 356 granules.

6.4.2 Velocity fields

The translational, radial and tangential velocity fields of the bed (at time $t = 0.420$ s) are shown in Figure 6.17, Figure 6.18 and Figure 6.19. From the translational velocity field plot, it is evident that the spray is in fact *not* inserted at the region with highest particle flux: the highest flux region is midway along the free surface. Also, with the current spray positioning, there is a wide range of particle velocities in the spray zone.

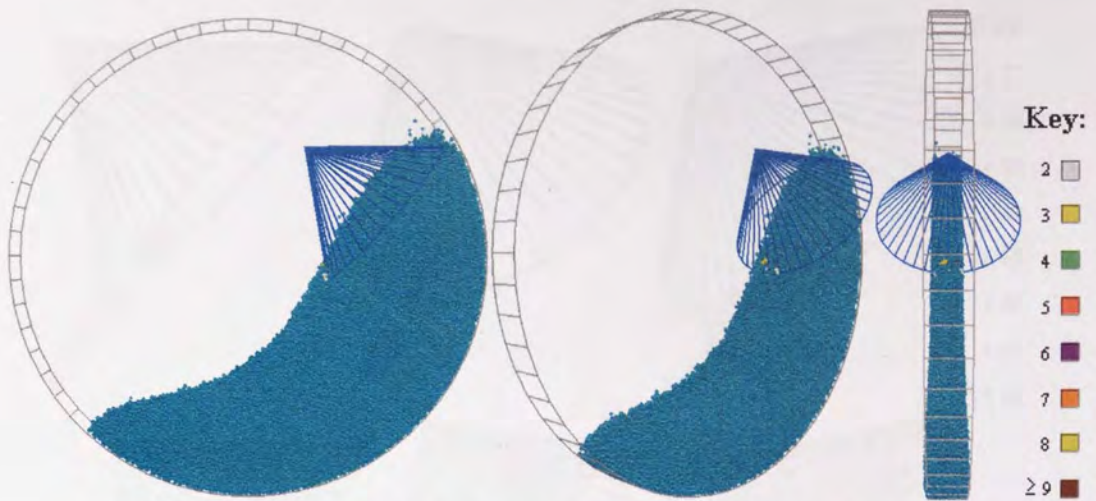


Figure 6.12: Particulate bed shortly after spray activation, at $t = 0.412s$.

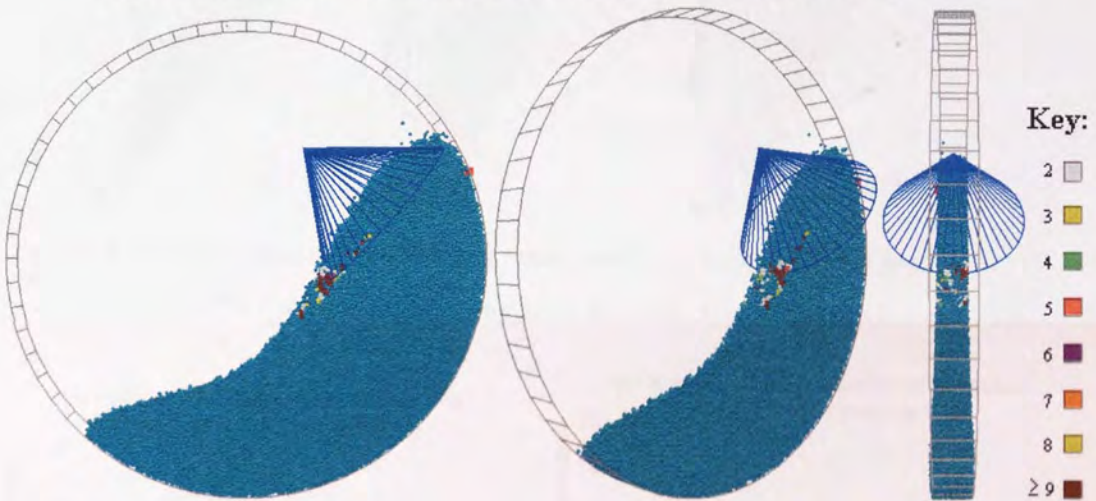


Figure 6.13: Particulate bed shows few granules leaving spray zone, at $t = 0.420s$.

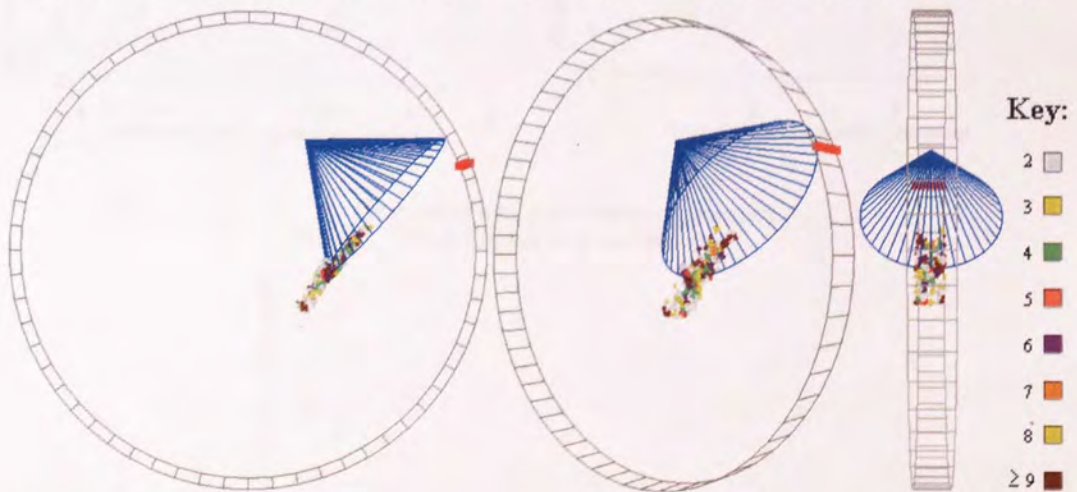


Figure 6.14: Granules are shown without the rest of the particulate bed, at $t = 0.420s$.

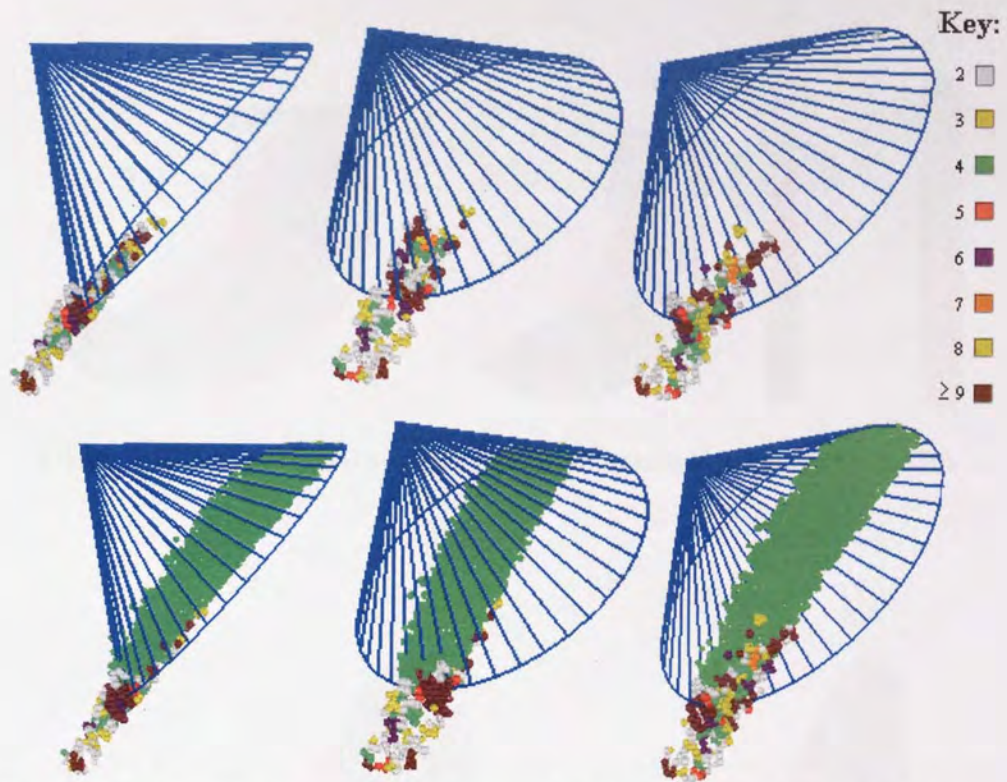


Figure 6.15: The granules are shown in more detail and from different angles, at $t = 0.420s$ (particles in the spray zone are also coloured green)

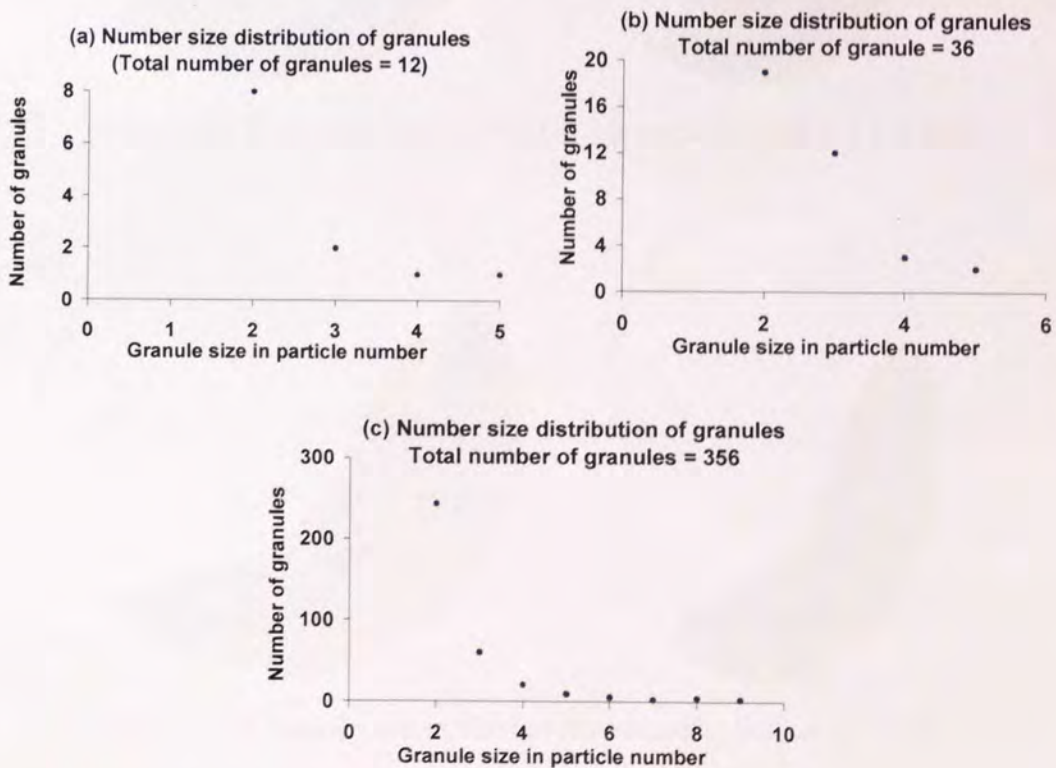


Figure 6.16: Size distribution of granules at times, (a) $t = 0.412s$, (b) $t = 0.420s$ and (c) $t = 0.643s$.

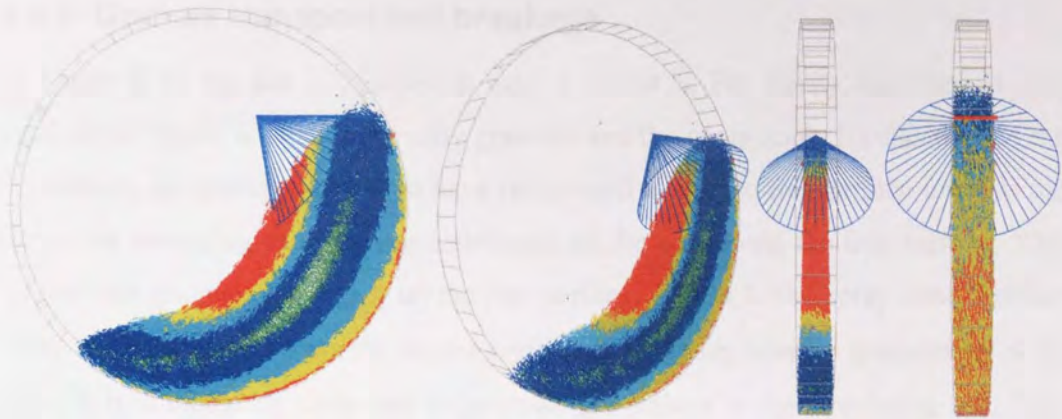


Figure 6.17: Translational velocity field of the cascading bed, at $t = 0.420s$.

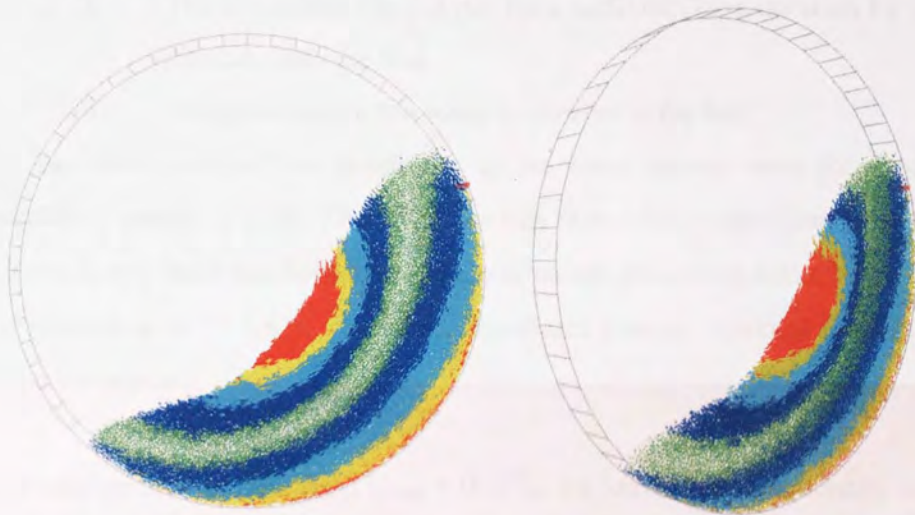


Figure 6.18: Tangential velocity field of the cascading bed, at $t = 0.420s$.

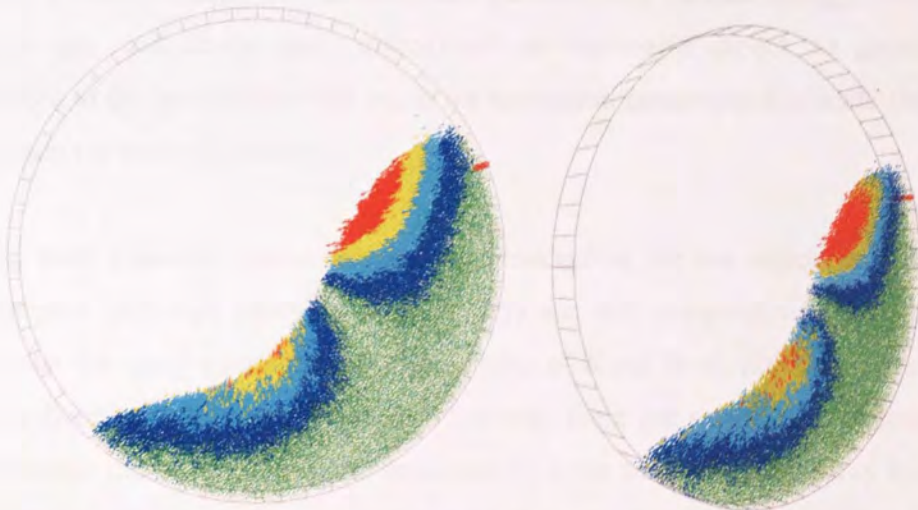


Figure 6.19: Radial velocity field of the cascading bed, at $t = 0.420s$.

6.4.3 Granule transport and breakage

In Figure 6.20, the bed is depicted at time, $t = 0.643\text{s}$. For clarity, this state is also depicted in Figure 6.21 showing only granules and the spray zone. By this time in the simulation, the granules appear to have progressed along the free surface towards the toe of the cascading bed, and are distributed all the way along the free surface. The largest size granules are higher up the free surface, closest to the spray zone. Further down the free surface towards the toe region we find only smaller granules ($N \leq 5$). Also, it is immediately clear that no granules are present in the circulating bed. This could be for two possible reasons:

- (i) The simulation has not run for a sufficient long duration for granules to circulate into the bed.
- (ii) The granules are too weak to survive in the bed.

We can discount the first possibility as we have already seen the mean particle circulation period is 0.28s . From this, we can reasonably expect that granules formed at $t \approx 0.4\text{s}$ will have had sufficient time to circulate around the entire bed by the end of the simulation at $t = 0.67\text{s}$. Therefore, significant granule breakage must be occurring in the toe region.

From our parameter definition $t_{d\text{max}} = 0.157\text{s}$, we know that a maximally wet granule will be fully dry after 0.157s . Given that particles in the spray zone will likely acquire only a small fraction of the maximum possible wet surface energy, (because they never get close to the spray source) we can reasonable expect the granules in the system to dry by the time they reach the toe region (assuming a cascade time of 0.1s , as seen for tracer particle 1).

The most plausible reason for granule breakage in the toe region is that the bond strengths (although likely to be fully dry) are still comparatively weak. We have chosen the spray parameters to match those of *Kafui et al. (2008)*, where relatively long-lived granules were observed. However, there are several key differences with respect to that work. Firstly, the residence time for particles in the spray zone may be comparatively short for our system. From inspection of the particles trajectories (Figure 6.8) and calculations of the period of circulation (Figure 6.11), we estimate that particle residence times in the spray region are relatively short (approximately

0.005 – 0.01 s). From equation 6.1, this results in a very large attenuation (at least 99%) of γ_{\max} . The expected dry bond strength will therefore be much lower than that reported by Kafui (although this has not been measured directly for our simulation). Secondly, the spray zone of Kafui is effectively submersed in the fluidised bed, whereas our spray source is a substantial distance *above* the free surface. The exponential decay of the spray energy with distance (equation 6.1) is intended to model particles far from the source being obscured by those which are closer (in addition to the natural inverse square flux decrease). This obscuration is effective at *any* distance from the source for Kafui's system, because the spray is submersed. However, in our simulation, we have no obscuration of the spray source above the free surface. Therefore the exponential decay with distance from the source is rather pessimistic for our system. Based on the closest approach of the bed to the spray source, we estimate the maximum achievable wet surface energy is additionally only 40% to 45% of the maximum that can be obtained for a submersed spray like Kafui's system. Thirdly, particles flowing in the cascade surface will be subject to high energy collisions and increased shear forces as they approach the toe region and underlying bed. It is therefore possible that the dynamics of our system produce particle-particle interactions which are either more vigorous or more frequent than in Kafui's system, which we would expect to lead to increased breakage. Particle interactions in the toe region have not been characterized quantitatively so this possibility cannot be confirmed, however. Any breakage of particles at the toe due to large interaction forces could be counteracted by adjusting the system parameters so that agglomerates are more strongly bonded by the time they reach the toe. The most obvious adjustment to the system would be to ensure that all particles at the free surface attain a wet surface energy of γ_{\max} in the spray zone. The exponential attenuation of the spray energy with distance could be retained to model obscuration, but this should be based on the depth beneath the free surface, rather than the distance from the notional spray source. It is clear that the low residence time in the spray zone permits only a small fraction of γ_{\max} to be picked up. Because of this, it would also be sensible to parameterize the wetting rate in the spray zone. From these considerations, we believe future drum granulation studies would benefit from a modified model for wetting based on equation 6.1:

$$\gamma_w = \gamma_{w\max} e^{-s} (1 - e^{-t}), \quad t = t_s/t_w, s = d_p/d_m \quad (6.8)$$

where t_s is the residence time in the spray zone, t_w is a parameterised characteristic 'wetting time', d_p is the depth of the particle beneath the free surface and d_m is the penetration depth of the spray into the free surface.

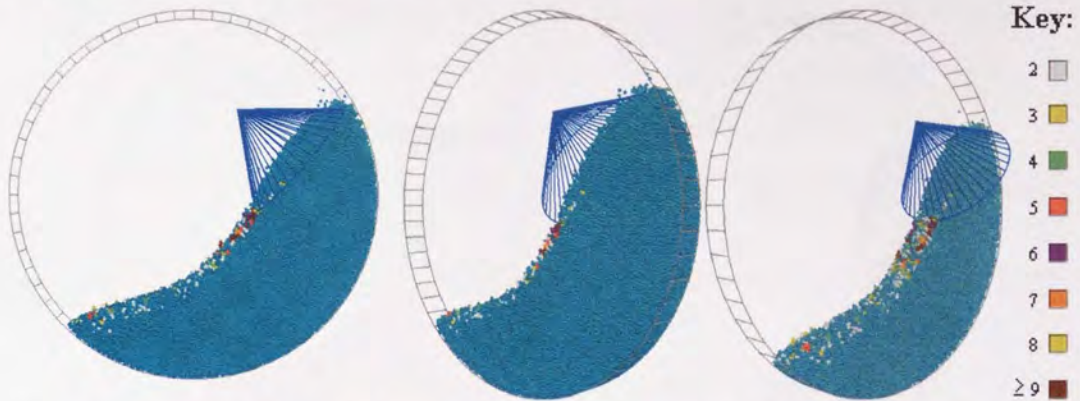


Figure 6.20: Particulate bed shows granules leaving spray zone and progressing down the free surface, at $t = 0.643s$.

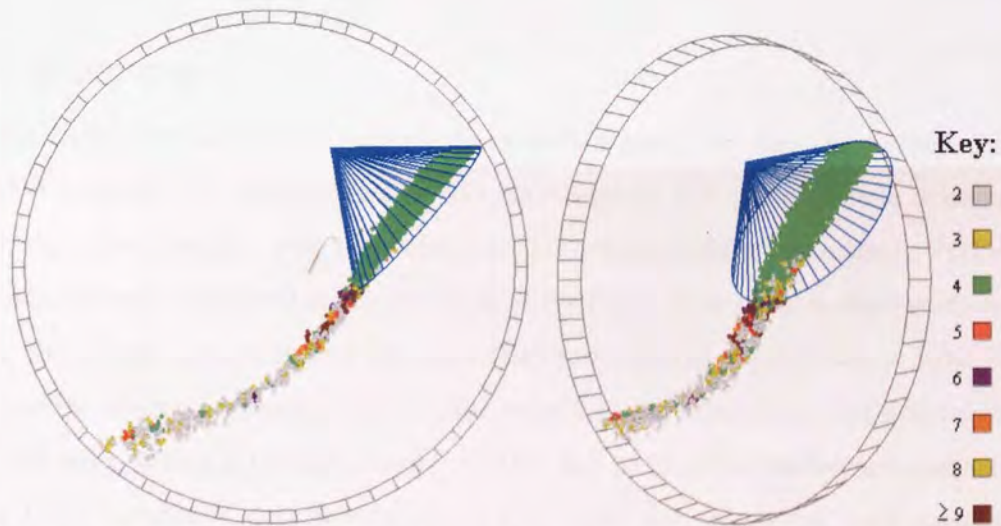


Figure 6.21: Granules are shown without the particulate bed except for wet particles in spray zone (indicated also by green), at $t = 0.643s$.

The connection diagram of the bed at this time is shown in Figure 6.22. The figure shows little connectivity of particles in the spray zone. For a more realistic spray model, for example where liquid drops are used to simulate the spray, this spray region would give good penetration of the spray as particles are very loosely connected. However, in our spray model we define the spray depth and all particles within the spray region are 'wetted' even when obscured from the spray source. The simplistic spray model with fixed bed penetration and the concentric trajectories of particle circulation mean that only a small fraction of the bed can be sprayed. It would

appear therefore that the position of the spray cone was not good. A better choice may have been closer to the shoulder of the bed so that at least some particles would get a 'good dose' of fluid.

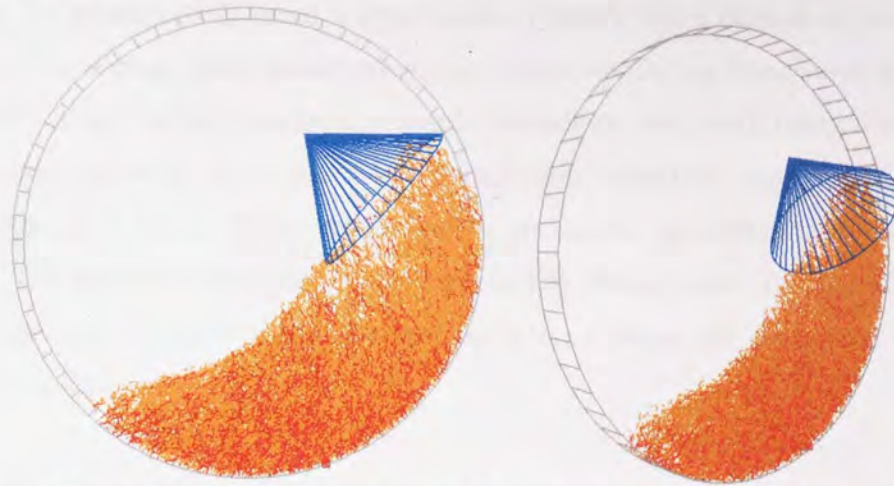


Figure 6.22: Connection diagram of cascading bed, at $t = 0.643\text{s}$.

6.5 Summary

A 3D DEM simulation of a rotating drum with a spray has been performed using 50,000 particles. The drum diameter was equivalent to 136 mean particle diameters and the drum length was equivalent to 10 mean particle diameters. Periodic boundaries were employed at the two ends of the drum. Five particle sizes were used with an average particle size of $250\ \mu\text{m}$. The drum fill was approximately 30%. The axis of the drum was inclined by 5° with respect to the horizontal. The drum speed was $20\ \text{rad/s}$, giving a Froude number of ~ 0.8 , and produced a moderately cascading bed. DEM simulation data corresponding to 2 drum revolutions has been generated over 0.68s real time and 15 months of CPU time.

A wide-angle conical spray was positioned close to the shoulder region and above the cascading layer as recommended by *Brook (1957)*. The spray was modelled with a conceptual spray "zone": a conical region of fine mist of 'adhesive' or liquid where the apex of the zone is the spray source. Pick up of liquid binder in the spray zone was modelled with a surface energy dependent on the distance from the source and the time spent in the zone. Particle drying and bond drying are both modelled as an exponential evolution of the bond energy and wet surface energy.

A dynamic steady state was identified visually after 0.4s, and at this time the spray was activated, and particle trajectories were observed. The effective axial transport was found by 'unrolling' the periodic boundaries. For a particle cascading in the free surface, the average axial speed is approximately 8cm/s. For a particle circulating in the bed, the average axial speeds are 4cm/s (when circulating downwards from the toe) and 1.3 cm/s (when circulating upwards towards the shoulder), respectively. The mean axial velocity over the whole circulation trajectory was found to be approximately 4.7cm/s. These results are in reasonable agreement with Saeman's model. The bed circulation period was extracted by fitting a sine function to the x-coordinate data for each of the 22-tracer particles; a mean bed circulation time of 0.277s was obtained.

Qualitative observations of granulation in the drum system have been presented. During the simulation time $0.412 < t < 0.643$, the number of granules in the system increases from 12 to 356 and the maximum granule number-size increases from only 5 to 9. Granule breakage is inferred in the toe region, since no granules survive past this point and circulate into the bed.

Granule formation, growth and breakage have all been shown in the DEM simulation results presented here. The limiting factor in obtaining more extensive results has been the very large CPU time requirements. The basic particle motion in the drum in both this simulation and the previous 2D work have given us good confidence in the DEM model, and it has also been shown that the spray code can produce granules in this context.

Further investigations in the same system would be of much interest, specifically to examine the time evolution of the granule size distribution, the dependence on Froude number, spray variables and spray location. All of these dependencies are of key interest in industrial systems.

In order to pursue further granulation studies with the system, the problem of breakage at the toe region would need to be addressed. The principle reason for breakage is that the maximum wet surface energy which be attained is too low, due to short residence time in the spray region, and unphysical exponential attenuation of the

spray above the free surface. A modified parameterised model for wetting in the spray zone has been proposed which may avoid the issues encountered in this simulation.

7 Conclusions

This thesis has presented DEM results for particle motion and granulation in a rotating drum. We have seen that the rotating drum is an important tool in a wide variety of applications, including, but not limited to, granulation.

Before examining the granulation process itself, it is clearly important to understand all aspects of particle motion in the drum. To this end, the DEM simulation results were compared qualitatively with published experimental data in order to demonstrate that realistic particle motion is produced. Having shown that realistic motion can be generated via simulation, we then considered the granulation process in the rotating drum apparatus.

7.1 Results from 2D rolling bed simulations

A two dimensional system of 5000 particles has been simulated with a Gaussian size distribution comprising 5 discrete particle sizes. The mean particle diameter was 1mm, and the drum diameter was chosen to be 15cm. The fractional fill of the system was 30%. Particle properties were chosen which closely match those of glass, since this facilitated ready comparison with other workers who have studied the motion of glass beads in rotating drums.

A settled bed in an equilibrium state was prepared before commencing the dynamic simulation studies. Validation checks were made for (i) equilibrium balance and (ii) tangential forces. Good agreement with the expected Newtonian result was found.

Rolling, cataracting and centrifuging motions have all been demonstrated. Much of the published work on particle motion focuses on the rolling mode, which has been analysed in depth.

A rolling drum simulation was run for 17 months on an SGI workstation, and generated 7.6s of equivalent real-time data. At a drum speed of 1rad/s, approximately 1.2 full drum revolutions have been simulated. The dynamic angle of repose of the

material was found to be approximately 23° , and the static angle of repose was found to be approximately 29° .

Qualitative observations were made of the particle motion and the velocity field; both showed good agreement with PEPT experimental data. The main features of the particle motion are: (1) solid body motion close to the drum wall, (2) a cascading layer close to the free surface, (3) a bow shaped region distinguishing the active and passive layers.

Avalanches in the material were analysed by considering the time evolution of the contact line. Small-scale fluctuations of order 1° have been shown to be consistent with a single layer of particles avalanching in the free surface. Particles arriving at the drum wall quickly acquire a constant angular velocity after avalanching. No correlation was found between the avalanche interval and the avalanche amplitude in the rolling regime.

The majority of particles close to the drum wall were shown to move with speeds within 5% of the drum wall speed, but significant slip was observed near the toe and shoulder regions. The slip at the drum wall in the central region (equidistant between the toe and shoulder) is negligible when the drum speed is 1rad/s. Over the total angular coverage of the drum (approximately 140°), significant slip has been shown over 60° of the angular region.

Particle motion in the free surface is largely parallel with the free surface. The maximum particle speed in the cascading layer was found to be 30cm/s. Particle velocities show a clear variation with the position along the free surface; these results are consistent with the experimental data of *Ding et al. (2001b)*. The highest particle velocity in the cascading layer is close to midpoint of the free surface.

Particle velocities in a bed cross section were also investigated. Three main features were observed: (1) there is solid body rotation about the drum centre for those particles close to the drum wall, (2) there is a point of minimum translational velocity at $r=4.3\text{cm}$, and (3) there is solid body rotation around the point $r=0.4\text{cm}$ for those particles near the free surface. The solid body rotation near the drum wall is

approximately 1rad/s for all particles with $r > 0.055\text{m}$. The ratio of the active to passive bed depths is found to be 0.72, in comparison to *Parker et al. (1997)* who report approximately 2/3 for all their experiments.

No evidence for radial size segregation was found from the DEM data. However, no definite conclusions regarding segregation can be drawn given the short real-time duration of the simulation.

7.2 Results from 3D cascading bed simulations

In order to study granulation in the cascading regime, a three-dimensional DEM simulation was performed using 50,000 particles in a drum of diameter 3.4cm and length 0.25cm. The 3D drum was inclined by 5° with respect to the horizontal. A Gaussian particle size distribution with 5 discrete sizes was used, with a mean particle diameter of $250\mu\text{m}$. Periodic boundaries were implemented at the two ends of the drum to give an effectively infinite drum length. The drum speed was chosen as 20rad/s (Froude number ≈ 0.83) to give moderate cascading. The total simulation time for the generated cascading drum data was 0.676s (2.2 drum revolutions).

A spray was incorporated in the drum, which was 'switched on' at time 0.4s, so generated data for the granulation simulation is 0.27s - nearly 1 full drum revolution. The spray was modelled with a surface energy concept for particle "wetting". Wetting, drying and particle-particle bond drying were all modelled with simple exponential time evolution functions. The spray was positioned in order to wet material along the free surface, close to the shoulder, similar to the suggestion of *Brook (1957)*. A large spray coverage angle of 80° was used to ensure good wetting of the free surface, and the spray penetrated a distance of 3 to 4 particle diameters into the free surface. The maximum wet surface energy in the spray model was 1Jm^{-2} , and the maximum particle-particle bond drying time was chosen to be $\frac{1}{2}$ a drum revolution. A bond "dry out" factor of 5 was used, such that fully dry bond energies are 5 times higher than the initial wet surface energy of the pair.

A particle trajectory analysis in 3D has shown that:

- (i) Transverse particle trajectories in the bed circulate concentrically around a focal point.
- (ii) Axial velocity of particles along the drum is correlated with the transverse motion. When particles are rotating in the bed, only a small axial velocity is observed. There is a much larger axial velocity when particles are cascading in the free surface. Particles circulating close to the centre of the bed do not show this correlation, and these central trajectories exhibit a constant axial velocity.

Analysis of a single particle trajectory has shown a mean axial velocity of 4.7cm/s. In the cascade the axial velocity was 8cm/s, but whilst rotating in the bed the axial velocity was 4cm/s (when circulating downwards from the toe) and 1.3 cm/s (when circulating upwards towards the shoulder), respectively. This is contradictory to several simplistic models (like Saeman's), which assume zero axial velocity whilst rotating in the bed. Despite this it has been shown that upper and lower bounds (8.3cm/s to 3.3cm/s) on the axial velocity predicted by Saeman's model nicely bracket the measured mean.

A range of circulation periods from 0.19 to 0.38s was found, with a mean circulation period of 0.28s. For comparison, the drum period was 0.314s.

The spray model has been shown to produce granules in the cascading system; the granule population increases from 0 to 356 during the 0.243s of spray simulation. The maximum granule size was also shown to increase from 5 particles (the initial maximum size) to 12 particles at the end of the simulation. Granule sizes close to the toe region are shown to be generally smaller than those nearer the spray zone. No granules circulate into the bed, which implies that granule breakage occurs at the toe.

7.3 Limitations

The work presented here has 3 major limitations:

- (i) System size.
- (ii) Simulation duration.
- (iii) Modelling of the spray zone.

The dimensions of the system, particularly the axial length of the 3D drum, have restricted the analysis somewhat. Some experimental results elsewhere show that particles in a long rotating drum segregate axially according to size or density. This phenomenon cannot be studied easily with the small axial dimensions used in this work. Additionally, since the system is small and scaling relations have not been established, the results presented here cannot easily be compared quantitatively with those in industry or even in the laboratory.

The limited simulation time has restricted in particular the study of transverse (radial) mixing and segregation. It has not been possible to draw conclusions on radial segregation of the bed here because the simulation time has been too short.

The spray model used in the simulation is simplistic, in that it does not model discrete binder droplets. Instead we have modelled the binder flux as a simple function of the distance from the spray source. A more correct model would ideally account for the actual *obscuring* of the spray source by, say, particles on the surface of the bed. In the rotating drum system, this effect may be quite important. The spray model nevertheless facilitates the possibility of both agglomeration and breakage.

7.4 Recommendations for further work

The first and most obvious extension of this work is to run the simulation model with many different drum diameters, fractional fills, and drum speeds. The resulting scaling relations would permit more direct quantitative comparison with PEPT data.

One result from the 3D trajectory studies has been that the frequency of circulation has a relatively wide scatter for different trajectories in the cascading regime. This is apparently in contradiction with results reported by *Parker et al. (1997)* for the rolling regime who finds that the frequency of circulation is approximately constant for all trajectories. This suggests that the frequency of circulation in our 2D rolling simulation should be checked and compared with Parker's results. It might also be interesting to relate the period of circulation of the 3D trajectories with the radii of circulation, and the axial motion along the drum.

Spray position has not been investigated here; we have simply inserted the spray at a position similar to that of *Brook (1957)*. However, some workers have reported that for optimum granulation the spray should be inserted to wet the region of highest particle flux, which is midway along the free surface in our cascading system. However this may not give good spray penetration into the bed, because particles at this point are not as loosely connected as they are at close to the shoulder. Further work should investigate the effect of spray position. To properly model this effect, a more accurate spray model would be required.

In order to conduct studies of the granule size evolution, the spray parameters must be altered in order that granules can survive past the toe region. The following spray simulation parameters could be altered as follows to ensure granule survival:

- Adopt the proposed modification to the particle wetting model given in equation 6.8, and use a small value for the characteristic wetting time so that particles can still be fully wetted even for short residence times in the spray zone.
- Increase the maximum wet surface energy in the spray zone.
- Increase the bond “dry out” factor to model stronger dry bonding.
- Increase the maximum dry out time, which may allow more granule growth outside the spray zone. It is also likely that with the current system parameters, the granules are fully dry by the time they arrive at the toe region.
- Lower the drum speed, which may reduce the granule breakage at the toe region.

Finally, it would be of great interest to study various other drum granulator designs. For example, it is quite common to insert lifter bars inside the drum to encourage lifting of material and a better cascading action. The dynamics of such a system may be quite different to those of the simple rotating drums simulated here. Comparatively little DEM or PEPT results have been published on such systems.

References

1. Adetayo, A. A., Litster, J. D. and Desai, M. (1993). The Effect of Process Parameters on Drum Granulation of Fertilizers with Broad Size Distributions. *Chem. Eng. Sci* **48**(23): 3951-3961.
2. Boateng, A. A. and Barr, P. V. (1997). Granular flow behaviour in the transverse plane of a partially filled rotating cylinder. *J. Fluid Mech.* **330**: 233.
3. Brook, A. T. (1957). Developments in Granulation Techniques. *Proc. Fert. Soc.* **47**.
4. Browning, J. E. (1967). Agglomeration: Growing Larger in Applications and Technology. *Chem. Eng.* **74**(25): 147.
5. Capes, C. E. (1980). *Handbook of Powder Technology*. Elsevier, Netherlands.
6. Capes, C. E. (1980). Particle size enlargement. *Handbook of Powder Technology*. J. C. Williams and T. Allen, Eds. Elsevier, Amsterdam, Oxford, New York. **1**.
7. Capes, C. E. and Danckwerts, P. V. (1965). Granule formation by the agglomeration of damp powders Part I: The mechanism of granule growth. *Trans. Instn. Chem. Engrs* **43**: T116-T124.
8. Chatterjee, A., Mukhopadhyay, P. K., Srivastava, M. P. and Sathe, A. V. (1983). Flow of materials in rotary kilns used for sponge iron manufacture. *Metall. Trans. B* **14B**: 375.
9. Cleary, P. W. (2000) DEM simulation of industrial particle flows: case studies of dragline excavators, mixing in tumblers and centrifugal mill. *Powder Technology* **109**: 83-104.
10. Cleary, P. W., Morrison, R. and Morrell, S. (2003). Comparison of DEM and experiment for a scale model SAG mill. *Int. J. Miner. Process.* **68**: 129-165.
11. Cleary, P. W. and Sawley, M. L. (2002). DEM modelling of industrial granular flows: 3D case studies and the effect of particle shape on hopper discharge. *Applied Mathematical Modelling* **26**: 89-111.
12. Cundall, P. A. (1971). A computer model for simulating progressive, large-scale movements in blocky rock system. *Proc. Symp. Intl. Society of Rock Mechanics, Nancy 2, France*.

13. Cundall, P. A. (1974). Rational Design of Tunnel Supports: A Computer Model for Rock Mass Behavior Using Interactive Graphics for the Input and Output of Geometrical Data, Technical Report MRD-2-74, Missouri River Division, Corps of Engineers, September.
14. Cundall, P. A. and Strack, O. D. L. (1979a). A discrete numerical model for granular assemblies. *Geotechnique* **29**(1): 47-65.
15. Cundall, P. A. and Strack, O. D. L. (1979b). The discrete numerical model as a tool for research in granular media. Part II. Report to National Science Foundation, Dept. of Civil & Mineral Engrg., University of Minnesota, Minneapolis, Minnesota.
16. Ding, Y. L., Forster, R. N., Seville, J. P. and Parker, D. J. (2001a). Scaling relationships for rotating drums. *Chemical Engineering Science* **56**: 3737-3750.
17. Ding, Y. L., Seville, J. P., Forster, R. and Parker, D. J. (2001b). Solids motion in rolling mode rotating drums operated at low to medium rotational speeds. *Chemical Engineering Science* **56**: 1769-1780.
18. Dury, C. M. and Ristow, G. H. (1998). Boundary effects on the angle of repose in rotating cylinders. *Physics Review E* **57**: 4491-4497.
19. Ennis, B. J., Li, J., Tardos, G. and Pfeffer, R. (1990). The influence of viscosity on the strength of an axially strained pendular liquid bridge. *Chemical Engineering Science* **45**(10): 3071-3088.
20. Ennis, B. J. and Litster, J. D. (1997). Size Reduction and Size Enlargement. *Perry's Chemical Engineers' Handbook*. R. H. Perry and D. W. Green, Eds. McGraw-Hill: 20-58.
21. Fauve, S., Laroche, C. and Douady, S. (1991). Dynamics of avalanches in a rotating cylinder. *Physics of Granular media*. D. B. a. J. A. Dodds, Ed. Nova Science, New York.
22. Finnie, G. J., Kruyt, N. P., Ye, M., Zeilstra, C., and Kuipers, J. A. M. (2005). Longitudinal and transverse mixing in rotary kilns: A discrete element method approach. *Chemical Engineering Science* **60**: 4083-4091.
23. Goldschmidt, M. (2001). Hydrodynamic Modelling of Fluidised Bed Spray Granulation. PhD thesis, Twente University.
24. Goldschmidt, M., Weijers, G. G. C., Boerefijn, R. and Kuipers, J. A. M. (2003). Discrete Element Modelling of Fluidised Bed Granulation. *Powder Technology* **138**: 39-45.

25. Hapgood, K. P. (2000). Nucleation and Binder Dispersion in Wet Granulation. PhD thesis, The University of Queensland.
26. He, Y. R., Chen, H. S., Ding, Y. L. and Lickiss, B. (2007). Solids motion and segregation of binary mixtures in a rotating drum mixer. *Trans IChemE* **85**: 963-973.
27. Henein, H., Brimacombe, J. K. and Watkinson, A. P. (1983). Experimental study of transverse bed motion in rotary kilns. *Metall. Trans* **14B**: 191-205.
28. Ingram, A., Seville, J. P. K., Parker, D. J., Fan, X. and Forster, R. G. (2005). Axial and radial dispersion in rolling mode rotating drums. *Power Technology* **158**: 76-91.
29. Iveson, S. M., Litster, J. D., Hapgood, K. and Ennis, B. J. (2001). Nucleation, growth and breakage phenomena in agitated wet granulation processes: a review. *Powder Technology* **117**(1-2): 3-39.
30. Jaeger, J. D. (1993). Grain shape and size influence on low stress behaviour observing discrete avalanches in a rotating cylinder. *Powders and Grains*. C. Thornton, Ed. Balkema, Rotterdam.
31. Johnson, K. L., Kendall, K. and Roberts, A. D. (1971). Surface energy and the contact of elastic solids. *Proc. R. Soc. Lond. A.* **324**:301-313.
32. Johnson, K. L. (1985) *Contact Mechanics*. Cambridge University Press, Cambridge, UK.
33. Kafui, D. and Thornton, C. (2000). Numerical simulation of impact breakage of a spherical crystalline agglomerate. *Powder Technology* **109**(1-3): 113-133.
34. Kafui, D. and Thornton, C. (2008). Fully-3D DEM simulation of fluidised bed spray granulation using an exploratory surface energy-based spray zone concept. *Powder Technology* **184**: 177-188.
35. Kano, J., Kasai, E., Saito, F. and Kawaguchi, T. (2005). Numerical Simulation Model for Granulation Kinetics of Iron Ores. *ISIJ International* **45**(4): 500-505.
36. Kapur, P. C. (1978). Balling and Granulation. *Applications of Cryogenic Technology* **10**: 55-123.
37. Kapur, P. C. and Fuerstenau, D. W. (1964). Kinetics of Green Pelletization. *Trans. AIME* **229**: 348-355.

38. Kasai, E., Ramos, M. V., Kano, J., Saito, F., and Waseda, Y. (1998). Simulation model for the agglomeration process of granules during iron ore sintering by discrete element method. Proc. 3rd World Congress Particle Technol. **89**.
39. Khakhar, D. V., Ottino, J. M., Shinbrot, T. and McCarthy, J. J. (1997). Transverse flow and mixing of granular materials in a rotating cylinder. Phys. Fluids **9**: 31.
40. Kramers, H. and Croockewit, P. (1952). The passage of granular solids through inclined rotary kilns. Chem. Eng. Sci. **1**: 259.
41. Kwapinska, M., Saage, G. and Tsotsas, E. (2005). Mixing of particles in rotary drums: A comparison of discrete element simulations with experimental results and penetration models for thermal processes. Powder Technology **161**: 69-78.
42. Lebas, E., Houzelot, J. L., Ablitzer, D. and Hanrot, F. (1995). Experimental study of residence time, particle movement and bed depth profile in rotary kilns. Can. J. Chem. Eng. **73**: 173.
43. Link, J. M., Godlieb, W., Deen, N. G. and Kuipers, J. A. M. (2007). Discrete element study of granulation in a spout-fluidized bed. Chemical Engineering Science **62**: 195-207.
44. Lian, G., Thornton, C. and Kafui, D. (1998). Departmental Report, Civil Engineering Department, TRUBAL - A 3D computer program for modelling particle assemblies, Aston University.
45. Liu, X. Y., Specht, E. and Mellman, J. (2005). Slumping-rolling transition of granular solids in rotary kilns. Chemical Engineering Science **60**: 3629-3636.
46. Mellmann, J. (2001). The transverse motion of solids in rotating cylinders-forms of motion and transition behaviour. Powder Technology **118**: 251-270.
47. McBride, A., Govender, I., Powell, M. and Cloete, T. (2004). Contributions to experimental validation of the discrete element method applied to tumbling mills. Engineering Computations **21**: 119-136.
48. McCarthy, J. J., Khakhar, D. V. and Ottino, J. M. (2000). Computational studies of granular mixing. Powder Technology **109**: 72-82.
49. Mindlin, R. D. (1949). Compliance of elastic bodies in contact. Journal of Applied Mechanics, **16**: 259-268.

50. Mindlin, R. D. and Deresiewicz, H. (1953). Elastic spheres in contact under varying oblique forces. *Journal of Applied Mechanics* **20**: 327-344.
51. Morrison, R. D. and Cleary, P. W. (2004). Using DEM to model ore breakage within a pilot scale SAG mill. *Minerals Engineering* **17**: 1117-1124.
52. Newitt, D. M. and Conway-Jones, J. M. (1958). A Contribution to the theory and practice of granulation. *Trans. Inst. Chem. Eng., London*. **36**: 422-442.
53. Pandey, P., Song, Y., Kayihan, F. and Turton, R. (2006). Simulation of particle movement in a pan coating device using discrete element modeling and its comparison with video-imaging experiments. *Powder Technology* **161**: 79-88.
54. Parker, D. J., Dijkstra, A. E., Martin, T. W. and Seville, J. P. K. (1997). Positron emission particle tracking studies of spherical particle motion in rotating drums. *Chem. Eng. Sci.* **52**: 2011.
55. Perron, J. and Bui, R. T. (1990). Rotary cylinders: solid transport prediction by dimensional and rheological analysis. *Can. J. Chem. Eng.* **68**: 61.
56. Pietsch, W. (1991). *Size Enlargement by Agglomeration*. John Wiley & Sons, Chichester.
57. Rumpf, H. (1962). The strength of granules and agglomerates. *Agglomeration*. Knepper, Ed. Wiley-Interscience, New York. 379-418.
58. Rutgers, R. (1965). Longitudinal mixing of granular material flowing through a rotating cylinder - Part I. Descriptive and theoretical. *Chemical Engineering Science* **20**: 1079-1087.
59. Saeman, W. C. (1951). Passage of solids through rotary kilns. *Chemical Engineering Progress* **47**(10): 508.
60. Santomaso, A. C., Ding, Y. L., Lickiss, J. R. and York, D. W. (2003). Investigation of the granular behaviour in a rotating drum operated over a wide range of rotational speed. *Trans. IChemE* **81A**: 936-945.
61. Sastry, K. V. S. and Fuerstenau, D. W. (1973). Mechanisms of Agglomerate Growth in Green Pelletization. *Powder Technology* **7**: 97-105.
62. Savkoor, A. R., Briggs, G. A. D. (1977). The effect of tangential force on the contact of elastic solids in adhesion. *Proc. R. Soc. Lond., Ser. A* **356**: 103-114.
63. Sepulveda, N., Krstulovic, G. and Rica, S. (2005). Scaling laws in granular continuous avalanches in a rotating drum. *Physica A* **356**: 178-183.

64. Sherrington, P. J. and Oliver, R. (1981). Granulation. Heyden, London.
65. Shi, D. and McCarthy, J. J. (2008). Numerical simulation of liquid transfer between particles. *Powder Technology* **184**: 64-75.
66. Snow, R. H., Kaye, B. H., Capes, C. E. and Sresty, G. C. (1997). Size Reduction and Size Enlargement. *Perry's Chemical Engineers' Handbook*. R. H. Perry and D. W. Green, Eds. McGraw-Hill: 8-66.
67. Spurling, R. J. (2000). Granular flow in an inclined rotating cylinder: steady state and transients. PhD thesis, University of Cambridge.
68. Stanley-Wood, N. G. (1990). Size Enlargement. *Principles of Powder Technology*. M. J. Rhodes, Ed. John Wiley and Sons Ltd: 205.
69. Tardos, G. I., Khan, M. I. and Mort, P. R. (1997). Critical parameters and limiting conditions in binder granulation of fine powders. *Powder Technology* **94**: 245-298.
70. Thornton, C (1991). Interparticle sliding in the presence of adhesion. *J. Phys. D: Appl. Phys.*, 24: 1942-1946.
71. Thornton, C. and Randall, C. W. (1988). Applications of the theoretical contact mechanics to solid particle system simulation. *Micromechanics of Granular material*. Satake and Jenkins, Eds.: 133-142.
72. Thornton, C. and Yin, K. K. (1991) Impact of elastic spheres with and without adhesion. *Powder Technology* **65**: 153-166.
73. Thornton, C., Yin, K. K. and Adams, M. J. (1996). Numerical simulation of the impact fracture and fragmentation of agglomerates. *J. Phys. D: Appl. Phys.* **29**: 424-435.
74. Wang, F. Y. and Cameron, I. T. (2002). Review and future directions in the modelling and control of continuous drum granulation. *Powder Technology* **124**: 238-253.
75. Wildeboer, W. J. (2002). Design and Operation of Regime Separated Granulators. PhD thesis, The University of Queensland.
76. Yamane, K., Nakagawaa, M., Altobelli, S. A., Tanaka, T. and Tsuji, Y. (1998). Steady particulate flows in a horizontal rotating cylinder. *Phys. Fluids* **10**(6): 1419-1427.
77. Yang, R.Y., Zou, R.P. and Yu, A.B. (2003). Microdynamic analysis of particle flow in a horizontal rotating drum. *Powder Technology* **130**: 138-146.

78. Yang, R.Y., Yu, A.B., McElroy, L. and Bao, J. (2008). Numerical simulation of particle dynamics in different flow regimes in a rotating drum. *Powder Technology* **188**: 170-177.
79. Yule, A. J. (1998). 12th UMIST Short Course: Atomizer and Spray Technology, 17, 18, 19 and 20 March: 4/8.
80. Zablony, W. W. (1965). The movement of the charge in rotary kilns. *International Chemical Engineering* **5**(2): 360-366.

Appendix A. The Discrete Element Method

This appendix gives details of algorithms and equations used for three dimensional sphere assemblies in the DEM GRANULE program.

A.1 *Newton's second law of motion*

A time-dependent finite difference scheme is applied to the iterative calculation of the incremental contact forces and progressive movements of the particles. For each iteration, Newton's second law of motion gives accelerations for each of the constituent particles. The motion of a particle over a time step Δt are governed by the equations:

$$\text{Translation} \quad F_i - \beta_g v_i = m \frac{\Delta v_i}{\Delta t} \quad (\text{A.1})$$

$$\text{Rotation} \quad M_i - \beta_g \omega_i = I \frac{\Delta \omega_i}{\Delta t} \quad (\text{A.2})$$

In the equations, i ($=1,2,3$) indicates the three components in x, y, and z directions respectively. The variable F_i denotes the out-of-balance force component of the particle. M_i is the out-of-balance moment on the particle due to the tangential contact forces. The translational velocity component is denoted by v_i , and ω_i is the rotational velocity component. m and I denote the mass and rotational inertia of the particle respectively. β_g is the global damping coefficient (if used).

A.2 *Force-displacement laws*

A.2.1 *Contact force without adhesion*

Normal Contact Force

A contact is defined between two particles of radii R_1 , R_2 if their boundaries overlap. The relative approach α satisfies the following condition when there is a contact,

$$\alpha < R_1 + R_2 - D \quad (\text{A.3})$$

where $D = \sqrt{(x_2 - x_1)^2 + (y_2 - y_1)^2 + (z_2 - z_1)^2}$ is the distance between the centres of the two particles. The coordinates of the centres of the two particles are given by (x_1, y_1, z_1) and (x_2, y_2, z_2) .

Hertz theory (see *Johnson (1985)*) gives the normal pressure distribution acting over a small circular contact area with radius a . The normal contact force N is expressed as,

$$N = \frac{4E^*}{3R^*} a^3 \quad (\text{A.4})$$

where E^* and R^* are defined as,

$$\frac{1}{E^*} = \frac{1 - \nu_1^2}{E_1} + \frac{1 - \nu_2^2}{E_2} \quad (\text{A.5})$$

$$\frac{1}{R^*} = \frac{1}{R_1} + \frac{1}{R_2} \quad (\text{A.6})$$

E_i and ν_i ($i=1, 2$) denote the Young's moduli and Poisson's ratios of the two particles. Since $\alpha = a^2/R^*$, which may be substituted into (A.4), the normal contact force due to the relative approach α is given by

$$N = \frac{4E^*}{3} (R^* \alpha^3)^{1/2} \quad (\text{A.7})$$

from which the normal contact stiffness is defined as

$$k_n = \frac{\partial N}{\partial \alpha} = 2E^* (R^* \alpha)^{1/2} \quad (\text{A.8})$$

If the increment of the relative approach is $\Delta\alpha$ over a time-step, then the corresponding incremental normal force at the contact is given by,

$$\Delta N = 2E^* a \Delta\alpha \quad (\text{A.9})$$

Tangential Contact Force

The theory of *Mindlin et al. (1953)* gives a model for the tangential force at the contact of two spheres. The theory predicts that for two contacting surfaces under an increasing tangential displacement δ , the relative slip is initiated at the perimeter and progresses inward over an annular area of the contact surface. There is an incremental tangential force ΔT , due to the incremental tangential displacement $\Delta\delta$. The tangential force depends not only on the loading history but also on the variation of the normal

force. The incremental tangential force can be obtained from the following equation (for more detail see *Thornton et al. (1988)*).

$$\Delta T = 8G^* a \theta_k + (-1)^k \mu \Delta N (1 - \theta_k) \quad (\text{A.10})$$

where

$$\theta_k = 1 \quad (\text{A.11})$$

if $|\Delta T| < \mu \Delta N$. Otherwise,

$$\theta_k = \begin{cases} \sqrt[3]{1 - \frac{T + \mu \Delta N}{\mu N}} & \text{if } k = 0 \\ \sqrt[3]{1 - \frac{(-1)^k (T - T_k) + 2\mu \Delta N}{2\mu N}} & \text{if } k = 1, 2 \end{cases} \quad (\text{A.12})$$

where $k=0, 1, 2$ denotes the paths of loading, unloading and reloading respectively. $\Delta \delta$ is the increment of the relative tangential displacement of the two contact spheres at the contact, μ is the friction coefficient, T_k represents the historical tangential force from which unloading or reloading commenced and G^* is defined as,

$$\frac{1}{G^*} = \frac{2 - \nu_1}{G_1} + \frac{2 - \nu_2}{G_2} \quad (\text{A.13})$$

where G_i ($i=1, 2$) is the shear modulus of each particle. In (A.12), T_k needs to be updated as $T_k = T_k - (-1)^k \mu \Delta N$ to account for the variation of the normal force with each time-step.

Further detailed analysis of the contact mechanics for this case can be found in the work of *Thornton et al. (1991)*, *Thornton et al. (1988)* and *Mindlin et al. (1953)*.

A.2.2 Contact force with adhesion

Normal Contact Force

In order to consider surface adhesion, normal contact forces are computed according to the JKR model from *Johnson et al. (1971)*. In this model, the effective normal contact force is still given by the Hertz equation as,

$$N_1 = \frac{4E^*}{3R^*} a^3 \quad (\text{A.14})$$

where the effective normal force is defined as,

$$N_1 = N + 2N_c \pm 2\sqrt{NN_c + N_c^2} \quad (\text{A.15})$$

N_1 is referred to as the “effective” normal force because it is equivalent to the Hertzian force that would be necessary to cause the same contact area. N is the applied normal force or out-balance force and $N = -N_c$ is the pull-off force, the force required to separate the two particles. According to the JKR theory the pull-off force is

$$N_c = -3p\gamma R^* \quad (\text{A.16})$$

where γ is the surface energy of the adhering spheres. From JKR theory it can be shown that,

$$N = \frac{4E^*}{3R^*} a^3 - 4\sqrt{\pi\gamma E^*} a^3 \quad (\text{A.17})$$

and the relative approach of the two spheres is given as,

$$\alpha = \frac{a^2}{R^*} - \sqrt{\frac{4\pi\gamma a}{E^*}} \quad (\text{A.18})$$

The incremental normal force, ΔN , corresponding to the incremental relative approach of the two spheres can be derived from equation A.17 and A.18 to be,

$$\Delta N = 2E^* a \left(\frac{3\sqrt{N_1} - 3\sqrt{N_c}}{3\sqrt{N_1} - \sqrt{N_c}} \right) \Delta\alpha \quad (\text{A.19})$$

Tangential Contact Force

The tangential force between two adhering spheres in contact is calculated according to a combined theory of *Savkoor et al. (1977)* and *Mindlin et al. (1953)*, which has been developed by *Thornton (1991)*. Depending on the relative magnitude of the tangential force in relation to the normal force and loading history, the tangential force is modelled by Mindlin’s partial-slip and no-slip solution respectively. At the beginning of contact, the application of a tangential force, according to *Savkoor et al. (1977)*, is to reduce the contact area. This corresponds to a peeling mechanism. At this stage, Savkoor and Briggs suggested that the tangential force could be prescribed by the no-slip solution of *Mindlin (1949)*,

$$T = 8G^* a d \quad (\text{A.20})$$

From which the incremental tangential force is,

$$\Delta T = 8G^* a^2 \Delta d \quad (\text{A.21})$$

where the reduced contact area α was derived as,

$$a^3 = \frac{3R^*}{4E^*} \left(N + 2N_C \pm \sqrt{4NN_C + 4N_C^2 - \frac{T^2 E^*}{4G^*}} \right) \quad (\text{A.22})$$

Savkoor and Briggs argued that the peeling mechanism continues until a critical value of T is reached, given by the equation,

$$T_C = 4 \sqrt{\frac{G^*}{E^*} (NN_C + N_C^2)} \quad (\text{A.23})$$

When T reaches T_C , the peeling process is complete and the contact area has been reduced to,

$$a_p = \sqrt[3]{\frac{3R^*}{4E^*} (N + 2N_C)} \quad (\text{A.24})$$

However, the theory of Savkoor and Briggs does not provide the solution once the peeling process is completed. *Thornton (1991)* suggested that if the tangential force at the end of peeling is greater than the sliding force, the tangential force immediately falls to the sliding force. If the tangential force $T=T_C$ is less than the sliding force, a subsequent slip annulus is assumed to spread radially inwards and the partial-slip solution of Mindlin and Derenciewicz is applied until sliding occurs. The incremental tangential force after peeling is given by equation A.10 – A.12, but with N replaced by $N+2N_C$.

A.3 Motion update

The contact point is defined to be midway between the intersecting points C_A and C_B of the two contacting spheres, as shown in Fig A1. Unit vectors \mathbf{n} and \mathbf{t} are orthogonal; \mathbf{n} is normal to the contact plane and is the vector between the two particle centres. The direction cosines n_i are defined as,

$$n_i = \frac{x_{Bi} - x_{Ai}}{D} \quad (\text{A.14})$$

x_{Ai} and x_{Bi} are the centre coordinates of the two spheres. In 2D, n_i may be written as $n_1 = \cos\theta$ and $n_2 = \sin\theta$ where θ is the inclination of the contact normal vector to the horizontal axis of the global reference frame.

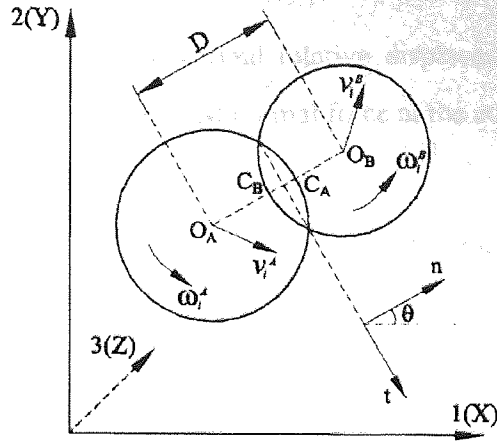


Figure A1: Kinematics of two contacting spheres

Since \mathbf{n} and \mathbf{t} are orthogonal,

$$\mathbf{n}_i \mathbf{t}_i = 0 \quad (\text{A.15})$$

The interaction force between each pair of contacting particles is computed incrementally in GRANULE. At the contact, the relative movement has three components: the relative normal approach along the centre line of the two particles, the relative tangential displacement between the two contacted surfaces and the relative rotation of the two particles. Only the normal and tangential contact forces are considered, because the contact area is very small and the twisting resistant at the contact due to the relative rotation about the line joining the centroids of the two particles can be ignored.

For a pair of particles (A, B) in contact, if the linear and rotational velocities are noted as v_i^A , ω_i^A and v_i^B , ω_i^B respectively, the relative normal displacement increment at the contact in a time step can be given as,

$$\Delta\alpha = (v_i^B - v_i^A) n_i \Delta t \quad (\text{A.16})$$

where $i=1, 2, 3$ indicates the three components of the velocity.

At the contact, the relative tangential displacement increment over a time-step is,

$$\Delta\delta_i = (v_i^B - v_i^A) \Delta t - \Delta\alpha n_i - (\omega_{i+1}^A n_{i+2} - \omega_{i+2}^A n_{i+1}) R_A \Delta t - (\omega_{i+1}^B n_{i+2} - \omega_{i+2}^B n_{i+1}) R_B \Delta t \quad (\text{A.17})$$

where R_A and R_B are the radii of the two sphere. All the subscripts $i, i+1, i+2$ should be rotated from 1 to 3.

The incremental force due to the normal relative displacement increment is found by substituting $\Delta\alpha$ into (A.9). The updated normal force at the contact, N_C^{new} , is given as,

$$N_C^{new} = N_C^{old} + \Delta N \quad (A.18)$$

where N_C^{old} is the previous normal contact force and ΔN is the normal force increment.

A normal damping force is calculated from,

$$N_D = 2\beta_c \sqrt{nk_n} \Delta\alpha / \Delta t \quad (A.19)$$

where $\beta_c (<1)$ is the coefficient of contact damping, and k_n is the normal stiffness. The total normal force contribution to the out-of-balance force of each sphere is calculated as,

$$N^{new} = N_C^{new} + N_D \quad (A.20)$$

The computation of the tangential force increment due to the tangential displacement increment depends on the interaction law used. If Mindlin's no-slip solution is used, the tangential force-displacement relationship is linear elastic. In this case the resultant tangential force increment can be calculated by substituting $\Delta\delta_i$ into (A.10). However, updating the tangential force with the tangential force increment is much complicated due to the fact that the contact plane may have rotated. Consequently, the direction of the previous tangential force and displacement should be adjusted.

To identify the loading path of the resultant tangential force we must resolve the direction of tangential displacement. In three dimensions, this resultant tangential displacement can have any orientation in the contact plane. The GRANULE program considers the direction of the resultant tangential displacement *at the first time step* of each contact to be positive. For subsequent time steps, we have a *previous* resultant tangential displacement δ . After correcting for the rotation of the contact plane, the orientation of δ is defined by the components δ_i ($i=1, 3$). The new tangential displacement due to the incremental displacement is given by:

$$\delta_i^{new} = \delta_i + \Delta\delta_i \quad (A.21)$$

The sign and magnitude of the updated resultant are given:

$$\delta^{new} = \text{sign}(\delta)\text{sign}(\delta\Delta\delta_i)\sqrt{\delta_i^{new}\delta_i^{new}} \quad (\text{A.22})$$

Further details are given in *Lian et al. (1998)*. Having found the new resultant tangential displacement, we find the magnitude of the resultant tangential displacement increment from:

$$\Delta\delta = \delta^{new} - \delta \quad (\text{A.23})$$

We then obtain the resultant tangential *force* increment ΔT by using (A.10-12), and the resultant tangential force is updated as follows:

$$T_C^{new} = T_C^{old} + \Delta T \quad (\text{A.24})$$

The new resultant tangential force is then set to a limiting value if it exceeds the sliding criterion. The direction of the resultant tangential force is taken to be in the same direction as the resultant tangential displacement:

$$T_i^{new} = T_C^{new} \frac{\delta_i^{new}}{\delta^{new}} \quad (\text{A.25})$$

The tangential damping force at a contact is given by:

$$T_D = 2\beta_c \sqrt{mk_t} \Delta\delta / \Delta t \quad (\text{A.26})$$

(where k is the tangential stiffness).

The tangential force contribution to the out-of-balance force of each sphere is calculated from:

$$T^{new} = T_C^{new} + T_D \quad (\text{A.27})$$

From the new normal and tangential contact forces, the contribution to the out-of-balance force of each sphere is obtained from the following equations:

$$\text{Sphere A} \quad F_i^A = -N^{new} n_i - T_i^{new} \quad (\text{A.28})$$

$$M_i^A = R_A (n_{i+1} T_{i+2}^{new} - n_{i+2} T_{i+1}^{new}) \quad (\text{A.29})$$

Sphere B
$$F_i^B = N^{new} n_i + T_i^{new} \quad (A.30)$$

$$M_i^B = -R_B (n_{i+1} T_{i+2}^{new} - n_{i+2} T_{i+1}^{new}) \quad (A.31)$$

The new resultant forces and moments acting on each sphere are used to determine the new acceleration \ddot{x}_i and $\ddot{\theta}_i$ according to Newton's second law of motion (incorporating global damping):

$$F_i + mg_i - \beta_g \frac{v_i^{new} + v_i^{old}}{2} = m \frac{v_i^{new} - v_i^{old}}{\Delta t} \quad (A.32)$$

$$M_i - \beta_g \frac{\omega_i^{new} + \omega_i^{old}}{2} = I \frac{\omega_i^{new} - \omega_i^{old}}{\Delta t} \quad (A.33)$$

The updated translational and rotational velocities v_i and ω_i are then obtained from:

$$v_i^{new} = \frac{m/\Delta t - \beta_g/2}{m/\Delta t + \beta_g/2} v_i^{old} + \frac{F_i + mg_i}{m/\Delta t + \beta_g/2} \quad (A.34)$$

$$\omega_i^{new} = \frac{I/\Delta t - \beta_g/2}{I/\Delta t + \beta_g/2} \omega_i^{old} + \frac{M_i}{I/\Delta t + \beta_g/2} \quad (A.34)$$

The translation and rotational displacement increments are calculated by simple numerical integration as follows:

Translational
$$\Delta x_i = v_i \Delta t \quad (A.36)$$

Rotational
$$\Delta \Phi_i = \omega_i \Delta t \quad (A.37)$$

Finally the position and rotational orientation of each particle is updated from the following:

$$x_i^{new} = x_i^{old} + \Delta x_i \quad (A.38)$$

$$\Phi_i^{new} = \Phi_i^{old} + \Delta \Phi_i \quad (A.39)$$

These new displacements increments are used to determine the contact force in the next calculation cycle. Equations are applied to each particle in turn. At the end of each cycle, the force sum F , and the moment sum M , of each particle are reset to zero.

A.4 Program GRANULE

The current structure of the GRANULE program is similar to the original program developed by Cundall. The main component of GRANULE is the cyclic simulation module, which calculates the evolution of contact forces and particle movements as described in the previous section. Amongst the other components is an output module which produces graphical and textual output for interpretation of the simulation results.

In the original TRUBAL code all data are stored in a single array $A(I)$. The array $A(I)$ is partitioned into several sub-arrays containing data for the particles, boxes and the link lists of address for particles and contacts. The data structures of this array are shown in Figure A2(a).

The address variables M_1 , M_2 , M_3 and M_5 are set to fixed values at the start of a simulation, after the user has specified how many particles and boxes are required. M_5 indicates the memory limit, which is set in the program. M_2 , M_3 and M_{3A} indicate the upper limits of the arrays of ball data, wall data and box data, respectively. Variables M_{1A} , M_{2A} and M_4 can be dynamically located as the user creates more particles and walls or as the requirements for contacts change during the test. The storage scheme for the link lists and contact arrays is shown in Figure A2(b).

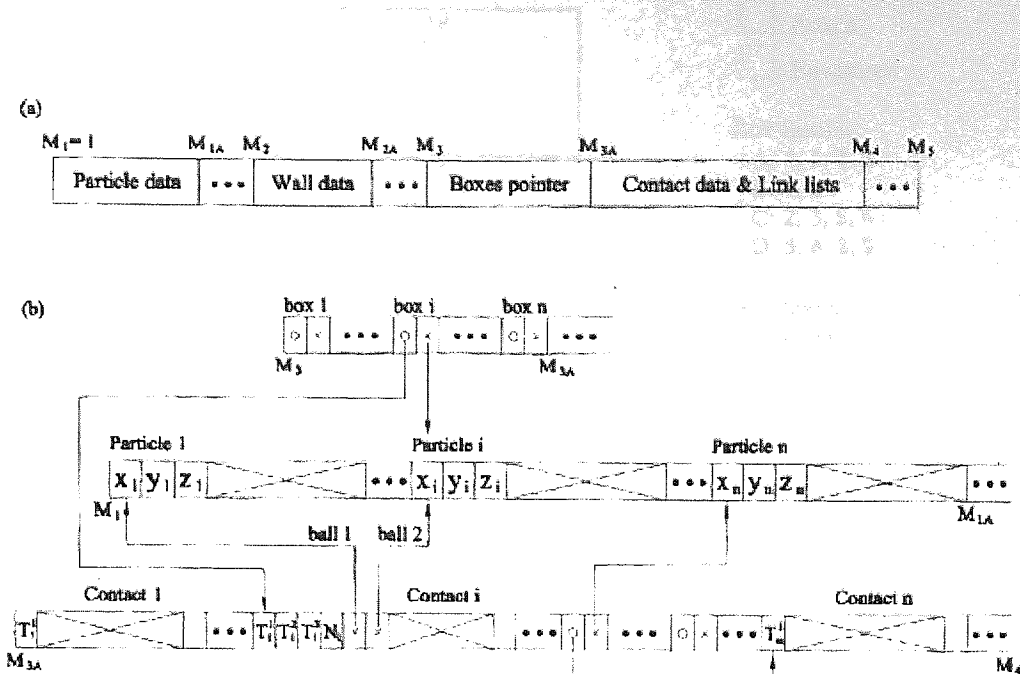
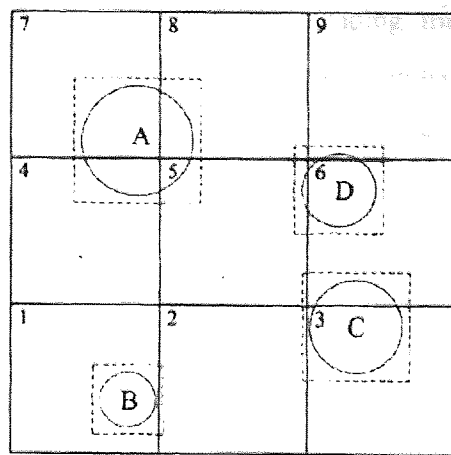


Figure A2: Data structure of TRUBAL: (a) partition of array A(I); (b) scheme of contacts and links

A.5 Contact detection

We require an efficient method for finding possible contacts in the system, since it is computationally prohibitive to test all possible pairs of particles for a contact. The method used in TRUBAL restricts the search to pairs that are in contact or close enough to be in contact at a later time during the simulation. Firstly, the cuboid containing the entire assembly of particles is divided into smaller cubes. These smaller cubes are initially of dimension DEL, where DEL should be larger than the diameter of the largest sphere. In order to search efficiently, DEL should normally be less than twice the largest sphere diameter. Linked lists for each small cube are made by mapping all particles into their appropriate boxes. An “envelope space” with is assigned to each particle and mapped into the box or boxes it occupies (see Figure A3). The envelope dimension is set to $2(R+TOL)$, where R is the radius of the particle and TOL is the tolerance of a specified gap distance (which is a very small value). An exact contact test is then performed over all pairs of “neighbours”. Two particles are considered to be neighbours if they are both mapped into at least one common small cube (see figure A3).



□: Boxes
 □: Envelopes

Box Entries:
 A: 4, 5, 7, 8
 B: 1, 2
 C: 2, 3, 5, 6
 D: 5, 6, 8, 9

Neighbours:
 A: C, D
 B: C
 C: A, B, D
 D: A, C

Figure A3: Searching scheme in 2D

A.6 Damping

In order to model a quasi-static process using DEM, we must include some means to absorb the kinetic energy in the system. A viscous damping can be added into the equations of motion to achieve convergence to a static steady state.

Damping in granular materials is the combined effect of all mechanisms of energy dissipation present in the system. However, these mechanisms are complex and difficult to model. Therefore, simplified “artificial damping” is used to model the global damping response. GRANULE models two types of viscous damping:

- Contact damping considers the energy losses during the force transmission through solid particles, and is required to permit for an assembly of particles to reach quasi-equilibrium. Without contact damping, the contact forces between particles may oscillate indefinitely.
- Global damping is equivalent immersing the constituent particles in a viscous fluid. It is useful to dissipate the kinetic energy during the final stage of preparation of a system in order to avoid excessive computer time. However, the global damping must be switched off before the dynamical DEM simulation is started.

Contact damping is modelled by a dashpot. The damping force is calculated to be proportional to the normal and tangential force increments. After calculating the

contact forces between spheres, damping forces are calculated and added to the contact forces to give the total contributions to the out-of-balance forces of each sphere. The contact damping parameter β_c is given by:

$$\beta_c = \frac{frac}{2\pi\omega} \quad (A.43)$$

where *frac* is the fraction of critical damping at the modal frequency ω .

Global damping is a classical, mass-proportional Rayleigh damping, and is handled in the subroutine that calculates the motion of each sphere. It is analogous to an array of dashpots that connect all particles to the reference axes of the system. The global damping resistance force exerted on each sphere is opposite to its velocity vector (both translational and rotational). The global damping parameter β_g is given by:

$$\beta_g = 2\pi * frac * \omega \quad (A.44)$$

A.7 Numerical stability

Numerical instability is a potential problem in the TRUBAL simulation method. If the integration time-step is greater than a critical value, the scheme is unstable and the results of the simulation are unreliable. In GRANULE, the time step is based on the consideration of the Rayleigh wave speed of force transmission around the surface of elastic bodies. Upon application of a force on an elastic body, the Rayleigh waves are propagated along the surface with a velocity given by:

$$v_R = \alpha \sqrt{\frac{G}{\rho}} \quad (A.45)$$

where ρ is the density of the particle and α is the root of the following equation:

$$(2 - \alpha^2)^4 = 16(1 - \alpha^2) \left[1 - \frac{1 - 2\nu}{2(1 - \nu)} \alpha^2 \right] \quad (A.46)$$

where ν is Poisson's ratio. An approximate solution to this equation is:

$$\alpha = 0.1631\nu + 0.876605 \quad (A.47)$$

The smallest sphere determines the highest velocity of Rayleigh wave propagation in the system. From this, we have the critical time-step as:

$$\Delta t_c = \frac{\pi R_{\min}}{v_R} = \frac{\pi R_{\min}}{\alpha} \sqrt{\frac{\rho}{G}} \quad (\text{A.48})$$

This assumes that all constituent particles have the same properties. If there are different material types for the constituent particles, the critical time-step should be the lowest value found for any particle type. The actual time-step used in GRANULE is a multiple of the Rayleigh critical time-step. The scaling factor "FRAC" is normally less than 0.5:

$$\Delta t = \Delta t_c * FRAC \quad (\text{A.49})$$

Appendix B. Modifications to GRANULE for rotating drum work

This appendix provides further or additional information on the main code changes implemented into GRANULE to facilitate drum simulations in 2D and 3D. See section 3.2 in the main body of the thesis for an outline of each change.

B.1 Data array modifications

The wall array data structure was modified to contain data for the drum wall. The wall array allocated between M2 and M2A contains the following data:

- W(1) Radius of drum wall
- W(2) X-component for the drum centre (computed from W(1) and W(4))
- W(3) Y-component for the drum centre (computed from W(1) and W(4))
- W(4) Displacement of the drum wall from the x-axis and y-axis
- W(5) Drum length
- W(6) Drum speed
- W(10) X-coordinate of drum marker
- W(11) Y-coordinate of drum marker
- W(25) imat, identifies the material properties of the drum wall

B.2 Code additions to GRANULE

B.2.1: A numerical instability check was inserted in subroutine **cycle** (the main calculation loop which iterates once per time step). Unrealistic displacement due to numerical instability can result in a particle leaving the drum. This is checked for explicitly:

```
.....  
  
c      if((N-1).gt.0.and.MOD(N-1,iprt).eq.0) then  
          diffx=a(iab)+a(iab+3)-a(m2+1)  
          diffy=a(iab+1)+a(iab+4)-a(m2+2)  
          distt=sqrt(diffx**2+diffy**2)  
          if(distt.gt.(a(m2)+rball)) then
```

```

nbout=nbout+1
print*, 'Ball-> ',iab, ' GOT OUT of MILL', nbout,n
print*, 'Cords: ',a(iab)+a(iab+3),a(iab+1)+a(iab+4),
      a(iab+2)+a(iab+5)
c----- set it right
111 a(iab) = a(m2+1)-cos(atan(1.0))*radmill*trbran(seed)
a(iab+1) = a(m2+2)+sin(atan(1.0))*radmill*trbran(seed)
diffx=a(iab)-a(m2+1)
diffy=a(iab+1)-a(m2+2)
distt=sqrt(diffx**2+diffy**2)
if(distt.gt.(a(m2)+rball)) goto 111

DFLAG=.TRUE.
GAPMIN=1.0E10
CALL REBOX(iab)
DFLAG=.FALSE.
IF(GAPMIN.LT.0.0) THEN
WRITE(LUNW,*) 'OVERLAP OCCURED -- TRYING AGAIN !!'
GOTO 111
ENDIF

print*, 'Corrected Cords: ',a(iab),a(iab+1),a(iab+2)
a(iab+3) = 0.0
a(iab+4) = 0.0
a(iab+6) = 0.0
a(iab+7) = 0.0
rflag=.true.
c stop
endif
c endif

```

B.2.2: In subroutine **hford**, which models particle force laws, additional code was written to describe the wall velocity, and particle-wall forces.

```

... ..
c Cylindrical wall
else if(iwc.eq.3) then
radius=b2(1)
angvel=b2(6)
dpb2(i)= b2(i+1)
dpb2(i3) = 0.0
endif
... ..

c Cylindrical drum calculations begin to set mill velocity
if(wFlag.and.iwc.eq.3) then

```

```

      call contpt(iab1,iab2,xc)
c      print*, xc(1),xc(2),iab1,iab2
      dzm2=0.0
      do 32 i=1,2
      dpb2(i)=xc(i)
      dpz(i)=dpb2(i)-dpbl(i)-dpbl(i+3)
      rr(i) = dpb2(i) - a(iab2+i)

      dzm2=dzm2+dpz(i)**2
32      continue
      dpz(3)=0.0
      dpb2(3)=dpbl(3)+dpbl(6)
      B2(7)=-angvel*rr(2)
      B2(8)= angvel*rr(1)
      B2(9)=0.0
      endif

      dZM = dSQRT(dZM2)

      ... ..

c----Cylindrical drum calculations begin for overlap between particle
c----and drum wall
c
      if(wflag.and.iwc.eq.3) then
      diffx=a(iab1)+a(iab1+3)-a(iab2+1)
      diffy=a(iab1+1)+a(iab1+4)-a(iab2+2)
      distt=sqrt(diffx**2+diffy**2)
      amlap= radius-(distt+dra)
      drdif=amlap
      endif

      rdif = drdif

      DO 5 I=1,3
      I6=I+6
      z(i) = dpz(i)

      if(wflag.and.iwc.eq.3) then
      UDR(I) = B1(I6) - B2(I6)
      else
      UDR(I) = B2(I6) - B1(I6)
      endif

      ... ..

```

A new subroutine **setwal** was added; it was used to create and setup a cylindrical drum wall:

```

subroutine setwal(iaw)
EXTERNAL WBTEST

```

```

LOGICAL NBYTES
include 'grcom.inc'
COMMON /TCOM/ NBUF(5000),MBUF(5000),NBN(5000),NBM(5000),
MCALL(5000),IBCALL,RAD,X(3),NFN,NFM,NBYES,NB,IWCODE
COMMON /GENCOM/ GAPMIN

pi=4.0*atan(1.0)
degrad = pi/180.
a(iaw) = radmill
do 1 i=1,2
a(iaw+i)= agap+radmill
1 continue
a(iaw+3) = agap
a(iaw+4) = alength
a(iaw+5) = tempomega

c
c wall velocity in x,y, and z direction not required
a(iaw+6)= 0.0
a(iaw+7)= 0.0
a(iaw+8)= 0.0

c location of a point on the mill shell
a(iaw+9) = radmill+agap
a(iaw+10) = agap
ia(iaw+11) = 3
ia(iaw+12) = 3
iwcode=3

c Force sum on wall
a(iaw+18) = 0
a(iaw+19) = 0
a(iaw+20) = 0

c Set nwalan according to the size of the box
nwalan =1.0
num = 360.0/nwalan

c box at least 120 points on the circle (trace of the cylinder
c on the xy-plane) get a point on the circle as xc and yc
radius=radmill

tolm=0.001*radmill
ggap=agap
do 100 jj=1,3

if(jj.eq.2) then
radius=radmill-tolm
ggap=agap+tolm
endif

if(jj.eq.3)then
radius=radmill+tolm
ggap=agap-tolm
endif

```

```

chord = 2*radius*sin(nwalan/2.0*degrad)
diag_box=sqrt(del(1)*del(2))
if(chord.gt.diag_box) error=.true.

xp = radius+ggap
yp = ggap
size=del(1)
c Box the mill shell
do 11 i=1,num
xp = xp + chord*cos(((i-1)*nwalan+nwalan/2)*degrad)
yp = yp + chord*sin(((i-1)*nwalan+nwalan/2)*degrad)

nxx = int(xp/size) + 1
nyy = int(yp/size) + 1
nprime = (nyy-1)*nx(1)+(nxx-1)
num1 = int(ggap/size) + 1
num2 = int((ggap+alength)/size)+1
if (jj.eq.1.or.jj.eq.2) num2 = int((ggap+alength)/size)

do 12 ii=num1,num2
nb = 2*(nprime+(ii-1)*nx(1)*nx(2)) + m3

write(lunwcl, ' (2(i10,1x),2(e10.3,1x),4(i7,1x),e10.3,1x) '
(nb-m3),nb, xp, yp, nxx, nyy, num1, num2, alength

nbytes = .true.

GAPMIN=1.0E10
DFLAG=.TRUE.
CALL SEARCH(WBTEST,IAW)
IF(GAPMIN.LT.0.0) THEN
WRITE(LUNW,*) 'WALL REJECTED BECAUSE OF OVERLAP'
NERR=2
ERROR=.TRUE.
ENDIF
IF(ERROR) THEN
WRITE(LUNW,*) 'ERROR RETURN IN SETWAL CALL'
STOP
ENDIF

nbytes = .true.
dflag = .false.
call search(wbtest,iaw)

12 continue
11 continue
100 continue
nwall=nwall+1
c Note that iaw is not incremented. Therefore all segments point
c to the beginning of the wall location in the array.
return

```


end

In subroutine **bbtest**, a number of extra calculations are performed for the drum to check for collisions:

```
c---- Do calculations for cylindrical wall
      if(iwcode.eq.3) goto 39
36 GAP=ZM-RAD
      IF(GAP-TOL.GT.0.0) GOTO 5000
      IF(DFLAG) THEN
        GAPMIN=AMIN1(GAPMIN,GAP)
        GOTO 5000
      ENDIF
      IF(ZM.LE.0.0) THEN
        WRITE(LUNW,1700) IAB1,ZM
        STOP
      ENDIF
c --- CONTACT COORDINATE ----
      RAT=(RAD+0.5*GAP)/ZM
      DO 38 I=1,3
        IF(IWCODE.EQ.1) THEN
          if(ia(iab1+12).eq.0) then
c ----contact with infinite plane wall---
            XC(I)=XCALL(I)
            IF(Z(I).NE.0.0) XC(I)=XCALL(I)+(r1-XCALL(I))*RAT
          else
c ----contact with finite plane wall----
            xc(1)=xc1(1)
            xc(2)=xc1(2)
            xc(3)=xc1(3)
          endif
        ENDIF
      c Is it true????

      IF(IWCODE.EQ.2) THEN
        XC(I)=XCALL(I)+Z(I)*RAT*ZM/ZM1
      ENDIF
38 CONTINUE
      goto 12
c----- Mill calculation-----
39      if(.not.wbflag) then

        ibpp=ibcall
        iwpp = iab1
        if(iwpp.lt.m2) print*, 'ERROR in BBTEST'
      else
        ibpp=iab1
        iwpp=iab
```

```

endif

radius = a(iwpp)
diffx=a(ibpp)+a(ibpp+3)-a(iwpp+1)
diffy=a(ibpp+1)+a(ibpp+4)-a(iwpp+2)
distt=sqrt(diffx**2+diffy**2)
gap= radius-(distt+rad)

if(dflag) then
  gapmin=amin1(gapmin,gap)
  goto 5000
endif
if((gap-tol).gt.0.0) goto 5000
call contpt(ibpp,iwpp,xc)
goto 12

```

B.2.3: A new subroutine **pmill** was written to plot the drum wall:

```

c      =====
c      subroutine pmill
c      =====
c      to plot balls
c
  save
  external ball2d, gensphere, plotdrum
  integer ptflag
  include 'grcom.inc'
  include 'matcom.inc'
  common/pltcom3/ scal,xl(3),thl(3),z(3),znorm(3),sxm(3),udot(3),
.   tdot(3),disp(3),rotl(3),xcav(3),dxm(3),xml,xm2,xm3,icn,ifn
  dimension thrad(3)
  double precision dprad,xmx
  common /gpblk1/ dprad,xmx(3),cenx,ceny,cenz,rtx,rtz,rtz,
.
.   ibopt,iball,iaxes,ncls,iaggm,kcl,kveloc,
.   kforce,kcndgm,krdsp,kstress,kwall,kwind,kmill,
.   narg,kcolvel,kradvel,ktanvel,kcradvel,kctanvel,
.   kwet,kdry,knrelv,ktrelv
  common /gpblk2/ udMIN,udMAX,udMEAN,vorig(3),vleng(3),vend(3),
.   wv1(3),wv2(3),wv3(3),wv4(3),idim,ictyp,ne,nd,nn,
.   icnd,isl,iaggm,itic,ptflag
  common /gpblk5/ sprayc(5),kspray,betal
c      to plot drum wall
  ptflag=1
  iab=m2
  dprad=a(m2)
  cenx=a(m2+1)
  ceny=a(m2+2)
  cenz=a(m2+3)
  rtx=a(m2+4)
  iaggm=2

```

```

ncls=0
wv1(1)=a(m2+14)
wv1(2)=a(m2+15)
wv1(3)=a(m2+16)
xmx(1) = 2.0*(agap+a(m2))
xmx(2) = xmx(1)
if(.not.twod) then
  call plotdrum
else if(twod) then
  call ball2d
endif
ptflag=0
return
end

```

B.2.4: A new subroutine called **pcolvel** was written to plot particles in the system as colour coded solid balls according to their velocity. Another subroutine called **pveloc** was written to plot the particle velocities with colour-coded arrows. In addition, similar routines were written to plot the radial and tangential components of velocities as colour coded solid balls and colour-coded arrows called **pradvel**, **ptanvel**, **pcradvel** and **pectanvel**. Subroutine **pcolvel** is given here as one example of the functions:

```

c      =====
c      subroutine pcolvel
c      =====
c
c      to color code balls according to there velocity range
c
c      save
c      external colorvel
c      logical clplot,cl_flg
c      include 'grcom.inc'
c      include 'matcom.inc'
c      common /clcom/ icarray,clplot,cl_flg,ncsize1,ncsize2,bndflag
c      common /pltcom3/ scal,x1(3),th1(3),z(3),znorm(3),sxm(3),udot(3),
c      .   tdot(3),disp(3),rot1(3),xcav(3),dxm(3),xm1,xm2,xm3,icn,ifn
c      dimension icarray(120000,16)
c      double precision dprad,xmx,const1,const2,const3,const4
c      common /gpblk1/ dprad,xmx(3),cenx,ceny,cenz,rtx,rtz,rtz,
c      .   ibopt,iball,iaxes,ncls,iaggm,kcl,kveloc,
c      .   kforce,kcndgm,krdsp,kstress,kwall,kwind,kmill,
c      .   narg,kcolvel,kradvel,ktanvel,kcradvel,kctanvel,
c      .   kwet,kdry,knrelv,ktrelv,kcvel
c      common /gpblk2/ udMIN,udMAX,udMEAN,vorig(3),vleng(3),vend(3),
c      .   wv1(3),wv2(3),wv3(3),wv4(3),idim,ictyp,ne,nd,nn,
c      .   icnd,isl,iaggm,itic,ptflag,krefresh
c

```

```

idim = 3
if(twod) idim = 2
c          --- scan to get MAXimum and MEAN velocities
udMAX = 0.0
udSUM = 0.0
udMIN = 1.0e30
IAB   = M1
DO 305 N = 1,NBALL
    ud1 = a(iab+6)
    ud2 = a(iab+7)
    ud3 = a(iab+8)
    ud  = sqrt (ud1*ud1 + ud2*ud2 + ud3*ud3)
    udMIN = aMIN1(udMIN,ud)
    udMAX = aMAX1(udMAX,ud)
    udSUM = udSUM + ud
305 IAB=IAB+NVARB
    if (udMAX .eq. 0.0) goto 999
    udMEAN = udSUM/float(NBALL)

    itic = 3

c scale the velocity to the mill linear velocity and print
c ranges of the color coded velocity

const1=0.35
const2=0.70
const3=0.85
const4=0.94
write(*,*)
write(*,*) 'VELOCITY RANGE FOR COLOURS>'
write(*,*) '>= 0          and          <',const1
write(*,*) '>= ',const1,' and <',const2
write(*,*) '>= ',const2,' and <',const3
write(*,*) '>= ',const3,' and <',const4
write(*,*) '>= ',const4
write(*,*)

    IAB=M2
    radmill=A(IAB)
    gap=A(IAB+3)
    vscal = 80.00 * RMAX / (radmill*A(IAB+5))
    vorig(1)=radmill+(0.1*gap)
    vorig(2)=0.1*gap
    vorig(3)=xmax(3)/2.0
    vleng(1)=radmill*A(IAB+5)*vscal
    vleng(2)=0.0
    vleng(3)=0.0
    itic=3
    iaggmv=1
    idim=2
    itic = 0

```

```

c ----- scan again to plot
  IAB = M1
  DO 320 N = 1,NBALL
    DO 310 I = 1,3
      IAB1 = IAB+I-1
      IAB2 = IAB+I+2
      XL(I) = (A(IAB1)+A(IAB2))
      vorig(i) = (A(IAB1)+A(IAB2))
      vleng(i) = a(iab+i+5) * vscal
      tdot(i) = a(iab+i+14)
      ITYP1 = IA(IAB+24)
      ITPS1 = ITYP1 / 64
      ITPM1 = ITYP1 - ITPS1 * 64
      if(ITPS1.eq.0) then
        rad = A(IAB+30)
      else
        rad = R(ITPS1)
      endif
      nagm = ia(iab+29)
      iaggm = nagm
310    CONTINUE
c if not in current window do not plot
  DO 315 I=1,idim
    IF(XL(I).LT.WINDL(I).OR.XL(I).GT.WINDU(I)) GOTO 320
315  continue
    itic=1
c --arrow for 2-d --
    if(twod) itic=2
    iaggmv=ia(iab+29)
c --choose color of arrow according to size of velocity
    ud1 = a(iab+6)
    ud2 = a(iab+7)
    ud3 = a(iab+8)
    ud = sqrt (ud1*ud1 + ud2*ud2 + ud3*ud3)
    IIAB=M2
    rmillspeed=A(IIAB)*A(IIAB+5)
    if (ud.lt.(const1*rmillspeed)) then
      iaggmv=1
      goto 330
    elseif (ud.lt.(const2*rmillspeed)) then
      iaggmv=2
      goto 330
    elseif (ud.lt.(const3*rmillspeed)) then
      iaggmv=3
      goto 330
    elseif (ud.lt.(const4*rmillspeed)) then
      iaggmv=4
      goto 330
    else
      iaggmv=5
      goto 330

```

```

endif
330 continue
dprad = rad
cenx = vorig(1)
ceny = vorig(2)
cenz = vorig(3)
call colorvel
320 IAB=IAB+NVARB
999 return
End

```

B.2.5: The code modifications taken from David Kafui's DEM fluidized bed spray granulation program are listed in this section.

The "spray" command is defined in subroutine **next** (which parses user input).

```

. 'R','O','T',' ','S','J','E',' ','S','P','R',' ',' ',item/
. 895,800,810),JUMP

-----read parameters for spray-----
810 id_sp = ivar(2)
if (miss) goto 1010
if (bad) goto 1020

if(id_sp.gt.nsprays) then
write(lunw,*)'Spray id greater than storage allocatio'
goto 5
endif

xs=rvar(3)
ys=rvar(4)
zs=rvar(5)
thets=rvar(6)
sh=rvar(7)
gwmax=rvar(8)
dof=rvar(9)
tdmax=rvar(10)
if(miss) goto 1010
if(bad) goto 1020

if(dof.lt.1.0)then
write(lunw,*)'Dry out factor must be greater or equal to 1'
goto 5
endif

spray(id_sp,1)=xs
spray(id_sp,2)=ys
spray(id_sp,3)=zs

```

```

spray(id_sp,4)=thets
spray(id_sp,5)=sh
spray(id_sp,6)=gwmax
spray(id_sp,7)=dof
spray(id_sp,8)=tdmax

```

```
sprayflag=.true.
```

```
goto 5
```

The ball array B(*) and contact array C(*) were extended, and a few of these array elements were changed for the spray code, as below.

```

c      =====
c      SUBROUTINE SETUP
c      =====

c B(27) -- used to store "wet" surface energy gw
c B(31) -- used to store the time spent in spray zone ts (s)
c B(32) -- max surface energy for wet adhesive gwmax (J/m^2)
c B(33) -- surface energy dry out factor, dof (>=1)
c B(34) -- max. dry out time - tdmax (s)
c B(35) -- time since leaving spray zone tso (s)

c C(28) -- active surfacw energy gd
c C(28) -- age of bond, ta
c C(28) -- wet surface energy, gw
c C(28) -- dry out factor, dof
c C(28) -- dry out time td

```

The main spray code calculations are done in subroutine, subroutines 'cycle', 'hford', and 'motion' (which handles the update of particle positions):

```

c      =====
c      SUBROUTINE CYCLE
c      =====

... ..

if(.not.sprayflag) then

    if(wflag)then
        COHES2=coh(itpm2)
    else
        COHE2=ARGAM(ITPM1,ITPM2)
    endif

else if(sprayflag) then

```

```

cohe2=0.

c extract appropriate surface energy value from particles
c if zero gactive, in contact array but non-zero in particle

      if(a(iad+27).LE.0.0.AND.(a(iab1+26).GT.0.0.OR.(iab2.lt.M2.AND.
x      a(iab2+26).GT.0.0))) then
c use average surface energy of balls 1 & 2

      blactive = .false.
      b2active = .false.
      blspray = .false.
      b2spray = .false.
      bondflg = .false.

c check ball 1
      if(a(iab1+34).gt.0.0) then
c ball1 left spray zone - surface energy decaying
c establish if surface is still active
c* use max decay period for all surface energy values in check run
      tdecay=a(iab1+26)*a(iab1+33)/a(iab1+31)
      if(a(iab1+34).le.tdecay)blactive=.true.
      else if(a(iab1+30).gt.0.) then
c if tsp gt 0, ball1 still in spray zone
      blspray=.true.
      endif
c check ball2
      if(iab2.lt.M2.and.a(iab2+34).gt.0.0) then
c ball2 left spray zone - surface energy decaying
c establish if surface is still active
c* use max decay period for all surface energy values in check run
      tdecay=a(iab2+26)* a(iab2+33)/ a(iab2+31)
      if(a(iab2+34).le.tdecay)b2active = .true.
      else if(a(iab2+30).gt.0.)then
c if tsp gt 0, ball2 still in spray zone
      b2spray=.true.
      endif

      if(blactive.AND.b2active) then
c both balls outside spray zone & active
      a(iad+27) = 0.5 * (a(iab1+26) * exp(-a(iab1+34)) +
x      a(iab2+26) * exp(-a(iab2+34)))
      a(iad+29) = 0.5 * (a(iab1+26) + a(iab2+26))
      a(iad+30) = 0.5 * (a(iab1+32) + a(iab2+32))
      a(iad+31) = 0.5 * (a(iab1+26) * a(iab1+33)/ a(iab1+31) +
x      a(iab2+26) * a(iab2+33)/ a(iab2+31))
      a(iad+28) = 0.
      bondflg=.true.

      else if (.not.b2spray.AND.blactive) then

```



```

c ball1 active out-SZ, ball2 out-SZ inactive
  a(iad+27) = 0.5 * (a(iab1+26) * exp(-a(iab1+34)))
  a(iad+29) = 0.5 * (a(iab1+26))
  a(iad+30) = 0.5 * (a(iab1+32))
  a(iad+31) = 0.5 * (a(iab1+26) * a(iab1+33)/ a(iab1+31))
  a(iad+28) = 0.
  bondflg=.true.

  a(iab2+26)=0.0
  a(iab2+30)=0.0
  a(iab2+31)=0.0
  a(iab2+32)=0.0
  a(iab2+33)=0.0
  a(iab2+34)=0.0

  else if (.not.blspray.AND.b2active) then
c ball2 active out-SZ, ball1 out-SZ inactive
  a(iad+27) = 0.5 * (a(iab2+26) * exp(-a(iab2+34)))
  a(iad+29) = 0.5 * (a(iab2+26))
  a(iad+30) = 0.5 * (a(iab2+32))
  a(iad+31) = 0.5 * (a(iab2+26) * a(iab2+33)/ a(iab2+31))
  a(iad+28) = 0.
  bondflg=.true.

  a(iab1+26)=0.0
  a(iab1+30)=0.0
  a(iab1+31)=0.0
  a(iab1+32)=0.0
  a(iab1+33)=0.0
  a(iab1+34)=0.0

  else if (blactive.AND.b2spray) then
c ball1 active out-SZ, ball2 in-SZ
  a(iad+27) = 0.5 * (a(iab1+26) * exp(-a(iab1+34)) + a(iab2+26))
  a(iad+29) = 0.5 * (a(iab1+26) + a(iab2+26))
  a(iad+30) = 0.5 * (a(iab1+32) + a(iab2+32))
  a(iad+31) = 0.5 * (a(iab1+26) * a(iab1+33)/ a(iab1+31) +
x      a(iab2+26) * a(iab2+33)/ a(iab2+31))
  a(iad+28) = 0.
  bondflg=.true.

  else if (b2active.AND.blspray) then
c ball2 active out-SZ, ball1 in-SZ
  a(iad+27) = 0.5 * (a(iab2+26) * exp(-a(iab2+34)) + a(iab1+26))
  a(iad+29) = 0.5 * (a(iab1+26) + a(iab2+26))
  a(iad+30) = 0.5 * (a(iab1+32) + a(iab2+32))
  a(iad+31) = 0.5 * (a(iab1+26) * a(iab1+33)/ a(iab1+31) +
x      a(iab2+26) * a(iab2+33)/ a(iab2+31))
  a(iad+28) = 0.
  bondflg=.true.

```

```

else
c both balls out-SZ and inactive

      a(iab1+26)=0.0
      a(iab1+30)=0.0
      a(iab1+31)=0.0
      a(iab1+32)=0.0
      a(iab1+33)=0.0
      a(iab1+34)=0.0

      a(iab2+26)=0.0
      a(iab2+30)=0.0
      a(iab2+31)=0.0
      a(iab2+32)=0.0
      a(iab2+33)=0.0
      a(iab2+34)=0.0

      bondflg = .false.

      goto 104

endif

else if(a(iad+27).GT.0.0)then
c drying bond - update age and strength
      a(iad+28)=a(iad+28)+tdel
      t_age=a(iad+28)
      dof=a(iad+30)
      gdry=dof*a(iad+29)
      if(t_age.GE.a(iad+31).AND.a(iad+27).NE.gdry)then
          a(iad+27)=gdry
      else if(t_age.LT.a(iad+31))then
          a(iad+27)=a(iad+29)+(dof-1.0)*(1.0-exp(-t_age))
      endif
endif
endif

104 continue

      COHE2=a(iad+27)

endif

c =====
      SUBROUTINE MOTION
c =====

      ... ..

DIMENSION B(*),SY(20)

```

```

c-----spray array content-----
c spray(id,1)    spray point x-coordinate
c spray(id,2)    spray point y-coordinate
c spray(id,3)    spray point z-coordinate
c spray(id,4)    spray cone angle
c spray(id,5)    vertical extent of spray cone
c spray(id,6)    maximum energy for "wet" binder
c spray(id,7)    dry out factor (gdry=dof*gwet)
c spray(id,8)    maximum dryout time
c-----

IF (sprayflag) THEN

c check if particle is in a spray zone
c if left spray zone, accumulate time since it left spray zone
c if ts exceeds td and it has not reentered a spray zone, set
c gwet, gdry, tdry to zero and ts to zero for any new contacts
c if it reenters spray zone before dryout, retain previous
c spray values and replace with new ones only if higher

      xp  =B(1)+B(4)
      yp  =B(2)+B(5)
      zp  =B(3)+B(6)
      gactive =B(27)
      gwmax =B(32)
      dof  =B(33)
      tdmx =B(34)
      ts   =B(35)
c **daksha's code addition, to change cords of ball to those in the new system

      betal=50.0*degrade
      xp=((B(1)+B(4))*cos(betal)+(B(2)+B(5))*sin(betal)
      yp=((B(2)+B(5))*cos(betal)-(B(1)+B(4))*sin(betal)

c** change cords of ball to those in the new system
c** temp holds old spray cords and spray holds the ones in new system as expected
      temp(1,1)=spray(1,1)
      temp(1,2)=spray(1,2)
      spray(1,1)=(temp(1,1)cos(betal)+(temp(1,2))*sin(betal)
      spray(1,2)=(temp(1,2)cos(betal)+(temp(1,1))*sin(betal)
c**daksha's changes stop here
c outside vertical range of any spray zone?

do ii=1,nsprays
  if(spray(ii,5).ne.0.)then
    sy(ii)=spray(ii,2)-spray(ii,5)
    if(yp.LT.spray(ii,2).and.yp.GE.sy(ii).and.
x    spray(ii,5).NE.0.)goto 38
    endif
  enddo

```

```

c not within vertical range of any active spray
c check if it has been in an active spray zone and
c if wet accumulate active time; if dry switch off

35 if(gwmax.gt.0.)td=gactive*tdmax/gwmax
   if(td.GT.0.0.AND.gactive.GT.0.0.AND.ts.LT.td) then

       B(35)=B(35)+tdel

   else if(td.GT.0.0.AND.gactive.GT.0.0.AND.ts.GE.td) then
       B(27)=0.
       B(31)=0.
       B(32)=0.
       B(33)=0.
       B(34)=0.
       B(35)=0.
   endif

   goto 40

c within vertical range of at least one active spray

138 continue

c detailed check if in spray zone and which one
c distance to nearest spray zone

dspm=1.0e10
iin=0

do ii=1,nsprays
  if(spray(ii,5).NE.0.)
x   dsp=sqrt((xp-spray(ii,1))*(xp-spray(ii,1))+
x       (yp-spray(ii,2))*(yp-spray(ii,2))+
x       (zp-spray(ii,3))*(zp-spray(ii,3)))
  if(dsp.LT.dspm)then
    dspm=dsp
    iin=ii
  endif
end do

c is particle within spray zone of spray iin ?
c compare substended angle of particle from spray source with
c cone spray angle

if(iin.NE.0.AND.spray(iin,5).NE.0.)then
  ptheta=ATAN(sqrt((xp-spray(iin,1))*(xp-spray(iin,1))+
x       (zp-spray(iin,3))*(zp-spray(iin,3)))/
x       (spray(iin,2)-yp))
  ptheta=ptheta/deggrad
  hthets=0.5*spray(iin,4)

```

```

    else
c nearest spray is inactive
    goto 40

endif

    if(ptheta.LE.hthets)then
c time in spray zone iin
    B(31)=B(31)+tdel
    B(35)=0.
    If(B(32).LE.0.)then
        B(32)=spray(iin,6)
        B(33)=spray(iin,7)
        B(34)=spray(iin,8)
    endif

    sm=spray(iin,5)/cos(degrad*spray(iin,4)/2.0)
    s =dspm/sm
    ts=B(31)

    gactive=B(32)*(exp(-s))*(1.-exp(-ts))
    if(gactive.GT.B(27)) B(27)=gactive

c not in spray zone
    else
c if has been in spray zone check if surface activity fully decayed
    if(B(32).GT.0.)tds=B(27)*B(34)/B(32)
    if(tds.GT.0.0.AND.B(27).GT.0.0.AND.B(35).LT.tds)then
c not fully decayed, increment time spent outside spray zone
        B(35)=B(35)+tdel

        else if(tds.GT.0.0.AND.B(27).GT.0.0.AND.B(35).GE.tds)then
c fully decayed, zero appropriate storage locations
            B(27)=0.
            B(31)=0.
            B(32)=0.
            B(33)=0.
            B(34)=0.
            B(35)=0.
        endif

    endif

40 continue

c **Daksha's code addition, restore spray and ball cords to original value
    xp=B(1)+B(4)
    yp=B(2)+B(5)
    spray(1,1)=temp(1,1)
    spray(1,2)=temp(1,2)

```

```

        ENDIF

c =====
SUBROUTINE HFORD
c =====

        ... ..

IF(.not.sprayflag) THEN
  if (impflag.and.cohflg) then
    if (c(16).le.0.0.or.c(16).eq.cohes1) cohes=cohes1
  else if (.not.cohflg.and.impflag.and.((ngm1.eq.1.and.ngm2.eq.2)
x      .or.(ngm1.eq.2.and.ngm2.eq.1).or.(ngm1.eq.1.and.
x      ngm2.eq.0))) then
    cohes=cohes1
  endif
ENDIF

. . . . .

212 DO 211 I=7, NVARC
211 C(I)=0.0
    If (conext) then
      DFLAG=.true.
      goto 225
    endif

c if sprayflag and reached this point, then contact broken
c hence set active surface energy (c28), wet surface energy (c30),
c age of bond (c29), dry-out factor (c31) and dry-out time (c32)
c to zero

    if(sprayflag.and.c(30).ne.0.)then
      c(28) = 0.
      c(29) = 0.
      c(30) = 0.
      c(31) = 0.
      c(32) = 0.
    endif

220 continue

```

B.2.6: Additional code was written to incline the spray by 50⁰ in subroutine **cycle** as below:

```

    betal=50.0*degrad
    xp=(a(iab)+a(iab+3))*cos(betal)+(a(iab+1)+a(iab+4))*sin(betal)
    yp=(a(iab+1)+a(iab+4))*cos(betal)-(a(iab)+a(iab+3))*sin(betal)

```

... ..

c change spray coordinates to those in the new system

tempo(1,1)= spray(1,1)

tempo(1,2)= spray(1,2)

spray(1,1)= (tempo(1,1))*cos(betal)+(tempo(1,2))*sin(betal)

spray(1,2)= (tempo(1,2))*cos(betal)-(tempo(1,1))*sin(betal)

... ..

c restore spray and ball coordinates to original value

xp=a(iab)+a(iab+3)

yp=a(iab+1)+a(iab+4)

spray(1,1)=tempo(1,1)

spray(1,2)=tempo(1,2)

... ..

Appendix C. Ball-wall contacts only

Below is a list of the forces acting on the drum wall. Each force, F is given in its components form (F_x, F_y) and also in terms of the normal and tangential force to the wall, (T_x, T_y) and (N_x, N_y) respectively.

T_x	T_y	N_y	N_z	F_x	F_y
0.108052E+00	-.378145E-01	-.176185E+00	-.498000E+00	-.681331E-1	-.535815E+0
0.262683E-01	0.271085E+00	0.585701E-01	-.784116E+00	0.848384E-1	-.513032E+0
-.298215E-01	-.114636E-01	0.106705E+00	-.278693E+00	0.768834E-1	-.290157E+0
0.810292E-02	-.121133E-01	-.368651E-01	-.504399E-01	-.287622E-1	-.625532E-1
-.889927E-01	-.684486E-01	0.208028E+00	-.269850E+00	0.119035E+0	-.338299E+0
0.157809E+00	0.113975E+00	-.493104E+00	-.266560E+00	-.335295E+0	-.152586E+0
-.237620E-01	-.330568E-01	0.120653E+00	-.866759E-01	0.968913E-1	-.119733E+0
0.512443E-02	-.286260E-01	-.839076E-01	-.148032E-01	-.787831E-1	-.434292E-1
0.113873E-02	0.110179E-01	0.110699E+00	-.127071E-01	0.111838E+0	-.168919E-2

The ball number and its coordinates $(x+\Delta x, y+\Delta y)$ are listed for all ball-wall contact:

Ball no.	$x+\Delta x$	$y+\Delta y$
4	0.632E-01	0.233E-01
1	0.899E-01	0.197E-01
5	0.108E+00	0.238E-01
10	0.464E-01	0.321E-01
8	0.125E+00	0.331E-01
14	0.274E-01	0.539E-01
19	0.138E+00	0.468E-01
22	0.205E-01	0.736E-01
21	0.150E+00	0.775E-01

Sum of F_x = $-2.1487288293428719E-02$

Sum of F_y = -2.057291805744171

Below is a list of the resultant force acting on each particle.

Force components:

Ball no.	ADDRESS	x	y	z
1	1	-0.5160E-04	0.9345E-01	0.0000E+00
2	35	-0.4627E-05	0.9335E-01	0.0000E+00
3	69	0.9798E-05	0.9338E-01	0.0000E+00
4	103	0.2181E-02	0.9955E-01	0.0000E+00
5	137	-0.3896E-04	0.9335E-01	0.0000E+00
6	171	0.5849E-06	0.9334E-01	0.0000E+00
7	205	-0.1416E-04	0.9338E-01	0.0000E+00
8	239	-0.3035E-03	0.9375E-01	0.0000E+00
9	273	0.3342E-04	0.9338E-01	0.0000E+00
10	307	0.2618E-04	0.9345E-01	0.0000E+00
11	341	0.3953E-04	0.9348E-01	0.0000E+00
12	375	0.1925E-04	0.9338E-01	0.0000E+00
13	409	0.1548E-04	0.9338E-01	0.0000E+00
14	443	0.2073E-04	0.9337E-01	0.0000E+00
15	477	-0.2384E-04	0.9335E-01	0.0000E+00
16	511	0.5106E-04	0.9335E-01	0.0000E+00
17	545	-0.1319E-03	0.9342E-01	0.0000E+00
18	579	-0.8652E-04	0.9346E-01	0.0000E+00
19	613	0.2862E-02	0.9135E-01	0.0000E+00
20	647	-0.1141E-03	0.9326E-01	0.0000E+00
21	681	0.1704E-01	0.9149E-01	0.0000E+00
22	715	0.3529E-04	0.9335E-01	0.0000E+00

TOTAL SUM of x force component = 0.21562913E-01

TOTAL SUM of y force component = 0.20570147E+01

TOTAL SUM of z force component = 0.00000000E+00

Particle Radius = 0.94999997E-02

Pi = 0.31415927E+01

Particle Density = 0.26500000E+04

Gravity = 0.00000000E+00 -0.981004E+01 0.00000000E+00

1 Particle Weight = -0.93362890E-01

Total Weight = -0.20539837E+01

Appendix D. Circulation period of tracked particles

In order to find an approximate period of circulation for each of the twenty-two particles that was tracked in the 3-D cascading drum, see section 6.3.2 of the thesis, the sinusoidal function,

$$x(t) = a \sin (bt + c) + d \quad (\text{D.1})$$

was fitted to the x-t evolution plot for each of the tracked particles and values of a, b, c and d were obtained for each of these fitted curves. The following table summaries the results from the fitted curves for all the tracked particles.

Particle no.	a	b	c	d
1	-0.01066	22.16963	3.759625	0.022417
2	0.012774	16.89387	18.87943	0.021447
3	-0.00848	24.78777	6.491107	0.023931
4	0.013695	16.60749	18.80336	0.020283
5	0.009081	23.13674	6.675593	0.023099
6	-0.00782	25.415	6.317511	0.024179
7	-0.01066	22.16963	3.759625	0.022417
8	0.003996	30.55519	2.746129	0.024928
9	0.010701	19.53193	4.067502	0.02776
10	0.011729	19.7829	9.223748	0.021459
11	0.012144	19.31191	9.806923	0.021244
12	-0.01235	21.19823	3.646203	0.021041
13	0.004841	29.1694	3.631765	0.024616
14	-0.00334	30.45856	4.998043	0.025094
15	-0.00173	32.50582	2.373691	0.025538
16	0.008863	23.55898	9.604188	0.024179
17	-0.01243	20.46407	14.69699	0.020759
18	0.008157	23.54022	8.758084	0.023863
19	0.009622	20.63424	9.765987	0.022642
20	0.007648	25.00717	5.808675	0.023836
21	-0.01125	23.18425	7.549844	0.020608
22	-0.0068	26.78832	11.45521	0.024522

The frequency b for the fitted curve is related to the period of circulation as simply $2\pi/b$.